



ELSEVIER

Available online at www.sciencedirect.com



Surface Science Reports 48 (2003) 53–229

surface science
reports

www.elsevier.com/locate/surfrep

The surface science of titanium dioxide

Ulrike Diebold*

Department of Physics, Tulane University, New Orleans, LA 70118, USA

Manuscript received in final form 7 October 2002

Abstract

Titanium dioxide is the most investigated single-crystalline system in the surface science of metal oxides, and the literature on rutile (1 1 0), (1 0 0), (0 0 1), and anatase surfaces is reviewed. This paper starts with a summary of the wide variety of technical fields where TiO_2 is of importance. The bulk structure and bulk defects (as far as relevant to the surface properties) are briefly reviewed. Rules to predict stable oxide surfaces are exemplified on rutile (1 1 0). The surface structure of rutile (1 1 0) is discussed in some detail. Theoretically predicted and experimentally determined relaxations of surface geometries are compared, and defects (step edge orientations, point and line defects, impurities, surface manifestations of crystallographic shear planes—CSPs) are discussed, as well as the image contrast in scanning tunneling microscopy (STM). The controversy about the correct model for the (1 × 2) reconstruction appears to be settled. Different surface preparation methods, such as reoxidation of reduced crystals, can cause a drastic effect on surface geometries and morphology, and recommendations for preparing different TiO_2 (1 1 0) surfaces are given. The structure of the TiO_2 (1 0 0)-(1 × 1) surface is discussed and the proposed models for the (1 × 3) reconstruction are critically reviewed. Very recent results on anatase (1 0 0) and (1 0 1) surfaces are included.

The electronic structure of stoichiometric TiO_2 surfaces is now well understood. Surface defects can be detected with a variety of surface spectroscopies. The vibrational structure is dominated by strong Fuchs–Kliewer phonons, and high-resolution electron energy loss spectra often need to be deconvoluted in order to render useful information about adsorbed molecules.

The growth of metals (Li, Na, K, Cs, Ca, Al, Ti, V, Nb, Cr, Mo, Mn, Fe, Co, Rh, Ir, Ni, Pd, Pt, Cu, Ag, Au) as well as some metal oxides on TiO_2 is reviewed. The tendency to ‘wet’ the overlayer, the growth morphology, the epitaxial relationship, and the strength of the interfacial oxidation/reduction reaction all follow clear trends across the periodic table, with the reactivity of the overlayer metal towards oxygen being the most decisive factor. Alkali atoms form ordered superstructures at low coverages. Recent progress in understanding the surface structure of metals in the ‘strong-metal support interaction’ (SMSI) state is summarized.

Literature is reviewed on the adsorption and reaction of a wide variety of inorganic molecules (H_2 , O_2 , H_2O , CO, CO_2 , N_2 , NH_3 , NO_x , sulfur- and halogen-containing molecules, rare gases) as well as organic molecules (carboxylic acids, alcohols, aldehydes and ketones, alkynes, pyridine and its derivates, silanes, methyl halides).

* Tel.: +1-504-862-8279; fax: +1-504-862-8702.
E-mail address: diebold@tulane.edu (U. Diebold).

The application of TiO₂-based systems in photo-active devices is discussed, and the results on UHV-based photocatalytic studies are summarized.

The review ends with a brief conclusion and outlook of TiO₂-based surface science for the future.

© 2002 Elsevier Science B.V. All rights reserved.

Keywords: Titanium oxide; Scanning tunneling microscopy; Single-crystalline surfaces; Adhesion; Catalysis; Chemisorption; Epitaxy; Growth; Interface states; Photochemistry; Surface relaxation and reconstruction; Surface structure; Morphology; Roughness; Topography

Contents

1. Introduction	57
1.1. Motivation	57
1.2. Applications of TiO ₂	59
1.3. Outline of this review	64
2. The structure of TiO ₂ surfaces	65
2.1. Bulk structure	66
2.1.1. Bulk defects	68
2.2. The structure of the rutile TiO ₂ (1 1 0) surface	70
2.2.1. The (1×1) surface	70
2.2.1.1. Bulk truncation	70
2.2.1.2. Relaxations	72
2.2.1.3. Appearance in STM and AFM	74
2.2.1.4. Surface defects	78
2.2.1.4.1. Step edges	78
2.2.1.4.2. Oxygen vacancies created by annealing	81
2.2.1.4.3. Oxygen vacancies created by other means	84
2.2.1.4.4. Line defects	84
2.2.1.4.5. Impurities	84
2.2.1.4.6. Crystallographic shear planes	85
2.2.2. Reconstructions	88
2.2.2.1. Reconstruction under reducing conditions: the structure(s) of the (1×2) phase	88
2.2.2.2. Restructuring under oxidizing conditions	89
2.2.3. Recommendations for surface preparation	92
2.3. The structure of the rutile (1 0 0) surface	93
2.3.1. The TiO ₂ (1 0 0)-(1×1) surface	93
2.3.2. Reconstructions	95
2.3.2.1. The microfacet model of the rutile TiO ₂ (1 0 0)-(1×3) surface	95
2.3.2.2. Is the simple microfacet model valid?	96
2.4. Rutile (0 0 1)	96
2.5. Vicinal and other rutile surfaces	99
2.6. Anatase surfaces	99
2.6.1. Anatase (1 0 1)	100
2.6.2. Anatase (0 0 1)	102
2.6.3. Other anatase surfaces	103
2.7. Conclusion	103

3.	Electronic and vibrational structure of TiO ₂ surfaces	105
3.1.	Stoichiometric TiO ₂ surfaces	105
3.2.	Reduced TiO ₂ surfaces	109
3.2.1.	Defect states	109
3.2.2.	Band bending	110
3.2.3.	Identification of the reduction state with spectroscopic techniques	110
3.3.	Vibrational structure	111
4.	Growth of metal and metal oxide overlayers on TiO ₂	112
4.1.	Overview and trends	112
4.1.1.	Interfacial reactions	112
4.1.2.	Growth morphology (thermodynamic equilibrium)	115
4.1.3.	Growth kinetics, nucleation, and defects	121
4.1.4.	Film structure and epitaxial relationships	122
4.1.5.	Thermal stability of metal overlayers on TiO ₂ -SMSI	122
4.1.6.	Chemisorption properties	124
4.2.	Metals and metal oxides on TiO ₂	124
4.2.1.	Lithium	124
4.2.2.	Sodium	124
4.2.3.	Potassium	125
4.2.4.	Cesium	126
4.2.5.	Calcium	127
4.2.6.	Aluminum	127
4.2.7.	Titanium	127
4.2.8.	Hafnium	128
4.2.9.	Vanadium	128
4.2.10.	Vanadia	129
4.2.11.	Niobium	130
4.2.12.	Chromium	132
4.2.13.	Molybdenum	132
4.2.14.	Molybdena	133
4.2.15.	Manganese	133
4.2.16.	Manganese oxide	133
4.2.17.	Iron	133
4.2.18.	Ruthenium	135
4.2.19.	Ruthenium oxide	135
4.2.20.	Cobalt	135
4.2.21.	Rhodium	136
4.2.22.	Iridium	137
4.2.23.	Nickel	137
4.2.24.	Palladium	138
4.2.25.	Platinum	139
4.2.26.	Copper	142
4.2.27.	Silver	143
4.2.28.	Gold	144
4.3.	Conclusion	147
5.	Surface chemistry of TiO ₂	148
5.1.	Inorganic molecules	148

5.1.1.	Hydrogen	148
5.1.2.	Water	148
5.1.3.	Oxygen	155
5.1.4.	Carbon monoxide and carbon dioxide	156
5.1.4.1.	CO.	156
5.1.4.2.	CO ₂	159
5.1.5.	Nitrogen-containing molecules (N ₂ , NO, NO ₂ , N ₂ O, NH ₃)	159
5.1.5.1.	N ₂ (Table 12)	159
5.1.5.2.	NO.	161
5.1.5.3.	N ₂ O	161
5.1.5.4.	NO ₂	161
5.1.5.5.	NH ₃	163
5.1.6.	Sulfur-containing molecules (SO ₂ , H ₂ S, S _n)	163
5.1.6.1.	SO ₂	163
5.1.6.1.1.	TiO ₂ (1 1 0)	163
5.1.6.1.2.	TiO ₂ (1 0 0)	164
5.1.6.2.	H ₂ S	165
5.1.6.3.	Elemental sulfur (S _n , n ≥ 2)	165
5.1.7.	Halogen-containing molecules (Cl ₂ , CrO ₂ Cl ₂ , HI)	167
5.1.7.1.	Cl ₂	167
5.1.7.2.	Other halogen-containing molecules	169
5.1.8.	Rare gases (Ar, Xe)	170
5.2.	Adsorption and reaction of organic molecules	170
5.2.1.	Carboxylic acids (formic acid, acetic acid, propanoic acid, acrylic acid, benzoic acid, bi-isonicotinic acid, oxalic acid, glycine, maleic anhydride)	179
5.2.1.1.	Formic acid (HCOOH)	179
5.2.1.2.	Formate: adsorption geometry and structure	180
5.2.1.2.1.	TiO ₂ (1 1 0)-(1×1)	180
5.2.1.2.2.	TiO ₂ (1 1 0)-(1×2)	181
5.2.1.2.3.	Modified TiO ₂ (1 1 0) surfaces	181
5.2.1.2.4.	Other TiO ₂ surfaces	183
5.2.1.2.5.	Anatase	183
5.2.1.3.	Reaction of formic acid	183
5.2.1.4.	Formic acid—conclusion	187
5.2.1.5.	Acetic acid (CH ₃ COOH)	187
5.2.1.6.	Propanoic acid (C ₂ H ₅ COOH)	189
5.2.1.7.	Acrylic acid (CH ₂ =CHCOOH)	189
5.2.1.8.	Benzoic acid (C ₆ H ₅ COOH)	189
5.2.1.9.	Bi-isonicotinic acid	189
5.2.1.10.	Oxalic acid (HOOC-COOH)	190
5.2.1.11.	Glycine (NH ₂ CH ₂ COOH)	190
5.2.1.12.	Maleic anhydride	191
5.2.2.	Alcohols (methanol, higher alcohols)	191
5.2.2.1.	Methanol	191
5.2.2.1.1.	Methanol on TiO ₂ (1 1 0)	192
5.2.2.1.2.	Methanol on TiO ₂ (0 0 1) and TiO ₂ (1 0 0)	192
5.2.2.2.	Higher alcohols	194

5.2.3.	Aldehydes (RCHO) and ketones (RCOCH_3) (formaldehyde, acetaldehyde, benzaldehyde, acetone, acetophenone, <i>p</i> -benzoquinone, cyclohexanone, cyclohexenone)	194
5.2.3.1.	Formaldehyde	195
5.2.3.2.	Acetaldehyde.	195
5.2.3.3.	Benzaldehyde	196
5.2.3.4.	Acetone and acetophenone	196
5.2.3.5.	Cyclic ketones.	196
5.2.4.	Cyclo-trimerization of alkynes ($\text{RC}\equiv\text{CH}$) on reduced TiO_2 surfaces and related reactions	196
5.2.5.	STM of pyridine, its derivates, and other aromatic molecules (pyridine, 4-methylpyridine, benzene, <i>m</i> -xylene, phenol)	198
5.2.6.	Adsorption and reaction of silanes (RSiX_3) (TEOS, diethyldiethoxysilane, vinyltriethoxysilane, aminopropyltriethoxysilane, (3,3,3-trifluoropropyl)-trimethoxysilane)	199
5.3.	Photocatalysis on TiO_2	200
5.3.1.	Heterogeneous photocatalysis	201
5.3.2.	Photovoltaic cells	202
5.3.3.	Photocatalysis on single-crystalline TiO_2	204
5.3.3.1.	Oxygen, water, CO, and CO_2	204
5.3.3.2.	Alcohols	205
5.3.3.3.	CHX_3 ($X = \text{Cl}, \text{Br}, \text{I}$)	205
6.	Summary and outlook	206
6.1.	What has been learned and what is missing?	206
6.2.	TiO_2 in relation to other transition metal oxides.	207
6.3.	TiO_2 —mixed and doped	209
6.4.	Nanostructured TiO_2	209
6.5.	Going beyond single crystal and UHV studies	211
6.6.	Concluding remarks	212
	Acknowledgements	212
	References	212

1. Introduction

1.1. Motivation

The surface science of metal oxides is a relatively young field that enjoys a rapidly increasing interest. The general trend to take the ‘next step’ in surface science—to move on to more realistic and complex model systems—lets many researchers to develop an interest in oxide surfaces. This is motivated by the desire to contribute to the numerous applications where oxide surfaces play a role; after all, most metals are oxidized immediately when exposed to the ambient.

The knowledge of well-characterized single-crystalline metal oxide surfaces is reviewed extensively by Henrich and Cox [1] in 1993. This excellent book (which has become a classic in the field) starts by showing the number of publications per year on fundamental surface-science studies on all metal oxides. The number of papers culminates with around 100 articles in 1991, the last year reviewed. A

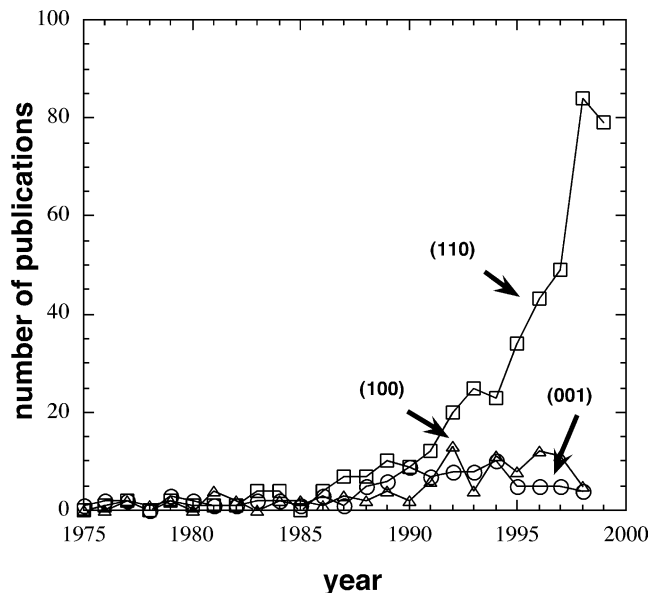


Fig. 1. Number of publications on single-crystalline TiO₂ surfaces/year. Courtesy of M.A. Henderson, Pacific Northwest National Laboratory.

similar analysis (Fig. 1) of (experimental) papers on single-crystalline TiO₂ surfaces shows that more than 70 articles were published on the TiO₂(1 1 0) surface alone in the year 2000.

What is the reason for the popularity of this system? One driving force for pursuing research on single-crystalline TiO₂ surfaces is the wide range of its applications and the expectation that insight into surface properties on the fundamental level will help to improve materials and device performance in many fields. Titanium dioxide is a preferred system for experimentalists because it is well-suited for many experimental techniques. Polished crystals with a high surface quality can be purchased from various vendors. They can be reduced easily, which conveniently prevents charging of this wide band gap semiconductor. One also should not underestimate the ‘self-promoting’ effect of popularity—new phenomena are studied most easily on well-characterized, often tested systems, and TiO₂, especially the most stable rutile (1 1 0) surface, falls certainly into this category. All these factors have contributed in making TiO₂ *the* model system in the surface science of metal oxides.

Despite this high interest, a comprehensive review of the surface science of TiO₂ is lacking at this point. Several excellent reviews of different aspects of single-crystalline metal oxide surfaces were written in recent years [1–10], and TiO₂ surfaces are considered in almost all of them. Still, the time may be ripe to review the wealth of knowledge on TiO₂ itself, and an attempt is made in this paper. It is intended to give the interested reader an introduction into TiO₂, and clarify some confusing and conflicting results, e.g. on the structure of TiO₂ surfaces as observed with scanning tunneling microscopy (STM), the adsorption of test molecules such as water and formic acid, and the rich body of literature on metal growth on TiO₂ surfaces. There is also a hope that the insights obtained on this model oxide can be transferred, at least in part, to other systems. The focus is on the more recent literature (>1990). While an attempt was made to include most of the single-crystalline work on TiO₂

surfaces, the sheer number of papers excludes comprehensiveness, and apologies are extended to any authors whose work was unfortunately not represented.

1.2. Applications of TiO_2

Before dwelling on actual surface science results, a brief glimpse on the applications of TiO_2 (which, after all are the deeper motivation for most of the performed work) is in order. Titanium dioxide is used in heterogeneous catalysis, as a photocatalyst, in solar cells for the production of hydrogen and electric energy, as gas sensor, as white pigment (e.g. in paints and cosmetic products), as a corrosion-protective coating, as an optical coating, in ceramics, and in electric devices such as varistors. It is important in earth sciences, plays a role in the biocompatibility of bone implants, is being discussed as a gate insulator for the new generation of MOSFETS and as a spacer material in magnetic spin-valve systems, and finds applications in nanostructured form in Li-based batteries and electrochromic devices.

A better understanding and improvement of catalytic reactions is one main driving force for surface investigations on TiO_2 . Because most heterogeneous catalysts consist of small metal clusters on an oxide support, many growth studies of metals on TiO_2 were performed. These metal/ TiO_2 systems often serve as a model for other metal/oxide surfaces. Traditionally, TiO_2 is a component in mixed vanadia/titania catalysts used for selective oxidation reactions [11]. The surface science of vanadium and vanadia/ TiO_2 systems was addressed by several groups [12–15]. TiO_2 is not suitable as a structural support material, but small additions of titania can modify metal-based catalysts in a profound way. The so-called strong-metal support interaction (SMSI) is, at least in part, due to encapsulation of the metal particles by an reduced TiO_x overlayer (see review by Haller and Resasco [16]). Recently, this phenomenon was revisited using surface science techniques [17–20]. The discovery that finely dispersed Au particles supported on TiO_2 and other reducible metal oxides oxidize CO at low temperature [21] has spurred some excitement in the surface science community. Many experiments that may clarify the underlying phenomena leading to this processes are still underway [22–24].

The photoelectric and photochemical properties of TiO_2 are another focus of active research. The initial work by Fujishima and Honda [25] on the photolysis of water on TiO_2 electrodes without an external bias, and the thought that surface defect states may play a role in the decomposition of water into H_2 and O_2 , has stimulated much of the early work on TiO_2 [26–28]. Unfortunately, TiO_2 has a low quantum yield for the photochemical conversion of solar energy. The use of colloidal suspensions with the addition of dye molecules has been shown to improve efficiency of solar cells [29], and has moved TiO_2 -based photoelectrochemical converters into the realm of economic competitiveness [30].

By far, the most actively pursued applied research on titania is its use for photo-assisted degradation of organic molecules. TiO_2 is a semiconductor and the electron–hole pair that is created upon irradiation with sunlight may separate and the resulting charge carriers might migrate to the surface where they react with adsorbed water and oxygen to produce radical species. These attack any adsorbed organic molecule and can, ultimately, lead to complete decomposition into CO_2 and H_2O . The applications of this process range from purification of wastewaters [31]; desinfection based on the bactericidal properties of TiO_2 [32] (for example, in operating rooms in hospitals); use of self-cleaning coatings on car windshields [33], to protective coatings of marble (for preservation of ancient Greek statues against environmental damage [34]). It was even shown that subcutaneous injection of a TiO_2 slurry in rats, and subsequent near-UV illumination, could slow or halt the development of tumor cells [35–37]. Several review papers discuss the technical and scientific aspects of TiO_2 photocatalysis

[31,38–42]. An extensive review of the surface science aspects of TiO₂ photocatalysis has been given by Linsebigler et al. [43], and some of these more recent results are discussed in Section 5.3.3.

Semiconducting metal oxides may change their conductivity upon gas adsorption. This change in the electrical signal is used for gas sensing [44]. TiO₂ is not used as extensively as SnO₂ and ZnO, but it has received some attention as an oxygen gas sensor, e.g. to control the air/fuel mixture in car engines [45,46]. Two different temperature regimes are distinguished [47]. At high temperatures, TiO₂ can be used as a thermodynamically controlled bulk defect sensor to determine oxygen over a large range of partial pressures. The intrinsic behavior of the defects responsible for the sensing mechanism can be controlled by doping with tri- and pentavalent ions. At low temperatures, addition of Pt leads to the formation of a Schottky-diode and a high sensitivity against oxygen [47].

The sheer volume of TiO₂ pigments produced world-wide—currently ca. 4 million tons per year—is stunning [48]. TiO₂ pigment is used in virtually every kind of paint because of its high refractive index. (See Table 1 for a summary of bulk properties of TiO₂. A more detailed resource on rutile was given in [49].) The surface properties play a role even in these wide-spread applications, e.g. the photocatalytic degradation of binder in paints is a major problem for the paint industry. TiO₂ is non-toxic and safe, and can be dispersed easily [48]. In pure form it is also used as a food additive [50], in pharmaceuticals, and in cosmetic products [51].

Titanium dioxide is used extensively in thin-film optical-interference coatings [52]. Such coatings are based on the interference effects between light reflected from both the upper and lower interface of a thin film. (The same effect gives rise to the different colors of an oil film on water.) The relative ratios between transmission and reflection of light are governed by the index of refraction of the thin film and the surrounding media. By depositing a stack of layers with the appropriate optical index, the refraction/transmission properties of a stack of thin layers on a glass substrate can be designed to meet a great number of applications. Examples for such devices include antireflective coatings, dielectric mirrors for lasers, metal mirrors with enhanced reflection, and filters [52]. For most films a combination of materials with indices as high and as low as possible is an advantage. Titanium dioxide has the highest index of all oxides (see Table 1), making it ideally suited for this application.

One of the ‘hot’ issues currently debated in materials science is the search for the best dielectric gate material for replacing SiO₂ MOSFET devices [53]. It appears that the limit for miniaturization, when electric tunneling through ever thinner SiO₂ films becomes significant, will be reached in the very near future. Ultrathin metal oxide films might be well-suited as the gate material of the future, and TiO₂, with its high dielectric constant (Table 1), would be an attractive candidate for this application. A new kind of gate oxide must meet very stringent requirements—no surface states, virtually pin-hole free, stoichiometric ultrathin films, good interface formation with the Si substrate, etc. [53]. TiO₂ could be a viable approach to dielectrics whose oxide equivalent thickness is less than 2.0 nm. CVD-grown TiO₂ films on Si show excellent electric characteristics, but a low resistivity layer, probably SiO₂, forms at the interface [54]. Interestingly, modified TiO₂ films are also promising materials for spintronics applications, although TiO₂ itself is not a magnetic material. When anatase TiO₂ films are doped with a few percent of Co, they become ferromagnetic [55,56]. Such films are optically transparent, semiconducting, and ferromagnetic at room temperature, and might be ideal candidates for spin-based electronic devices.

Nanostructured TiO₂ electrodes have received quite a bit of attention. One particularly interesting application is the implementation of nanocrystalline TiO₂ films in electrochromic devices [57]. Such devices control light transmission in windows or light reflection in mirrors and displays. They are based

Table 1
Bulk properties of titanium dioxide^a

Atomic radius (nm)									
O	0.066 (covalent)								
Ti	0.146 (metallic)								
Ionic radius (nm)									
O(−2)	0.14								
Ti(+4)	0.064								
Crystal structure	System	Space group	Lattice constants (nm)						
			<i>a</i>	<i>b</i>	<i>c</i>				
rutile	Tetragonal	D _{4h} ¹⁴ -P4 ₂ /mnm	0.4584	—	0.2953 0.644				
anatase	Tetragonal	D _{4h} ¹⁹ -I4 ₁ /amd	0.3733	—	0.937 2.51				
brookite	Rhombohedral	D _{2h} ¹⁵ -Pbca	0.5436	0.9166	0.5135 0.944				
Density (kg/m ³)									
rutile	4240								
anatase	3830								
brookite	4170								
Melting point (°C) (decomposes)		Boiling point (°C) (at pressure <i>p</i> O ₂ 101.325 kPa)							
1870		2927							
Standard heat capacity, C _p ⁰ , 298.15 J/(mol °C)									
55.06 (rutile)									
55.52 (anatase)									
Heat capacity, C _p (J/kg K) (rutile)			Temperature (K)						
—			10						
243			25						
1788			50						
6473			100						
10718			150						
14026			200						
18255			298.15						
Temperature (K)			Thermal conductivity (W/(m K)) (rutile)						
373			6.531						
473			4.995						
673			3.915						
873			3.617						
1073			3.391						
1273			3.307						
1473			3.307						

Table 1 (Continued)

Linear coefficient of thermal expansion ($\alpha \times 10^{-6}$, $^{\circ}\text{C}^{-1}$), rutile	Temperature ($^{\circ}\text{C}$)
8.19	0–500
Anisotropy of linear coefficient of thermal expansion ($\alpha \times 10^{-6}$, $^{\circ}\text{C}^{-1}$), rutile	
Parallel to <i>c</i> -axis	Perpendicular to <i>c</i> -axis
$\alpha = 8.816 \times 10^{-6} + 3.653 \times 10^{-9} \times T + 6.329 \times 10^{-12} \times T^2$	$\alpha = 7.249 \times 10^{-6} + 2.198 \times 10^{-9} \times T + 1.198 \times 10^{-12} \times T^2$
Modulus of normal elasticity <i>E</i> (GPa) (rutile)	Density (kg/m^3)
244.0	4000
254.5	4100
273.0	4200
284.2	4250
289.4	
Hardness on mineralogical scale (Mohs scale)	
5–6.5	
Microhardness (MPa)	Load <i>P</i> $\times 10^{-5}$ N
6001.88	98070
7845.66–1961.40	49035–98070
Compressibility coefficient, β , $10^{-11} \text{ m}^2/\text{N}$, rutile	Pressure, <i>p</i> , 10^{11} m^2 (N Pa)
0.59	Temperature (K)
125	273
Electrical resistance (rutile)	
Temperature (K)	Resistivity ($\Omega \text{ m}$)
773	3×10^5
1073	1.2×10^2
1473	8.50×10^2
Thermoelectric properties (rutile)	
Temperature (K)	Thermo-emf coefficient ($\mu\text{V}/\text{K}$)
400	0.75
600	−2.75
800	−6
1000	−9
1200	−12

Table 1 (Continued)

Galvanometric properties (rutile)		
Hall constant (m^3/c) (rutile)	Temperature (K)	
2×10^{-6}	500	
Electron mobility, μ ($\text{cm}^2/\text{V s}$)		
TiO ₂ * (rutile)	~ 1 [209]	
TiO ₂ ** (anatase)	~ 10 [209]	
Dielectric properties		
Frequency (Hz)	Temperature (K)	Dielectric constant
10^8	290–295	86
–	290–295	170
10^4	298	160
10^7	303	100
Band gap (eV)		
rutile	3.0 (indirect) [209]	
anatase	3.2 (indirect) [209]	
Refractive index		
n_g	n_m	n_p
$\alpha\text{-TiO}_2$ (rutile)	–	2.621
$\beta\text{-TiO}_2$ (anatase)	–	2.561
$\gamma\text{-TiO}_2$ (brookite)	2.5843	2.5831
TiO ₂ (rutile)	–	2.6506
TiO ₂ (anatase)	–	2.6584
TiO ₂ (brookite)	–	2.677
Integral normal emissivity, ε_{\pm} (smooth surface) (rutile)		
0.82	400	
0.83	500	
0.84	600	
0.85	700	
0.86	800	
0.87	900	
0.875	1000	
0.88	1100	
0.89	1200	
0.90	1300	
Monochromatic normal emissivity, ε_{in} (powder) (rutile)		
	Wavelength, λ (nm)	Temperature (K)
0.27	1.0	1223
0.15	2.0	1223

Table 1 (Continued)

	0.20	3.0	1223
	0.30	4.0	1223
	0.32	5.0	1223
	0.50	6.0	1223
	0.67	7.0	1223
	0.76	8.0	1223
	0.80	9.0	1223
	0.84	10.0	1223
	0.85	11.0	1223
	0.86	12.0	1223
	0.87	13.0	1223
	0.88	14.0	1223
	0.89	15.0	1223
Refractive index, n , of rutile single crystal for ordinary (1) and extraordinary (2) rays in visible and IR regions of spectrum, at 298 K			

^a Data from [65] unless noted otherwise. A more detailed compendium of bulk properties of rutile is given in [49].

on two complementary electrodes (TiO_2 and WO_3 in the case of [57]), which change their color upon reduction/oxidation cycles induced by an electrical current.

Polycrystalline ZnO , TiO_2 and SnO_2 , exhibit a high non-linearity between the current density and the electric field and are thus suitable as ‘varistors’ for the suppression of high transient voltages [58]. Doped TiO_2 ceramics have useful varistor properties with non-linearity coefficient (α) values in the range $\alpha = 3–12$, α being defined by the relationship $I = KV^\alpha$, where I is the current, V the voltage, and K the proportionality constant. The presence of this potential barrier is due to the creation of defects formed during sintering of TiO_2 systems. A potential barrier associated with a double space charge distribution can originate at these defects. This phenomenon establishes variable resistance as a function of the applied electric field to the solid.

Metallic implants in the human body have a significant economic and clinical impact in the biomaterials field [59]. ‘Commercially pure’ (CP) titanium (ASTM F67) and ‘extra-low interstitial’ (ELI) Ti–6Al–4V alloy (ASTM F136) are the two most common implant biomaterials. There is an increasing interest in the chemical and physical nature of the oxide layer on the surface of both materials [60]. The oxide provides corrosion resistance and may also contribute to the biological performance of Ti at molecular and tissue levels, as suggested in the literature on osseointegrated oral and maxillofacial implants by Branemark, Kasemo and co-workers [61] in Sweden.

1.3. Outline of this review

The geometric structure of various TiO_2 surfaces is discussed in Section 2. A detailed knowledge of the surface structure is the crucial first step in obtaining a detailed knowledge of reaction mechanisms

on the molecular scale. Metal oxide surfaces are prime examples of the close relationship between structure and reactivity [6], as local non-stoichiometries or geometric defects directly affect the electronic structure. Well-tested models are available for both, ‘perfect’ surfaces as well as surface defects on TiO₂. Titanium dioxide crystallizes in three crystallographic phases, and the surfaces of the rutile phase have been investigated extensively. Surface science research on the technologically quite important anatase phase is just starting. The structure and stability of metal oxide surfaces can be predicted using the concept of autocompensation [5] or non-polarity [62]. Bulk-truncated models of various rutile and anatase TiO₂ surfaces are derived using this concept, and are compared with ab initio calculations and experimental results on surface geometrical models and relaxations. Recent scanning probe microscopy results have given enormous insight into defect structures at TiO₂ surfaces, and have provided some surprises as well.

Section 3 gives a brief summary of the electronic structure of TiO₂. Most of the basic understanding of the electronic structure of TiO₂ surfaces has been discussed in previous reviews [1], hence this section is kept short. Surface defects that are related to oxygen deficiencies can be identified with most electron spectroscopies, some of which are discussed in this section.

The growth of metal and metal oxide overlayers on TiO₂ substrates is reviewed in Section 4. This is a very active and exciting area of research, and almost all metals across the periodic table have been investigated on TiO₂. Most of the current literature on metal/TiO₂ growth has been summarized in Table 6. It is comforting to see that the basic trends for the propensity of interfacial reactions, growth morphology, geometric structure, and thermal stability that have been identified early on [63] are in agreement with the more recent results.

The surface chemistry of TiO₂ is reviewed in Section 5. The adsorption of inorganic molecules is discussed first, and the results for each group of molecules is summarized in tables. Results on small organic molecules is then reviewed. This section closes with a brief summary of photoinduced reactions on TiO₂ surfaces. A summary and outlook is given at the end.

2. The structure of TiO₂ surfaces

Unraveling the relationship between atomic surface structure and other physical and chemical properties is probably one of the most important achievements of surface science. Because of the mixed ionic and covalent bonding in metal oxide systems, the surface structure has an even stronger influence on local surface chemistry as compared to metals or elemental semiconductors [6]. A great amount of work has been performed on TiO₂ over the years, and has lead to an understanding that is unprecedented for a metal oxide surface.

This section starts with a brief description of the bulk structure of titanium dioxide crystals, and their stable crystal planes. Because bulk non-stoichiometries influence the surface properties of TiO₂ in a variety of ways, a short discussion of bulk defects is included as well. A substantial part of the section is devoted to the rutile (1 1 0) surface. The (bulk-truncated) (1 × 1) surface is known with a very high accuracy from experimental as well as theoretical studies. Nevertheless, there are some puzzling disagreements between theory and experiment in some aspects [64]. Surface defects are categorized in step edges, oxygen vacancies, line defects (closely related to the (1 × 2) reconstruction), common impurities, and the manifestation of crystallographic shear planes (CSPs) at surfaces. The long-standing argument of the structure of the (1 × 2) phase seems to be settled, as discussed in Section 2.2.2. STM

and, more recently, atomic force microscopy (AFM), studies have revealed the complexity of the seemingly simple rutile (1 1 0) surface, hence the section on TiO_2 (1 1 0) commences with a recommendation on the best way to prepare this surface. The two other low-index planes, rutile (1 0 0) and (0 0 1) are described in [Sections 2.3 and 2.4](#), respectively. Until fairly recently the (1 × 3) reconstruction of the rutile (1 0 0) seemed well understood, but inconsistencies in theoretical calculations as well as new interpretations of X-ray diffraction data show that a closer look on the structure of this phase may be needed ([Section 2.3.2.2](#)). New developments on structural investigations of anatase samples are included at the end.

2.1. Bulk structure

Titanium dioxide crystallizes in three major different structures; rutile (tetragonal, $D_{4h}^{14}\text{-P}4_2/\text{mnm}$, $a = b = 4.584 \text{ \AA}$, $c = 2.953 \text{ \AA}$ [\[49\]](#)), anatase (tetragonal, $D_{4h}^{19}\text{-I}4_1/\text{amd}$, $a = b = 3.782 \text{ \AA}$, $c = 9.502 \text{ \AA}$) and brookite (rhombohedral, $D_{2h}^{15}\text{-P}bca$, $a = 5.436 \text{ \AA}$, $b = 9.166 \text{ \AA}$, $c = 5.135 \text{ \AA}$) [\[65\]](#). (Other structures exist as well, for example, cotunnite TiO_2 has been synthesized at high pressures and is one of the hardest polycrystalline materials known [\[66\]](#).) However, only rutile and anatase play any role in the applications of TiO_2 and are of any interest here as they have been studied with surface science techniques. Their unit cells are shown in [Fig. 2](#). In both structures, the basic building block consists of a titanium atom surrounded by six oxygen atoms in a more or less distorted octahedral configuration. In each structure, the two bonds between the titanium and the oxygen atoms at the apices of the octahedron are slightly longer. A sizable deviation from a 90° bond angle is observed in anatase. In rutile, neighboring octahedra share one corner along ⟨1 1 0⟩—type directions, and are stacked with their long axis alternating by 90° (see [Fig. 2](#) as well as [Fig. 6](#)). In anatase the corner-sharing octahedra form (0 0 1) planes. They are connected with their edges with the plane of octahedra below. In all three TiO_2 structures, the stacking of the octahedra results in threefold coordinated oxygen atoms.

Rutile TiO_2 single crystals are widely available. They can be bought in cut and polished form from companies such as Commercial Crystal Laboratories, USA; Kelpin Kristallhandel, Germany; Goodfellow, UK; Earth Jewelry, Japan and many others. A very small roughness is achieved by grinding the sample, and then polishing the surface for many hours with a chemo-mechanical treatment. This is also referred to as epitaxial polish. Practical aspects of surface preparation and handling are discussed in [\[67\]](#).

Ramamoorthy and Vanderbilt [\[68\]](#) calculated the total energy of periodic TiO_2 slabs using a self-consistent ab initio method. The (1 1 0) surface has the lowest surface energy, and the (0 0 1) surface the highest. This is also expected from considerations of surface stability, based on electrostatic and dangling-bonds arguments discussed in [Section 2.2.1.1](#). below. The thermodynamic stability of the (1 0 0) surface was also considered, and was found to be stable with respect to forming (1 1 0) facets. The (0 0 1) surface was almost unstable with respect to the formation of macroscopic (1 × 1) (0 1 1) facets. From the calculated energies a three-dimensional (3D) Wulff plot was constructed, see [Fig. 3](#). The Wulff construction [\[69\]](#) gives the equilibrium crystal shape of a macroscopic crystal. For comparison with experimental crystal shapes one has to take into account that only four planes were considered and that the calculations are strictly valid only at zero temperature.

The experimental results on the three low-index rutile surfaces discussed below fit rather well with the stability expected from these calculations. For rutile, the (1 1 0), (0 0 1) and (1 0 0) surfaces have been studied, with (1 1 0) being the most stable one. These three surfaces are discussed in this section.

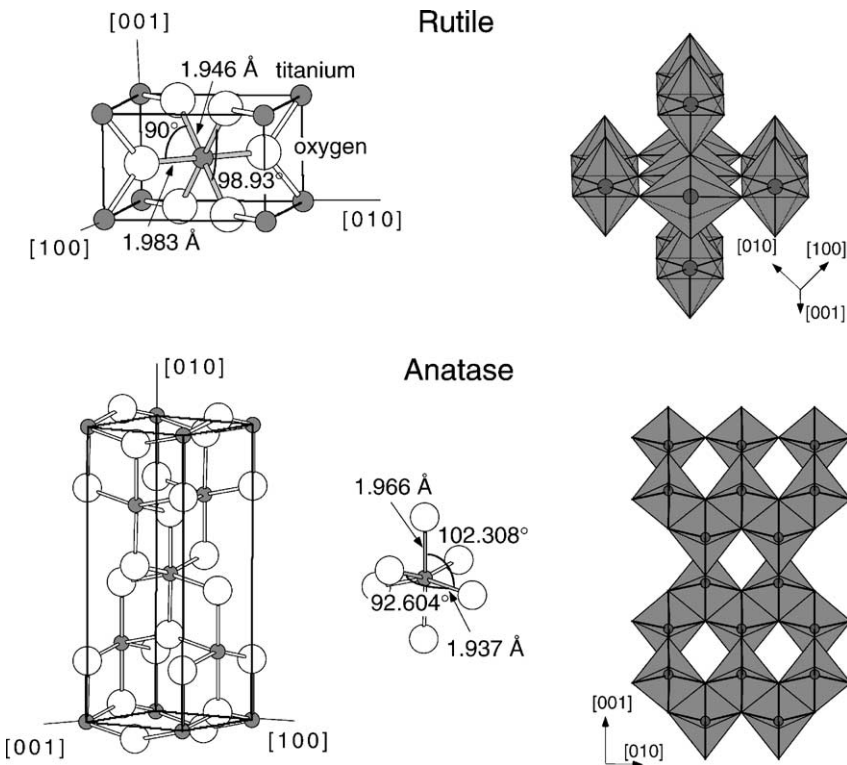


Fig. 2. Bulk structures of rutile and anatase. The tetragonal bulk unit cell of rutile has the dimensions, $a = b = 4.587 \text{ \AA}$, $c = 2.953 \text{ \AA}$, and the one of anatase $a = b = 3.782 \text{ \AA}$, $c = 9.502 \text{ \AA}$. In both structures, slightly distorted octahedra are the basic building units. The bond lengths and angles of the octahedrally coordinated Ti atoms are indicated and the stacking of the octahedra in both structures is shown on the right side.

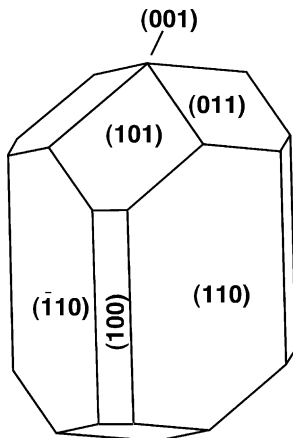


Fig. 3. The equilibrium shape of a macroscopic TiO_2 crystal using the Wulff construction and the calculated surface energies of [68]. Taken from Ramamoorthy and Vanderbilt [68]. © 1994 The American Physical Society.

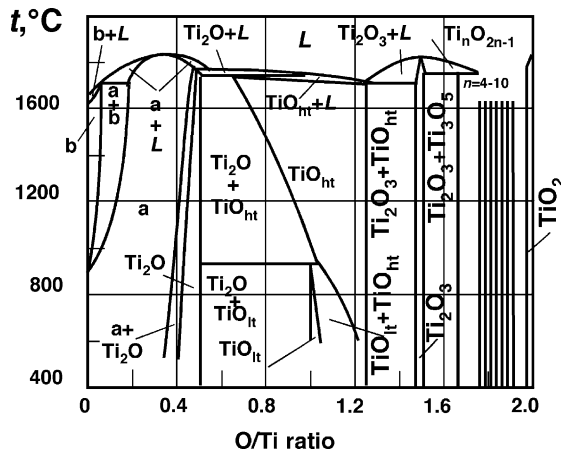


Fig. 4. Phase diagram of the Ti–O system taken from Samsonov [65]. The region Ti_2O_3 – TiO_2 contains Ti_2O_3 , Ti_3O_5 , seven discrete phases of the homologous series Ti_nO_{2n-1} (Magneli phases), and TiO_2 . See [65] for a more detailed description.

The two approaches that are commonly used to predict the structure and stability of oxide surfaces are exemplified in detail for the rutile (1 1 0) surface. For anatase, the (1 0 1) and the (1 0 0)/(0 1 0) surface planes are found in powder materials, together with some (0 0 1). The (1 0 1) surface was calculated to have the lowest surface energy, even lower than the rutile (1 1 0) surface [70]. First experimental results on anatase (0 0 1) and (1 0 1) are discussed at the end of this section.

2.1.1. Bulk defects

The titanium–oxygen phase diagram is very rich with many stable phases with a variety of crystal structures, see Fig. 4 [65]. Consequently, TiO_2 can be reduced easily. Bulk reduction and the resulting color centers are reflected in a pronounced color change of TiO_2 single crystals from initially transparent to light and, eventually, dark blue, see Fig. 5. These intrinsic defects result in n-type doping and high conductivity, see Table 2. The high conductivity makes TiO_2 single crystals such a convenient oxide system for experimentalists.

As has been pointed out recently [71], bulk defects play a major role in a variety of surface phenomena where annealing to high temperatures is necessary, e.g. during the encapsulation of Pt [18,20,72], in bulk-assisted reoxidation [73,74], in restructuring and reconstruction processes [75,76], and adsorption of sulfur and other inorganic compounds [77]. The relationship between crystal color, conductivity, bulk defects as characterized by EPR measurements, and surface structure of rutile (1 1 0) has been investigated systematically by Li et al. [71], and the samples reproduced in Fig. 5 have been used in this study. The electric properties in dependence on the bulk defect concentration has been investigated in [78,79].

The bulk structure of reduced TiO_{2-x} crystals is quite complex with a variety of defects such as doubly charged oxygen vacancies, Ti^{3+} and Ti^{4+} interstitials, and planar defects such as CSPs. The defect structure varies with oxygen deficiency which depends on temperature, gas pressure, impurities, etc. Despite years of research, the question of which type of defect is dominant in which region of oxygen deficiency is still subject to debate [78,80]. It was shown that the dominant type are Ti interstitials in the region from $TiO_{1.9996}$ to $TiO_{1.9999}$ (from 3.7×10^{18} to 1.3×10^{19} missing O atoms

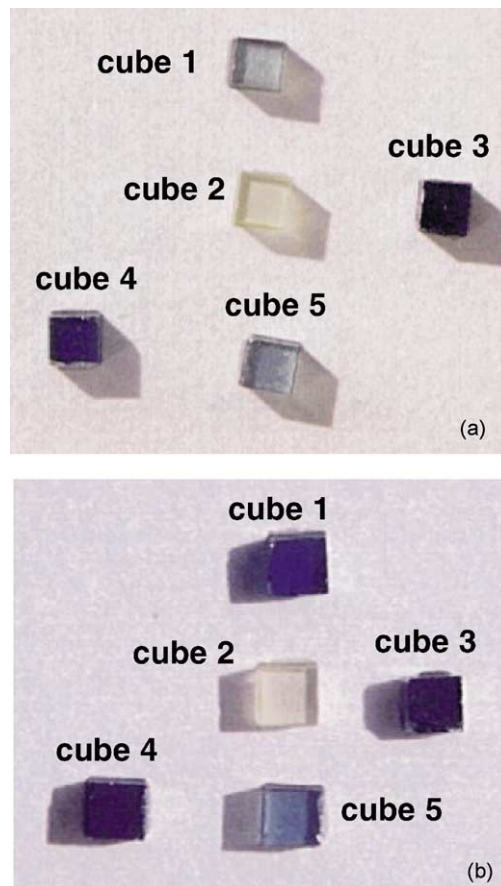


Fig. 5. Color centers associated with bulk defects that are formed upon reduction of TiO_2 single crystals cause a change in crystal color. (a) Photograph of rutile single crystals heated in a furnace to various temperatures: (cube 1) 19 h at 1273 K, (cube 2) 21 h 40 min at 1450 K (was like cube 3) then reoxidized in air at 1450 K, (cube 3) 4 h 55 min at 1450 K, (cube 4) 35 min at 1450 K, (cube 5) 1 h 10 min at 1350 K. (b) Same samples after prolonged experiments on cubes 1, 3, and 4. The samples were sputtered daily and annealed to 973 K for a total of 690 min. Adapted from Li and co-workers [71]. © 2000 The American Chemical Society.

per cubic centimeter) [78]. CS planes precipitate on cooling crystals across the TiO_{2-x} ($0 \leq x \leq 0.0035$) phase boundary [81]. They show a very strong dependence on the cooling history and are absent in quenched specimen. The formation mechanism was reviewed by Smith et al. [81–83]. Such CS planes may extend all the way to the surface [84–88] and their appearance is discussed in Section 2.2.1.4.

Table 2

Resistivity ($\Omega \text{ cm}$) at 300 K measured at room temperature of different TiO_2 samples^a

	Cube 2	Cube 5	Cube 1	Cube 4	Cube 3
Resistivity	1835.0	108.24	46.76	24.06	8.94

^a The colors of cubes 1, 3, and 4 are shown in Fig. 5b; cubes 2 and 5 were additionally reduced. From [156].

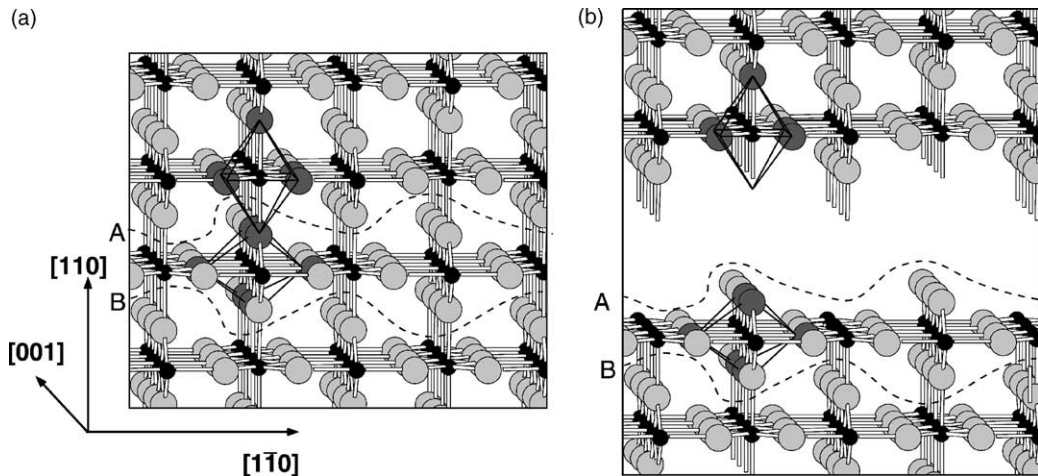


Fig. 6. (a) Ball-and-stick model of the rutile crystal structure. It is composed of slightly distorted octahedra, two of which are indicated. Along the $[1\bar{1}0]$ direction these octahedra are stacked with their long axes alternating by 90° . Open channels are visible along the $[001]$ direction. The dashed lines A and B enclose a charge-neutral repeat unit without a dipole moment perpendicular to the $[1\bar{1}0]$ -direction (a ‘type 1’ crystal plane according to the classification in [62]). (b) The crystal is ‘cut’ along line A. The same number of $\text{Ti} \rightarrow \text{O}$ and $\text{O} \rightarrow \text{Ti}$ bonds are broken, and the surface is autoccompensated [5]. The resulting (110) surfaces are stable and overwhelming experimental evidence for such (1×1) -terminated $\text{TiO}_2(110)$ surfaces exists.

The diffusion mechanism for the various types of defects is quite different; oxygen migrates via a site exchange (vacancy diffusion) mechanism, while excess Ti diffuses through the crystal as interstitial atoms. The interstitial diffusion happens especially fast through the open channels along the (001) direction (the crystallographic c -axis) [89,90], see Fig. 6a. A Ti interstitial located in these channels is in an octahedral configuration, similar to the regular Ti sites [91]. Consequently, the diffusing species in oxidation reactions of reduced Ti_aO_b surfaces (where $a > b/2$ but probably less than b) produced by sputtering and/or Ti deposition is the Ti atom and not the O vacancy, as has been shown in a series of elegant experiments with isotopically labeled ^{18}O and ^{46}Ti by Henderson [73,74].

2.2. The structure of the rutile $\text{TiO}_2(110)$ surface

The rutile (110) surface is the most stable crystal face and simple guidelines can be used to essentially predict the structure and the stability of $\text{TiO}_2(110)-(1 \times 1)$. Because these concepts are very useful for the other crystal faces of TiO_2 as well other oxide materials, they are exemplified for this surface. The relaxations from the bulk-terminated coordinates are reviewed, and the types and manifestations of defects are discussed. Although the $\text{TiO}_2(110)$ surface is very stable, it nevertheless reconstructs and restructures at high temperatures under both oxidizing and reducing conditions.

2.2.1. The (1×1) surface

2.2.1.1. Bulk truncation. Two concepts have been introduced to predict the stability of oxide structures. Tasker [62] discussed the stability of ionic surfaces based on purely electrostatic considerations.

The second concept, autocompensation, was originally developed for surfaces of compound semiconductors and applied to metal oxide surfaces by LaFemina [5]. The most stable surfaces are predicted to be those which are autocompensated, which means that excess charge from cation-derived dangling bonds compensates anion-derived dangling bonds. The net result is that the cation- (anion-) derived dangling bonds are completely empty (full) on stable surfaces. This model allows for the partially covalent character found in many metal oxides, including TiO_2 . Both concepts are used in a complementary way, and represent a necessary (but not sufficient) condition for stable surface terminations. Very often, stable metal oxide surfaces for which the structure is known are non-polar [62] and fulfill the autocompensation criterion [5].

Tasker's and LaFemina's approaches are exemplified in creating a stable (1 1 0) surface (Fig. 6). In Tasker's concept, the dipole moment of a repeat unit perpendicular to the surface must be zero in order for the surface energy to converge. He introduced three categories for ionic (or partially ionic) structures. Type 1 (neutral, with equal number of cations and anions on each plane parallel to the surface) is stable. Type 2 (charged planes, but no dipole moment because of a symmetrical stacking sequence) is stable as well. Type 3 surfaces (charged planes and a dipole moment in the repeat unit perpendicular to the surface) will generally be unstable.

Consider, for example, the rutile structure as being composed of (1 1 0)-oriented planes such as drawn in Fig. 6a. The top plane in Fig. 6a consists of the same number of Ti and O atoms. In a purely ionic picture, the titanium and oxygen atoms have nominal charges of +4 and -2, respectively. Hence, the top layer has a net positive charge. The next two layers consist of oxygen atoms, hence both of them have a net negative charge. A Type 2 repeat unit is outlined by the dashed lines A and B in Fig. 6a. It consists of a mixed Ti, O layer, sandwiched between two layers of oxygen atoms. The total unit does not have a dipole moment (and from counting the charges it turns out that it is neutral as well). A crystal, cut or cleaved¹ to expose a (1 1 0) surface, will naturally terminate with the surface created by cutting along line A (or B) in Fig. 6a. In Fig. 6b, the top of the model is shifted along the (1 1 0) direction (cutting the crystal in a ‘Gedankenexperiment’). The resulting surface is very corrugated because one ‘layer’ of oxygen atoms is left behind. As shown below, there is overwhelming evidence that the (1 × 1) surface of TiO_2 (1 1 0) closely resembles the ‘bulk-terminated’ structure depicted in Fig. 6b.

The same surface structure is also predicted using the rules of autocompensation. In Fig. 6b, the same number of oxygen-to-titanium bonds are broken as titanium-to-oxygen. Transferring electrons from the dangling bonds on the Ti cations will just compensate the missing charge in the dangling bonds on the O anions. Hence, the surface is autocompensated [5]. Note that only the longer bonds are broken when the crystal is sliced in this way.

The rutile (1 1 0)-(1 × 1) surface in Fig. 6b contains two different kinds of titanium atoms. Along the [0 0 1] direction, rows of sixfold coordinated Ti atoms (as in the bulk) alternate with fivefold coordinated Ti atoms with one dangling bond perpendicular to the surface. Two kinds of oxygen atoms are created as well. Within the main surface plane, they are threefold coordinated as in the bulk. The so-called bridging oxygen atoms miss one bond to the Ti atom in the removed layer and are twofold coordinated. These bridging oxygen atoms are subject to much debate. Because of their coordinative undersaturation, atoms from these rows are thought to be removed relatively easily by thermal annealing. The resulting point defects (Section 2.2.1.4) affect the overall chemistry of the surface, even in a macroscopic way [92].

¹ Unfortunately, TiO_2 fractures and does not cleave well.

A (1×1) LEED pattern is generally observed upon sputtering and annealing in UHV. To this author's knowledge no quantitative LEED study has been reported, probably because of the defects are easily created when the sample is bombarded with electrons which poses an additional complication (see [Section 2.2.1.4](#)). A medium-energy electron diffraction (MEED) study of $\text{TiO}_2(1\ 1\ 0)$ employed an ESDIAD optics with a channelplate; this setup is more sensitive than a conventional LEED apparatus, and allows for very small electron currents to be used. The results of this study were consistent with the (1×1) structure depicted in [Fig. 6b](#). X-ray photoelectron diffraction (XPD) spectra also fit the expected (1×1) termination [93], as do the STM results discussed in [Section 2.2.1.3](#).

2.2.1.2. Relaxations. Every surface relaxes to some extent. In recent years, the geometry of the $\text{TiO}_2(1\ 1\ 0)$ - (1×1) surface has been studied in some detail both experimentally and theoretically. The results of a surface X-ray diffraction (SXRD) experiment [94] and of several total-energy calculations are listed in [Table 3](#). The experimentally determined directions of atoms in the first layers are sketched in [Fig. 7](#). As is expected from symmetry, the main relaxations occur perpendicular to the surface. Only the in-plane oxygens (4, 5 in [Fig. 7](#)) move laterally towards the fivefold coordinated Ti atoms. (These relaxations are symmetric with respect to the row of fivefold coordinated Ti atoms, hence do not increase the size of the surface unit cell.) The bridging oxygen atoms (labeled 3 in [Fig. 7](#)) are measured to relax downwards considerably, and the sixfold coordinated Ti (1) atoms upwards. The fivefold coordinated Ti atoms (2) move downwards and the neighboring threefold coordinated oxygen

Table 3

Displacements (\AA) determined experimentally and theoretically by several groups using different computational techniques^a

	Charlton, SXRD, experiment	Harrison, FP-LAPW, seven layers	Harrison, LCAO, seven layers	Rama-moorthy, PW-PP-LDA, five layers	Bates, PW-GGA, five layers	Lindan, PW-PP-GGA, three layers	Vogten-huber, FP-LAPW, three layers	Reinhardt, HF-LCAO, three layers
Ti(1) (sixfold)	0.12 ± 0.05	0.08	0.23	0.13	0.23	0.09	-0.05	0.09
Ti(2) (fivefold)	-0.16 ± 0.05	-0.23	-0.17	-0.17	-0.11	-0.12	-0.18	-0.15
O(3) (bridging)	-0.27 ± 0.08	-0.16	-0.02	-0.06	-0.02	-0.09	-0.16	-0.14
O(4,5) [1 1 0]	0.05 ± 0.05	0.09	0.03	0.12	0.18	0.11	-0.12	0.07
[1 $\bar{1}$ 0]	$\pm 0.16 \pm 0.08$	± 0.06	± 0.05	± 0.04	± 0.05	± 0.05	± 0.07	± 0.08
O(6)	0.03 ± 0.08	-0.09	0.02	-0.07	0.03	-0.05	-	-0.07
Ti(7)	0.07 ± 0.04	0.07	0.14	0.06	0.12	-	-	-
Ti(8)	-0.09 ± 0.04	-0.13	-0.10	-0.08	-0.06	-	-	-
O(9)	0.00 ± 0.08	-0.05	0.00	0.02	0.03	-	-	-0.02
O(10,11) [1 1 0]	0.02 ± 0.06	-0.04	0.03	-0.03	0.00	-	-	-
	$\pm 0.07 \pm 0.06$	± 0.03	± 0.03	± 0.05	± 0.02			
O(12)	-0.09 ± 0.08	-0.04	-0.01	-0.01	0.03	-	-	-
Ti(13)	-	0.02	0.05	-	-	-	-	-
Ti(14)	-	-0.08	-0.06	-	-	-	-	-
O(15)	-0.12 ± 0.07	-0.07	0.01	-	-	-	-	-
O(16,17) [1 1 0]	-	-0.03	0.01	-	-	-	-	-
[1-10]	-	± 0.02	± 0.02	-	-	-	-	-
O(18)	-	-0.02	0.01	-	-	-	-	-
O(19)	-	0.02	-0.01	-	-	-	-	-

^a The atomic labels and the directions of the experimentally determined relaxations are given in [Fig. 7](#). The results are grouped by first authors: Charlton [94], Harrison [64], Ramamoorthy [68], Bates [249], Lindan [233], Vogtenhuber [100], and Reinhard [101]. Acronyms used are SXRD (surface X-ray diffraction), FP-LAPW (full-potential linear augmented plane wave), LCAO (linear combination of atomic orbitals), HF (Hartree–Fock), PW-PP (plane-wave pseudopotential), LDA (local density approximation), and GGA (generalized gradient approximation). Indicated are the number of TiO_2 repeat units used for the various calculations. Expanded from a similar compendium given in [64].

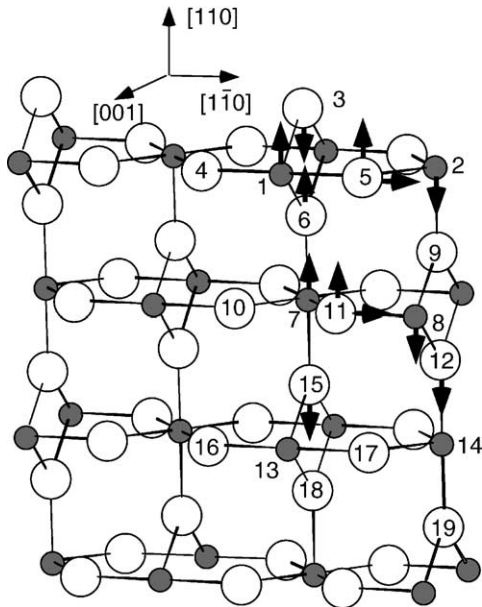


Fig. 7. Model of the $\text{TiO}_2(1\ 1\ 0)$ - (1×1) surface. The relaxations of surface atoms, determined with SRXD are indicated [94]. The labels refer to the relaxations listed in Table 3. Redrawn from Charlton et al. [94]. © 1997 The American Physical Society.

atoms (4, 5) upwards, causing a rumpled appearance of the surface. The relaxations in the second TiO_2 layer are approximately a factor of two smaller.

The most striking feature in the experimentally determined (relaxed) coordinates is the large relaxation of the bridging oxygen atoms by $-0.27\ \text{\AA}$. The measured geometry would indicate a very small bond length between the sixfold coordinated Ti atom (1) and the bridging oxygens (3) of only $1.71 \pm 0.07\ \text{\AA}$ instead of the $1.95\ \text{\AA}$ expected from the bulk structure. The relaxation results in vertical distances of 0.89 ± 0.13 and $1.16 \pm 0.05\ \text{\AA}$ from the sixfold (1) and fivefold coordinated (2) Ti atoms, respectively. This is in agreement with ion scattering measurements, where vertical distances of 87 and $1.05 \pm 0.05\ \text{\AA}$ were found [95,96]. (Another ion scattering study found the height of the bridging oxygen atoms comparative to that of the bulk structure but the interlayer distance largely relaxed with about $-18 \pm 4\%$ [97].) Photoelectron diffraction results [98] are also in agreement with relaxations from the X-ray diffraction work given in Table 3.

The results of total-energy calculations by several groups [64,68,99–102] are compared to the measured relaxations in Table 3. Two complementary approaches were used, the linear combination of atomic orbitals (LCAOs) and plane-wave techniques. Either periodic or free-standing supercells with different numbers of layers (in the sense of Tasker's non-polar repeat units in Fig. 6a) were used. For example, the configuration drawn in Fig. 7 represents part of the upper half of the seven-layer slab used by Harrison et al. [64]. Because of the localized nature of the $\text{Ti}3d$ electrons in the TiO_2 structure, plane-wave expansions are challenging. A rather high-energy cutoff needs to be used for convergence, and the functional for the LDA- or GGA-based calculations may also influence the results [103]. In addition, the thickness of the slab may play a role in the accuracy of the calculated geometry.

The directions of the calculated relaxations agree in (almost) all the theoretical papers with the experimentally determined coordinates. The quantitative agreement is not as good as one could expect from state-of-the art ab initio calculations, however. As Harrison et al. [64] pointed out, the extensive experience of calculations on bulk oxides which has been built up in recent years leads one to expect that DFT and HF calculations will reproduce experimental bond lengths to somewhat better than 0.1 Å. For example, the bulk structural parameters of TiO₂ rutile agree better than 0.06 Å using soft-core ab initio pseudopotentials constructed within the LDA, and a plane-wave basis [104].

In particular, all the calculations find a much smaller relaxation for the position of the bridging oxygen atom. A possible reason for this disagreement was given by Harrison et al. [64]. All the theoretical results listed in Table 3 are strictly valid only at zero temperature. It is conceivable that strong anharmonic thermal vibrations at the TiO₂(1 1 0) surface cause the discrepancy between experimental and theoretical results. However, molecular dynamics simulations using the Carr–Parinello approach [105] found that the average position in dynamic calculations is only relaxed by 0.05 Å rather than by 0.27 Å, discarding this explanation. Instead, it was suggested that the O atom might relax laterally so that it is displaced into an asymmetric position.

Based on these theoretical results, the finite temperature has to be taken into account for a proper evaluating diffraction results. Hopefully, future experiments will show whether a better agreement with theoretically predicted relaxations can be achieved. When considering surface reactions, one also needs to depart from a static picture of this and other oxide surfaces, and has to keep in mind the substantial distortions and bond length changes that take place during such large-amplitude vibrations.

It is now well-known that adsorbates often have a significant influence on ‘re-relaxing’ the surface. Computational studies, e.g. the one given in [106] for the adsorption of Cl, clearly show strong effects upon adsorption. Only a few experimental exist so far. For example, Cu overlayers on TiO₂(1 1 0) cause the Ti atoms at the Cu/TiO₂(1 1 0) interface relax back to the original, bulk-like positions. The O atoms relax even stronger, which was attributed to Cu–O bonding [107].

2.2.1.3. Appearance in STM and AFM. Naturally, scanning probe techniques are extremely useful tools for studying atomic-scale structures at TiO₂ and other metal oxide surfaces, where local changes in stoichiometry or structure can severely affect surface reactivity. On TiO₂(1 1 0), STM and, more recently, non-contact AFM, have been used by many different groups. These techniques have provided valuable and very detailed insight into local surface structure. However, the interpretation of STM images of oxides is somewhat challenging because of strong variations in the local electronic structure, and because tips can easily ‘snatch’ a surface oxygen atom, which can cause a change in tip states and result in ‘artifacts’ in STM images. There is now consensus among different groups on what is ‘really’ observed with STM, at least under ‘normal’ operating conditions.

The dominant tunneling site on TiO₂(1 1 0) surfaces has been subject to some debate in the past. In principle, there is uncertainty as to whether the image contrast is governed by geometric or electronic-structure effects. For TiO₂, atomic-resolution STM is often only successful when imaging unoccupied states (positive sample bias) on reduced (n-type) samples. In reduced TiO₂ crystals, the Fermi level is close to the conduction-band minimum (CBM) in the 3 eV gap, and electronic conduction occurs predominantly through high-lying donor states [78]. Under a typical bias of +2 V, electrons can thus tunnel from the tip into states within ~2 eV above the CBM, and be conducted away from the surface. On the one hand, these CBM states have primarily cation 3d character (the valence band having primarily O 2p character, see Section 3) so that one might expect to image the metal atoms as the

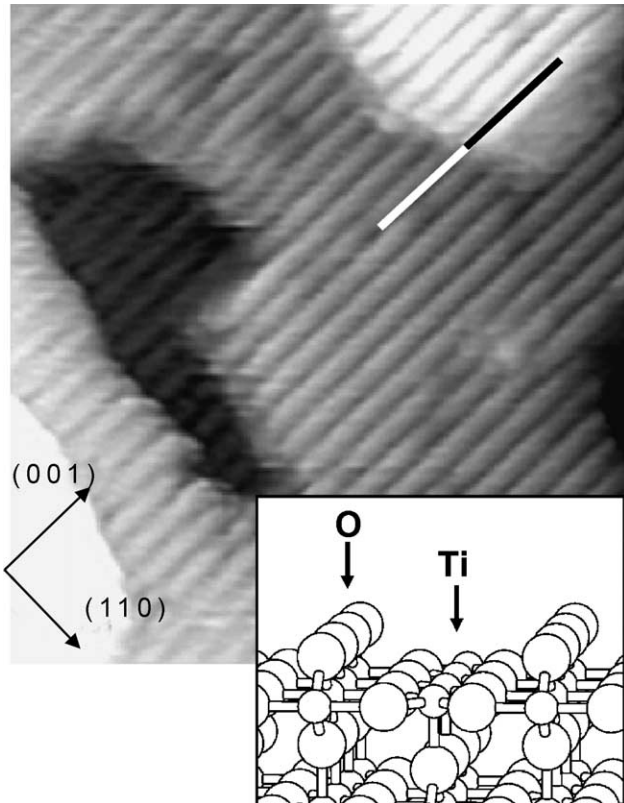


Fig. 8. STM image of a stoichiometric $\text{TiO}_2(1\ 1\ 0)$ -(1×1) surface, $140\text{\AA} \times 140\text{\AA}$. Sample bias +1.6 V, tunneling current 0.38 nA. The inset shows a ball-and-stick model of the unrelaxed $\text{TiO}_2(1\ 1\ 0)$ -(1×1) surface. There is now overwhelming evidence that the contrast on this surface is normally electronic rather than topographic, and that the bright lines in STM images normally correspond to the position of the Ti atoms rather than the bridging oxygen atoms. From Diebold et al. [116]. © 1998 The American Physical Society.

“white” features in STM topographs. On the other hand, the bridging oxygen atoms protrude above the main surface plane and dominate the physical topography (see inset in Fig. 8). Hence it seems equally plausible that geometrical considerations might dominate the contrast in STM images.

Fig. 8 shows an STM image of a stoichiometric (1×1) surface. Bright and dark rows run along the $[0\ 0\ 1]$ direction in Fig. 8. The distance between the rows is $6.3 \pm 0.25\text{\AA}$, in agreement with the unit cell dimension of 6.5\AA along $[1\bar{1}\ 0]$. At neighboring terraces they are staggered by half a unit cell. It is not immediately obvious if these bright rows correspond to lines of bridging oxygen atoms or fivefold coordinated Ti^{4+} ions. The “bridging oxygen” rows protrude from the surface plane on a relaxed $\text{TiO}_2(1\ 1\ 0)$ surface (see Table 3), so if STM were dominated by topographical effects, they would appear as rows with high contrast in Fig. 8. There is strong evidence that, normally, this is not the case, and that the Ti sites are imaged bright in this and similar images. Onishi and Iwasawa [108] have observed formate ions (which are expected to adsorb to Ti sites) on top of the bright rows. This is now confirmed for many other adsorbates, e.g. chlorine [109] and sulfur [77] appear as bright spots on top of bright or dark rows when adsorbed on Ti sites or oxygen sites, respectively, see Fig. 56 in Section 5.1.6.

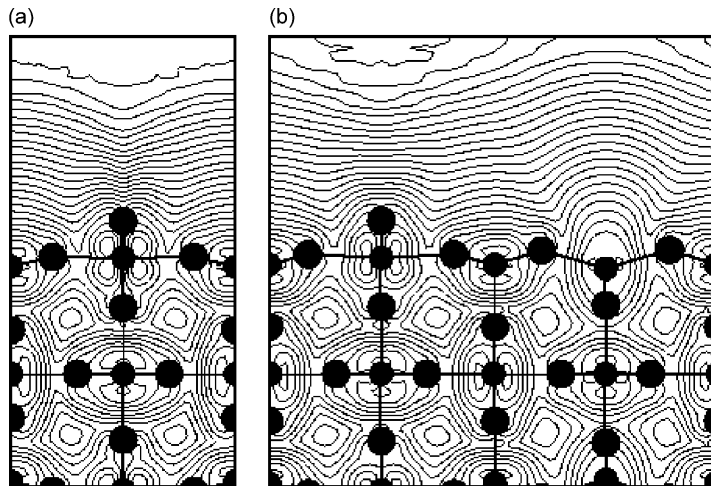


Fig. 9. Contour plots of [0 0 1]-averaged charge densities associated with electron states within 2 eV of the CBM for (a) the relaxed stoichiometric (1×1) surface, and (b) the relaxed oxygen-deficient (1×2) surface. Contour levels correspond to a geometric progression of charge density, with a factor of 0.56 separating neighboring contours. To first approximation, the STM tip will follow one of the equal-density contours several Ångstroms above the surface. From [110,116].

A theoretical approach to determine the image contrast in STM is shown in Fig. 9. Pseudopotential calculations were used to analyze the local density of states in the vacuum region above the surface [110]. In rough correspondence with the experimental bias conditions, the charge density of conduction-band states were summed up from 0 to 2 eV above the conduction-band minimum. This quantity was then averaged over the [0 0 1] direction and plotted as a function of the other two coordinates as shown in Fig. 9. Under constant-current tunneling conditions, the STM tip is expected to follow roughly one of the equal-density contours several Ångstroms above the surface. The plot in Fig. 9a clearly shows that the charge-density contours extend higher above the fivefold coordinated Ti atoms when the tip is a few Å above the surface, in spite of the physical protrusion of the bridging oxygen atoms. This confirms that the STM is imaging the surface Ti atoms, i.e., that the apparent corrugation is reversed from the physical one by electronic-structure effects. The slab in Fig. 9b has a (1×2) symmetry with every other bridging oxygen row missing. This configuration has been proposed originally to account for the (1×2) structure observed in LEED [111]. More recent experimental evidence, resulting predominantly from STM measurements, has shown that this is not a likely structure (see Section 2.2.2). However, the charge density contours in Fig. 9b indicate that single vacancies in the bridging oxygen rows are expected to appear as bright features on the dark oxygen rows.

A different and computationally less expensive computational approach has been taken by Gülsen et al. [112]. They have used a first-principles atomic-orbital base scheme with limited self-consistency. From analyzing the radial distributions of O and Ti wave functions, it was concluded that the STM tip should sample electrons from different surface atoms, depending on the tip-sample separation. For close distances (<4 Å) the contributions from the oxygen atoms should dominate, while for larger separations, the Ti atoms are dominant. Hence a ‘reversal’ of the tunneling site should be possible. STM images, taken with high tunneling current and relatively low bias voltages ($I_t = 2.0$ nA, $V_s = +0.75$ V) seem to confirm this conclusion [113]. Such images show an enhanced resolution, and

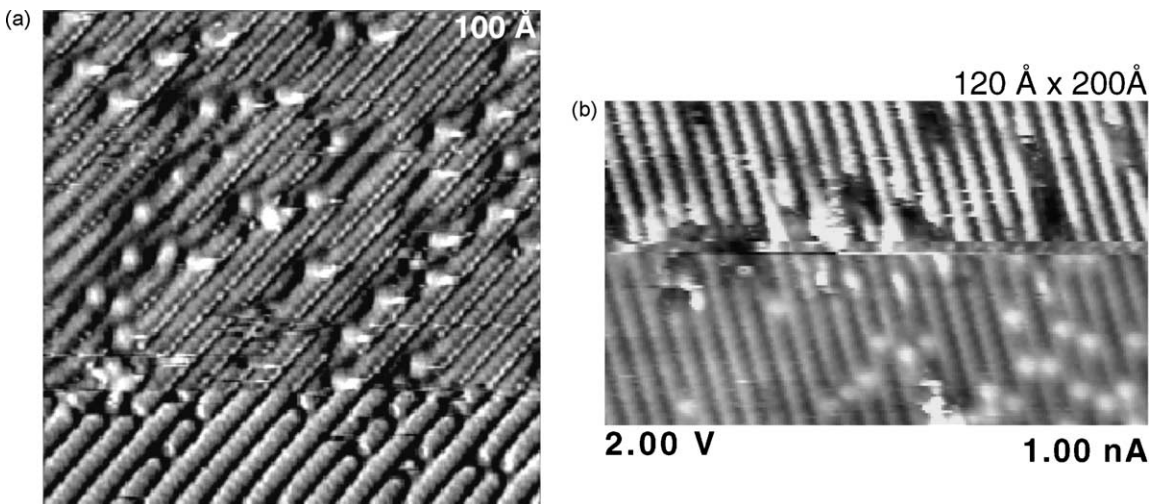


Fig. 10. Two examples for spontaneous tip changes that give rise to a changed appearance of STM images of $\text{TiO}_2(1\bar{1}0)$ –(1 × 1). When the tip is treated with high voltage/high current pulses the ‘normal’ tip state is usually re-gained that renders images as shown in Fig. 8. From [116]. © 1998 Elsevier.

alternating rows of individual dots and white rows. High resolution was also reported in [114] and has been explained as tunneling centered at the fivefold coordinate Ti^{4+} ions and at the bridging oxygen ions. After ‘functionalizing’ the STM tip by scanning over a Si surface with +10 V sample bias and 20 nA, enhanced resolution has been observed by another group [115]. These images were interpreted as tunneling into the sixfold coordinated Ti atoms underneath the bridging oxygen’s. The tunneling process was interpreted as being influenced by a strong chemical interaction and formation of a partial chemical bond between Si at the tip and surface oxygen.

Two examples for spontaneous tip changes are shown in Fig. 10 [116]. In the upper half of Fig. 10a, the lateral resolution appears to be enhanced as compared to ‘normal’ images, and additional small, bright spots are visible between the bright rows in some areas. This change in appearance did not result from an intentional lowering of the tunneling resistance as in [113], but was interpreted as an interference effect caused by a double tip with widely spaced apex atoms that are tunneling on different terraces by the authors in [116]. In Fig. 10b, a spontaneous tip change occurred about half-way through the image. At the lower half, bright spots are located between the bright rows. As indicated in the context of Fig. 9b, the position and appearance of oxygen vacancies can be taken as a tell-tale signal on whether the row of O or Ti are imaged, and the lower half is consistent with imaging the Ti rows. In one report, dark spots on bright rows have been assigned as point defects at $\text{TiO}_2(1\bar{1}0)$ surfaces [117]. Consequently, bright rows were assigned as the location of bridging oxygen atoms. The images shown in [117] resemble the upper part of Fig. 10b, where pronounced black spots appear on the bright rows. At first sight, the image shown in Fig. 10b could be taken as an indication for image reversal caused by such a compositional change. Note that the bright rows continue as dark rows on the right side of Fig. 10b. However, on the left side of Fig. 10b the bright rows are in phase on the upper and lower part of the image. This indicates that the observed change in contrast is caused by a lateral shift of the outermost atom on the tip apex rather than by an actual image reversal.

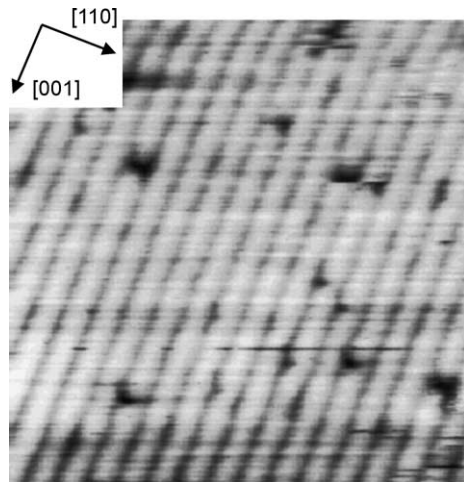


Fig. 11. Non-contact AFM image of a $\text{TiO}_2(1\bar{1}0)$ - (1×1) surface. From Fukui et al. [118]. © The American Physical Society.

A definite interpretation of images as shown in Fig. 10 is rather difficult. For the sake of studying surface structure and adsorbates, it is maybe better (and sufficient) to focus on results obtained with the ‘normal’ tip state that can be obtained reproducibly by ‘cleaning’ with high voltage/high current pulses.

As mentioned above, only few reports exist where satisfactory images have been obtained with negative sample bias (filled-state images) [77]. These were taken with a bias voltage that is too small to bridge the 3 eV gap. It is likely that a real ‘contrast reversal’ would occur under the tunneling conditions where the filled state of the VB are imaged, but, to this author’s knowledge, such images have not yet been reported.

Recently, non-contact AFM has been introduced as a complementary technique to study TiO_2 surfaces with atomic resolution. An image of the $\text{TiO}_2(1\bar{1}0)$ - (1×1) surface, obtained by Fukui et al. [118], is reproduced in Fig. 11. Frequency modulation described in [119] was used as the feed back signal. While the contrast formation of atomically resolved AFM images using this technique is also somewhat controversial [120], one would assume that the physical geometry should dominate in AFM. The registry of (1×2) strands (see Section 2.2.2) in AFM images is consistent with the bright rows in Fig. 11 being the protruding bridging oxygens. Consequently, the black spots in Fig. 11 were assigned as oxygen vacancies in [118].

2.2.1.4. Surface defects. The ability to control the amount of defects is one of the main attractions of TiO_2 as a ‘well-characterized’ model system. Because imperfections such as vacancies introduce changes in the electronic structure (in particular a band gap feature at ~ 0.8 eV below E_{Fermi} , and a shoulder in the XPS $\text{Ti}2\text{p}$ peak, see Section 3.2), they have been investigated with spectroscopic techniques for years. Much has been learned about the structure of defects, mainly because of recent investigations with scanning probe techniques. The following discussion considers steps; vacancies produced by thermal annealing, sputtering, and electron bombardment; as well as common impurities such as Ca and H.

2.2.1.4.1. Step edges. Sputtering and annealing in UHV (at not too high temperatures) renders flat (1×1) surfaces. As is expected for annealing of sputter-damaged surfaces, the terrace size increases with

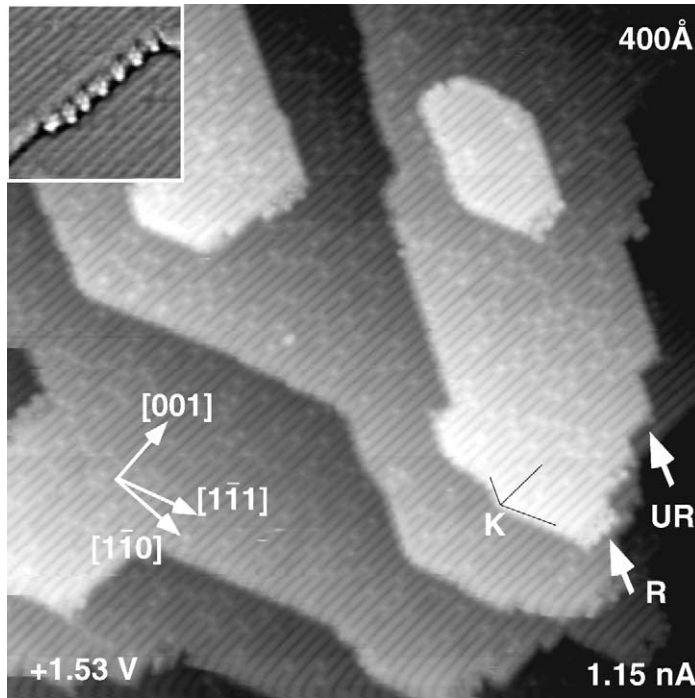


Fig. 12. STM image of a clean stoichiometric $\text{TiO}_2(1\ 1\ 0)$ - (1×1) surface after sputtering and annealing to 1100 K in UHV. The step structure is dominated by step edges running parallel to $\langle 1\bar{1}\bar{1} \rangle$ and $\langle 0\ 0\ 1 \rangle$ directions. A kink site at a $\langle 1\bar{1}\bar{1} \rangle$ step edge is marked with ‘K’. Smooth (‘UR’) and rugged (‘R’reconstructed) $\langle 0\ 0\ 1 \rangle$ -type step edges appear with roughly equal probability and are marked with arrows. The inset shows a $100\text{\AA} \times 100\text{\AA}$ wide image of a reconstructed step edge. From [116].

annealing temperatures. This has been shown nicely in an STM work by Fischer et al. [117]. The correlation length in SPA-LEED measurements (which corresponds to the average terrace size) has increases with a $T^{1/4}$ dependence at temperatures above 800 K [121]. Interestingly, Ar implanted during the sputtering process at relatively moderate ion energies (1000 eV) and fluences (typically $1\ \mu\text{A}/\text{cm}^2$ and 30 min) does not completely leave the near-surface region during annealing up to 1000 K and is still visible in XPS and AES [77].

An example for a typical terrace-step structure is shown in Fig. 12. Step edges on annealed surfaces run predominantly parallel to $\langle 0\ 0\ 1 \rangle$ - and $\langle 1\bar{1}\bar{1} \rangle$ -type directions [116,117,122]. These steps are measured to be 3.2\AA high, in agreement with the value expected from the rutile structure [123]. In Fig. 12, a kink site at the point where a $\langle 1\bar{1}\bar{1} \rangle$ -type step edge turns into a $\langle 1\bar{1}\bar{1} \rangle$ -type step edge is labeled with K. Such kink sites are located at the end of dark rows (the bridging oxygens). Two kind of $\langle 0\ 0\ 1 \rangle$ -type steps are pointed out by arrows in Fig. 13. One kind appears smooth (marked as UR), the other one rugged (marked as R for reconstructed) with a high number of kinks. The inset in the upper left hand corner shows a blow-up ($100\text{\AA} \times 100\text{\AA}$) of a rugged step edge. Both types of step edges appear with roughly equal probability in images.

It is relatively straightforward to construct models for step edges following the rules of autocompensation [5]. For example, Fig. 13 shows a ball-and-stick model of two layers of $\text{TiO}_2(1\ 1\ 0)$

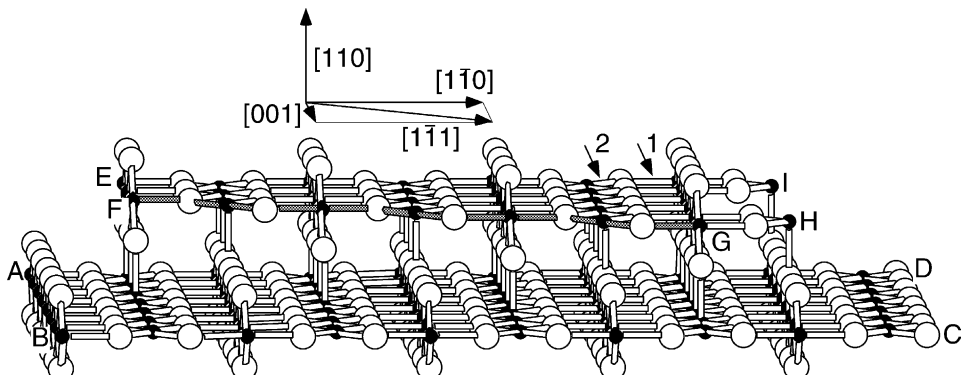


Fig. 13. Ball-and-stick model of two terraces of $\text{TiO}_2(1\bar{1}0)$. Small black balls represent Ti atoms and large white balls represent oxygen atoms. The step edge FG runs parallel to $\langle 1\bar{1}1 \rangle$ -type directions. The smooth and rugged step edges along $\langle 001 \rangle$ in Fig. 12 are attributed to step edges AB and HI, respectively. From [116].

that contains several step edges [116]. As outlined above (Section 2.2.1.1) the same number of $\text{O} \rightarrow \text{Ti}$ bonds and $\text{Ti} \rightarrow \text{O}$ bonds need to be broken when cutting a TiO_2 crystal, for example, by forming a step edge by removing part of the upper terrace. A $\langle 1\bar{1}1 \rangle$ step edge (parallel to the diagonal of the surface unit cell) runs between the corners labeled F and G. For clarity, the bonds along this step edge are shaded with gray color. The orientation of the step plane is $(1\bar{1}5)$. The O atoms along the $\langle 1\bar{1}1 \rangle$ step edge in Fig. 13 are alternately threefold (as in the bulk) and twofold coordinated. Formation of the step edge creates fourfold coordinated Ti atoms (terminating the Ti rows of the upper terrace) and fivefold coordinated Ti atoms (terminating the bridging O rows). It should be pointed out that either these fourfold coordinated Ti atoms have a formal oxidation state of +4, or their concentration is very low, because photoemission results of ‘unreduced’ surfaces show no evidence of Ti^{3+} .

A change in step orientation from the $\langle 1\bar{1}1 \rangle$ to the $\langle 1\bar{1}\bar{1} \rangle$ direction occurs always at the bridging oxygen rows (K in Fig. 12). The local environment of the atoms at such a kink site is not different from the rest of the step edge. Similarly constructed models of step edges oriented along $[1\bar{1}2]$ and $[1\bar{1}5]$ directions are given in [124].

There are several possibilities to form step edges parallel to the $\langle 001 \rangle$ direction. One can either cut next to the Ti atoms underneath the bridging oxygens (parallel to the arrow labeled 1 on the upper terrace in Fig. 13) or between the in-plane oxygen and titanium atoms (parallel to arrow 2). If one cuts at position 1, an uncompensated step edge is formed: for each $\text{Ti} \rightarrow \text{O}$ bond that is broken in the upper plane, one $\text{O} \rightarrow \text{Ti}$ bond is broken between the newly formed bridging oxygens of the lower plane and the fivefold coordinated titaniums of the upper plane. Note that there are two different terminations for such a step edge; the terrace may be terminated either by a row containing in-plane oxygen atoms (step edge DC in Fig. 13) or by a row of bridging oxygens (step edge AB). Because of the observed contrast at step edges (smooth step edges terminate with a dark row, Fig. 12), a termination with bridging oxygen atoms (step AB in Fig. 13) is favored. (Fischer et al. [117] have presented a model for a $\langle 001 \rangle$ step terminating in in-plane oxygen rows. However, these authors adapted a different interpretation of the bright rows in STM as being caused by bridging oxygen rows.)

If one cuts a terrace parallel to the $\langle 001 \rangle$ direction at position 2, the step edge that is formed is not uncompensated: only oxygen \rightarrow titanium bonds are broken on both the upper and on the lower

terrace. Hence, a step edge that terminates in a row of in-plane Ti atoms is not stable and may reconstruct. This is consistent with the observation of reconstructed step edges (R in Fig. 13) appearing whenever a terrace *would* terminate in a bright row. A ‘reconstruction’ was proposed [116] by removing three of four Ti atoms as well as the neighboring in-plane O atoms (step edge HI in Fig. 13). Such a structure is consistent with the bright bumps separated by 12 Å that are observed in STM. It also fulfills the criterion of autocompensation. As has been pointed out before [116], step edges that run parallel to $\langle 1\bar{1}0 \rangle$ type directions (step edge BC in Fig. 13) are generally not observed. This also fits well into the concept of autocompensation. Such a step edge would not be autocompensated and therefore is not expected to be stable. It should be noted that step edges play an important role in the $(1 \times 1) \rightarrow (1 \times 2)$ phase transformation [125]. It is interesting that the two-step $\langle 0\bar{0}1 \rangle$ terminations with very different geometries are seen. So far no temperature-dependent STM studies have been performed to find out how annealing temperature affects the relative contribution of these two step edge terminations. In principle, the presence of very small amounts of trace impurities can also not be ruled out. In this sense, the model in Fig. 13 for the reconstructed step edge must remain speculative until supported by more theoretical or experimental evidence.

This detailed insight into step geometries and coordination number of atoms at step edges and kink sites is important, because a decrease in coordination number of surface atoms often correlates with an enhancement in chemical reactivity. Microscopic or nanoscopic particles naturally exhibit a much higher step/kink concentration than flat single crystals used for surface-science studies, so this issue is even more important in applications that use such materials, see Section 1.2. A few systematic studies of the effect of step edges on surface chemistry under UHV conditions have been reported. For example, pyridine molecules have been found to be more strongly adsorbed at fourfold coordinated Ti atoms at step sites than at the fivefold coordinated Ti atoms on the terraces [124]. On the other hand, the opposite effect has been observed by Iwasawa et al. [126] for adsorption of formic acid on $\text{TiO}_2(1\bar{1}0)$. Adsorption at 400–450 K resulted in particles with a strongly suppressed presence in the vicinity of step edges. Possibly, electrostatics plays a role. To this author’s knowledge, virtually no theoretical work has been done to determine step geometry with the same detail as flat surfaces. Because step edges break the symmetry, first-principles calculations would require huge unit cells. With the advent of ever faster computers and more powerful programs such calculations may soon become viable.

2.2.1.4.2. Oxygen vacancies created by annealing. There is overwhelming spectroscopic and chemical evidence for the presence of point defects on samples sputtered and annealed in UHV. These are attributed to vacancies in the bridging oxygen rows. Their concentration is typically reported as several percent [127,128]. These defects are of high importance for the surface properties of $\text{TiO}_2(1\bar{1}0)$. No systematic study on the correlation between defect concentration and bulk properties has been performed on single crystals. EPR studies on a polycrystalline TiO_2 powder [129], reduced at temperatures between 723 and 923 K in vacuo, showed that the ratio of surface-to-bulk Ti^{3+} cations decreases as the reduction temperature is increased.

Thermally induced point defects are visible as distributed black points on the bright oxygen rows in the AFM image in Fig. 11. As already pointed out, STM results are harder to interpret because of strong electronic effects. STM images of titanium dioxide surfaces that have been annealed in UHV often exhibit two kinds of atomic-scale features (Fig. 14). These appear as short bright features centered on dark rows (labeled A) and as connecting neighboring bright rows, and as dark spots on the bright rows (labeled B). The features labeled A have a density of $7 \pm 3\%$ per surface unit cell, consistent with O

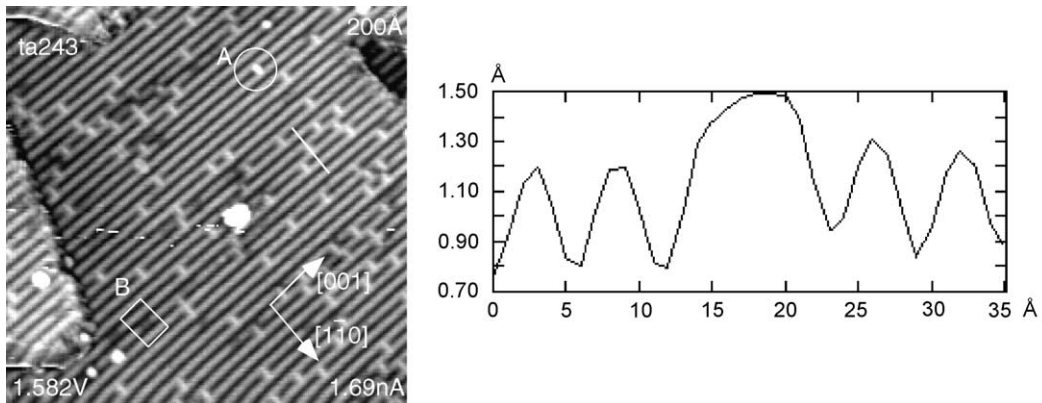


Fig. 14. STM image ($200\text{\AA} \times 200\text{\AA}$) of a $\text{TiO}_2(1\ 1\ 0)$ surface, sputtered and annealed in UHV to 1100 K for 10 min, showing point defects. Features labeled with 'A' have been assigned as oxygen vacancies. The position of the line scan shown is indicated in the image. From [116].

vacancy density estimates from spectroscopic measurements. The size of the bright spots is of the order of one single atom (FWHM 5 Å in line scans along the [0 0 1] direction) when taking into account convolution with the tip. They always appear as isolated spots with no apparent short-range ordering but a slight tendency to be staggered perpendicular to the rows. It is well-known that oxygen vacancies are healed by dosing a reduced TiO_2 sample with oxygen [127,130,131]. When the sample in Fig. 14 was stepwise exposed to oxygen, the density of the bright spots (A) decreased. This, and the contrast expected from electronic structure calculations (missing bridging oxygens give rise to a protrusion in empty-states charge-density contours, see Fig. 9b) led to the assumption of the bright spots being missing oxygen vacancies [110,116]. As was reported in [116], their appearance in STM is strongly tip-dependent.

The dark features (B in Fig. 14) are less common (surface concentration of $\sim 1\text{--}2\%$) than the oxygen vacancies. They can extend over several unit cells. Upon adsorption of oxygen, the number of the dark spots stays constant within the statistical error. They were tentatively assigned as subsurface oxygen vacancies [109], however, first-principles total-energy calculations show that such a configuration is highly unlikely [132]. Their nature is unclear at this point.

The 'A' features, assigned to oxygen vacancies in Fig. 14, are mobile in STM images, albeit in a somewhat erratic fashion [116]. They can be removed by scanning with a high bias voltage [116,133], hence one needs to consider that they represent adsorbates, specifically H atoms adsorbed on a bridging O atom. In [116] this possibility was discarded because the density of these features decreases upon exposure to molecular oxygen, as expected for a 'filling' of vacancies, and because they could not be flashed off. Suzuki et al. [133], however, argued that these features represent H atoms on bridging oxygen atoms because their number density decreases upon irradiation with 20 eV-electrons and increases upon exposure of the surface to atomic hydrogen. A few 'A' features were resistant against irradiation with electrons and were attributed to H atoms trapped on an oxygen vacancy. These authors concluded that H adatoms, either on bridging oxygen atoms or on O vacancies, still exist on $\text{TiO}_2(1\ 1\ 0)$ when surfaces were prepared by sputtering and annealing. The H was supposed to stem from the bulk. Recent STM of clean and water-covered surfaces showed that oxygen vacancies and hydroxylated bridging oxygen atoms are imaged slightly different in STM images [134], see Fig. 15. The main

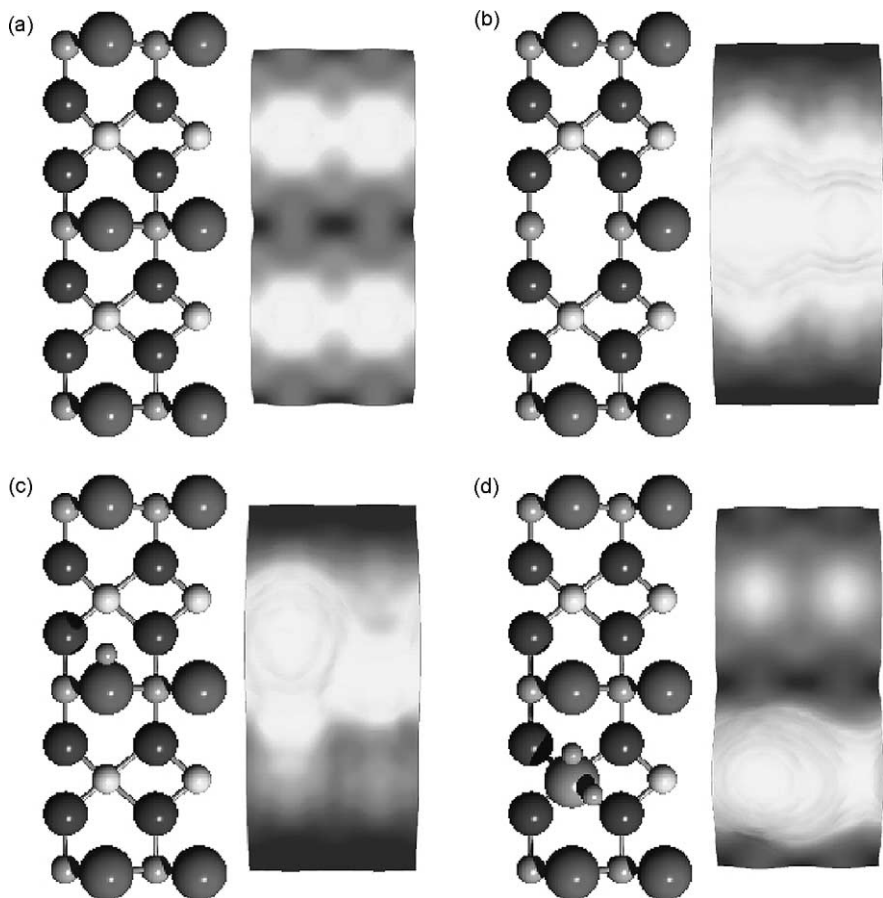


Fig. 15. Ball-and-stick model and corresponding simulated STM image at 1 V showing the appearance of a: (a) vacancy-free surface, (b) bridging oxygen vacancy, (c) bridging OH group and (d) water molecule on top of a fivefold coordinated Ti atom. Big atoms: O, smaller atoms: Ti, smallest atoms: H. Note that both, a vacancy and an OH group in the bridging oxygen rows, appears as bright spots on dark rows in STM images. From Schaub et al. [134]. © 2001 The American Physical Society.

difference in their appearance is their extent in $[0\ 0\ 1]$ direction (vacancy 6.6 \AA , OH 4.8 \AA), and their apparent height (0.4 \AA , 0.2 \AA) [134].

In this author's opinion, most of 'A' features should still be attributable to O vacancies, at least at 'fresh' surfaces that have been prepared in a good vacuum. There is overwhelming evidence from spectroscopic measurements that such O vacancies exist, and the increasing experience with STM measurements of slightly defective surface supports this interpretation. One needs to point out, however, that an (inadvertent) exposure to a few Langmuirs of water (which dissociates at vacancies, hence fills them with a hydroxyl) could be sufficient to replace all O vacancies with two H-covered bridging oxygen atoms. While the calculated difference in image contrast (Fig. 15) gives hope to distinguish between an O vacancy and a H-covered bridging O atom, the strongly tip- and bias-dependent appearance of the 'A' features [116,133] in actual images makes their quantification tricky.

2.2.1.4.3. Oxygen vacancies created by other means. Oxygen vacancies can also be created by bombardment with electrons. TiO_2 is the classic example for a maximum-valency compound material where electron-stimulated desorption occurs via the Knotek–Feibelman process [135]. Bombardment with energetic electrons creates a core hole in the $\text{Ti}3\text{p}$ level. With a certain probability, this hole is filled through an inter-atomic Auger process from a neighboring O atom. If two (instead of the usual one) valence electrons are emitted during the Auger decay, the oxygen anion becomes positively charged. The previously attractive Madelung potential changes into a repulsive one, and an O^+ ion is emitted [136]. This process has a threshold energy that correlates with, but is not exactly located at, the $\text{Ti}3\text{p}$ edge as discussed in detail in [137]. Such electron-stimulated defects behave somewhat different than thermally created ones [138]. It is generally assumed that electron bombardment results in ejection of bridging oxygen atoms, but direct evidence from STM studies points towards more complicated structures [139]. The high current and high field provided by an STM tip has been used to create protrusions and craterlike depressions structures [140]. Irradiation with high-energy electrons (300 keV) induced a TiO as well as an intermediate TiO_2 -II phase [141].

Defects can also be created by irradiation with UV light, but nothing is known about their structure [142]; as is generally the case, the cross-section for photon-stimulated desorption is much less as compared to electron-stimulated desorption. Sputtering with rare gas ions reduces the surface oxygen content. Usually, the long-range order of the surface is lost, and the LEED pattern disappears. Spectroscopic measurements as well as adsorption experiments indicate the defects are more complex, involving more than one atom, and are partially subsurface [138]. There are indications that sputtering does not completely randomize the surface but results in a surface with short-range order that is changed from a twofold to a fourfold symmetry [143]. Generally, sputter-induced damage can be removed easily by annealing in UHV [74].

2.2.1.4.4. Line defects. STM images of UHV-annealed surfaces (which exhibit a (1×1) LEED pattern) often show dispersed bright stands, typically several tens of Ångstroms long. They are distributed across terraces and have a tendency to grow out of step edges onto the lower terrace (see Fig. 16a). The strands are centered on top of bright rows of the lower terrace (on top of the fivefold coordinated Ti atoms). STM often shows a bright spot at the end. A double-strand structure is resolved in high-resolution images (Fig. 16a). As shown in Fig. 16, these strands are precursors for the (1×2) reconstruction. Conflicting geometric models have been proposed for this reconstruction. These are discussed in Section 2.2.2.

The presence of such dispersed strands is sample-dependent. Li et al. heated samples cut from the same specimen to different temperatures in a furnace in order to achieve different levels of bulk reduction (see Fig. 5). After sputtering and annealing at 973 K for 10 min, strands were present on dark blue samples. Less reduced samples that exhibit a lighter color did not show any strands [144]. The reduction state of the crystal may not only influence the density but also the geometric structure of the strands [76]. Investigations with numerous TiO_2 samples in this author's laboratory have shown that small amount of bulk impurities (well below the detection limit of commonly used surface analytical techniques) can also cause strands on the surface. This is in addition to the bright strings caused by Ca segregation discussed in the next section.

2.2.1.4.5. Impurities. Commercial TiO_2 single crystals are generally quite clean. A common impurity that has been investigated on $\text{TiO}_2(1\ 1\ 0)$ is calcium. It tends to segregate to the surface upon high-temperature annealing [145–148]. Typically, Ca can be depleted from the near-surface region in a few

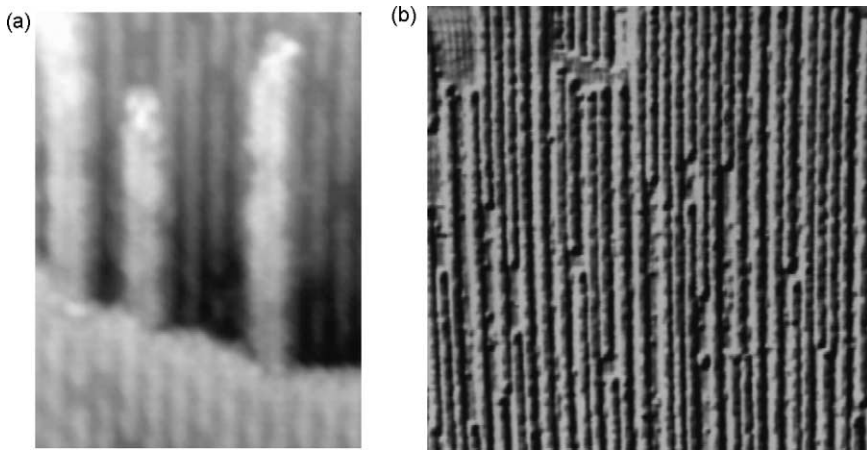


Fig. 16. (a) STM image of strings growing out of the upper terrace. These strings are centered at the fivefold coordinated Ti rows of the lower terrace. They are precursors of the (1×2) reconstruction. The surface was annealed at 1020 K for 1 min ($8.5 \text{ nm} \times 12.3 \text{ nm}$, sample bias: +0.7 V, tunneling current: 0.3 nA). (b) Variable current scan of the (1×2) -ordered strings on the surface annealed at 1150 K ($70 \text{ nm} \times 70 \text{ nm}$, sample bias +2.0 V, tunneling current 0.3 nA). The vertical axis in both images is parallel to the $[0\ 0\ 1]$ direction. From Onishi and Iwasawa [123]. © 1994 Elsevier.

sputter/annealing cycles. For high coverages, it forms a well-ordered overlayer which can clearly be observed in LEED [145–147]. Zhang et al. reported a

$$\begin{pmatrix} 6 & 0 \\ 3 & 1 \end{pmatrix}$$

structure in LEED and $[0\ 0\ 1]$ -oriented, bright strands in STM. The formation of a CaTiO_3 -like surface compound was tentatively proposed. This structure was questioned by Nörenberg and Harding [147], who reported a $p(3 \times 1)$ reconstruction and antiphase boundaries which could give rise to the LEED pattern observed in [145]. Model calculations suggest that Ca substitutes fivefold coordinated surface Ti atoms. Two vacancies form at the sites of the threefold coordinated O atoms located next to the Ca atom. Ordering is energetically favorable, and the relaxed structure is predicted to be buckled [147]. The Ca-segregated surface is very flat which points to a rather low surface free energy. Such a flattening takes place also in other segregated oxide systems [149]. Ca segregation also appears to affect the formation of CSPs (see next section). It has been reported that plasma treatment is efficient for the removal of Ca at low temperatures [150].

The presence of H on nominally clean surfaces has been discussed in the context of STM of O vacancies, above. In addition to Ca, some Mg segregation is sometimes observed with LEIS. Persistent Al impurities were detected with static SIMS [151]. This technique is very sensitive to certain elements. The Al probably resulted from the polishing procedure. SSIMS measurements have also shown that the most common impurity in samples from different vendors is K [152]. All alkali and earth alkali impurities can be removed to a large extent by sputtering/annealing cycles. A persistent impurity, which was only apparent in STM images, was attributed to V contamination [153].

2.2.1.4.6. Crystallographic shear planes. As pointed out above, the oxygen loss through thermal annealing that occurs in the bulk of TiO_2 crystals can lead to CSPs. An overview of CSPs and their

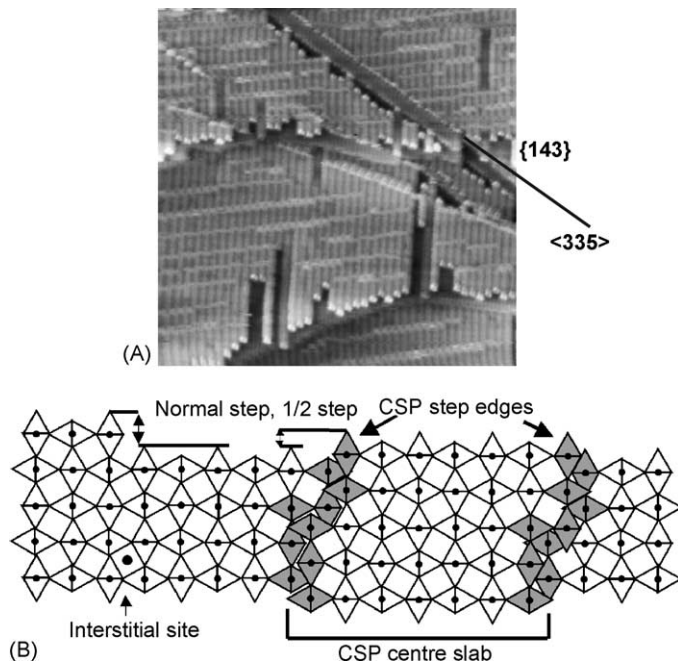


Fig. 17. (A) STM image ($400 \text{ \AA} \times 400 \text{ \AA}$, 0.2 nA , 1 V , 773 K) showing a pair of CSPs running in the $\langle 3\ 3\ 5 \rangle$ direction across (1×2) -reconstructed terraces. (B) Schematic diagram of a $\langle 0\ 0\ 1 \rangle$ projected view of a pair of CSPs terminating at the $[1\ 1\ 0]$ surface. Oxygen ion distorted octahedra centered on the Ti^{4+} ions (dark dots) are indicated by the diamond shapes (cf. Fig. 6). The interstitial Ti populates the $\langle 0\ 0\ 1 \rangle$ channels in the bulk lattice as indicated at the bottom left while a normal step edge is shown in the top left corner. The distorted octahedra forming the CSPs are shown in gray and have not been relaxed from their bulk positions in the normal and displaced lattices. Where the CSPs terminate at the surface $1/2$ height steps are formed which have differing structures. From Bennett [157]. © 2000 Royal Society of Chemistry.

relation to surface structure is given by Bennett et al. [87]. The CSPs are formed by shifting the normally edge-sharing octahedra (see Fig. 6a) to a face-sharing arrangement. They can be thought as consisting of small, undisturbed volumes of the regular rutile lattice, separated by CSPs (see Fig. 17). As their concentration increases, they can order into a regular array known as Magnéli phases (see Fig. 4). Two homologous series of Magnéli phases are known to exist with shear planes along $\{1\ 2\ 1\}$ and $\{1\ 3\ 2\}$ directions (see Table 1 in [87]). The CSPs intersect the $(1\ 1\ 0)$ surface with adjacent sections of the crystal being displaced by 1.6 \AA . A good example of CSPs intersecting with a (1×2) -reconstructed surface is shown in Fig. 17.

One of the first STM studies of reduced TiO_2 showed various periodic structures which were interpreted as CSPs [84,154], but these images look quite different from later investigations of CSPs. TiO_2 crystals that were subjected to heat-treatment only (without sputtering) showed Ca segregation and step edges along $[\bar{1}\ 1\ 0]$, $[\bar{1}\ 1\ \bar{1}]$ and $[\bar{1}\ 1\ 1]$ directions [85]. These were interpreted as CSPs belonging to a close packed family of $\{1\ 1\ 2\}$ planes [85]. The substantial Ca segregation may have influenced this structure. The surface structure of the most oxygen deficient Magnéli phase, Ti_4O_7 , was investigated also [155].

After repeatedly sputtering and heating (1223 K) of a $\text{TiO}_2(1\ 1\ 0)$ crystal (which diminished the initially observed Ca segregation), Bennett et al. [87] reported STM and LEED results of CSPs on a crystal with dark blue/black color. The crystal showed a rippled texture that was visible with the naked eye.

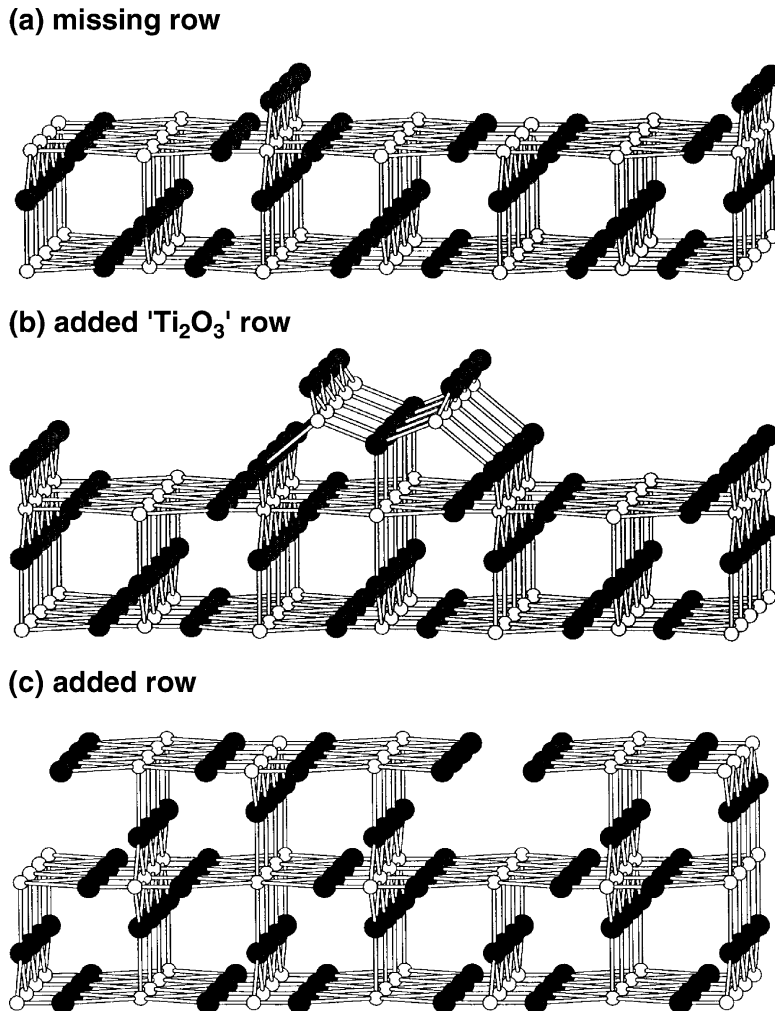


Fig. 18. Models for the $\text{TiO}_2(110)-(1 \times 2)$ surface. Small white balls: Ti, large black balls: O. (a) The ‘missing row’ model, obtained by removal of one row of bridging oxygens, was originally proposed by Møller and Wu [111]. This model is inconsistent with more recent STM images and first-principles calculations. (b) The ‘added-row model’ has Ti_2O_3 stoichiometry. It was suggested by Onishi et al. [122]. (c) The ‘missing unit’ model was proposed by Pang et al. [163]. Recent evidence suggests that the structures in (b) and (c) might be both present at $\text{TiO}_2(110)-(1 \times 2)$ for different conditions. From Tanner et al. [113]. © 1998 Elsevier.

The Ti (390 eV)/O (510 eV) AES ratio was 1.22 for the heavily reduced surface². This is to be compared to a ratio of 1.14 for the (1×1) -terminated surface. On different parts of the crystal, streaks along the $[1\bar{1}1]$ and $[1\bar{1}2]$ directions, or a superposition of the two, were observed with LEED. STM images show a large concentration of steps running along $\langle\bar{1}12\rangle$ and $\langle1\bar{1}2\rangle$ with the expected step height of 1.6 Å, as well as a strong variation in mesoscopic morphology [87]. The CSPs also act as nucleation sites for re-growth of new TiO_2 layers during high-temperature oxidation (see Section 2.2.2) [157].

²Probably the color of the sample in [87] was very dark. No CSPs have been observed on any of the cubes shown in Fig. 5 [156].

2.2.2. Reconstructions

2.2.2.1. Reconstruction under reducing conditions: the structure(s) of the (1×2) phase. The most commonly observed reconstruction on $\text{TiO}_2(1\bar{1}0)$ surfaces has a (1×2) symmetry with a doubling of the periodicity along the $[1\bar{1}0]$ direction. Various models have been suggested for this reconstruction and the most popular ones are depicted in Fig. 18 [113].

A (1×2) LEED pattern was originally observed after high-temperature annealing of a reduced $\text{TiO}_2(1\bar{1}0)$ sample in ultrahigh vacuum (UHV). Based on Ti:O AES ratios it was interpreted as alternate rows of bridging oxygen missing from the regular (1×1) surface (“missing-row model” [111], Fig. 18a). One of the first atomically resolved STM results on this surface was also interpreted as missing bridging oxygen rows [114,158]; however, the Ti atoms underneath the missing oxygen atoms had to be shifted by half a unit cell in $[001]$ direction to account for the observed image contrast. A structure with a (3×2) symmetry was reported in [159]. A model for this reconstruction was discussed where this symmetry is achieved by removing $1/3$ or $2/3$ of the oxygen in the bridging oxygen rows. However, such a reconstruction has not been reported by other groups.

The simple missing row model for the (1×2) structure in Fig. 18a has been abandoned on the basis of more recent results. In STM the (1×2) reconstruction is commonly observed as a series of bright strings along the $[001]$ direction [113,114,123,158,160–162], see Fig. 16. At low coverage, the strings grow preferentially out of the upper terrace onto the lower one (Fig. 16a) [123]. At first, they are scattered across the terraces with a minimum distance of 13 \AA along the $[001]$ direction. They consist of bright double strings (although the double-ridge structure is often not resolved), with a bright dot at the end. Antiphase boundaries are observed in high-resolution images of a fully developed (1×2) -reconstructed surface [113]. Higher periodicities, i.e., a local (1×3) reconstruction, have also been observed [161,163,164]. In STM images the (1×2) strands generally have an apparent height smaller than a regular TiO_2 step edge of 3.2 \AA , and are in registry with the bright rows of the (1×1) substrate. Because most researchers report empty-state images and because these are dominated by the tunneling into mostly Ti^{3d} -derived states (see Section 2.2.1.3), bright strands in line with bright substrate rows imply that the (1×2) strands are at the position of fivefold coordinated Ti atoms and not at the bridging oxygen atoms. STM images of a simple missing row structure are expected to show a bright feature above the missing bridging oxygen row (provided the STM tip is a reasonable distance from the surface [112]), inconsistent with the registry observed experimentally. The rows can be removed by tunneling under ‘extreme conditions’ ($V_s = +1.5 \text{ V}$, $I = 10 \text{ nA}$ [113]). First-principles total-energy calculations show that the added Ti_2O_3 model (discussed next) is energetically favored [165] and that the missing row structure is energetically equivalent to a (2×1) structure (where every other bridging oxygen is removed) [99]. For all these reasons, the missing-row reconstruction is no longer considered a viable model.

Early on, Onishi et al. [122,123] suggested a quite different model. It consists of double rows of Ti cations in a distorted tetrahedral configuration (Fig. 18b). The structure has Ti_2O_3 stoichiometry, and the model is often called ‘added Ti_2O_3 rows’. However, it needs to be emphasized that the structure does not resemble the one found in the corundum Ti_2O_3 structure. Rather, the Ti cations reside in positions similar to interstitial sites in the rutile lattice [91]. Self-consistent total-energy and electronic structure calculation found that this added ‘ Ti_2O_3 ’ row structure has a lower surface free energy than the missing row structure and that it is consistent with the contrast in STM [165]. Recent VASP calculations show that such strands can be added at low energy cost [91], but also that many other

configurations are energetically likely. The model is also supported by ESDIAD [166], high-resolution STM [113], and ion scattering [164] measurements.

Based on the fact that (1×2) rows extend out of step edges, a modified model of the missing row structure has been proposed by Murray et al. [88] which involves narrow rows with missing bridging oxygens that are effectively part of the upper terrace. Lateral relaxations were also included [88]. This model was shown to be consistent with calculated surface charge densities [112]. Based on the same scheme, an ‘added-row model’ was proposed by Pang et al. [163] for the fully reconstructed surface. This consists of narrow, long regions of the regular TiO_2 structure with all the atoms in bulk-like positions and with all bridging oxygen atoms missing (Fig. 18c). The black grooves between the bright rows are then due to the missing TiO_2 units separating the rows. (Consequently, this model has also been called ‘missing unit’ structure [113].) The stoichiometry of the added rows is Ti_3O_5 . The model was based on STM images with unusually high resolution and the observation of a (1×3) phase consisting of thicker rows. Charge-density calculations by Pang et al. supported the added-row model, but were inconsistent with either the added Ti_2O_3 or the simple missing row model (Fig. 18a and b, respectively). The off-normal lobes in ESDIAD images were supposed to stem from the O atoms at either side of the added ‘rows’, adjacent to the missing units.

Pang’s model has been questioned by Tanner et al. [113,167,168]. The (1×2) strands that are part of ‘restructured’ surfaces after low-temperature oxidation (see Section 2.2.2.2) are consistent with the added Ti_2O_3 model rather than the added Ti_3O_5 row model [144]. Ion scattering measurements are also consistent with the added ‘ Ti_2O_3 ’ model [164] although (somewhat surprisingly) extra oxygen atoms at the position of the fivefold coordinated Ti atoms were postulated according to these measurements. In a recent paper, several energetically accessible reconstructions were considered [91]. As is discussed in the next section (2.2.2.2), the two added-row models appear not to be mutually exclusive, and the formation of one or the other structure may just depend on the sample preparation parameters and crystal reduction state of the crystal.

2.2.2.2. Restructuring under oxidizing conditions. The first atomic-level investigation of the dynamic processes that occur when reduced TiO_2 crystals are exposed to oxygen was reported by Onishi and Iwasawa [169]. These authors used a blue crystal with a resistivity of $2 \Omega \text{ m}$, i.e., with a color probably comparable to cube 5 in Fig. 5b, see Table 2. They acquired STM images while the sample was kept at a temperature of 800 K and under an O_2 background pressure of $1 \times 10^{-5} \text{ Pa}$. Added rows (interpreted as Ti_2O_3 rows, Fig. 18b) and ‘hill-like features’, appeared while imaging the surface, and disappeared when the oxygen was pumped out from the chamber. This effect was not tip-induced; the same structures were observed on areas of the sample that were not imaged during the high-temperature oxygen exposure.

It is now established [75,76,156,170–172] that such an oxygen-induced surface restructuring effect is attributed to the reoxidation of the reduced crystal, as already suggested by Onishi and Iwasawa [169]. As mentioned above, the bulk of sub-stoichiometric TiO_{2-x} samples contains, in addition to O vacancies, Ti interstitials which show a high diffusivity at elevated temperatures. When these interstitials appear at the surface, they can react with gaseous oxygen and form additional TiO_2 (or Ti_aO_b) structures. For extreme cases a complete reoxidation of the whole crystal can be achieved, see cube 2 in Fig. 5 that has been re-oxidized to a transparent color. This reoxidation process has pronounced effects on the surface structure.

The kinetics of the oxygen-induced restructuring process as well as the resulting surface morphologies depend on sample temperature, annealing time, gas pressure, and reduction state (i.e.,

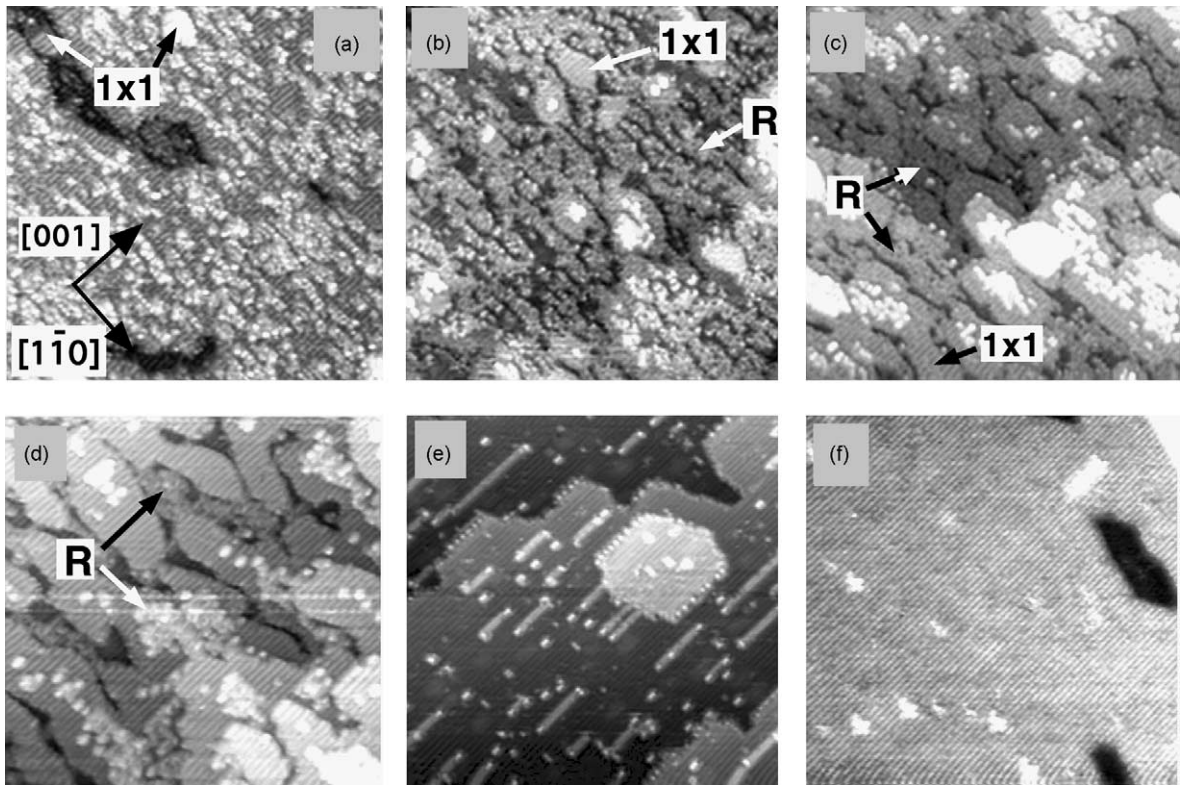


Fig. 19. STM images ($500 \text{ \AA} \times 500 \text{ \AA}$) of a TiO_2 (110) surface taken at room temperature. $^{18}\text{O}_2$ (1×10^{-6} mbar) was dosed at (a) 500 K, (b) 520 K, (c) 550 K, (d) 660 K for 10 min, (e) 710 K for 15 min, and (f) 830 K for 20 min. Before each gas exposure, the sample was sputtered and annealed in UHV at 880 K for 30 min which renders flat, (1×1) -terminated surfaces. From Li et al. [75]. © 1999 Elsevier.

'age' or color) of the crystal. These parameters have been investigated in detail by Li et al. [75,144,156,170,171]. For example, Fig. 19 shows the effect of annealing in 1×10^{-6} mbar O_2 at various temperatures [75]. Before each gas exposure, a flat (1×1) -terminated surface was prepared by sputtering and annealing in UHV. The surface morphology of the oxygen-exposed sample is very temperature dependent. For medium temperatures, surfaces are relatively rough with many small-scale features. Isotopically labeled $^{18}\text{O}_2$ gas was used for the annealing excursions. In SSIMS and low-energy He^+ ion scattering measurements, the signal from ^{18}O atoms can clearly be separated from the (naturally much more common) ^{16}O isotope in the crystal. All the surfaces in Fig. 19 showed an enrichment with ^{18}O , with a maximum of ^{18}O surface concentration around 660 K. The structures that form for intermediate annealing temperatures (520–660 K) are better seen in the small-scale image in Fig. 20. They consist of small, (1×1) -terminated islands and irregular networks of connected 'rosettes', i.e., six bright spots in a pseudohexagonal arrangement, as well as small strands. A model for the rosette network is shown in Fig. 21. It consists of atoms in bulk-like positions with some atoms missing from the regular (1×1) structure. LDA-based first-principles calculations [75] showed that such a rosette structure is stable. The same calculations also predict sizable relaxations.

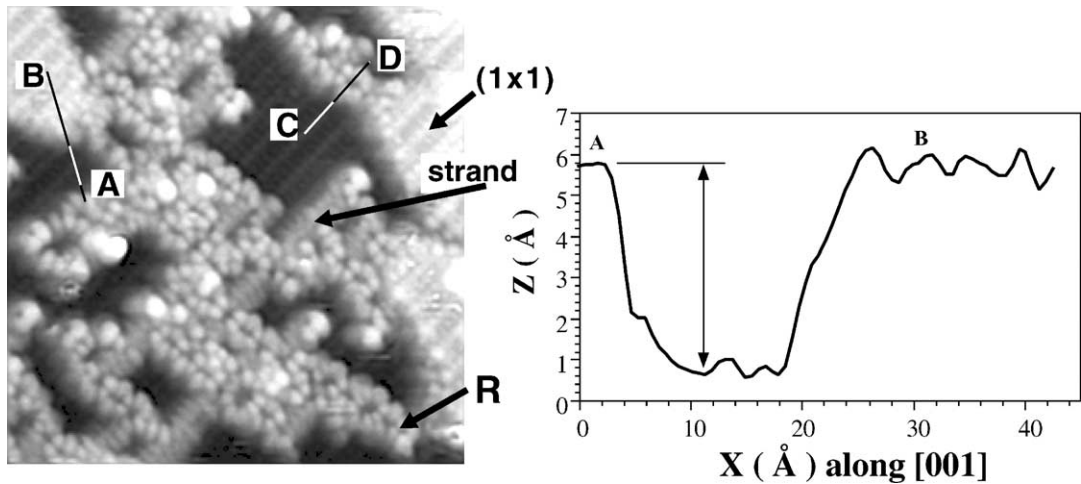


Fig. 20. An atomically resolved STM image ($150\text{ \AA} \times 150\text{ \AA}$) of a surface prepared as in Fig. 19. Small (1×1)-terminated islands and patches of connected pseudohexagonal rosettes are seen. From Li et al. [75]. © 1999 Elsevier.

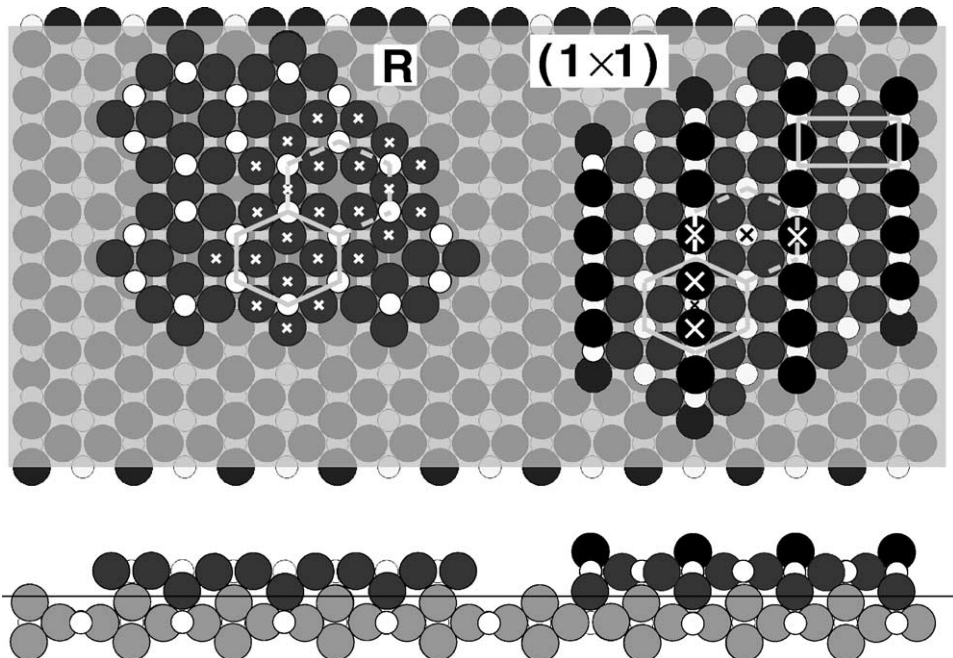


Fig. 21. Atomic model (top and side view) for the oxygen-induced structure observed in (a). A bulk-terminated (1×1) island is shown on the right side and the unit cell is indicated. Small white balls are Ti atoms. Shadowed large balls represent oxygen atoms; darker shading indicates higher z -positions. The rectangle indicates the unit cell of the (1×1) structure. The network patch ('R') on the left side consists of an incomplete $\text{TiO}_2(1\ 1\ 0)$ -(1×1) layer and contains only atoms at bulk positions. The strands probably have a structure similar to the added Ti_2O_3 model in Fig. 18b. From Li et al. [75]. © 1999 Elsevier.

The rosette structure can be explained simply by the formation of (partially incomplete) TiO_2 layers through a growth process where the Ti atoms come from the reduced bulk and the ^{18}O from the gas phase. The kinetics of the growth determines the relative concentration of the incomplete structures (the rosettes and strands) and the (1×1) islands on the surface. The surface is flat and (1×1) -terminated when the growth is slow in comparison with surface diffusion processes. This can be achieved in various ways, either during annealing at high temperatures, Fig. 19f, or when the flux of one of the constituents is small (in very light samples with a small concentration of interstitials [156]) or at lower O_2 background pressures. Conversely, on very dark crystals, or at intermediate temperatures, a substantial part of the surface can be covered with rosette networks. Note that 60% of the Ti atoms in the rosettes are fourfold coordinated, whereas the Ti atoms exposed on the (1×1) surface are fivefold coordinated. Clearly the possibility that such structures can form needs to be taken into account when preparing rutile $(1\ 1\ 0)$ surfaces for surface chemistry experiments (see Section 5).

The surface structure in Fig. 19e, obtained after annealing in 1×10^{-6} mbar $^{18}\text{O}_2$ at 710 K, shows the presence of (1×2) strands on otherwise flat, (1×1) -terminated surfaces. This is in agreement with Onishi and Iwasawa's [169] results described above. From atomically resolved images of strands connected to rosettes as well as UHV annealing experiments of restructured surfaces it was concluded [144] that these strands also have the Ti_2O_3 structure depicted in Fig. 18b.

The dependence of the restructuring (as well as the type of (1×2) reconstruction) on the reduction state of the bulk was resolved by Bennett et al. [76]. High-temperature STM studies were performed on two different TiO_2 samples. On a dark blue/black crystal (that showed already evidence for CSP formation, i.e., darker than cube 3 in Fig. 5) two different structures were observed (see Fig. 22). The dark and bright strings in Fig. 22 were attributed to added Ti_2O_3 rows (Fig. 18b) and added rows of a bulk-terminated TiO_2 layer (Fig. 18c, but with bridging oxygens at the center of the strands), respectively. The latter structure also appears cross-linked with partial 'rosettes' (Fig. 21). Both the added-row structure and the rosettes are just incomplete TiO_2 structures that form during the growth of additional $\text{TiO}_2(1\ 1\ 0)$ - (1×1) layers. The authors have published impressive web-based STM 'movies' [173] (which can be viewed at <http://www.njp.org/>) of the growth process that show the cyclic completion of terraces and new formation of the cross-linked added-row structures. In contrast, the dark rows (the Ti_2O_3 added rows) appeared relatively unreactive for additional growth.

2.2.3. Recommendations for surface preparation

Although the $\text{TiO}_2(1\ 1\ 0)$ - (1×1) surface is considered the 'best-characterized', prototypical metal oxide surface, the above summary clearly shows that its atomic-level structure is quite complex. The recent STM results summarized above clearly indicate that both the oxidation conditions and the history of the $\text{TiO}_2(1\ 1\ 0)$ sample have significant bearing on the morphology of the surface, the presence of strands, rosettes, or CSPs. The variations in the surface structure with O_2 pressure, crystal temperature and bulk defect density are so vast that one could suspect chemistry of the $\text{TiO}_2(1\ 1\ 0)$ surface to be significantly variant for samples oxidized under different conditions. For example, the issue of whether water is molecularly or dissociatively adsorbed on $\text{TiO}_2(1\ 1\ 0)$ [127,128,138,174,175] (see Section 5.1.2) may be significantly clouded in the literature because of studies in which the morphology of the surface was unknowingly disordered by the presence of the rosettes and/or strands observed recently by STM. This level of ambiguity may also permeate many other adsorption studies on $\text{TiO}_2(1\ 1\ 0)$.

Guidelines of surface preparation of $\text{TiO}_2(1\ 1\ 0)$ can be extracted from recent work [75,76,150,156,172]. If solely (1×1) -terminated surfaces are desired, light blue crystals (as depicted in Fig. 5) should be used.

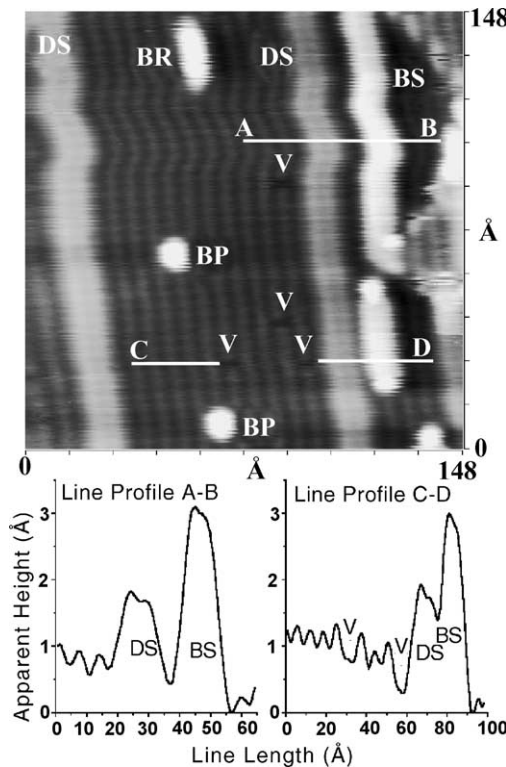


Fig. 22. High-temperature STM image of oxygen-induced features on a rather dark, non-stoichiometric $\text{TiO}_2(1\ 1\ 0)$ crystal. The crystal was exposed to oxygen (5.5×10^{-7} mbar, 833 K), stopped mid-reaction by removal of the oxygen overpressure, and imaged at the same temperature. The two types of strands with different apparent height (dark strands (DS) and bright strands (BS)) are attributed to the presence of different (1×2) structures. The added Ti_2O_3 rows account for the dark strings. The bright strands are interpreted as a slightly modified (addition of bridging oxygens at the strands) added-row structure (Fig. 18c). Additionally, bright rows and vacancies are visible on the (1×1) surface (marked BR and V, respectively). Line profiles are taken in the fast scan direction to minimize thermal drift and tip change problems. From Bennett et al. [76]. © 1999 The American Physical Society.

Annealing in oxygen will then result in stoichiometric (1×1)-terminated surfaces. On the other hand, more complex morphologies with a range of different coordination sites can be formed if dark crystals are annealed in oxygen. Oxygen vacancies, achieved after UHV annealing, can possibly be quenched by exposing to O_2 gas. However, one has to be careful that the O_2 gas is free of water which adsorbs quite readily (see Section 5.1.2) and that O_2 dissociated at vacancies can result in O radicals (see Section 5.1.3). The rich array of surface structures achievable on $\text{TiO}_2(1\ 1\ 0)$ may provide a playground for surface science experiments where the influence of different adsorption sites can be tested.

2.3. The structure of the rutile ($1\ 0\ 0$) surface

2.3.1. The $\text{TiO}_2(1\ 0\ 0)$ - (1×1) surface

The rutile ($1\ 0\ 0$) surface has received considerably less attention than the ($1\ 1\ 0$) crystal face. The rules of autocompensation and creation of non-polar surfaces discussed above (Section 2.2.1.1) allows a

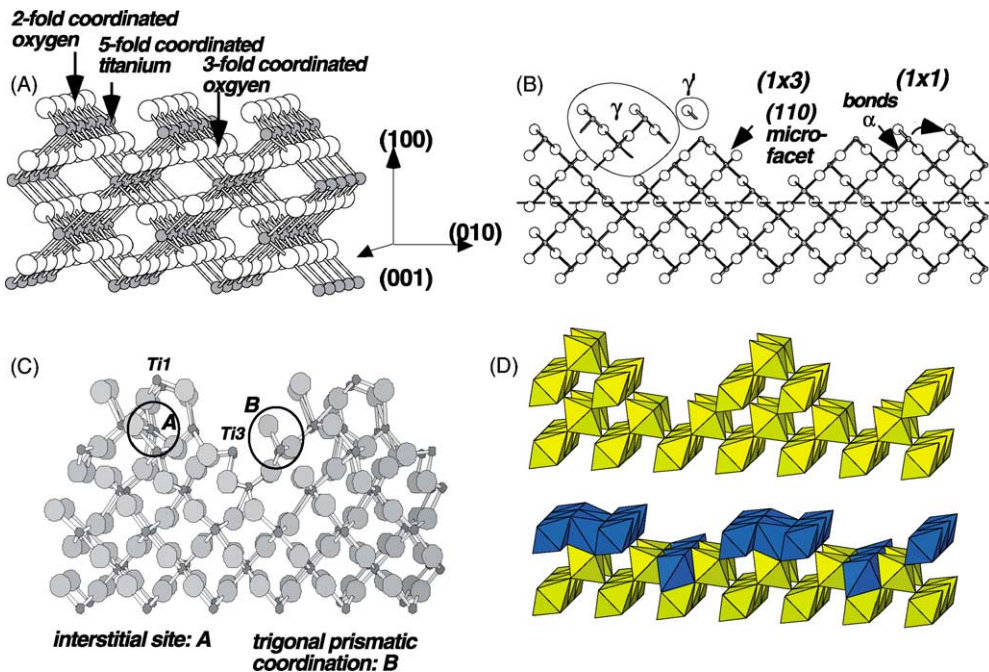


Fig. 23. (A) Geometry of the unreconstructed $\text{TiO}_2(100)$ -(1×1) surface. This surface results when the same number of $\text{Ti} \rightarrow \text{O}$ as $\text{O} \rightarrow \text{Ti}$ bonds are broken in a bulk crystal, see dashed line in (B). The formation of the (1×3) microfaceted surface, originally proposed by Zschak et al. [186] is displayed in (B). Removal of the volume labeled γ produces a stoichiometric surface with $\{110\}$ facets. In order to reconcile the reduced character of the (1×3) surface (observed in photoemission), the outermost bridging oxygen atoms (γ') are thought to be missing as well [187]. The transition from the (1×1) surface to the (1×3) microfaceted surface was proposed to occur via breaking the bonds α which leads to the indicated relaxation and creation of an intermediate (1×3) phase [176]. (C) A surface X-ray structure analysis by Zajonc et al. [192] implied a modified, heavily relaxed model. (D) The glancing angle X-ray diffraction data that had lead to the original microfacet model was re-evaluated by Landree et al. [193] and a new structure has been proposed. The octahedra model schematic representations in (D) show the microfacet model (top) and the new model (bottom) (from Landree et al. [193]).

straightforward prediction of the stable surface termination (Fig. 23A). Again, the same number of $\text{Ti} \rightarrow \text{O}$ as $\text{O} \rightarrow \text{Ti}$ need to be broken, as indicated by the line in Fig. 23B. This results in a strongly corrugated surface, with rows of bridging oxygen atoms at the outermost, (100) -oriented ridges (Fig. 23A). Indeed a (1×1) -terminated LEED pattern is observed on this surface after sputtering and annealing, and STM and non-contact AFM images are consistent with this model [176,177].

Several theoretical calculations have determined likely relaxations of the (1×1) surface [68,101,178,179]. In [178] different theoretical approaches and basis sets were tested. All these calculations agree in the general motions of the atoms, although the amount of relaxations differ somewhat. As expected from symmetry, no relaxations occur along $[001]$. In the $[100]$ direction only the fivefold coordinated Ti atoms show appreciable (downwards) relaxations [68]. Substantial relaxations occur along the $[010]$ direction with the twofold coordinated and the threefold coordinated oxygen atoms moving in opposite direction of the fivefold and sixfold coordinated Ti atoms. In Fig. 23A, O atoms would move to the right and Ti atoms to the left. The net effect of these displacements is to increase the effective coordination of the fivefold coordinated Ti atoms [178].

No experimental data on relaxations of the $\text{TiO}_2(1\ 0\ 0)$ - (1×1) surface exist. X-ray photoelectron and Auger electron diffraction were performed but are insensitive to the details of the surface structure [180].

2.3.2. Reconstructions

2.3.2.1. The microfacet model of the rutile $\text{TiO}_2(1\ 0\ 0)$ - (1×3) surface. In addition to the (1×1) -terminated surface, a (1×3) -reconstructed surface forms relatively easily upon annealing to high temperatures in UHV. It is clearly evident from photoemission experiments that this surface is partially reduced [27,181–183]. Initially, the observed reconstruction was interpreted as removal of every third row of the outermost, ‘bridging’ oxygen atoms [183]. Such a proposal was very much in line with the initially proposed [184] (and now largely abandoned) ‘missing row’ model for the (1×2) structure of the $\text{TiO}_2(1\ 1\ 0)$ surface (see Fig. 18a). The step structure on this surface may lead to a misinterpretation as additional (1×5) and (1×7) reconstructions as pointed out by Muryn [183]. The first STM work on a reconstructed $\text{TiO}_2(1\ 0\ 0)$ surface was reported by Clark and Kesmodel [185]. A glancing angle X-ray diffraction and low energy electron diffraction study [186] suggested a ‘microfaceted’ model, as shown in Fig. 23B. Removal of the volume assigned with γ in Fig. 23B creates facets of the lowest energy $(1\ 1\ 0)$ planes. Note that, again, the same number of $\text{O} \rightarrow \text{Ti}$ as $\text{Ti} \rightarrow \text{O}$ bonds are broken. This results in a stoichiometric surface, with twofold coordinated bridging oxygen atoms at the outermost ridges, as is the case for the $\text{TiO}_2(1\ 1\ 0)$ surface. The unit cell in $[0\ 1\ 0]$ direction is three times wider.

Atomically resolved STM images showed bright ridges with a geometry consistent with the microfaceted model [187,188]. The apparent height between top and bottom of the reconstruction was measured as 3 Å with STM, instead of the expected 5 Å. This has been associated with tip effects [187,188]. Scanning tunneling spectroscopy (STS) measurements showed considerable difference between dI/dV spectra taken on and in between the bright ridges, respectively [187,189]. This was interpreted as a consequence of missing oxygen atoms on the outermost ridges (i.e., removal of the oxygen atoms labeled γ' in Fig. 23C). This results in a surface termination with threefold coordinated Ti atoms in the outermost plane, consistent with the observation of a reduced surface in photoemission [183]. A photoelectron diffraction study of the $\text{Ti}3\text{p}$ level was performed by Hardman et al. [182]. The PED curves of the (curve fitted) Ti^{3+} feature were evaluated. These Ti^{3+} features are supposed to come from Ti atoms located next to oxygen vacancies, and diffraction effects should give information about their surface geometry. Three different positions for vacancies on the microfaceted (1×3) surface were tested. The most likely configuration has the missing oxygen atoms at the outermost ridge of the $(1\ 1\ 0)$ facets [182], consistent with the STS measurements. In this context, it is also interesting to note that the reduction state of the substrate plays a role in the formation of the (1×3) reconstruction. Almost stoichiometric, Nb-doped $\text{TiO}_2(1\ 0\ 0)$ films are thermally much more stable than reduced TiO_2 substrates and do not reconstruct at temperatures where reduced TiO_2 substrates already show a clear (1×3) structure [190].

A model involving ‘discrete bond breaking’ was proposed for the formation of the (1×3) surface [176,177]. Surfaces were prepared that exhibited both, the (1×1) termination and the ridges typical for the (1×3) surface. STM and non-contact AFM images showed an intermediate phase, which had (1×3) symmetry, but did not possess the characteristics of the microfaceted structure. Raza et al. [176] suggested that the bonds labeled α in Fig. 23B are broken, which allows the Ti atoms to relax towards the other rows of bridging oxygen atoms.

2.3.2.2. Is the simple microfacet model valid?? Despite the experimental results discussed in the previous section, it is presently not clear if the microfacet model for the (1×3) surface (Fig. 23B) is valid. In fact, recent evidence indicates that it may represent an oversimplification.

Theoretical calculations are not in agreement with the microfacet model. A tight-binding calculation derives a higher surface energy for the relaxed, microfaceted surface as compared to the (1×1) -terminated one [191]. DFT ab initio calculation [179] also showed a considerably higher surface free energy. This implies that there would be no driving force for the reconstruction, at least not at 0 K and under UHV conditions. These surprising results were attributed to the fact that stoichiometric surfaces were considered in the calculations (i.e., the oxygen atoms γ' , Fig. 23C, were not removed) while experimental spectroscopic data show that the (1×3) surface is partially reduced. As was pointed out by Lindan et al. [179], the Ti^{3+} state associated with the reduction should correctly be treated with spin-polarized DFT calculations.

A recent grazing incidence X-ray diffraction (GIXD) analysis shows strong lateral and vertical relaxations (1 Å and more) of the titanium and oxygen atoms in the top layer [192]. The coordination of the surface Ti atoms differ considerably from the simple microfacet model, see Fig. 23C. Threefold coordinated Ti atoms were found at the facet ridges ($Ti1$ in Fig. 23C), in agreement with previous work. In addition, various Ti atoms were found in different configurations, e.g. $Ti3$ in an oxygen bridge site, titanium B in a trigonal prismatic coordination, as well as an interstitial Ti site A. Obviously, this model deviates strongly from the simple microfaceted structure.

The original GIXD data, which were the basis for the microfaceted model, were re-evaluated recently by Landree et al. [193]. In [186] the data were interpreted using Patterson functions which show only interatomic vectors, not the ‘true’ atomic positions. The re-evaluation was based on a technique known as ‘direct method’, in essence a Fourier transform of the measured data in connection with a search for possible (unknown) phases [194]. It was found that the microfacet model gave very poor agreement with the data as compared to a model that contained four Ti and six to eight O atoms in the surface unit cell. In this model, the Ti atoms reside in edge- and corner-sharing octahedral units, as opposed to the normal rutile structure which is composed of corner-sharing octahedra only (see Fig. 23D). The reconstructed structure is rationalized as a standard configuration for non-stoichiometric defects such as CSPs, see Fig. 17. The reduced states observed with spectroscopic measurements would then be accommodated similar as in the bulk.

The surface unit cell of the $TiO_2(1\ 0\ 0)-(1 \times 3)$ structure is quite large with many atoms, hence it is no surprise that it is difficult to determine conclusively the exact surface geometry. While the electron diffraction [182], STM and AFM results [176,177,187–189], together with ESDIAD measurements [195] are consistent with the microfacet model of the (1×3) surface, none of these techniques gives direct evidence of surface geometries. The (1×1) and (1×3) reconstructions provide a convenient system for site-sensitive surface chemistry experiments, because one can reversibly cycle a $TiO_2(1\ 0\ 0)$ crystal between the (1×1) surface and the reconstructed one [196,197]. Hence, it would be quite important to have additional experimental as well as theoretical support for one of the models currently suggested and depicted in Fig. 23.

2.4. Rutile $(0\ 0\ 1)$

There is only one way to cut a rutile crystal in $(0\ 0\ 1)$ direction (Fig. 24). Although this creates a non-polar, autocompensated surface, it does not represent a low-energy configuration. It becomes clear

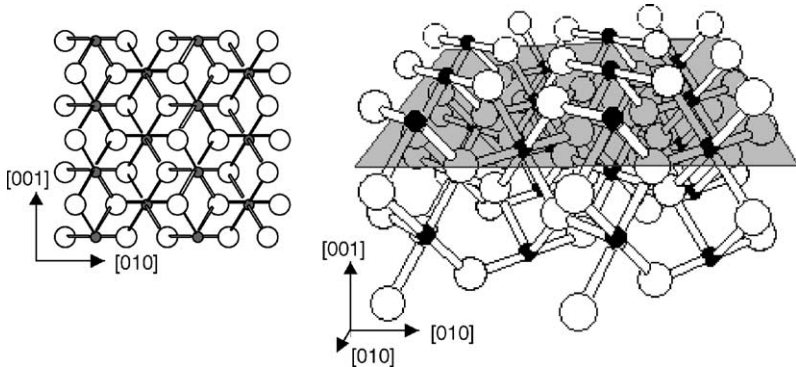


Fig. 24. Surface termination of the rutile $\text{TiO}_2(0\ 0\ 1)$ surface. Only one possibility exists to cut a TiO_2 crystal in this direction, see the side view at the left side. Surface Ti atoms are fourfold coordinated and surface O atoms twofold coordinated.

immediately when reviewing the coordination of the surface atoms. All the Ti atoms are fourfold coordinated, and all the O atoms twofold coordinated. Hence the number of broken bonds on this surface is higher than on the other low-index rutile surfaces discussed so far. Consequently, the $(0\ 0\ 1)$ surface has a high surface energy and tends to facet or reconstruct. Based on LEED studies, $\{0\ 1\ 1\}$ and $\{1\ 1\ 4\}$ facets have been identified by Tait and Kasowski [198] and Firment [199]. Poirier et al. [200] annealed a crystal at $400\ ^\circ\text{C}$ and performed STM and LEED studies. No atomic resolution was achieved, but several other crystal planes were additionally identified. AFM images showed relatively flat surfaces [201], but the resolution in the images was not high enough to identify the atomic structure of the facets.

A recent STM study with near-atomic resolution by Fukui et al. [202] showed the different structures that evolve when a sputtered surface is heated to increasingly higher temperatures, see Fig. 25. Similar preparation conditions are usually used to prepare surfaces with different ‘faceted’ terminations. The preparation conditions for Fig. 25b, which should give a (1×1) surface, showed hills instead. Some parts of these had an average $\{0\ 1\ 1\}$ orientation, but no ordered LEED was observed [202]. (In this context it might be worth mentioning that a rutile crystal, cut to expose a $(1\ 0\ 1)$ surface, showed faceting upon heating [152].) Thus the formation of facets which actually expose an unreconstructed $(1\ 0\ 1)$ surface is not likely.) Heating to a temperature of $1050\ \text{K}$ (Fig. 25c) showed well-resolved rows, running along the $[\bar{1}\ 1\ 0]$ and $[1\ \bar{1}\ 0]$ directions. High-resolution STM showed that these rows consist of a staircase of narrow terrace (a ‘bleacher-like structure’). The (unreconstructed) $\{1\ 1\ 4\}$ -faceted model of the $\text{TiO}_2(1\ 0\ 0)$ surface consists of a narrow terrace of the bulk-terminated $(0\ 0\ 1)$ surface with steps of $(1\ 1\ 1)$ orientation [202]. STM images of the rows are not consistent with this structure, although the average slope was $\{1\ 1\ 4\}$.

The image in Fig. 26 shows the drastic changes that can occur upon very high-temperature annealing of $\text{TiO}_2(0\ 0\ 1)$. The micrograph has been taken with an optical microscope after heating a $\text{TiO}_2(0\ 0\ 1)$ crystal for 1 h at $1300\ ^\circ\text{C}$ in UHV [203]. The lines are caused by slip. A non-equilibrium structure was observed after rapidly quenching a $\text{TiO}_2(0\ 0\ 1)$ crystal from a similar high temperature [204]. The most detailed structural results on $\text{TiO}_2(0\ 0\ 1)$ have been described below.

The rutile $(0\ 0\ 1)$ surface is the one where the least detailed structural information is available. This is particularly unfortunate, as the ‘faceted’ surface has been used extensively for the study of reactions of

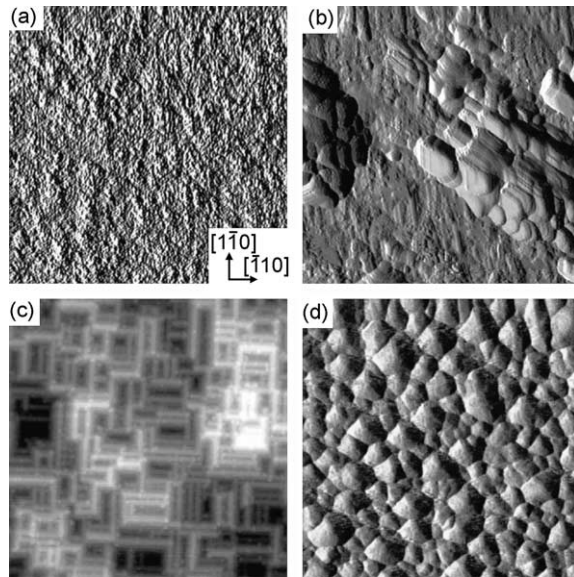


Fig. 25. STM images ($100\text{ nm} \times 100\text{ nm}$) of $\text{TiO}_2(1\ 0\ 0)$ surfaces depending on annealing temperature after Ar^+ -ion sputtering. (a) Before annealing. Variable current image ($V_s = +2.0\text{ V}$, $I_t = \sim 0.2\text{ nA}$). (b) After annealing at 970 K for 5 min . Some parts of the hill-like structures have an average plane of $\{0\ 1\ 1\}$, but most of the surface is disordered and no well-ordered pattern was observed by LEED. (c) After annealing to 1050 K for 5 min . A well-contrasted LEED pattern was observed that was previously assigned to a $\{1\ 1\ 4\}$ structure [199]. The surface is not microfaceted but instead consists of rows which show a ‘bleacher-like’ structure in high-resolution images. The average slope is identical to a $\{1\ 1\ 4\}$ face. (d) After annealing at 1160 K for 5 min the surface is covered with $\sim 5\text{ nm}$ high particles. The STM images in (a, b, d) are variable current images, the one shown in (c) a topographic image. From Fukui et al. [202]. © 2001 Japanese Society of Applied Physics.

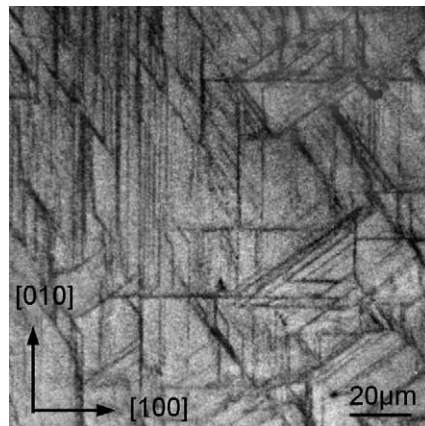


Fig. 26. A $\text{TiO}_2(0\ 0\ 1)$ surface after annealing at $(1300\text{ }^\circ\text{C}, 1\text{ h in UHV})$. The image was taken with an optical microscope. It shows lines due to slip along certain crystallographic directions. From Nörenberg et al. [203]. © 2000 Elsevier.

organic molecules, see [Section 5.2](#). The (0 0 1) surface is also the crystal orientation of choice for electrochemical studies, as the electrical conductivity is highest along the [0 0 1] direction. The recent work discussed here clearly shows that there are inconsistencies with the established interpretation of reconstructed $\text{TiO}_2(0\ 0\ 1)$. Additional theoretical and experimental work that could help to resolve the geometry of this surface would be quite valuable.

2.5. Vicinal and other rutile surfaces

Vicinal surfaces of TiO_2 have not been studied extensively. A study of Na adsorption on a stepped (4 4 1) surface was reported by Onishi et al. [\[205\]](#). Unpublished experiments from this author's laboratory with a similarly cut crystal showed macroscopic faceting upon annealing.

The most detailed investigation was performed recently on a $\text{TiO}_2(2\ 1\ 0)$ surface [\[206\]](#). In a formal sense, $\text{TiO}_2(2\ 1\ 0)$ lies midways between (1 1 0) and (1 0 0), and is the most simple vicinal surface. Atomistic simulations, based on Coulombic interaction between ions and a short-range repulsive interaction, predicted an asymmetric sawtooth-like structure of the surface, consisting of {1 1 0} nanofacets. The width of each nanofacet is 1.5 times the width of the surface unit cell of the (1 1 0)-(1 × 1) structure (i.e. $3a/\sqrt{2}$). The nanofacets terminate with a row of Ti atoms carrying bridging oxygen atoms. The surface energy of this structure is predicted to be 2.07 J/m^2 . (This is to be compared to a surface energy of 1.78 J/m^2 derived using a similar calculation for $\text{TiO}_2(1\ 1\ 0)$ [\[206\]](#).) STM images showed a (1 × 1)-terminated surface that could be consistent with this structure, although the interpretation was again made difficult by balancing electronic effects with the very strong corrugations of this surface.

The structure of the $\text{TiO}_2(1\ 1\ 1)$ surface was investigated by Onishi and co-workers [\[207\]](#) with LEED and STM. Depending on the annealing temperature, the surface shows a variety of reconstructions.

2.6. Anatase surfaces

Most commercial titania powder catalysts are a mixture of rutile and anatase (e.g. the most often used Degussa P25 contains approx. 80–90% anatase and the rest rutile [\[11\]](#)). For certain photocatalytic reactions and non-photoinduced catalysis such mixtures work best [\[208\]](#). There is growing evidence that anatase is more active than rutile for O_2 photo-oxidation, but not necessarily for all photocatalytic processes. Anatase behaves differently than rutile in gas-sensing devices, and most photovoltaic cells are based on granular thin films with an anatase structure [\[29\]](#). Anatase and rutile show inherent particle size differences and this might cause some of the observed differences in chemical properties. However, in order to gain a better understanding of TiO_2 -based devices, it is clearly important to obtain atomic-scale information on well-characterized anatase surfaces.

High-purity titania powder catalysts are typically made in a flame process from titanium tetrachloride [\[11\]](#). Many additional synthetic techniques processes have been applied [\[209–213\]](#). The shapes of the crystallites vary with preparation techniques and procedures. Typically, (1 0 1) and (1 0 0)/(0 1 0) surface planes are found, together with some (0 0 1) [\[70\]](#). Several theoretical studies have predicted the stability of the different low-index anatase surfaces [\[70,214,215\]](#). The (1 0 1) face is the thermodynamically most stable surface, see the calculated surface energies in [Table 4](#), [\[216,217\]](#). While it is difficult to obtain accuracy for surface energies numbers with DFT calculations, the relative surface energies in [Table 4](#) should still be meaningful. The calculated Wulff shape of an anatase crystal, based on these values, compares well with the shape of naturally grown mineral samples, see [Fig. 27](#).

Table 4

Comparison of calculated surface formation energies (J/m^2) for relaxed, unreconstructed TiO_2 surfaces^a

Rutile (1 1 0)	Anatase	(1 0 1)	(1 0 0)	(0 0 1)	(1 0 3)f	(1 0 3)s	(1 1 0)
0.31		0.44	0.53	0.90	0.84	0.93	1.09

^a Two different structures for the (1 0 3) surfaces (a ‘faceted’ and a ‘smooth’ one) have been considered. From [216,217].

Interestingly, the average surface energy of an equilibrium-shape anatase crystal is smaller than the one of rutile [216,217], which might explain the fact that nanoscopic TiO_2 particles are less stable in the rutile phase.

Experimental investigations on single-crystalline anatase are just starting. Meaningful surface science investigations necessitate single-crystalline samples. While rutile crystals are readily available, sufficiently large and pure anatase crystals are more difficult to obtain. Because anatase is a metastable phase, it transforms into rutile at relatively low temperatures [210], with the transition temperature dependent on impurities, crystal size, sample history, etc. From the recent progress in synthesizing single-crystalline anatase samples with high purity [209] as well as the successful growth of epitaxial thin-films on appropriate substrates [218–221] one can expect a rapid increase in the interest in anatase TiO_2 in the near future.

2.6.1. Anatase (1 0 1)

Two reports on the structure of anatase (1 0 1) surfaces have appeared very recently [220,222]. The (1 0 1) surface on an anatase sample grown by chemical transport [209] showed a (1 × 1) surface after mild sputtering and annealing [222]. A mineral sample similar to the one displayed in Fig. 27 was used in an STM study by Hebenstreit et al. [220]. In order to avoid the contaminations in this natural single crystal, a 700 Å thick, epitaxial film was grown on the surface, as described in [221]. Sputtering and

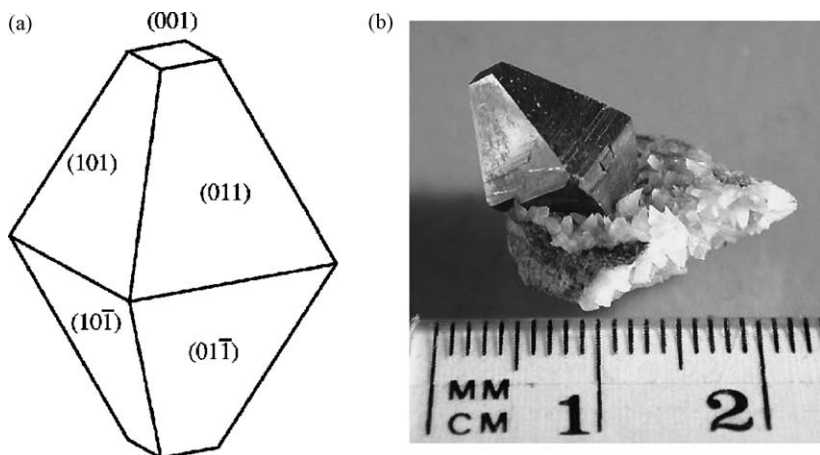


Fig. 27. (a) The equilibrium shape of a TiO_2 crystal in the anatase phase, according to the Wulff construction and surface energies calculated in [216] (from Lazzeri et al. [216], © 2001 The American Physical Society). (b) Picture of an anatase mineral crystal.

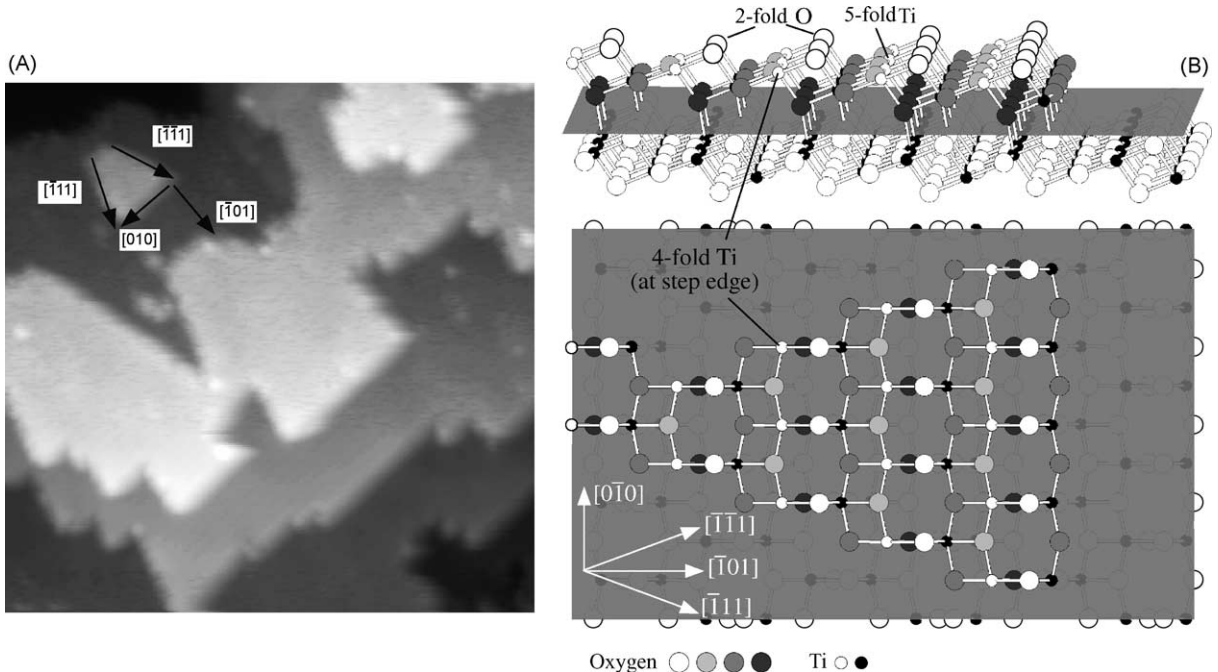


Fig. 28. (A) STM results of an anatase (1 0 1) single crystal. The monoatomic terraces terminate with step edges that run predominantly in certain preferred orientations. (B) Atomic models (side and top view) of the anatase (1 0 1) surface. From Hebenstreit et al. [220]. © 2000 The American Physical Society.

annealing again produced a (1×1) termination in LEED. The surface has only a pm symmetry, giving rise to a preferential orientation of step edges (Fig. 28A). Based on the rules of autocompensation for step edges (see Section 2.2.1.1) a reasonable model for steps is given in Fig. 28 [220]. Titanium atoms at the terraces have fivefold and sixfold coordination, and titanium atoms at the step edges are fourfold coordinated. These have a higher reactivity against gas adsorption [220]. Twofold coordinated oxygen atoms are located at the ridges of the saw tooth-like structure. According to [70], they relax inwards by ~ 0.21 Å. The threefold coordinated O atoms relax outwards by 0.06 Å and the fivefold coordinated Ti atoms inwards by ~ 0.17 Å, so that the surface exhibits a slightly buckled geometry. The tunneling site in the atomic-resolution image in Fig. 29 probably extends across both, the twofold coordinated oxygen atoms and the fivefold coordinated Ti atoms. In an image taken with a higher tunneling current (12 nA), where the tip was probably closer to the surface, the twofold coordinated oxygen atoms are distinguished as independent features [220].

In correspondence to the rutile (1 1 0) surface, one might expect that the twofold coordinated oxygen atoms are removed easily upon annealing in UHV, and thus give rise to point defects. Several imperfections with atomic dimensions are identified in the atomic-resolution image in Fig. 29. At this point it is not clear which one of these features, if any, are indicative of oxygen vacancies. Their number density is very small, certainly smaller than the usually quoted 5–10% [116,128] on rutile (1 1 0). This would be in agreement with the (calculated) low surface energy of the (1 0 1) surface [70]. Calculations of the electrostatic potential by Woning and van Santen [223] also predict that the rutile (1 1 0) surface can be reduced easier than the anatase (1 0 1) surface.

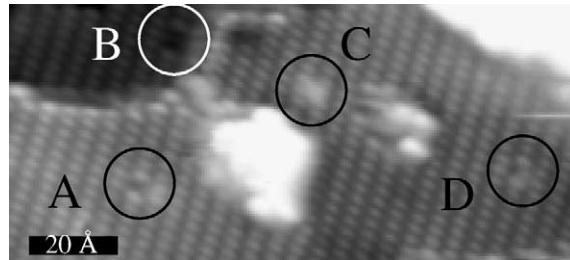


Fig. 29. STM image ($V_s = +1.22$ V, $I_t = 1.23$ nA, $130 \text{ \AA} \times 60 \text{ \AA}$) of an anatase (1 0 1) surface. Four features could possibly be representative of oxygen vacancies; single black spots (A), double black spots (B), bright spots (C), and half black spots (D). The density of these atomic defects is rather small, confirming the theoretically predicted high stability of anatase (1 0 1). From Hebenstreit et al. [220]. © 2000 The American Physical Society.

2.6.2. Anatase (0 0 1)

The stable, autocompensated anatase (0 0 1) surface exhibits exclusively fivefold coordinated Ti atoms, as well as twofold and threefold coordinated oxygen atoms, see Fig. 30a. Calculations show that the corrugation increases somewhat upon relaxation, from 0.82 to 0.92 Å [70].

The most detailed structural investigations on this surface so far have been performed on thin films, grown epitaxially on the $\text{SrTiO}_3(0\ 0\ 1)$ substrate [218,219,221]. The $\text{SrTiO}_3(0\ 0\ 1)$ surface shows a very good lattice match with the anatase (0 0 1) surface (~3%), but a poor one with the rutile phase. Their anionic sublattices bear substantial resemblance despite their overall crystallographic dissimilarities [224]. Heteroepitaxial growth of TiO_2 can be regarded as a continuous formation and extension of the oxygen atom network from the SrTiO_3 substrate into the film. Within this oxygen sublattice the (relatively small) Ti cations arrange in their appropriate sites. Formation of interfaces where the oxygen sublattice continues and the metal cation sublattice changes abruptly is often exploited for thin film heteroepitaxy of metal oxides [225]. On $\text{SrTiO}_3(0\ 0\ 1)$ epitaxial, stoichiometric anatase thin films of high crystalline quality have been grown by several techniques [224,226] and are stable up to 1000 °C [221].

The (0 0 1)-(1 × 1) surface is not very stable, however, and reconstructs when heated to elevated temperatures [219,227–229]. Only on as-grown samples that were slightly contaminated with carbon a (1 × 1)-terminated surface was observed [218]. Herman et al. [219] were the first to point out that a two-domain (1 × 4) reconstruction formed on an anatase film on SrTiO_3 after sputtering and annealing the (1 × 1) surface in UHV. Based on angle-resolved mass-spectroscopy of recoiled ions (AR-MRSI) a ‘microfaceted’ model was proposed. In this model (1 0 3) facets are exposed which contain twofold oxygen and both fourfold and fivefold coordinated Ti atoms. Such a model resembles in many ways the microfacet model for the rutile (1 0 0)-(1 × 3) surface discussed in Section 2.3.2. The appearance of the (1 × 4) reconstruction in STM [228] is not consistent with the (1 0 3) microfaceted model. Based on the STM images an ‘added and missing row model’ was proposed [228].

Based on first-principles calculations, Lazzeri and Selloni suggested the so-called ‘added molecule (ADM)’ structure, see Fig. 30b and c [230]. The high-resolution STM and NC-AFM images in Fig. 31 are consistent with the ADM model [229]. Kinks and defects in the bright rows of the (1 × 4) structure as well as the faint lines between the bright lines (which would be at the location of the Ti(5) atoms) fit very well to the proposed model. The NC-AFM images show elevated features which are also consistent with these added features.

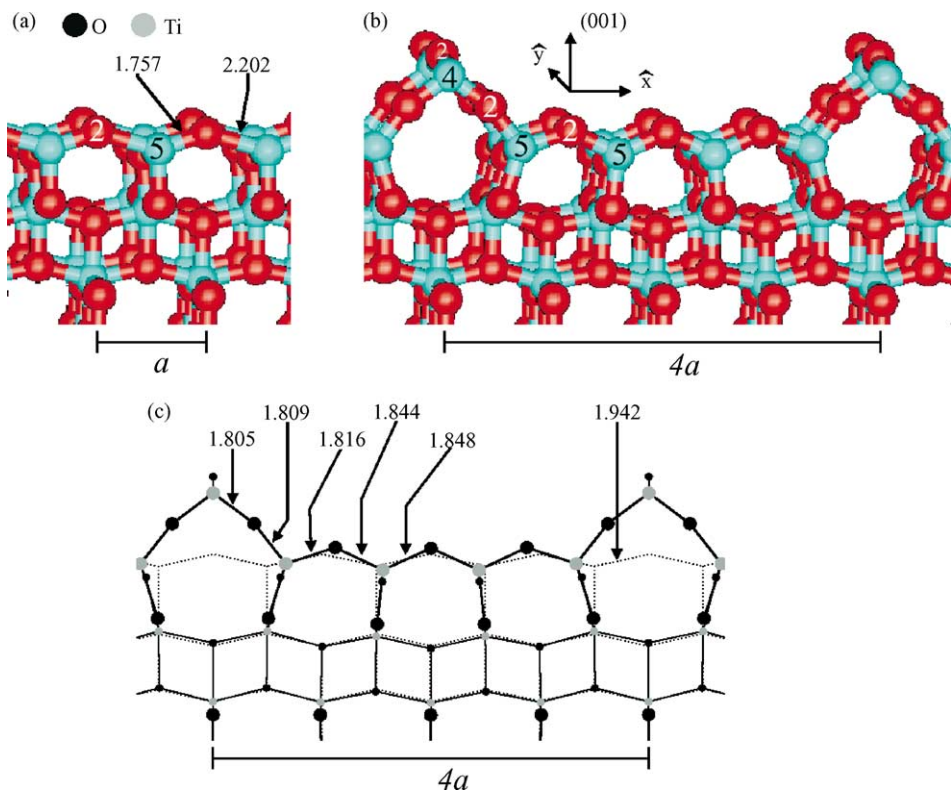


Fig. 30. (a) Relaxed (0 0 1)-(1 × 1) surface of anatase TiO₂. (b) Relaxed structure of the ‘ad-molecule’ (ADM) model for the (1 × 4) reconstruction. (c) Projection of the atomic positions of the ADM model on the plane perpendicular to the y direction. Dots with different sizes represent atoms belonging to different planes parallel to the figure. Dotted lines represent bonds in the ideally bulk-truncated surface. The length in Ångstrom of some surface bonds is indicated. a is the theoretical in-plane bulk lattice spacing ($a = 3.786 \text{ \AA}$). x and y correspond to the [0 0 1] and [0 1 0] directions. From Lazzeri and Selloni [230]. © 2001 The American Physical Society.

2.6.3. Other anatase surfaces

As seen from Table 4, the anatase (1 0 0) surface should be quite stable. While this plane is not a terminating face at an equilibrium-shape crystal (Fig. 27), such planes are observed in powder materials. Unpublished STM results from this author’s group [231] show that the (1 0 0) surface forms a (1 × n) reconstruction, which can be explained by a (1 0 1)-microfaceted model. The (1 0 3) surface also reconstructs to a (1 × n) termination, but a persistent Ca contamination on this crystal was always present and excludes a definitive statement about the structure of this surface.

2.7. Conclusion

Much has been learned about the surface structure of the titanium dioxide system in recent years. Two somewhat contradictory lessons can be drawn from all this work: (1) simple approaches work well for obtaining a first guess of surface structures and (2) oxide surfaces are even more complicated than anticipated.

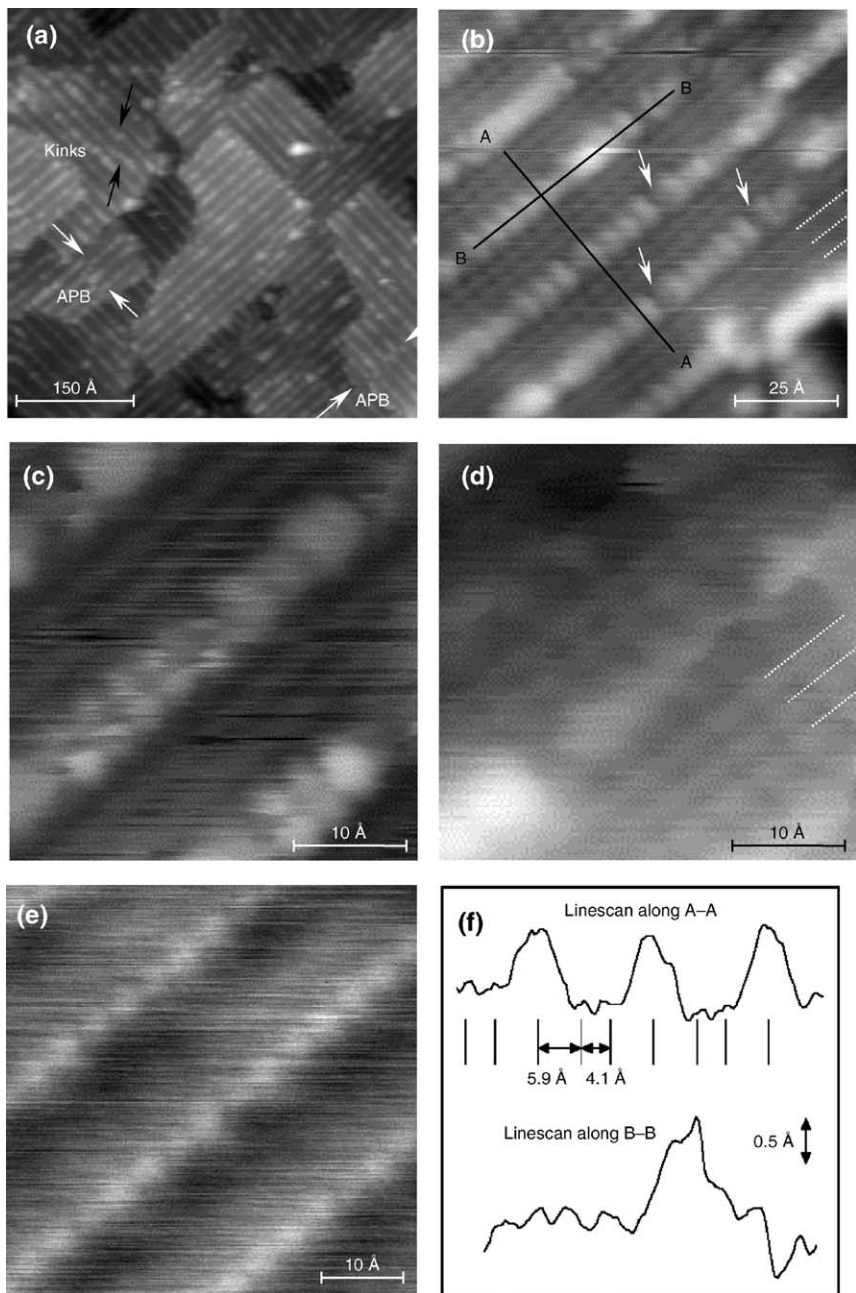


Fig. 31. SPM images of the anatase (0 0 1)-(1 × 4) surface. (a) Wide range STM image following annealing in oxygen and in UHV. Reconstructed step edges run along $\langle 0\ 0\ 1 \rangle$ directions, black arrows mark rows that contain a kink, and white arrows mark positions of anti-phase boundaries (APB). (b), (c) High-resolution STM shows that the bright rows are composed of two parallel rows of bright spots and defects. Between the rows are two fainter rows. (d) Between the bright rows are three fainter rows where a local (1×5) periodicity exists. (e) High-resolution NC-AFM image. (f) Line scans from the image in (b) taken along a line perpendicular to the bright rows (A–A) and parallel to the bright rows (B–B). A tunneling current set point of 1.0 nA was used in (a)–(d). (a) $V_s = 1.0$ V. From Tanner et al. [229]. © 2002 The American Chemical Society.

It is comforting that the elemental rules for predicting surface terminations outlined in [Section 2.2.1.1](#) work so well for predicting the structure of (1×1) terraces and step edges of all the orientations of both rutile and anatase surfaces. The extensive theoretical work has helped to refine the understanding of surface relaxations, and the level of detail on the atomic geometry of the $\text{TiO}_2(1\ 1\ 0)$ surface is certainly comparable to that of certain elemental semiconductors or metals.

On the other hand, scanning probe techniques have unraveled a very rich picture of surface structures. One interesting theme is the interplay between surface structure and bulk defects in rutile; the reduction state of the crystal is quite important for the presence of different structural features under exactly the same preparation conditions. It remains to be seen if such a behavior is also present for other metal oxides, or even in TiO_2 anatase. Total-energy calculations have helped enormously to confirm models for surface reconstructions, and have acted as a warning sign when models derived from experimental results were too naïve. The most credible models often are not simple variations of the TiO_2 bulk structure, see for example, the added ‘ Ti_2O_3 ’-row reconstruction of rutile $(1\ 1\ 0)$ - (1×2) and the ADM model of the anatase $(0\ 0\ 1)$ - (1×4) surfaces.

The expanding data base has made rutile TiO_2 a very popular model system for metal oxides. Nevertheless, there are still many open questions concerning the crystal structure of rutile surfaces as pointed out throughout this section. One interesting aspect is the advent of surface studies on anatase. From the recent progress in synthesizing single-crystalline anatase samples with high purity as well as the successful growth of epitaxial thin-films on appropriate substrates, one should expect an increase in the interest in anatase in the near future.

3. Electronic and vibrational structure of TiO_2 surfaces

An excellent introduction to the (bulk) electronic structure of transition metal oxides was given by Cox [\[232\]](#). This was followed up with a detailed discussion of the surface electronic structure in the book on oxide surfaces by Henrich and Cox [\[1\]](#). Since publication of this book in 1994, much progress has been made in the theoretical understanding of TiO_2 surfaces. Increasingly powerful computational approaches have been used as is described in a large number of recent publications [\[68,75,100,101,191,233–249\]](#). DFT calculations have helped in understanding the structure of TiO_2 surfaces, and have been a first warning sign when structural models based on experimental observations were too simplistic (e.g. the missing-row reconstruction for the $(1\ 1\ 0)$ surface [\[233,248\]](#) and the microfacet model for the $(1\ 0\ 0)$ surface [\[179,250\]](#), see [Section 2](#)). The current trend is to calculate and understand adsorption of molecules and metals, and the pertaining literature is reviewed in [Sections 4 and 5](#). The basic understanding of the electronic and vibrational structure of *clean* TiO_2 surfaces as given in [\[1\]](#) is still valid; consequently, this part of this review is held brief. In the following a distinction is made between stoichiometric surfaces, and oxygen-deficient, ‘reduced’ ones. This distinction is made somewhat arbitrarily as defects are introduced rather easily in rutile, and almost every work that discusses clean TiO_2 surfaces is also concerned with reduced, defective surfaces.

3.1. Stoichiometric TiO_2 surfaces

The electronic structure of TiO_2 has been calculated using a wide variety of theoretical approaches with varying degree of sophistication [\[68,100,101,191,233–248,251–258\]](#). There is wide agreement

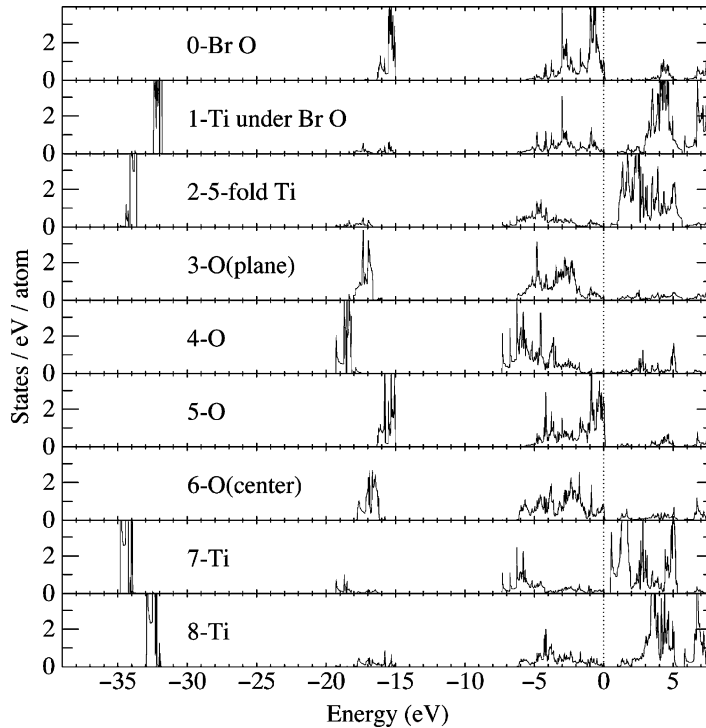


Fig. 32. Mulliken projected densities of states of a three-layer slab of a stoichiometric $\text{TiO}_2(1\ 1\ 0)$ surface. From Paxton and Thi n-Nga [245]. © 1998 The American Physical Society.

that the surface electronic structure is not too different from that of the bulk. No surface states are observed or predicted, except for non-stoichiometric surfaces (see [Section 4](#)).

The occupied states are mostly O2p derived, but exhibit a significant degree of covalency, see [Fig. 32](#). The use of LDA vs. GGA in DFT, and the inclusion of spin-polarization, has been shown to cause little change in the overall features of the LDOS of stoichiometric surfaces [245]. The hybridization of the Ti levels with oxygen are experimentally determined with resonant photoemission [259–262]. When the photon energy is swept across the Ti3p absorption edge, the photoemission cross-section for Ti3d-derived states increases [137]. These resonances can be used for a qualitative estimate of Ti–O hybridization. Projected partial density of states have also been extracted from photoelectron diffraction measurements [263]. The iono-covalent character of the $\text{TiO}_2(1\ 1\ 0)$ surface and of Ti_nO_m clusters with different sizes and charges has been studied by Albaret et al. [247]. On average, the Ti charge is close to +1.7 (as compared to the formal oxidation state of +4), and the oxygen charge is close to −0.85 (formal oxidation state of −2), with only small variations depending on the system. On the $\text{TiO}_2(1\ 1\ 0)$ surface, the covalency of bonds between the bridging oxygen atom and the underlying sixfold coordinated Ti atoms is enhanced compared to other surface bonds. This is similar to a Mullikan charge analysis of the calculations by Paxton and Thi n-Nga [245].

The conduction band is mostly Ti3d-derived. The octahedral coordination causes a crystal-field splitting of the d orbitals into two sub-bands, see [Fig. 33](#). The e_g orbitals (d_{z^2} and $d_{x^2-y^2}$) point

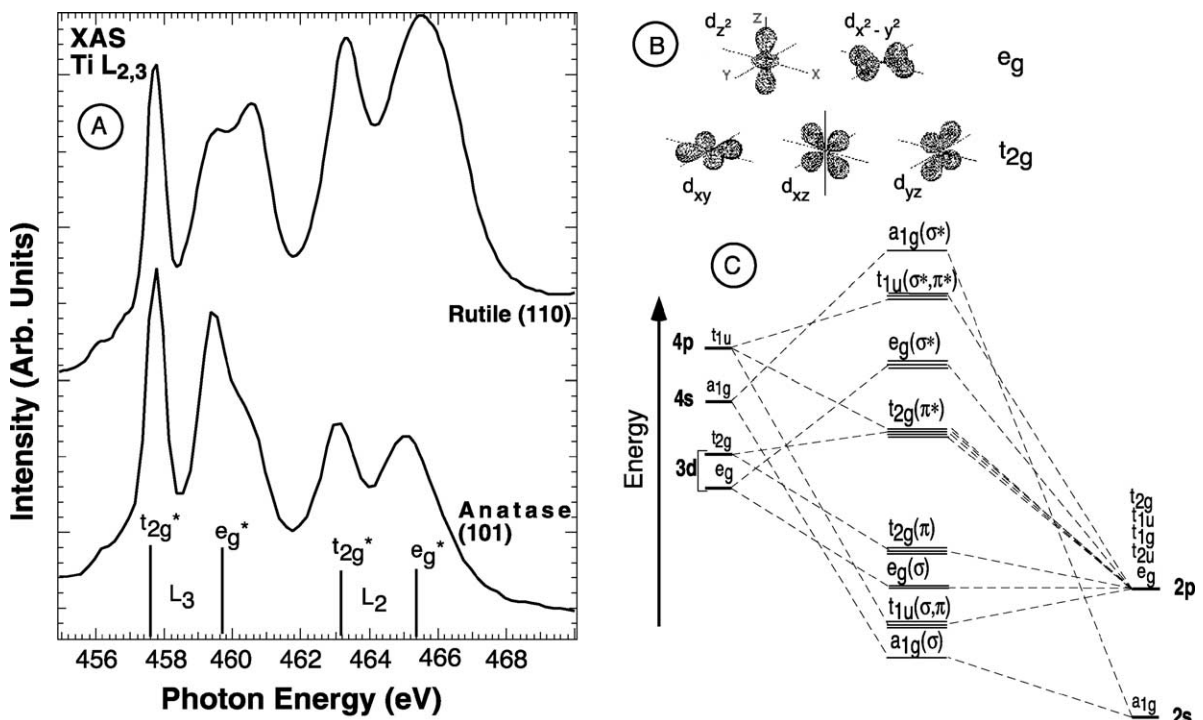


Fig. 33. X-ray absorption spectra of the Ti2p edge of a stoichiometric, well-ordered $\text{TiO}_2(1\ 1\ 0)$ surface. The effect of the crystal field of the oxygen ligands on the 3d electrons is sketched.

directly toward the oxygen ligands forming s-type orbitals. The t_{2g} orbitals (d_{xy} , d_{xz} and d_{yz}) point in-between the oxygen neighbors and form π -type bonds. The peaks in inverse photoemission spectra [264–266] have been interpreted along these lines. The crystal-field splitting is clearly seen in X-ray absorption, see Fig. 33. Naturally, these states are extremely sensitive to the presence of point defects and other imperfections [265]. Because the crystal field splitting changes when the configuration of the oxygen ligands is slightly altered in different structures (note the differences in bond angles and bond lengths in rutile vs. anatase, Fig. 2), X-ray absorption spectra are quite sensitive to the crystal structure and to local imperfections [267–269]. Their shape can successfully be calculated with short-range models [269,270]. XAS is also quite useful to investigate the oxidation/reduction reactions that occur when reactive metals are deposited on TiO_2 [271,272], see Section 4.

While calculations of the electronic structure of TiO_2 abound, this author is aware of only one photoemission experiment where measured dispersions were related to the calculated band structure [273], see Fig. 34. Normal-emission spectra were taken on a $\text{TiO}_2(1\ 1\ 0)$ and a $\text{TiO}_2(1\ 0\ 0)$ samples. Two angles of incidence for the photon beam were used. Because synchrotron radiation is polarized, this allowed the identification of the symmetry of the valence band states based on selection rules. Such an assignment is critical, because the valence band in photoemission is broad and complex (Fig. 35). Photon energies below the $\text{Ti}3\text{p}$ to 3d resonance have been used in the analysis. Very flat bands have been found in reasonable agreement with theory.

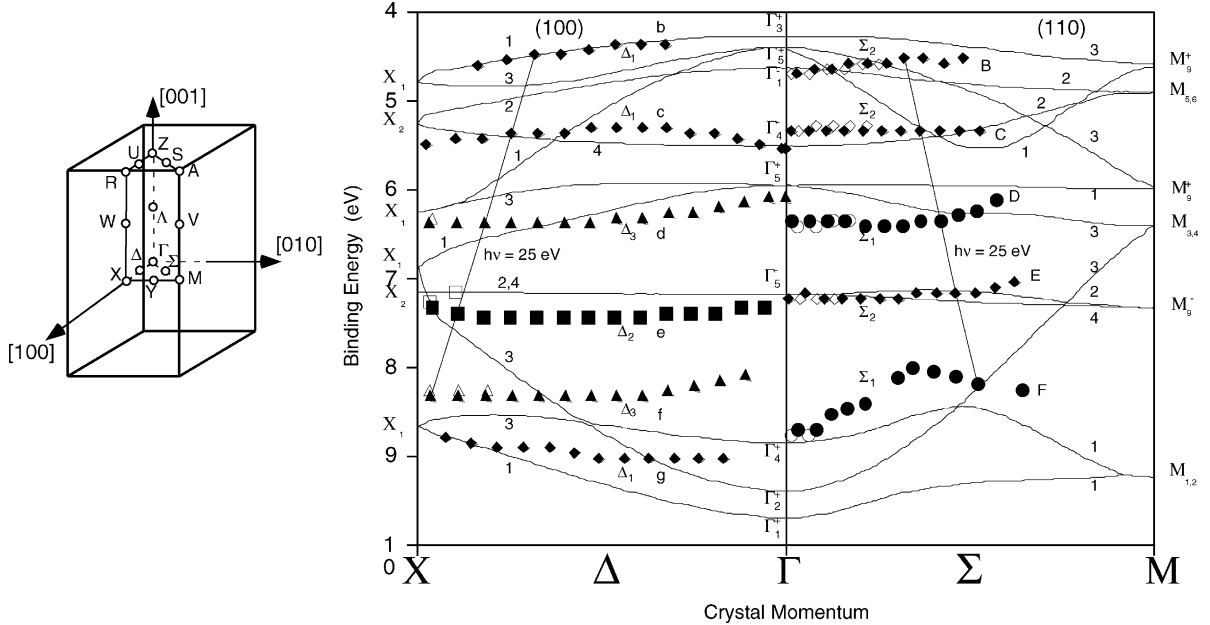


Fig. 34. Calculated and experimental dispersions for rutile TiO_2 along the $X-\Gamma-M$ directions of the reduced zone. The data were obtained from normal-emission spectroscopy from $\text{TiO}_2(1\bar{1}0)$ and $\text{TiO}_2(\bar{1}00)$ surfaces. The final states bands for $h\nu = 25 \text{ eV}$ are also shown. Closed and open symbols represent emission from different Brillouin zones in the extended zone scheme. Experimental bands are labeled by the symmetry derived from dipole selection rules. From Hardman et al. [273]. © 1994 The American Physical Society.

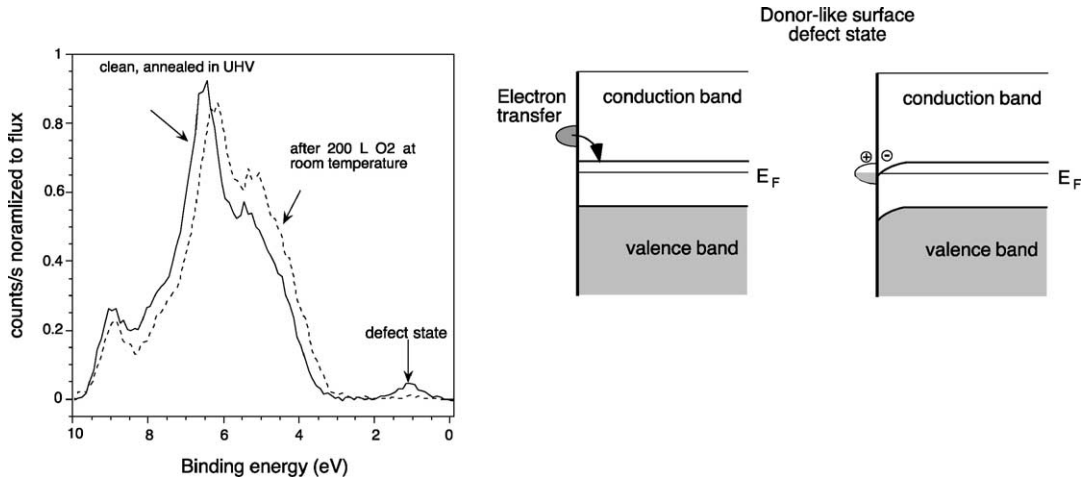


Fig. 35. (a) Photoemission spectra ($h\nu = 35 \text{ eV}$, normal emission) from the valence band region of a sputtered and UHV-annealed, clean $\text{TiO}_2(1\bar{1}0)$ surface. After adsorption of molecular oxygen at room temperature, the defect state in the band gap region disappears and the spectrum shifts by 0.2–0.3 eV to higher binding energy due to band bending. A Shirley background was subtracted from both spectra. (b) Schematic diagram of the band-bending effect due to donor-like surface defect states. Surface oxygen vacancies create a defect state and electrons are donated to the system. A charge accumulation layer is created in the near-surface region and the bands in the n-type semiconducting TiO_2 sample bend downwards.

3.2. Reduced TiO_2 surfaces

3.2.1. Defect states

As discussed in [Section 2.2.1.4](#), annealing at high temperatures (or bombarding with electrons) reduces the $\text{TiO}_2(1\ 1\ 0)$ surface and creates point defects in the rows of bridging oxygen atoms (see [Fig. 14](#)). [Fig. 35](#) shows two typical photoemission spectra from the valence band region which exemplify the presence of oxygen vacancies. The solid line is from a (blue) $\text{TiO}_2(1\ 1\ 0)$ crystal after sputtering and annealing in UHV. The defect state in the band gap is clearly visible. It shows almost no dispersion when the emission angle is changed [274]. Upon exposure to molecular oxygen gas at room temperature, the defect state disappears. As was shown with isotopically labeled $^{18}\text{O}_2$ experiments [127,275], the gaseous oxygen dissociates and fills the vacancies, which quenches the defect state. (See [Section 5.1.3](#) for more detail on oxygen adsorption on defective $\text{TiO}_2(1\ 1\ 0)$ surfaces.) In resonant photoemission the defect state shows a behavior clearly indicative of a Ti3d-derived nature [259,261,262].

The presence of point defects is also visible in other spectroscopies, e.g. a peak at 0.75 eV in electron energy loss spectra [276,277], and a shoulder in XPS which is formally assigned to a Ti^{3+} oxidation state ([Fig. 36](#)). The defect state in the band gap is usually not reproduced in theoretical calculations, however. One possible reason was pointed out by Lindan et al. [233]. Spin-polarized DFT calculations of ‘reduced’ models system (where all the bridging oxygen atoms were removed, and the coordinates were relaxed) show localized band gap states formed by Ti3d orbitals, see [Fig. 37](#) [233,245]. In spin-paired calculations, this feature is generally not present in the band gap [248]. The nature of the defect state is easily explained [1,233]. Removal of a neutral oxygen atom leaves behind two electrons which previously occupied O2p levels in the valence band. These states are no longer available, and the electrons must go into the conduction band, the bottom of which is formed by Ti3d states. Both, the neighboring fivefold and the sixfold Ti atoms receive an electron, and these electrons are unpaired [233,245].

Although the defect state is 100% spin-polarized, the interaction between spins is too weak for magnetic ordering to occur. In the HF approximation, the energy difference between ferromagnetic and

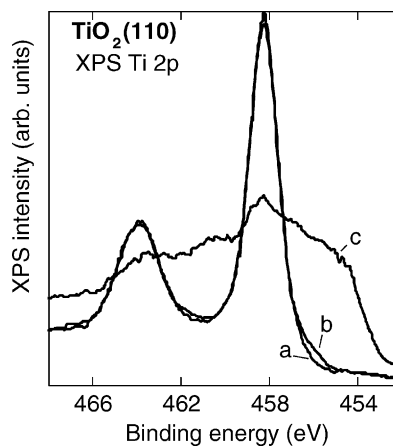


[Fig. 36.](#) XPS from a $\text{TiO}_2(1\ 1\ 0)$ (a) stoichiometric surface (b) after annealing in UHV, with point defects and (c) after sputtering.

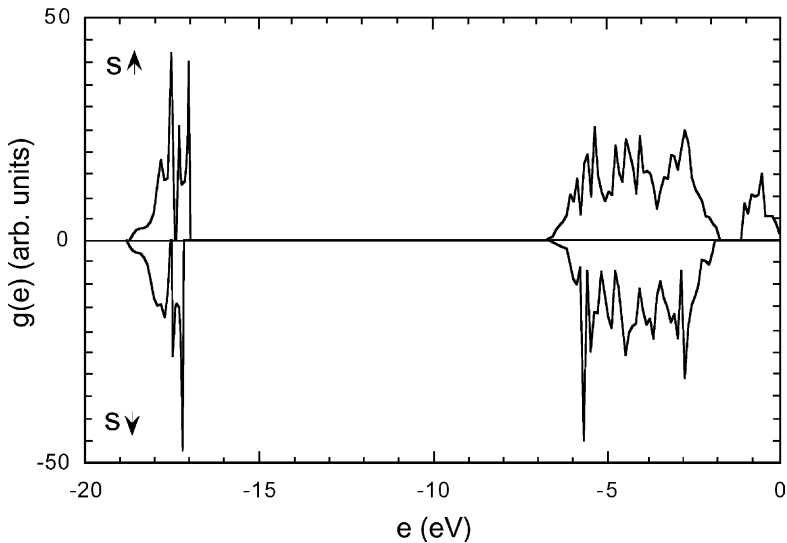


Fig. 37. Densities of states $g(e)$ for spin-up and spin-down electrons calculated for a stoichiometric $\text{TiO}_2(1\ 1\ 0)$ surface after structural relaxations. From Lindan et al. [233]. © 1997 The American Physical Society.

antiferromagnetic alignment is calculated to be 0.1 meV only [278]. To this author's knowledge, the spin-polarized nature of the 3d state on defective $\text{TiO}_2(1\ 1\ 0)$ surface has not been verified experimentally.

3.2.2. Band bending

Reduced titanium dioxide is an n-type semiconductor, and band-bending effects accompany the adsorption of gases or metals. An example for such a band-bending effect is clearly visible in Fig. 35. When oxygen vacancies are present, the extra electrons in the vacancies act as donor-like states that create an accumulation layer in the near-surface region. This causes a downward band bending. After adsorption of oxygen, only minimal changes occur in shape of the valence band in Fig. 35, but there is a rigid shift of all peaks in the photoemission spectrum upwards by 0.2–0.3 eV. This is caused by a downwards shift of the Fermi level and an ‘unbending’ of the bands.

3.2.3. Identification of the reduction state with spectroscopic techniques

The reduction state of the surface, i.e., the presence of lower oxidation states, can easily be identified with XPS and a variety of other spectroscopic techniques [276]. Fig. 36a shows the $\text{Ti}2\text{p}$ region of a clean, stoichiometric TiO_2 surface. In spectra with a carefully calibrated energy scale, the $\text{Ti}2\text{p}_{3/2}$ peak, attributed to (formally) Ti^{4+} ions, is located at 459.3 eV, and the $\text{O}1\text{s}$ peak at 530.4 eV [279]. Note, however, that surface defects can cause band bending and a rigid shift of the whole spectrum, as discussed above. This probably accounts for the scatter in experimental peak positions. A mean of 458.7 eV of 16 literature data is given in [280], and a similar value (458.5 eV) is sometimes used as an ‘internal standard’ [281] in XPS experiments. The $\text{Ti}2\text{p}$ spectra of TiO_2 and a variety of other Ti compounds have been calculated with a single impurity cluster model, and the experimental spectra (including the satellite features at higher binding energy, not shown in Fig. 36) were reproduced quite well [282].

After annealing a stoichiometric TiO_2 surface in UHV (and creating point defects), a shoulder in the $\text{Ti}2\text{p}$ spectrum appears, Fig. 36. This shoulder is attributed to a formal Ti oxidation state of +3.

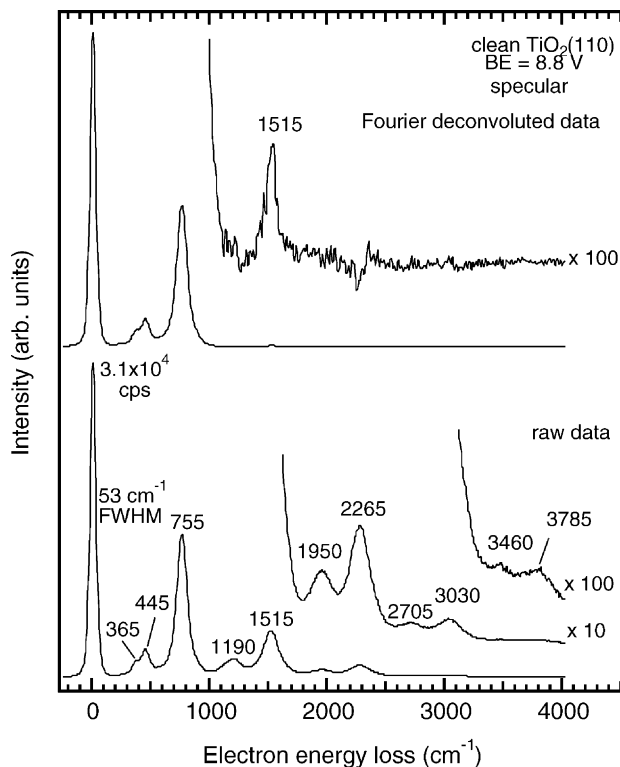


Fig. 38. Raw HREELS data (bottom) of a clean $\text{TiO}_2(1\bar{1}0)$ surface show losses caused by multiple excitations of Fuchs–Kliewer phonons. These can largely be removed from the spectrum by a Fourier deconvolution procedure. From Henderson [128]. © 1996 Elsevier.

Sputtering preferentially removes oxygen from the surface and creates lower oxidation states which broadens the spectrum further (Fig. 36). The peak shifts associated with these lower oxidation state have been obtained by peak fitting by several authors, and a review of different values is given in [280].

3.3. Vibrational structure

The study of the lattice dynamics of TiO_2 with charged particles is complicated by the high cross-section for excitation of optical phonons. HREELS measurements are dominated by the losses from these Fuchs–Kliewer phonons [128,283–286], see Fig. 38. The raw spectrum in the lower panel in Fig. 38 shows the primary phonon losses (at $365, 445$ and 755 cm^{-1}) and up to four multiple scattering events which give rise to the higher lying peaks. Because the electric field extends deep into the bulk, these phonons carry little information about the state of the surface, although they do change position and intensity upon sputtering [283–286] or metal deposition [280]. Unfortunately, these high-intensity peaks often overshadow small features which would be indicative of adsorbates on the sample. This is a general characteristic of all ionic oxides, and two techniques have been employed in order to circumvent this problem and make HREELS accessible to adsorption studies. Wu et al. [287] used a high energy of the primary electron beam and took HREELS spectra in an off-specular direction on a

$\text{MgO}(0\ 0\ 1)$ crystal. A more elegant way is to Fourier deconvolute the spectrum as suggested by Cox and Williams [288]. While this does not affect the primary losses, it clears the spectrum of most of the intensity at higher energies, as shown in the upper panel of Fig. 38. (The origin of the remaining peak at $1515\ \text{cm}^{-1}$ is discussed in [128].)

4. Growth of metal and metal oxide overlayers on TiO_2

Several excellent reviews on the growth of metals on oxide substrates are given in [4,8,10,63]. A comprehensive discussion of the structural, electronic, and chemisorption properties of metals on several metal oxides, including TiO_2 , was given by Campbell [4]. Metal overlayer growth specifically on $\text{TiO}_2(1\ 1\ 0)$ has been discussed by this author in [63], and more recently by Persaud and Madey [10]. The heteroepitaxy of metal oxides on metal oxide substrates was reviewed by Chambers [289] in a recent paper.

This field of the surface science of TiO_2 is very active, with a recent emergence of theoretical calculations of adsorbate studies on metals (and metal oxides) on TiO_2 . Fig. 39 shows the elements that have been studied on single-crystalline TiO_2 surfaces, and Table 6 gives a short summary of the main results. The growth mode, interfacial reaction, structure, and thermal stability of metal overlayers on TiO_2 follow clear trends across the periodic table, with the oxygen affinity of the metal overlayer being one of the most decisive factors for the properties of the metal/ TiO_2 systems. These trends are discussed in the first part of this section. Details about different systems, with an emphasis on the literature after 1997 are then discussed in the next part.

4.1. Overview and trends

4.1.1. Interfacial reactions

It has been pointed out in previous reviews of metal overlayer growth on single-crystalline TiO_2 surfaces [4,10,63] that the metal overlayers' reactivity towards oxygen is a very important parameter for

IA																VIII	
H	II A															He	
Li	Be															B	C
Na	Mg	III A	IV A	V A	VIA	VII A	VIII A		IB	IIB	Al	Si	P	S	Cl	Ar	
K	Ca	Sc	Ti	V	Cr	Mn	Fe	Co	Ni	Cu	Zn	Ga	Ge	As	Se	Br	Kr
Rb	Sr	Y	Zr	Nb	Mo	Tc	Ru	Rh	Pd	Ag	Cd	In	Sn	Sb	Te	I	Xe
Cs	Ba		Hf	Ta	W	Re	Os	Ir	Pt	Au	Hg	Tl	Pb	Bi	Po	At	Rn

Fig. 39. Adsorption and/or growth of the shaded elements on single-crystalline TiO_2 surfaces was studied and are described in the text and is summarized in Table 6.

predicting a variety of properties of the metal/TiO₂ interface. The more recent papers published since these reviews were written are consistent with this trend.

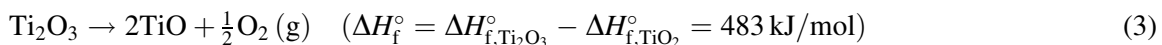
Thermodynamic considerations for metal films on oxides were given by Campbell [4] and, for the specific case of metals on TiO₂ by Persaud and Madey [10]. Generally, if a metal M is deposited onto TiO₂, then M should reduce the substrate and itself become oxidized if the reaction



is thermodynamically favorable, i.e., if the change in the standard free energy, ΔH_f° is negative. In the case of a TiO₂ substrate, formation of lower oxidation states such as Ti₂O₃ or TiO is possible (see Fig. 4). Thus, the ΔH_f° per mole of oxygen of oxide formation should be compared with



or



in order to judge whether or not such a reaction will take place. Thus, in thermodynamic equilibrium the reaction (Eq. (1)) can take place in principle if ΔH_f° is more negative in Eq. (1) than in Eq. (2) or Eq. (3). The heats of oxide formation were compiled by Campbell [4] and are reproduced in Table 5. (Note that the numbers in Table 5 are per mole of oxygen, while others [10] have referenced formation enthalpies per mole of molecular O₂.)

The heats of oxide formation are high for transition metals on the left side of the periodic table, and when a reactive metal is vapor-deposited on TiO₂ at room temperature, the corresponding oxidation/reduction reaction results in a reacted interface. This is clearly seen in XPS measurements of very thin overlayers, see Fig. 40. (The film thicknesses in the figure refers to quartz-crystal microbalance readings; i.e., they represent the nominal thickness if the overlayer were spread out uniformly across the

Table 5
Heat of formations of the most stable oxide of the metal^a

Heats of formation of oxide (ΔH_f° in kJ/mol O) ^b	Metal
>0	Au
0 to -50	Ag, Pt
-50 to -100	Pd
-100 to -150	Rh
-150 to -200	Ru, Cu
-200 to -250	Re, Co, Ni, Pb
-250 to -300	Fe, Mo, Sn, Ge, W
-300 to -350	Rb, Cs, Zn
-350 to -400	K, Cr, Nb, Mn
-400 to -450	Na, V
-450 to -500	Si
-500 to -550	Ti, U, Ba, Zr
-550 to -600	Al, Sr, Hf, La, Ce
-600 to -650	Sm, Mg, Th, Ca, Sc, Y

^a After [4].

^b For the most stable oxide of the metal.

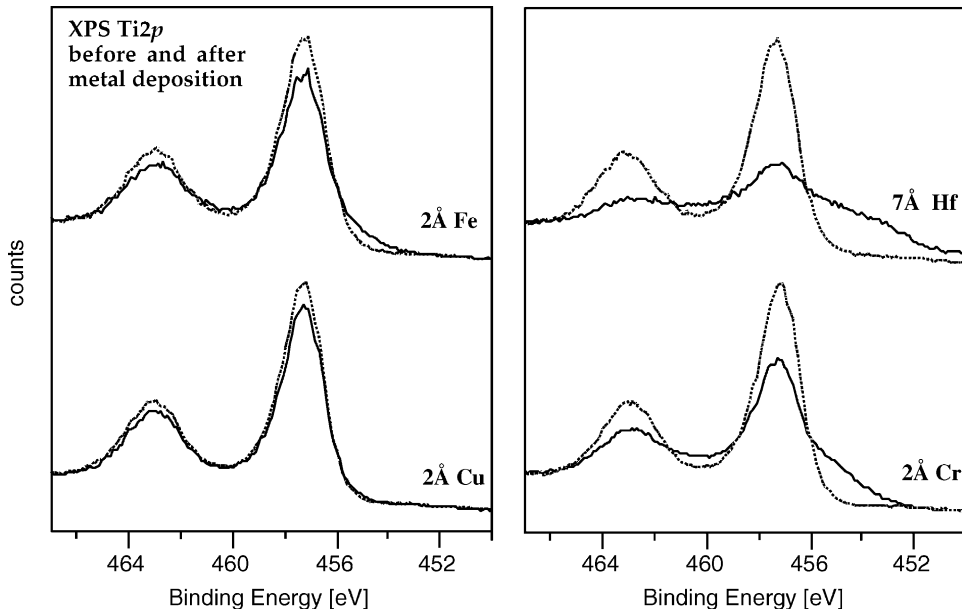


Fig. 40. The Ti2p region of several metal overlayers before (dotted lines) and after (full lines) overlayer deposition at room temperature. The sharp peaks of the clean surfaces are indicative of Ti atoms on a stoichiometric surface with a (formally) Ti^{4+} oxidation state. The more reactive the metal overlayer, the more the peaks smear out, indicating a reduction of the TiO_2 substrate (see also Fig. 36). From [63].

surface. However, this growth morphology rarely occurs, see below.) Fig. 40 shows the Ti2p XPS levels from the TiO_2 substrate before and after deposition of four different metals, representative for very different levels of reactivity. As discussed above (Section 3.2 and Fig. 36), the Ti2p core levels are a very good indicator for the stoichiometry of TiO_2 surfaces and the appearance of lower oxidation states (the shoulders at the lower binding energy side in Fig. 40) indicate a reduction of the substrate. The strength of this reduction reaction scales with the reactivity of the overlayer. It is virtually absent for Cu and strongest for Hf, which exhibits an oxide heat of formation of more than 550 kJ/mol, see Table 5. XPS core level measurements of the corresponding overlayer metals show that the substrate reduction is accompanied by oxidation of the overlayer, in agreement with Eq. (1). Such a solid-state oxidation/reduction reaction was observed for Co but not for Ni, which puts the limit around an oxide heat of formation of 250 kJ/mol, see Table 5. (Because the numbers in Eqs. (2) and (3) are referenced to bulk values, this smaller value derived from surface experiments is not too disturbing.) Hence the borderline between metals that induce an oxidation/reduction reaction, and the ones that do not, lies roughly along an axis connecting Co and Re in the periodic table (Fig. 39).

Do the observed changes in XPS line shape indicate a mere electron transfer from the reactive overlayer to the substrate Ti ions, or is oxygen physically extracted from TiO_2 and incorporated in the overlayer as suggested in Eq. (2)? At least for the more reactive metal overlayers, the latter is clearly the case. The impressive transmission electron microscopy image of a Nb/ $\text{TiO}_2(1\ 1\ 0)$ interface, discussed below (Section 4.2.11), clearly proves this point. A sharp, but reacted interface is seen. Complementary EELS measurements, taken across the interfacial region, support the presence of a reduced TiO_2 layer. Formation of a disturbed interface is consistent with surface studies of other reactive metals, e.g. for Hf

(see Section 4.2.8). The LEED pattern disappears rapidly with coverage, indicating interfacial disorder, and the oxidation/reduction reaction does not stop until at least 2 ML are deposited, see Fig. 40. This clearly means that oxygen is extracted from the substrate and incorporated into the film. Interestingly, in all the metal overlayers studied, reactive and non-reactive ones, a sharp interface is formed between the overlayer metal and the Ti when the film is grown at room temperature. No intermixing for Ti and the overlayer metal was observed, even in the cases where stable Ti alloys would exist, e.g. for Pd or Al overlayers.

The oxidation/reduction reactions at the interface lead to a substantial re-arrangement of atomic positions and/or charge that ultimately causes the effects observed in Fig. 40. Ionization of the overlayer metal introduces band gap states (see for example, the discussion on Fe adsorption below (Section 4.2.17)). A similar charge transfer and formation of gap states has been observed for all alkali metals. Donation of charge leads to changes in band bending and work function for all the metal overlayers. This is as discussed in great detail in [4].

Unfortunately, very few theoretical calculations of reactive metal adsorption on TiO_2 exist at this point. Thi  n-Nga and Paxton [290] have made a comparison across the 5d transition metals. These authors have found covalent bonding and very little charge transfer. However, this study took into account only one adsorption site (on top of fivefold coordinated Ti atoms) and no relaxations, in clear contradiction with the experimentally observed, reacted interface.

There is no spectroscopic evidence for an oxidation/reduction reaction for metals equally or less reactive towards oxygen than Ni. Core levels shift somewhat because of band bending or finite size effects in the small clusters formed by the metal overlayer. However, the substrate core levels show no sign for the formation of lower oxidation states, as seen in Fig. 40 for Cu. The fact that no interfacial oxidation/reaction occurs for unreactive metals does not preclude relaxations to happen at the interface. In contrary, the only system where interfacial coordinates were measured (an X-ray diffraction investigation of the Cu/ $\text{TiO}_2(1\ 1\ 0)$ system by Charlton et al. [107]) shows substantial relaxations of the substrate atoms.

4.1.2. Growth morphology (thermodynamic equilibrium)

It is useful (though a quite rough oversimplification, see below) to distinguish three film growth modes in thermodynamic equilibrium. When the difference between the surface free energy of the clean substrate, $\gamma_{\text{substrate}}$, and surface free energy of the overlayer metal, γ_{metal} , is greater than the interfacial energy, $\gamma_{\text{interface}}$, i.e.

$$\gamma_{\text{interface}} > \gamma_{\text{substrate}} - \gamma_{\text{metal}} \quad (4)$$

cluster growth (also called Volmer–Weber growth) should take place. When it is less, the film should wet. For thicker films, growth can proceed in a layer-by-layer fashion (Frank–van der Merwe growth mode). Often, epitaxial strain increases in thicker films and breaks up the overlayer (layer + clusters or Stranski–Krastanov growth mode). Because the surface energy of virtually all clean metals is higher than that of TiO_2 (where an experimental value of $\sim 0.35 \text{ J/m}^2$ was reported [291]) the term on the left side is negative. Hence, cluster growth should occur, unless $\gamma_{\text{interface}}$ itself has a *negative* value. It has been suggested [10,63,292] that this is the case for very reactive overlayers, where an interfacial reaction as in Eqs. (1)–(3) is thermodynamically favored.

Consequently, the tendency to wet the substrate should correlate with the numbers given in Table 5. Fig. 41 shows that this is indeed the case, at least to first approximation. The growth morphologies at the right side of the figure were extrapolated from combined XPS and LEIS measurements for four

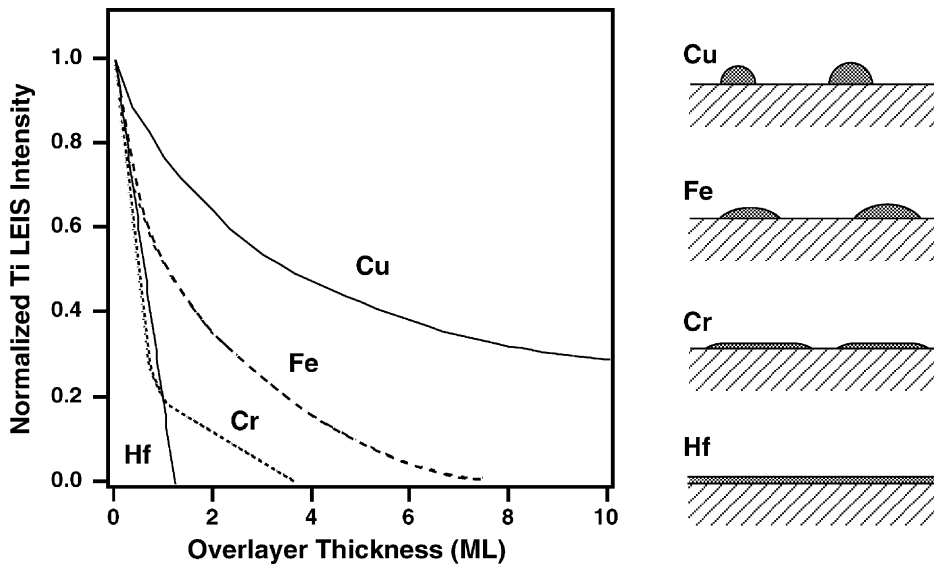


Fig. 41. Trends for the attenuation of the Ti LEIS signals for four selected overlayers on $\text{TiO}_2(1\ 1\ 0)$ and schematic drawing of the initial stages of film growth for Cu (3D clusters), Fe (flat islands), Cr (2D islands followed by 3D growth) and Hf (formation of a continuous overlayer). From [63].

selected metal overlayers (Cu, Fe, Cr and Hf; the same ones as in Fig. 40). Low-energy ion scattering is particularly useful for growth studies of ultrathin films. It is primarily sensitive to the top-most surface layer. If the film wets and grows in a 2D fashion, the LEIS signal from the substrate should linearly decrease with coverage and approach zero upon completion of the first monolayer. This is the case for Hf, a metal with a very high heat of oxide formation. In the case of 3D growth, the substrate signal should be visible up to fairly high coverages, as is the case for Cu. The strength of the oxidation/reaction, as evidenced in Fig. 40, is directly correlated with the growth mode extrapolated from the LEIS measurements. As XPS measurements have been performed for most of the metal overlayers considered to date (see second column in Table 6), a prediction of the growth morphology can be made for most overlayer metals.

For very unreactive overlayers, the work of adhesion, i.e., the work required to separate the overlayer from the substrate

$$W_{\text{adh}} = \gamma_{\text{substrate}} + \gamma_{\text{metal}} - \gamma_{\text{interface}} \quad (5)$$

can directly be extrapolated from contact angle measurements on a microscopic scale [293]. This was done in an impressive way by Cosandey and Madey [294] for Au clusters on a $\text{TiO}_2(1\ 1\ 0)$ surface, see below. According to Table 5, gold does not react with oxygen, which is consistent with the large contact angle observed. (Ironically, such supported small gold clusters do promote the catalytic oxidation of CO, see below!).

The correlation between heat of oxide formation, interfacial reaction and growth mode is intriguingly simple, but neglects several important issues. The growth modes discussed above are strictly only valid at thermodynamic equilibrium, whereas film growth is often performed at low temperatures, e.g. conveniently at or near room temperature. The substrate is considered rigid and its structure and

Table 6

Summary of growth results of metal and metal oxide overlayers on single-crystalline TiO₂ surfaces

Metal/substrate	Interfacial reaction	Techniques	Growth morphology/structure	Thermal stability	Reference
Li/rutile (1 1 0), anatase (1 0 1)	Formation of Ti ³⁺ states in the band gap	Semi-empirical Hartree–Fock calculations, ESD	Equilibrium position between two bridging oxygen on rutile (1 1 0), in structural void in anatase (1 0 1) Fig. 42	Intercalation in anatase much easier than rutile	[314–316,319]
Na/rutile (1 1 0)-(1 × 1), rutile (1 1 0)-(1 × 2), rutile (4 4 1), +CO ₂ , +NO	Reduced TiO _x , Ti3d gap states promotes adsorption of CO ₂	XPS, AES, NEXAFS, EELS, resoPE, LEED, D ⁺ scattering, STM, UPS, Hartree–Fock, molecular dynamics calculations			[160,205,304,305, 320–332]
K/rutile (1 1 0), rutile (1 0 0), +O ₂ , CO ₂	Reduced TiO _x , first ML oxidized	Ellipsometry, TPD, UPS, IPS, XPS, D ⁺ scattering, ARUPS, ARXPS, LEED, RHEED, SEXAFS, HREELS, MIES, UPS Hartree–Fock, LCAO	Metallic > 1 ML; multilayers at 140 K	Desorbs as KO _x , reduces the substrate	[278,319,322,333–342]
Cs/rutile (1 1 0), rutile (1 0 0)-(1 × 1), +CO ₂	Reduced Ti ⁺ , complete ionization for small coverages	D ⁺ scattering, MIES, XPS, TPD, UPS, work function	First layer bound strongly, multilayers at low temperatures	>0.5 ML desorbs at elevated temperatures	[321,342–344]
Ca/rutile (1 1 0)	Segregating impurities; deposition from solution	LEED, XPS, LEIS, STM, atomistic calculations	Ordered structures	Segregates towards the surface	[145–148,733]
Al/rutile (1 1 0), rutile (100), +K, +C	Reduced Ti at the interface, oxidized and metallic Al in the film	XPS, UPS, AES, LEED, STM	Fractional coverage disorders substrate; evenly distributed clusters, no preferred sites	Heating in UHV oxidizes Al and reduced TiO _x layer, no ordered structure	[281,345–349]
Ti and TiO _x /rutile (1 1 0)	4 Å Ti produces ~20 Å of reduced layer	EELS, LEIS, XPS, SSIMS, conductivity, LEED	Ti ⁰ clustering on top of reduced interface	Bulk diffusion >700 K, Ti main diffusing species	[74,280,350]
Hf/rutile (1 1 0)	Reduced Ti layer, oxidized Hf ⁴⁺ at the interface	LEIS, XPS, SXPS, LEED	Hf ⁰ clustering on top of oxidized Hf ⁴⁺ /Hf ^{x+} layer, see Fig. 43	Oxidation of Hf overlayer	[63,351]

Table 6 (Continued)

Metal/substrate	Interfacial reaction	Techniques	Growth morphology/structure	Thermal stability	Reference
V/rutile (1 1 0), rutile (1 1 0)- (1 × 2), rutile (1 0 0)	Ti ³⁺ , oxidized V, metallic for higher coverages	STM, AFM, UPS, XPS, LEED, work function, ARXPS, HREELS, AES, TPD	At low coverages: binds on top of (1 × 2) rows, see Fig. 44, no LEED, ARXPS: adsorption site underneath bridging oxygens (after anneal at 473 K), 5 ML: epitaxial bcc(1 0 0)[0 0 1] (1 1 0)[0 0 1]TiO ₂	Diffuses into substrate >600 K	[12,14,15,352–354,356,357,734,735]
VO _x /rutile (1 1 0), rutile (1 1 0)- (1 × 2), +methanol	Ti remains oxidized	SEXAFS, XPS, PES, work function, ARXPS, STM	Different vanadium oxides dependent on preparation conditions: V ₂ O ₃ : 10 ⁻⁶ Torr O ₂ at room temperature, VO ₂ : fractional ML + anneal 473 K, VO _x ($x \approx 1$) annealing of V film in UHV, 1 ML V ₂ O ₃ : methanol → formaldehyde	>1100 K agglomeration of V ₂ O ₃ particles + VTiO ₃ at interface	[13,15,272,358–362]
Nb/rutile (1 1 0), rutile (1 0 0), Nb _x Ti _{1-x} O ₂ mixed films	Intermediate reaction layer, see Fig. 45	RHEED, AES, HRTEM, EELS, STM, photoemission, MBE of mixed films, HF and density functional calculations of doping	At room temperature: 2 nm thick interlayer, 2 ML thick NbO _x , metallic Nb on top, intermixing between Nb and TiO ₂ kinetically hindered bcc(1 0 0)[0 0 1] (1 1 0)[0 0 1]TiO ₂	Formation of Nb _x Ti _{1-x} O ₂ solid solutions	[58,93,190,363–376]
Cr/rutile (1 1 0)	Reduced Ti, oxidized Cr at interface	LEIS, XPS, LEED, MEED, ARXPS, HF calculations of doping levels	Overlayer oxidized through a dynamic exchange with lattice oxygen, metallic Cr on top bcc(1 0 0)[0 0 1] (1 1 0)[0 0 1]TiO ₂	Diffusion into substrate competes with formation of metallic clusters at intermediate T ; diffusion into bulk at high T	[58,292,355,377–380]

Mo/rutile (1 1 0)	Ti ³⁺ and Ti ²⁺ at the interface	AES, XPS, RHEED, ex situ AFM, adsorption of Mo(CO) ₆	Completion of three monolayers followed by islands; different substrate pretreatments have no influence on growth mode	[382,736]
Mo _x /rutile (1 1 0)		XAFS	Well-dispersed Mo oxides prepared by impregnation/calcination; preferentially Mo dimers with Mo-Mo bond parallel to [1 $\bar{1}$ 0]	[383–392]
Mn/rutile (1 1 0)	Reacted, disordered interface with reduced Ti cations	SXPS, XAS	Oxidized Mn atoms, metallic Mn for thicker layers	$T > 625$ °C: metallic Mn desorbs, formation of ternary MnTiO _x at the interface [271]
β -MnO ₂ /rutile (1 1 0)		OPA-MBE, RHEED, LEED, XPS, XPD, AFM	400–500 °C: pseudomorphic films, island growth, 500–600 °C: intermixing	[393]
Fe/rutile (1 1 0), rutile (0 0 1), +CO, +O ₂	Ti ³⁺ and oxidized Fe; Ti 3d-derived and Fe 3d-derived band gap states, see Fig. 46	AES, LEED, LEIS, UPS, HREELS, resonant photoemission, XPS, MEED, ARXPS, IPS	Flat clusters bcc(1 0 0) [0 0 1]//(1 1 0)[0 0 1]TiO ₂ surface roughness influences morphology, oxygen flattens the films creates FeO _x and Fe ₂ O ₃ phases	Encapsulation in UHV [17,262,355,378,379, 394–397]
Ru	Ti substrate not reduced	Decomposition of Ru ₃ (CO) ₁₂ at 300 °C, XPS, LEED, ARXPS	Disordered nanoclusters	Substitutional alloys [400,401]
RuO ₂ /rutile (1 1 0)	Intermixing at the interface	OPA-MBE, LEED, RHEED, XPS, XPD, ARXPS, decomposition of Ru ₃ (CO) ₁₂	Stacks of films with decreasing degree of intermixing	Extensive intermixing at 600 °C [289,400–402]
Co/rutile (1 1 0)	Minor oxidation/reduction reaction at 300 K	XPS	Assumed homogeneous growth	Indiffusion at 500 K, reduces support (SMSI), less stable on reduced TiO ₂ [405]
Rh/rutile (1 1 0), rutile (1 1 0)- (1 \times 2), +CO, rutile (0 0 1)	No interfacial reaction	STM, AES, XPS, LEIS, [Rh(CO) ₆ Cl] ₂ IRAS	Mainly (1 1 1) oriented 3D particles, control of particle size by seeding/growing	Coalescence of particles, encapsulates upon heating (substrate and treatment dependent) [407–409,411,413, 737,738]

Table 6 (Continued)

Metal/substrate	Interfacial reaction	Techniques	Growth morphology/structure	Thermal stability	Reference
Ir/rutile (1 1 0)- (1 × 2), +CO		STM, AES	Round particles on the (1 × 2) rows, CO disrupts crystallites	Increase in particle size upon annealing	[414,415]
Ni/rutile (1 1 0), +CO, +air, rutile (1 0 0)	No interfacial reaction, interfacial Ni atoms slightly negatively charged	UPS, XPS, STM, HREELS, EXAFS, RHEED, LEED, SIMS, DFT-embedded cluster	AES: S–K, STM: VW, nucleation at step edges, ‘hut-clusters’ with {1 1 1} and {1 0 0} facets	Islands coalesce up to 880 K	[416–426]
Pd/rutile (1 1 0), +CH ₃ OOH, +CO, rutile (1 0 0)-(1 × 3)	No interfacial reaction	STM, LEED, AES, CAICISS, RHEED, HREELS, FT-RAIRS, DFT-embedded cluster	Clusters fcc(1 1 1) [1̄2 0] (1 1 0)[0 0 1]Ti possibly (1 1 0) or (1 0 0) at small coverages	In UHV: sintering, encapsulation. When annealed in O ₂ : encap- sulation and spillover	[19,162,172,297,303, 346,427–435,739,740]
Pt/rutile (1 1 0)- (1 × 1), rutile (1 1 0)-(1 × 2), rutile (0 0 1)-(1 × 3), +CO, +H ₂ O	No interfacial reaction	STM, LEIS, LEED, ARXPS, MEED, XPS, AES, ESD, first- principles calculations	Volmer–Weber growth, nucleation at step edges on well-annealed surfaces (1 1) (1 1 0)TiO ₂ , (1 1 1) (1 0 0)TiO ₂ : equal amounts of Pt [2 1 1] parallel and perpendicular to TiO ₂ [0 1 0]	Sintering, encapsulation on reduced TiO ₂ substrates, see Fig. 47	[18,20,71,72,190,302, 364,436–440,442–446, 741–746]
Cu/rutile (1 1 0)- (1 × 1), +CO	No interfacial reaction	STM, LEIS, XPS, LEED, MEED, EELS, AES, SXRD, UPS, inverse PE, ARUPS, HRTEM, FT-RAIRS	Clusters (see Fig. 48), sharp interface [1 1 0] (1 1 1)Cu [0 0 1] (1 1 0)TiO ₂	High mobility, sintering already at low temperatures	[107,159,184,295,355, 364,377–380,396, 447–449,451,452, 747–750]
Ag/rutile (1 1 0)- (1 × 1), rutile (1 1 0)-(1 × 2), O ₂ (high pressure)	No interfacial reaction	XPS, LEIS, LEED, STM, surface differential reflectance (SDR), AFM	3D cluster growth	Sintering upon annealing from 100 to 300 K	[308,346,453–455, 751,752]
Au/rutile (1 1 0), +O ₂ , CO	No interfacial reaction	[294]	2D initially, then 3D (1 1 1) and (1 1 1 2) oriented clusters, see Fig. 49	Sintering	[294,346] (reviews) [22–24,306,307,309, 310,461,464,465, 753–758]

stoichiometry unaltered upon metal deposition. Atomically sharp interfaces are assumed, while Hf, Nb, and other highly reactive metals clearly extract oxygen from the substrate, and some metals intermix with the TiO_2 substrate at higher temperatures. Most importantly, any kinetic considerations are neglected, as well as the role of surface defects for nucleation and growth. Some of these issues are considered in the next section.

4.1.3. Growth kinetics, nucleation, and defects

After decades of surface research and thousands of detailed film growth studies, it is almost a platitude to say that kinetics play a major role in the formation of overlayers. Very detailed information about growth mechanisms can be extracted from statistical information such as island density and height distributions, nucleation sites, etc. Interestingly, STM measurements on metal/ TiO_2 have not become available until fairly recently. Spatially resolved information of overlayers on $\text{TiO}_2(1\bar{1}0)$ have been obtained for very few reactive (in the sense described above) metals on $\text{TiO}_2(1\bar{1}0)$, as well as most of the unreactive overlayers (Rh, Ir, Ni, Pd, Pt, Cu, Ag, Au). However, very few growth studies have systematically varied growth parameters such as deposition flux, temperature, or angle.

Of the reactive metals, only Al and V have been investigated with STM. (The growth of alkalis is special and discussed below.) Because changes in the local electronic structure dominates STM images on TiO_2 , it is difficult to obtain atomic resolution from overlayers that are oxidized upon contact with the TiO_2 substrate. The diffusion length of metal adatoms is small because the metal/substrate interaction is quite vigorous. Consequently, nucleation occurs at terraces, and steps and point defects are less important in the nucleation process. Spectroscopic measurements comparing films grown on sputtered and smooth surfaces indicate some influence of surface roughness, however. As outlined above, a wetting of the metal overlayer is expected for reactive metals from thermodynamic considerations. For example, in the case of V (see [12] and discussion below), the thicker films cover most of the surface and become granular, consistent with Stranksi–Krastanov type growth mode. However, the growth does not proceed in the orderly layer-by-layer fashion suggested in the sketch in Fig. 41.

The non-wetting behavior of unreactive metal overlayers is clearly observed in STM images, see for example, $\text{Cu}/\text{TiO}_2(1\bar{1}0)-(1\times 1)$ below. In contrast to the more reactive metals, nucleation occurs preferably at step edges. Interestingly, the size distribution of the 3D metal clusters is very narrow, see the STM image of Cu/TiO_2 , below. A ‘self-limiting growth’ was suggested to be responsible for this phenomenon [295]. The relatively uniform cluster size makes such metal/ TiO_2 systems good candidates for ‘flat model catalysts’ where the size-dispersion can be very well controlled.

Even when a metal overlayer grows in a 3D fashion, quasi-2D islands are formed during the initial stages of the growth for kinetic reasons. These 2D islands are of particular interest; all the overlayer atoms have substrate atoms as neighbors and therefore possibly different chemisorptive properties [4]. The 2D to 3D transition occurs at a critical coverage. It has been measured for the noble metals Cu, Ag, and Au to range somewhere around 0.2 ML. For a similar system, $\text{Cu}/\text{ZnO}(10\bar{1}0)$, it has been shown that the 2D to 3D transition is also dependent on the number of nucleation sites on terraces, e.g. adsorbates or defects. At perfectly flat and clean surfaces, 3D growth is observed for the lowest coverages [296]. Defects might be of similar importance on a $\text{TiO}_2(1\bar{1}0)$ surface. Recent STM work by Frenken and co-workers [297] has pointed out the influence of defects on the size distribution and density of clusters for $\text{Pd}/\text{TiO}_2(1\bar{1}0)$.

The surface structure of rutile $(1\bar{1}0)-(1\times 1)$ is quite corrugated and the bridging oxygen atoms protrude from the surface. It is tempting to assume that such a surface should act as a template for the

formation of one-dimensional (1D) islands, either in the troughs or along the bridging oxygen atoms. This has not been observed with a direct-imaging method, however. The reaction with facile bridging oxygen atoms at the (1×1) surface is possibly too vigorous and disruptive. Non-reactive metals, on the other hand, are too mobile at room temperature and form clusters starting at the very smallest coverages. No measurements have been performed with low-temperature STM, where this aggregation could be prevented. On the $\text{TiO}_2(1\ 1\ 0)\text{-}(1 \times 2)$ structure, preferential nucleation on the (1×2) rows was reported for both, reactive overlayers (see Fig. 44) as well as non-reactive ones.

4.1.4. Film structure and epitaxial relationships

Experimentally, special adsorption sites have been identified only in the case of alkali metals. Ordered superstructures are observed for fractional monolayer coverages, e.g. $\text{TiO}_2(1\ 1\ 0)\text{-c}(4 \times 2)\text{Na}$ and $\text{K/TiO}_2(1\ 0\ 0)\text{-c}(2 \times 2)\text{K}$. The various models for superstructures of $\text{Na/TiO}_2(1\ 1\ 0)$ are discussed in the context of Fig. 42. Alkali metals tend to sit at positions that maximize the contact to oxygen atoms, see Fig. 42c.

Growth of ordered epitaxial overlayers has been observed for most transition metals. Exceptions (in the sense that no ordered LEED pattern was observed) are the very reactive materials Ti, Al and Hf. The bcc metals V, Nb, Cr, and Fe grow with their $(0\ 0\ 1)$ face parallel to the surface, and the $[1\ 0\ 0]$ orientation aligned with the oxygen rows of the $\text{TiO}_2(1\ 1\ 0)$ surface. Surprisingly, epitaxy is good despite the fact that there is a substantial re-arrangement of atoms at the interface. For the most part, the non-reactive materials Ni, Pd, Pt, Cu, Ag, and Au all form fcc overlayers. In most cases, $(1\ 1\ 1)$ facets of the clusters are parallel to the substrate, but other orientations have been observed as well, see Table 6.

4.1.5. Thermal stability of metal overlayers on TiO_2 -SMSI

The thermal behavior of the overlayer metal can roughly be classified in several groups. Metals with a very low cohesive energy such as the alkalis and Mn desorb upon annealing. Heating a TiO_2 substrate that has been covered by a very reactive metal (Al, Ti, Hf) induces oxidation of the overlayer, accompanied by either oxidation or further reduction of the substrate. The thermodynamically favorable reaction (oxidation of the overlayer and reduction of the substrate) is kinetically hindered at room temperature. At elevated temperature, the activation barrier is overcome, and a more complete oxidation of the overlayer takes place. Metals with an intermediate strength of the interfacial reaction (V, Nb, Cr, Ru) interdiffuse with the substrate, although some clustering of the overlayer metal can occur as well (Cr). Finally, the non-reactive metals all show sintering upon mild annealing. Cluster migration and coalescence has been observed for $\text{Pd/TiO}_2(1\ 1\ 0)$ [297] and might be the mechanism for other non-reactive overlayers as well.

The group VIII A metals Fe, Co, Rh, Ir, Ni, Pd, Pt all show a very interesting behavior upon annealing in a reducing atmosphere that has been discussed in the catalysis literature for several decades. The acronym SMSI has been termed by Tauster [298] to account for the changes in catalytic activity when catalysts, consisting of these metals supported on TiO_2 or other reducible oxides (TaO_5 , CeO_2 , NbO , etc.), are reduced at elevated temperature. Adsorption of H_2 and CO is drastically reduced, but competitive hydrogenation vs. hydrogenolysis reactions are greatly favored in SMSI systems. For example, methane production from CO or CO_2 and H_2 is enhanced by three orders of magnitude [16]. Hence the SMSI phenomenon allows to tailor the selectivity of a catalyst and has caused wide-spread interest. High-resolution electron microscopy (HREM) clearly shows that some sort of reduced

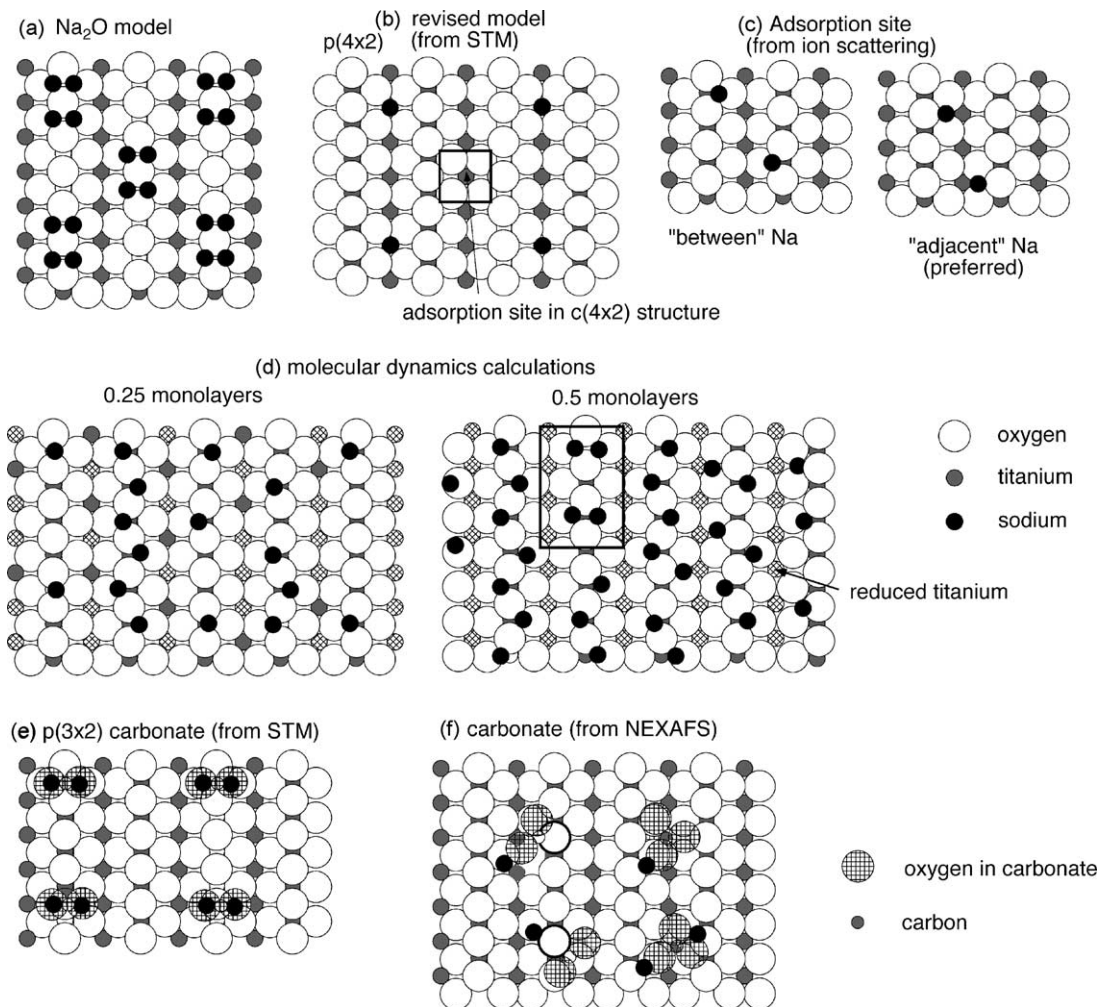


Fig. 42. Summary of models of Na adsorption on $\text{TiO}_2(1\ 1\ 0)$. (a) The Na_2O model was initially proposed by Onishi et al. [205,304,305] to account for the $c(4 \times 2)$ overlayer observed with LEED. (b) Recently, the same group performed STM measurements that seemed to indicate that Na is in fact adsorbed on Ti atoms and not at the bridging oxygen atoms [323]. A coordination to oxygen atoms seems much more likely, however (c) Two different adsorption sites of Na atoms at bridging oxygen atoms were considered, adjacent to one, or in between two bridging oxygen atoms, respectively. Ion scattering measurements are consistent with the ‘adjacent’ configuration [327]. Snapshots of molecular dynamics calculations [329,330], re-drawn in (d), show that most Na adatoms are in ‘between’ positions. Two proposals for the configuration of the CO_3^{2-} complex that forms upon adsorption of CO_2 on Na-precovered surfaces are pictured in (e) and (f). A linear configuration (e) is consistent with STM measurements [323]. (f) NEXAFS experiments indicate a tilted position [328].

titanium oxide migrates onto the clusters [299,300]. Special Ti^{3+} sites on this layer and/or at its interface with the metal cluster are thought to be responsible for the changed reactivity [298,301].

For a while there has been uncertainty as to whether the same phenomenon occurs when SMSI metal films are deposited on single-crystalline TiO_2 and annealed under UHV conditions. It has been shown to take place for some materials, e.g. Fe [17]. In other cases, such as Pt, different groups came to

opposite conclusions using the same experimental techniques. It is now clear that the reduction state of the TiO_2 substrate plays a decisive role on whether or not encapsulation of the supported metal clusters occurs, hence the effect can be sample-dependent. Some excess Ti atoms or ions must be in the near-surface region in order for the encapsulation to occur. The structure of encapsulated Pt clusters have recently been investigated by this author's group [20,302]. Details are discussed in the section on Pt overlayers below. Similar results have been obtained recently on encapsulated Pd layers [303].

4.1.6. Chemisorption properties

One of the main motivations for studying metals on TiO_2 is the desire to synthesize model systems for supported metal catalysts [293]. As listed in Table 6, adsorption of simple molecules has been investigated for a few metal overlayers or clusters on TiO_2 . A very nice example is the promotional effect of the $\text{TiO}_2(1\ 1\ 0)\text{-c}(4\times 2)\text{Na}$ overlayer for the adsorption of CO_2 [205,304,305]. The investigation of Au/TiO_2 has received a recent surge of interest in an attempt to understand low-temperature oxidation reactions [306]. In this context, recent high-pressure and high-temperature STM studies of supported clusters, performed in Goodman and co-workers [307–310] on Au and Ag, and by Bowker and co-workers [19] on Pd, are a particularly interesting attempt to bridge both the ‘materials’ and the ‘pressure gap’.

4.2. Metals and metal oxides on TiO_2

4.2.1. Lithium

Promotion of TiO_2 with Li is of technological importance in dye-sensitized solar cells [311], for energy storage in lithium intercalated nanostructured TiO_2 , and in humidity and oxygen sensors [312]. Doping with Li also affects the selectivity of TiO_2 catalysts in the conversion of methane to C2-hydrocarbons [313]. The only experimental surface study conducted so far has been an ESD investigation on thin polycrystalline films [314,315]. Semiempirical Hartree–Fock calculations on Li adsorbed on (and incorporated in) rutile and anatase TiO_2 have been reported by Stashans et al. [316]. The Li ion can occupy an interstitial position in one of the structural voids in the anatase crystal without big distortions in the crystal structure (see Fig. 2 for the anatase structure). For rutile, problems with self-consistency and large distortions around the Li ion point towards an unstable configuration. This is in agreement with experimental observations that Li can be intercalated with higher probability in anatase than rutile [209,317,318]. The equilibrium position on the rutile (1 1 0) surface is located between two bridging oxygen atoms [316,319]. On the anatase (1 0 1) surface, the Li ion moves into one of the structural voids, underneath the top surface layer. In all cases, a Li-induced local one-electron energy level appears in the gap between the upper valence band and the conduction band and could be attributed to Ti^{3+} states. This is similar to what is observed for other metals with a high affinity towards oxygen.

4.2.2. Sodium

The adsorption of Na on $\text{TiO}_2(1\ 1\ 0)$ has been studied with experimental [160,205,304,305,320–328] as well as theoretical [319,329–332] techniques. No reports for the growth on other faces exist at this point. The presence of Na strongly affects the electronic structure of TiO_2 , via oxidation of the adsorbed Na and reduction of the Ti atoms in the substrate. Changes in the electronic structure also reflected by a strong change in work function, a downward band bending (see Fig. 35), and in the neutralization and scattering of D^+ ions [321,322]. Resonant photoemission experiments [324] show that the Na-induced

feature in the band gap has a resonance behavior indicative of a Ti3d-derived feature, similar to the ‘defect state’ in Fig. 35. A mechanism for the adsorption process is proposed in which a long-distance electron transfer occurs from atomic Na towards a fivefold coordinated surface titanium atom. This is followed by physisorption of the Na^+ cation at the surface [330]. In calculations this electron transfer from the $\text{Na}3s$ atomic orbital to the surface gives rise to a highly spin-polarized state in the band gap which is localized at a 5-fold-coordinated Ti surface atom [331]. Again, this is similar to the spin-resolved calculations for the defect state on the clean surface, Fig. 37.

Interestingly, adsorbed Na promotes the adsorption of CO_2 and the dissociation of NO. Neither molecule binds to a clean surface at room temperature. Adsorbed CO_2 forms a carbonate (CO_3^{2-}) complex at the surface. Onishi et al. [205,304,305] were the first to observe that a critical Na coverage is necessary before this adsorption takes place at room temperature. This critical coverage coincides with the formation of an *ordered* $c(4 \times 2)$ superstructure. This interesting promotion effect has prompted some work on the adsorption geometry of Na. The results are partially conflicting and are summarized in Fig. 42.

The first structural model was introduced by Onishi et al. [205,304,305]. Based on XPS intensities, a Na coverage of 0.5 ML was calculated, and from the extinction of spots in LEED, a “ Na_2O -dimer” model was proposed (Fig. 42a). More recently, the same group has conducted STM experiments, and found bright spots on *bright* rows, i.e., on the position of the fivefold coordinated Ti atoms (Fig. 42 [323]). Consequently, their former model was revoked by the authors. A previous STM study was performed on the $\text{TiO}_2(1\ 1\ 0)-(1 \times 2)$ surface [160]. Based on photoemission experiments, Nerlov et al. [324–326] suggested two possible adsorption sites for Na in tetrahedral coordination with three oxygen atoms, see Fig. 42c. A Na atom on the “between” site is bonded to two bridging and one in-plane oxygen atom, a Na atom in the “adjacent” site is bonded to one bridging oxygen and two in-plane oxygen atoms. Hartree–Fock and Monte Carlo simulations of Na shows a preference for “between” sites, see Fig. 42c. In ion shadowing/blocking measurements it is seen that adsorption of Na removes a peak that is due to scattering from the fivefold coordinated Ti atoms [327]. Under the assumption of a ‘derelaxation’ of the bridging oxygen atoms, the results are consistent with “adjacent” Na, but inconsistent with “between” Na. This is in disagreement with the theoretical results (Fig. 42d) published in [329,330]. A molecular dynamics simulation of Na atoms at different coverages showed preferred adsorption sites neighboring two bridging oxygen atoms, in ‘between’ positions. However, a more recent calculation by the same group indicates that the position might depend on the Na coverage [319]. An adsorption on the Ti sites as proposed in [323] was not explicitly considered [327], but such a position does not seem to be likely on chemical grounds.

The proposed geometries of the carbonate ion that forms upon adsorption of CO_2 on a Na-covered surface are also summarized in Fig. 42e and f. A linear configuration was proposed based on STM images, see Fig. 42e. The third oxygen in the CO_3^{2-} complex is a bridging oxygen atom. NEXAFS experiments [328] show that the molecular plane of CO_3^{2-} is twisted by $32 \pm 5^\circ$ out of the $[0\ 0\ 1]$ direction with a tilt of $46 \pm 5^\circ$ away from the surface normal, in disagreement with this model. Two different configurations have been suggested (Fig. 42f), one where CO_2 reacts with the bridging oxygen atom (left side in Fig. 42f), and one where it occupies a site between the bridging O atoms (right side in Fig. 42f). In this case carbonate formation must involve abstraction of O from the selvedge [328].

4.2.3. Potassium

Adsorption of K has been studied on rutile $(1\ 0\ 0)$ and $(1\ 1\ 0)$. The experimental results on the electronic structure are similar on both surfaces [333–335], and consistent with other alkali metals. K

adsorption on the annealed $\text{TiO}_2(1\ 1\ 0)$ surface induces a $\text{Ti}3d$ state in the band gap and a change in work function [333,334]. Theoretical results indicate that this state is spin-polarized [278,336]. UPS data show two distinct features at 1.7 and 5.3 eV above E_F , associated with $\text{Ti}3d$ -derived t_{2g} and e_g states, respectively [337] (see also Fig. 33). The electronic structure has also been probed with D^+ ion scattering [322]. On the slightly defective surface, a decrease in the initial concentration of O vacancy was observed and assigned to O diffusion to the surface, induced by K adsorption [334]. This is also consistent with the observation of K_2O multilayers that grow by extracting oxygen from the substrate [335]. Heating a K-covered surface to a temperature above 1000 K causes a drastic reduction of the $\text{TiO}_2(1\ 1\ 0)$ substrate [333].

No long-range ordering was observed on $\text{TiO}_2(1\ 1\ 0)$, making a structural assignment difficult. Calculations indicate a strong repulsive interaction between adsorbed K, and a preference for K to adsorb in the vicinity of the bridging oxygen atoms [336] in a ‘between’ site (Fig. 42) for higher coverages. In contrast to the absence of a LEED pattern on $\text{TiO}_2(1\ 1\ 0)$, a $\text{TiO}_2(1\ 0\ 0)\text{-c}(2\times 2)\text{K}$ overlayer forms at 0.5 ML coverage [338–340]. This layer desorbs at 750 °C [340]. SEXAFS measurements [338,339] indicate that K occupies a bridge site, probably between two of the twofold coordinated oxygens protruding from the $\text{TiO}_2(1\ 0\ 0)\text{-(}1\times 1\text{)}$ surface (see Fig. 23A). This adsorption geometry was confirmed in a recent ab initio study [278]. Large relaxations of the neighboring O atoms were found.

The co-adsorption of O_2 on $\text{TiO}_2(1\ 0\ 0)$ indicates the formation of a peroxide or superoxide at the surface [341]. The uptake of CO_2 on the reconstructed $\text{TiO}_2(1\ 0\ 0)\text{-(}1\times 3\text{)}$ surface, promoted with K and Cs, was monitored with MIES and UPS [342]. Similar as in the case of Na, the surface needs to be alkaliated before any uptake of CO_2 occurs at room temperature, and the formation of a CO_3 has been invoked.

4.2.4. Cesium

The adsorption of Cs on a $\text{TiO}_2(1\ 1\ 0)$ rutile surface was investigated by Grant and Campbell [343]. The formation of a strongly bound, ionized Cs layer, followed by multilayers, was observed. From TPD and XPS data it was concluded that Cs displays a Stranski–Krastanov growth mode below room temperature, with the completion of a uniform ML, followed by the growth of 3D clusters of Cs that cover only a small fraction of the surface. The Cs in the first $\sim 1/2$ ML is very cationic, donating electron density to the substrate. Most of this charge is localized near the topmost atomic layers, with Ti^{4+} ions being reduced to Ti^{3+} . A local dipole moment of the adsorbate–substrate complex of ~ 6 Debye at ~ 0.1 ML was extracted from band-bending corrected work function measurements. A downward band bending of $\sim 0.2\text{--}0.3$ eV occurs and saturates at ~ 0.05 ML. A rapid and smooth decrease in the heat of adsorption with coverage from initially >208 kJ/mol (which is too high to be probed with TPD) down to ~ 78 kJ/mol for 1 ML was observed. No ordered LEED structures were observed.

Metastable ($\text{He}^*\text{1s2s}$) impact electron spectroscopy (MIES) and UPS results on $\text{Cs/TiO}_2(1\ 1\ 0)$, deposited at room temperature, were reported by Brause et al. [344]. With increasing coverage, a $\text{Ti}3d$ and a Cs6s feature in the band gap were identified with UPS and MIES, respectively. The MIES results for low Cs coverages are compatible with fully ionic adsorption of Cs. For larger coverages the charge transfer is incomplete. The ionicity, i.e., the charge transfer per adsorbed Cs atom, decreases from practically unity to 50% and 12% at coverages of 0.5 ML and 1 ML, respectively. This is in agreement with earlier experiments [321,343]. After turning off the Cs supply, the MIES spectrum of a surface covered with Cs

changes slowly. This was interpreted as a rearrangement of the oxygen in the surface layer whereby the Ti and Cs ions compete for the bonding to the oxygen. Cs promotes the adsorption of CO₂ on a TiO₂(1 0 0)-(1 × 3) surface [342].

4.2.5. Calcium

The interaction between Ca ions and TiO₂ plays a major role for the performance of Ti-containing steels as bone implants. No study of the deposition of Ca on TiO₂ has been performed. However, Ca impurities in the bulk of the crystal tend to segregate towards the surface upon annealing [145–148]. The interaction of such segregated Ca impurities to the surface of TiO₂(1 1 0) is discussed in Section 2.2.1.4.

4.2.6. Aluminum

The interactions of ultrathin Al films with both stoichiometric and oxygen deficient (sputtered) TiO₂(1 1 0) surfaces were studied with several electron spectroscopies and LEED by Dake and Lad [345]. The interfacial reactions in aluminum films resemble those of the early transition metals. It interacts strongly with both stoichiometric and sub-stoichiometric TiO₂(1 1 0) surfaces at room temperature. For monolayer Al doses, the Al layer is oxidized, the Ti ions in the TiO₂ substrate underneath reduced, and the long-range order of the substrate is lost. The interfacial oxidation/reduction reaction occurs also on pre-reduced TiO₂ surfaces. No evidence for an intermetallic Al–Ti alloy at the interface was found. An aluminum oxide film continues to grow at higher doses by extracting O anions from the TiO₂ substrate. When oxygen diffusion becomes rate-limiting, a heterogeneous mixture of aluminum oxide and metallic aluminum is created on top of the oxygen-deficient TiO_{2-x} substrate. This mixed layer is unstable upon heating and converts completely into aluminum oxide. In addition, the annealing treatment causes a reoxidation of the reduced substrate.

STM results of the initial stages of the growth are consistent with the growth mode deduced from spectroscopic results. A disordering of the substrate is seen for very small amounts of deposited Al [346,347]. Small clusters were visible on the terraces but no preferred nucleation sites were observed. STM studies of Al deposited on a faceted rutile (1 0 0) surface showed island growth [348].

The adsorption of Al on chemically modified TiO₂(1 1 0) surfaces has also been studied [281,349]. Aluminum deposited onto a TiO₂ surface pre-dosed with ~1 ML potassium competes with the potassium for oxygen, and reduces additional Ti⁴⁺ cations in the interface region, with the possible formation of a Ti–O–Al–K complex. Carbon species adsorbed on the TiO₂(1 1 0) surface by electron beam decomposition of C₂H₄ prior to the Al deposition interact only weakly with the oxide surface, but retard the oxidation rate of Al and decrease the temperature stability of the Al₂O₃ overlayer [349].

4.2.7. Titanium

Rocker and Göpel [350] showed that non-stoichiometric Ti-rich TiO₂ surfaces can be prepared by Ti evaporation. Spectroscopically, the resulting films resemble a surface reduced by sputtering. The growth of Ti was investigated by Mayer et al. [280] with XPS and LEIS. Ti interacts with the TiO₂ substrate, and forms a layer of reduced TiO_x that is thicker than the deposited film. From LEIS data it was concluded that Ti clusters form on top of this film. The thermal stability of TiO_x overlayers has been investigated by Henderson [74]. From SSIMS experiments with isotopically labeled ⁴⁶Ti and ¹⁸O it was concluded that diffusion at the surface takes place between 400 and 700 K, and that diffusion into the bulk starts at temperatures >700 K. The predominant diffusing species was identified as Ti cations, not O anions/vacancies.

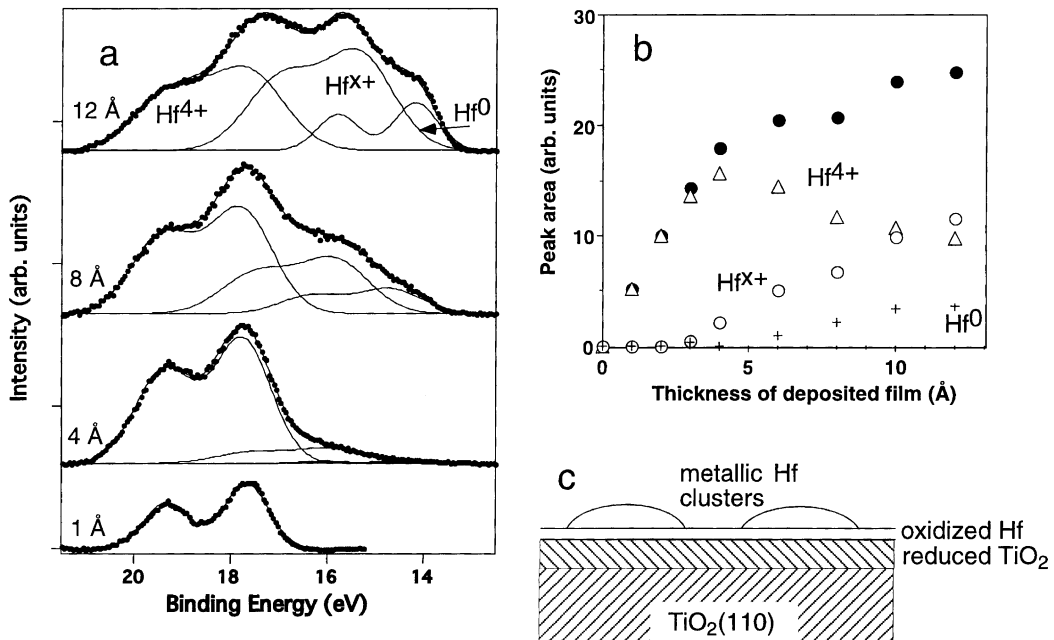


Fig. 43. (a) Soft X-ray photoemission spectra of Hf overayers on TiO₂(110) (photon energy of 110 eV). The spectra are deconvoluted to show the contributions of different oxidation states. The intensities of the contributions to the total peak area are shown in (b). The initial growth mode is depicted schematically in (c). From [351].

4.2.8. Hafnium

Hafnium is a very reactive material, and the growth mode as determined with soft X-ray photoemission and supporting LEIS measurements is summarized in Fig. 43 [351]. Upon Hf deposition at room temperature, an oxidized layer of HfO₂ is formed on top of a reduced layer of TiO_{2-x}. LEIS data clearly indicate that this layer covers the surface completely [63], and that oxygen migrates from the substrate into the overlayer. The substrate LEED pattern disappears very quickly, and no long-range ordered structure is formed. For thick layers, metallic Hf is observed, probably in the form of metallic clusters. This metallic Hf is oxidized upon heating [63]. A schematic diagram of the initial stages of the growth is drawn in Fig. 43.

4.2.9. Vanadium

Room-temperature deposition of metallic V shows a vigorous reaction with the TiO₂ substrate. A clear Ti³⁺ feature evolves, and the LEED pattern of the clean surface disappears for small coverages [14,15,352–354]. Concurrent with the reduction of the substrate, the V overlayer is oxidized, probably in a V³⁺ oxidation state [352]. For thicker films, metallic V forms. Metallic V was also observed when vanadium was deposited onto a sputter-reduced surface [15]. Electron diffraction experiments were performed on a film with a coverage of a fractional monolayer after annealing at 473 K. The results are consistent with an adsorption site underneath the bridging oxygen atoms, at the position of the sixfold coordinated Ti atoms [14]. At higher coverages (~5 ML) V islands form with a bcc (100) structure. No long-range ordering is visible, but epitaxy with alignment bcc(100)[100]VII(110)[110]TiO₂ is

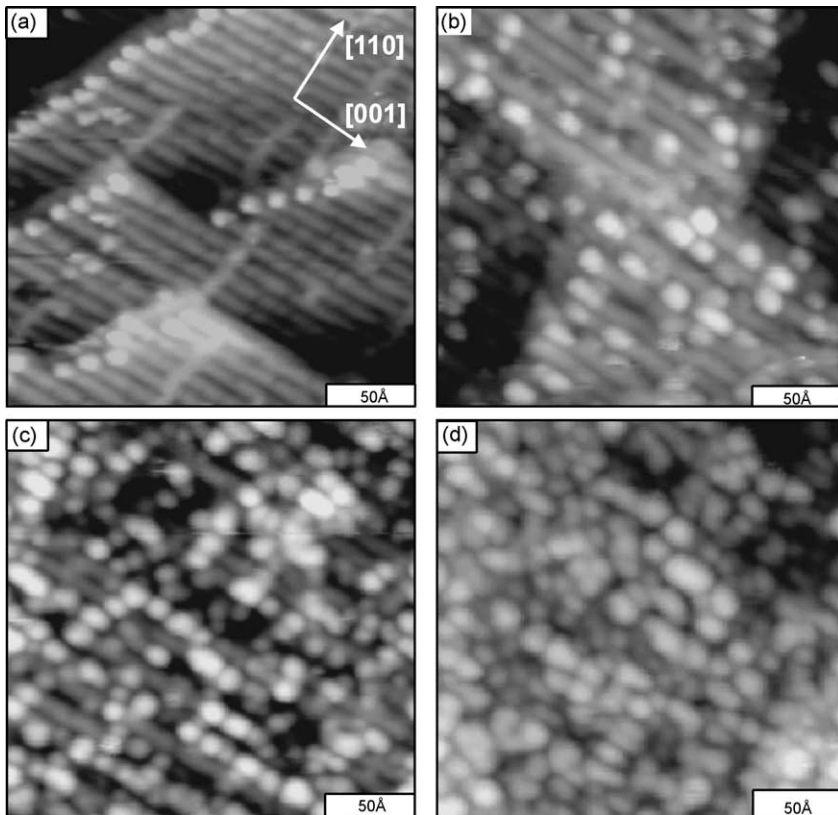


Fig. 44. STM images ($250\text{ \AA} \times 250\text{ \AA}$, $+2.0\text{ V}$, 0.1 nA) of a clean (a) and vanadium-covered $\text{TiO}_2(1\ 1\ 0)$ - (1×2) surface: (b) 0.05 ML V , (c) 0.2 ML V , (d) 0.6 ML V . From Biener et al. [12]. © 1999 Elsevier.

concluded from ARXPS measurements. This is similar to other bcc metals on $\text{TiO}_2(1\ 1\ 0)$ [355]. When oxygen is dosed on metallic $\text{V}/\text{TiO}_2(1\ 1\ 0)$ surfaces, the films are oxidized, probably to V_2O_3 [352].

Vanadium films, evaporated on a $\text{TiO}_2(1\ 1\ 0)$ - (1×2) surface at 300 K were studied by the group of Madix [12,354,356,357]. The V binds preferentially on top of the (1×2) strands with formation of small clusters, see Fig. 44. This maximizes the contact with surface oxygen (if one assumes an added Ti_2O_3 row model for the (1×2) reconstruction, see Fig. 18b). No preferential adsorption at step edges is visible. As the vanadium coverage is increased toward one monolayer, the density of vanadium clusters decorating the (1×2) rows increases, forming chains of more or less isolated clusters. At three monolayers coverage vanadium metal forms a granular film which covers the oxide surface uniformly. The film is thermally not stable with oxidation occurring at $\sim 500\text{ K}$ and the onset of diffusion into the bulk around 600 K [12,356]. Similar results have also been obtained on a $\text{TiO}_2(1\ 1\ 0)$ surface [354]. Atomically resolved images of subsurface impurity atoms have been attributed to substitutional V atoms [153].

4.2.10. Vanadia

Deposition of vanadium in an oxygen ambient results in vanadium oxide that interacts only weakly with the support [15,272]. The $\text{Ti}2\text{p}$ levels remain fully oxidized. The work function is increased [15,272].

The stoichiometry and short-range order of vanadia overlayers can be controlled by varying the deposition parameters. When V is deposited in an oxygen pressure of 2×10^{-6} Torr at room temperature, XPS and valence band photoemission as well as SEXAFS results are compatible with a V_2O_3 overlayer [272]. No long-range ordering is visible with LEED. The oxidized overlayer is much more stable than a metallic V film; annealing at 1100 K causes a structural re-arrangement with formation of larger vanadia particles and formation of a VTiO_3 layer at the interface [272], but no diffusion into the substrate.

A VO_2 layer can be grown by successive cycles of fractional-ML vanadium metal deposition followed by annealing at 473 K in 2×10^{-6} mbar O_2 [358]. The V3p photoemission peak consists of two distinct components chemically shifted by 1.3 eV. In angle resolved photoemission extended fine structure (ARPEFS) scans, the lower BE signal, associated with the VO_2 phase, shows well defined intensity modulations whose main features are similar to the ARPEFS scan of the Ti3p signal of the substrate. This indicates formation of an ordered VO_2 phase with a rutile structure epitaxial to the substrate. In addition a highly oxidized, less ordered phase forms.

The reaction to VO_2 can be stopped at VO_x ($x \approx 1$) when annealing of the metal film is carried out in UHV [359]. Under specific conditions, locally ordered VO_x films with a thickness of up to 5 ML can be prepared. A detailed structural analysis was given by Negra et al. [360]. A NaCl-like stacking of the overlayer with (1 0 0) orientation and alignment of the [0 0 1] overlayer azimuth with the substrate [1 1 2] direction was concluded from X-ray photoelectron measurements.

Methanol is oxidized to formaldehyde on a $\text{TiO}_2(1\ 1\ 0)$ -supported vanadium oxide monolayer (probably V_2O_3), whereas both clean $\text{TiO}_2(1\ 1\ 0)$ - and $\text{TiO}_2(1\ 1\ 0)$ -supported vanadia multilayers are inactive for the reaction [361,362]. This result is similar to the reactivity trends found for high-surface area catalysts.

4.2.11. Niobium

The growth of Nb overlayers was investigated by Marien et al. [363–365]. When Nb films are grown at room temperature, a reacted interface forms as is expected for an early transition metal. Direct evidence for this structurally distorted interlayer is given by the high-resolution transmission electron microscopy (HRTEM) image in Fig. 45. The about 2 nm thick interlayer contains many structural defects, but the image contrast clearly shows that it did not transform into an amorphous state. Electron-energy loss spectra have been taken with a scanning transmission electron microscope (STEM) in steps of 0.5 nm across the interface (Fig. 45). The shape of the TiL_{23} edge is very sensitive to changes in oxidation states and local bonding geometries, and the evolution of the spectra across the interface is consistent with a TiO_{2-x} layer depleted of oxygen. The first two monolayers of Nb adjacent to the substrate are oxidized. The interdiffusion of Nb with the TiO_2 substrate is kinetically hindered at the low deposition temperature used. On top of the interfacial reaction layer, Nb grows epitaxially with its (1 0 0) planes parallel to $\text{TiO}_2(1\ 1\ 0)$ and the [1 0 0] overlayer azimuth aligned with the substrate [0 0 1] direction.

The epitaxial growth of Nb-doped TiO_2 films on (1 0 0) and (1 1 0)-oriented substrates has been discussed in a series of papers from Chambers' group [93,190,366–374]. Nb substitutionally incorporates at cation sites in the rutile lattice, forming $\text{Nb}_x\text{Ti}_{1-x}\text{O}_2$ solid solutions. Analysis of the Nb 3d_{5/2} core-level binding energy suggests a Nb^{4+} oxidation state. The crystal quality and surface roughness of the films depend strongly on the substrate orientation. The epitaxial films grow in a layer-by-layer fashion and have excellent short- and long-range structural order at $x \leq 0.3$ on $\text{TiO}_2(1\ 1\ 0)$ and

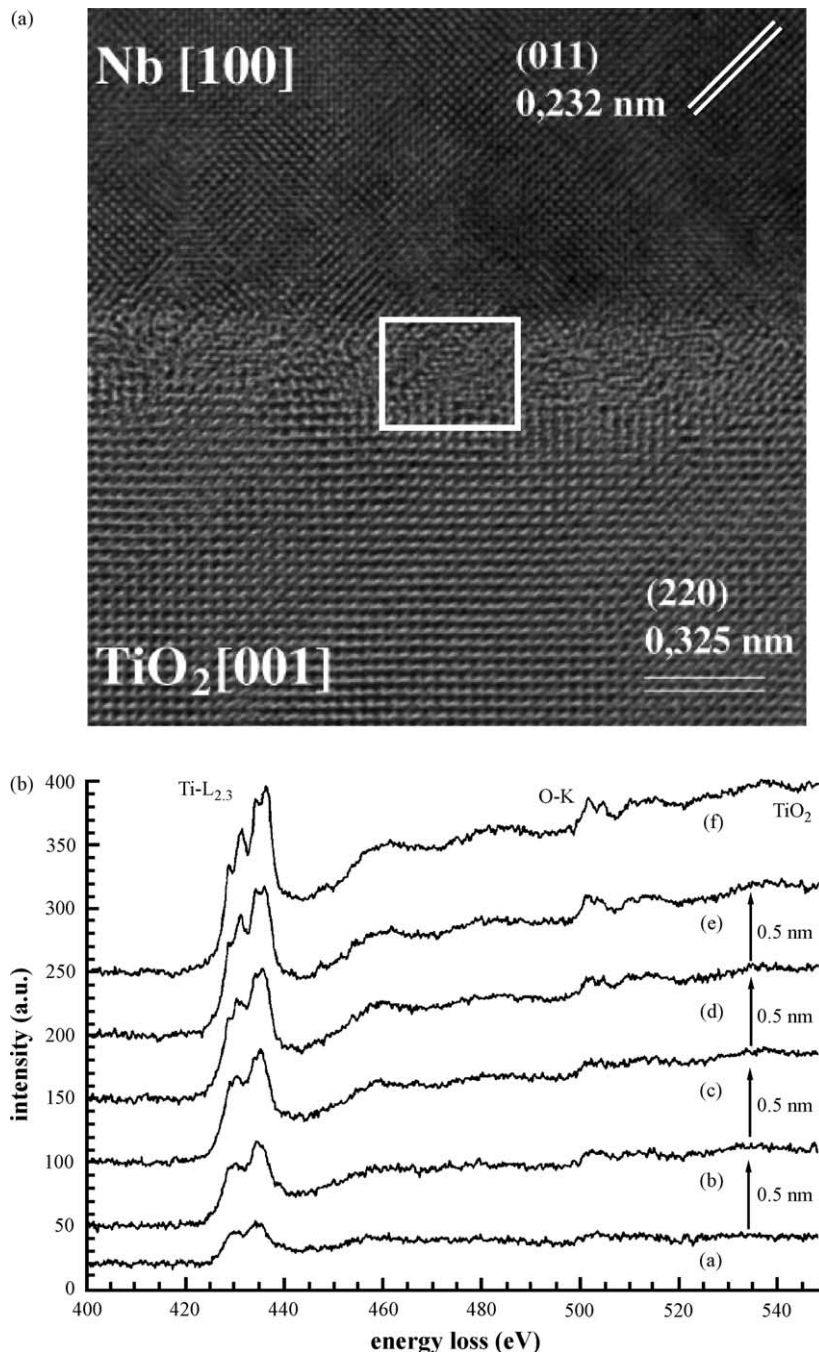


Fig. 45. (a) HRTEM micrograph of the Nb/TiO₂(1 1 0) interface. A distorted interlayer between the Nb and TiO₂ crystal is present. Due to the high defect concentration in this region, the atomic structure of this interlayer is poorly resolved. (b) Line profile of EEL spectra measured perpendicular to the interface by STEM. The spectra show a sharp transition from the interlayer of the perfect rutile (top curve) with crystal-field split Ti-L_{2,3} edges. The step width of the electron beam was 0.5 nm. From Marien et al. [365]. © 2000 Elsevier.

at $x \leq 0.1$ on $\text{TiO}_2(1\ 0\ 0)$. At higher doping levels dislocations form and the films become rough. The Nb–O bond lengths in $\text{Nb}_x\text{Ti}_{1-x}\text{O}_2$ are the same as the Ti–O bond lengths in pure TiO_2 prior to the onset of dislocation formation. The Nb substitution for Ti in the lattice introduces an additional valence electron per atom. These extra Nb electrons form a non-bonding band which is degenerate with the valence band; no new state density was found experimentally in either the band gap or conduction band.

The effect of Nb doping on the band gap was studied theoretically [58,375]. In these investigations Nb is found to introduce a shallow donor level in bulk TiO_2 [375]. An impurity related state is predicted to occur in the gap of Nb-doped $\text{TiO}_2(1\ 1\ 0)$ surfaces, in contradiction to the photoemission experiments quoted above [93,190,366–374]. A +5 rather than a +4 oxidation state for surface cations was predicted. The structural changes undergone by the (1 1 0) surface upon doping are small and insensitive to the impurity charge state. An experimental study by Morris et al. [376] showed core-level spectra consistent with a Nb^{5+} oxidation state and a gap state with Ti^{3+} . STM images of Nb-doped $\text{TiO}_2(1\ 1\ 0)$ showed bright spots that were attributed to a delocalization of charge to the neighboring atoms [376]. The dispute about the charge state of Nb in TiO_2 is not resolved at this point. Possibly it depends on the sample growth conditions.

4.2.12. Chromium

The growth, interfacial reaction, film structure and thermal stability was investigated in a series of papers by Pan et al. [292,355,377–380]. The overall growth behavior fits into the category of early transition metals, with an intermediate layer formed upon chromium deposition, and ‘wetting’ of the substrate by an oxidized chromium overlayer. The wetting correlates with the formation of reduced Ti species as observed with XPS. Low-energy ion scattering experiments with isotopically labeled ^{18}O showed that this oxidation/reduction reaction is due to a dynamic incorporation of lattice oxygen into the chromium overlayer. The same epitaxial relationship as already discussed for Nb and V, i.e., bcc(1 0 0)[1 0 0]Cr||[1 1 0][1 1 0] TiO_2 was also observed for chromium overlayers. Chromium is soluble in TiO_2 and chromium-doped TiO_2 ceramics are used in varistors. The annealing behavior of vapor-deposited films is complex, with clustering of metallic chromium competing with diffusion into the bulk. Prolonged annealing at high temperature of chromium overlayer leads to dissolution into the bulk. The band gap width and the charge state of chromium dopants was calculated by Sambrano et al. [58].

$\text{TiO}_2(1\ 1\ 0)$ is a useful substrate for the growth of CrO_2 , which also has the rutile structure. CrO_2 has properties that might be of interest for spintronics applications, as it is expected to be a half-metallic ferromagnet [381].

4.2.13. Molybdenum

The deposition of metallic molybdenum on $\text{TiO}_2(1\ 1\ 0)$ has been studied with AES, XPS, ex situ AFM, and RHEED [382]. The influence of different substrate preparations were tested. A stoichiometric surface was produced by sputtering and annealing in oxygen, a non-stoichiometric, rough surface by Ar^+ sputtering without annealing, and rough but stoichiometric surface by sputtering with O^+ . In each case, in situ AES and XPS studies and ex situ AFM and RHEED characterizations indicate a Stranski–Krastanov growth. After completion of three monolayers, island growth is observed. The first three monolayers consist of amorphous Mo oxide with a Mo oxidation state between Mo^{3+} and Mo^{4+} . The oxidation of the Mo layers generates a reduction of the substrate with the formation of Ti^{3+} and Ti^{2+} and induces a reconstruction of the surface. During the formation of the Mo oxide layers, the roughness of the surface strongly decreases. After the growth of the three layers, the

surface is flat whatever the initial roughness. The resulting islands are metallic (bcc structure) but without a preferential orientation.

4.2.14. Molybdena

The preparation of finely dispersed Mo oxide species, and their characterization with polarization dependent total reflection fluorescence EXAFS has been discussed in several papers [383–390]. A model sample for supported Mo oxide catalysts was prepared by impregnation of $(\text{NH}_4)_6\text{Mo}_7\text{O}_{24} \cdot 4\text{H}_2\text{O}$ dissolved in ultrapure water, followed by calcination at 773 K. The structure and orientation of Mo species are strongly affected by the pretreatment conditions and impurities. Mo dimers oriented to [1 1 0] direction or a Mo chain structure along [0 0 1] are present when they are prepared under oxidative conditions or reductive conditions, respectively. Mo tetrahedral monomers are formed when Na^+ and K^+ are present on the surface.

The deposition of molybdenum oxide monolayers by heating a $\text{TiO}_2(1\ 1\ 0)$ crystal surface covered by MoO_3 powder was also explored and investigated with XPS and electrochemical methods [391]. Deposited Mo films are progressively oxidized when heated at several hundred degrees centigrade, with the stoichiometry depending on the annealing conditions [392].

4.2.15. Manganese

X-ray absorption and photoelectron spectroscopies were used to study the adsorption and reaction of Mn films deposited on $\text{TiO}_2(1\ 1\ 0)$ at 25 °C and after annealing to ca. 650 °C [271]. Fractional monolayer coverages of Mn at 25 °C produce a reactive, disordered interface consisting of reduced Ti cations and oxidized Mn overlayer atoms. The electronic structure of the film resembles MnO , and the Mn L-edge adsorption spectra clearly indicate a Mn^{2+} oxidation state. Metallic Mn is found only for thicker layers. Annealing Mn films to ca. 650 °C leads to several changes that are largely independent of initial overlayer coverage: metallic Mn thermally desorbs leaving only Mn^{2+} ions; interfacial Ti cations are largely re-oxidized to the Ti^{4+} state; and the local order is increased at the interface. The formation of a crystalline ternary surface oxide, MnTiO_x , was proposed to account for these chemical and structural changes [271].

4.2.16. Manganese oxide

Oxygen plasma assisted MBE was used to grow epitaxial films of pyrolusite ($\beta\text{-MnO}_2$, rutile structure) on $\text{TiO}_2(1\ 1\ 0)$ for thicknesses of one to six bilayers (BL) [393]. In this work, one bilayer was defined as a layer of Mn and lattice O and an adjacent layer of bridging O within the rutile structure, see Fig. 6. The resulting surfaces have been characterized *in situ* by RHEED, LEED, XPS, XPD, and AFM. Despite a lattice mismatch with rutile TiO_2 of 3–4%, well-ordered, pseudomorphic overlayers form for substrate temperatures between 400 and 500 °C. Mn–Ti intermixing occurs over the time scale of film growth (ca. 1 BL/min) for substrate temperatures in excess of 500 °C. Films grown at 400–500 °C exhibit island growth, whereas intermixed films grown at temperatures of 500–600 °C are more laminar. One BL thick films grown at 450 °C are more laminar than multilayer films grown at the same temperature, and form a well-ordered surface cation layer of Mn on the rutile structure with at most 10% indiffusion to the second cation layer.

4.2.17. Iron

The first growth study of iron on a $\text{TiO}_2(0\ 0\ 1)$ surface was performed by Brugniau et al. [394]. During growth of the first layer, a decrease in the work function, changes in secondary electron

emission, and changes in Auger features were observed. On $\text{TiO}_2(1\ 1\ 0)$ a layer-by-layer growth mode was reported by Deng et al. [395]. CO was weakly adsorbed on a low Fe coverage system (0.2 ML) and adsorbed strongly to thicker Fe layers.

Low-energy ion scattering measurements from Madey and co-workers [379] showed a cluster growth when iron was deposited at room temperature, although Fe tends to wet the surface better than late-transition metal overlayers, see Fig. 41. A (not very strong) oxidation/reduction reaction occurs at the interface. Complete coverage of the substrate can be reached when a 1 ML film is oxidized by dosing oxygen. UPS measurements indicate a mixed iron-oxide layer composed of FeO and Fe_2O_3 phases [396]. The surface roughness also plays a role in the morphology of the metallic films [379]. Mostefa-Sba et al. [397] observed a 2D growth mode up to three monolayers for a high initial roughness of the substrate.

The orientation of the metal overlayer was determined as bcc(1 0 0)-oriented films with diffraction techniques sensitive to both long-range and short-range order [355]. As is the case for other bcc overlayers (Cr, Nb, and V) the overlayer [0 0 1] direction is aligned with the substrate [0 0 1] direction.

The electronic structure of Fe/ $\text{TiO}_2(1\ 1\ 0)$ was studied with inverse photoemission, UPS [396], and resonant photoemission [262]. As seen in Fig. 46, band gap states are induced by fractional Fe coverages on stoichiometric $\text{TiO}_2(1\ 1\ 0)$ surfaces. The higher lying band gap feature shows the same

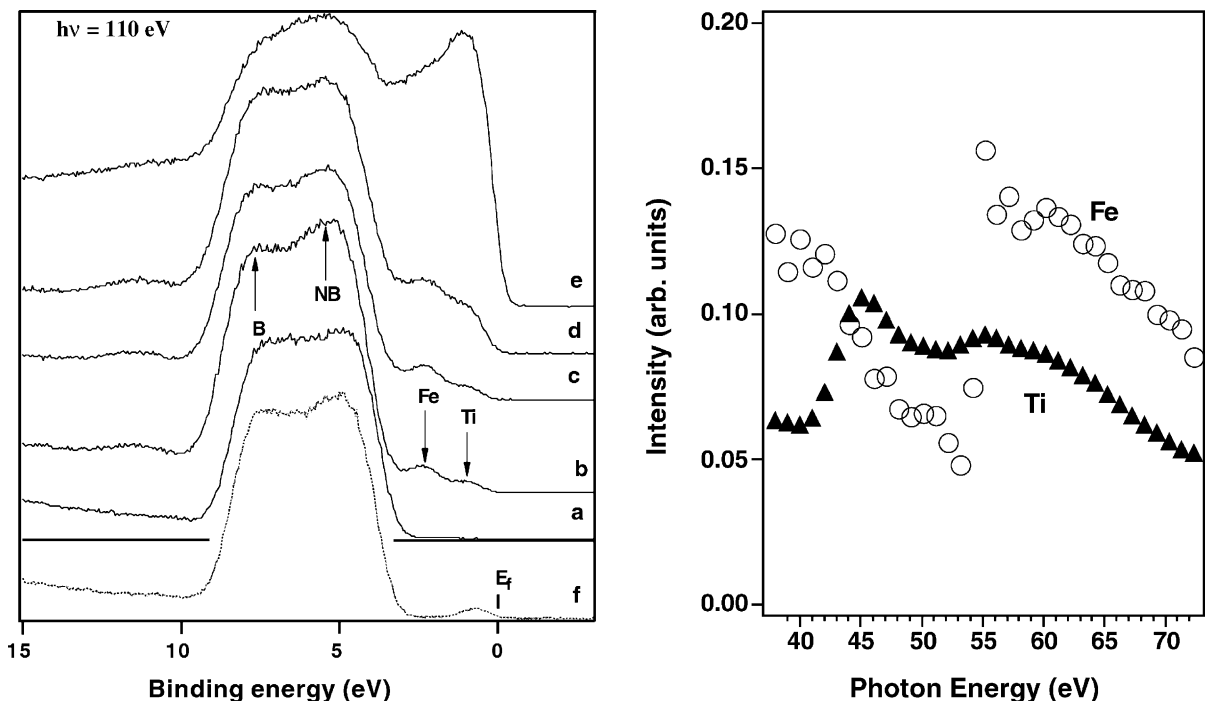


Fig. 46. Left panel: photoemission from the valence band of (a) stoichiometric $\text{TiO}_2(1\ 1\ 0)$ and (b)–(f) after deposition of Fe at room temperature onto a stoichiometric surface. Fe coverages (in equivalent ML) are (b) 0.16 ML, (c) 0.24 ML, (d) 0.4 ML, and (e) 1.3 ML. Spectrum (f) was taken after irradiation of an uncovered, stoichiometric surface with 3 keV electrons. All spectra are taken with a photon energy of 110 eV. Right panel: intensity of Fe3d-derived (circles) and Ti3d-derived (triangles) valence band features from 0.2 equivalent ML Fe on stoichiometric $\text{TiO}_2(1\ 1\ 0)$. The nature of the band gap states can be determined from their behavior in these resonant photoemission curves. From [262].

resonance behavior as an oxygen-vacancy induced Ti3d band gap state. The resonant line shape of the feature at higher energy is very similar to the shape observed for iron oxides [398,399].

After thermal annealing in UHV at 500–700 °C for several hours, Fe clusters are almost completely covered by Ti suboxides TiO_x while Fe remains mainly in the metallic state. The Fe signal disappears in LEIS, and re-emerges after small ion fluences during sputtering [17]. As mentioned above, this encapsulation process (SMSI) is common to all group VIII A metals studied (Fe, Co, Rh, Ir, Ni, Pd, Pt).

4.2.18. Ruthenium

The thermal decomposition of $\text{Ru}_3(\text{CO})_{12}$ has been used as a source for the growth of metallic ruthenium particles and RuO_2 films on a $\text{TiO}_2(1\ 1\ 0)$ surface [400–402]. After adsorption at room temperature and heating in UHV, the precursor completely decomposes at 300 °C. The deposited metal particles show some residual carbon contamination and are disordered, both in the short and long range. The high XPS binding energy found for the metal core levels suggests the presence of nano-clusters on the surface. The titanium atoms of the substrate are not reduced by reaction with the incoming metal atoms. Thermal treatment of the surface at 400 °C forms a $\text{Ti}_{1-x}\text{Ru}_x\text{O}_2$ surface compound [401].

The ‘reverse’ system, Ti and TiO_2 films on $\text{RuO}_2(1\ 1\ 0)$ and (1 0 0) was investigated with XPS, AES, and LEED [403]. RuO_2 also has rutile structure, and epitaxial TiO_2 layers could be achieved at 600 °C. Ru– RuO_x -promoted TiO_2 was shown to be a good catalyst for the selective methanation of CO_2 at room temperature and atmospheric pressures [404].

4.2.19. Ruthenium oxide

RuO_2 is a metallic oxide with the rutile structure and a lattice mismatch with respect to TiO_2 of 4.7 and –2.2% along the [0 0 1] and [1 1 0] directions, respectively. Epitaxial films on $\text{TiO}_2(1\ 1\ 0)$ were grown with oxygen-plasma assisted molecular beam epitaxy (OPA-MBE) in Chambers’ group [289]. Decomposition of $\text{Ru}_3(\text{CO})_{12}$, while heating in an oxygen atmosphere, also results in epitaxial RuO_2 films [400,402]. As mentioned above, the $\text{RuO}_2/\text{TiO}_2$ interface is thermodynamically not stable and prone to intermixing. This has been exploited for growing a ‘graded’ interface, essentially a crystalline stack of the form $\text{RuO}_2/\text{Ru}_x\text{Ti}_{1-x}\text{O}_2/\text{TiO}_2(1\ 1\ 0)$ where x increased with thickness. In this way, a smooth film was achieved [289].

4.2.20. Cobalt

Metallic cobalt and cobalt oxide deposited on oxidized and sputtered $\text{TiO}_2(1\ 1\ 0)$ was investigated by Shao et al. [405]. The Ti2p spectra show a small reduction upon Co deposition at room temperature, and a pronounced Ti^{3+} peak after heating at 900 K. The latter is consistent with other group VIII metals that show the SMSI effect. The doping of TiO_2 (anatase) films with Co has received some interest recently because such films are conductive, ferromagnetic, and optically transparent at room temperature [55]; these properties make it a possible candidate for spintronics applications [56]. In the weakly ferromagnetic films the Co is bound in the lattice in a substitutional form and exhibits in a 2+ oxidation state.

The interaction of aqueous Co(II) species with the (1 1 0) and (1 0 0) surface of rutile has been investigated with grazing-incidence XAFS spectroscopy under ambient conditions in a humid atmosphere [406]. The Co(II) surface complexes adsorbs at sites corresponding to Ti-equivalent positions in an extension of the rutile structure. This result suggests that even if different crystallographic surfaces of metal oxides have strongly differing adsorption properties for gaseous species in ultra-high vacuum, they can have similar properties for adsorption of metal ions in aqueous

solution. No evidence was found for well-ordered Co(II)-hydroxide-like precipitates that would show Co–Co pair correlations, or for Co–Ti pair correlations.

4.2.21. Rhodium

$TiO_2(1\ 1\ 0)$. A series of growth studies on $TiO_2(1\ 1\ 0)$ surfaces was published by Berkó et al. [407–409]. Rhodium was deposited on a $TiO_2(1\ 1\ 0)$ – (1×2) surface at room temperature and investigated with AES and STM. Nucleation of Rh particles occurs at terraces (no step decoration) [407]. At low coverages (0.01 ML), small clusters with ca. 2–6 atoms/cluster were observed, with a preferential location at the bright rows. A slight increase in cluster size was experienced after several hours, even at room temperature. Rhodium deposited on an oxidized Ti foil did not show any evidence of an interfacial oxidation/reduction reaction in XPS [410].

One of the motivations for surface-science studies of the Rh/ $TiO_2(1\ 1\ 0)$ system was to investigate the SMSI state of rhodium-based catalysts. Berkó et al. [408] found in an STM/XPS study that the surface pretreatment influences whether or not encapsulation occurs. A stoichiometric and well-ordered $TiO_2(1\ 1\ 0)$ – (1×1) surface covered by 3 ML of rhodium showed no evidence for encapsulation in the temperature range of 300–800 K in UHV [408]. A few minutes annealing in a H_2 atmosphere of 10^{-4} mbar at 750 K did produce encapsulation with a reduced overlayer. Pretreatment of the stoichiometric $TiO_2(1\ 1\ 0)$ – (1×1) surface by Ar^+ bombardment (creation of surface and subsurface Ti^{3+} states) before Rh deposition resulted in encapsulation of Rh particles after annealing in UHV (in the absence of hydrogen). It was concluded that the presence of lattice defects in the near-surface region is crucial for the SMSI state to form. On oxidized Ti films, monolayer coverages of Rh encapsulate upon UHV annealing around 750 K. Above 820 K, Rh diffuses into the substrate [410].

The encapsulation process between 500 and 700 K results in an increase of the size of clusters at very low Rh coverages (0.01 ML). At higher Rh coverages annealing does not cause appreciable changes in STM images. Annealing >1100 K causes the separation of the 3–5 nm wide and 3–5 atomic-layers thick Rh crystallites (with their $(1\ 1\ 1)$ plane parallel to the substrate), probably due to the de-encapsulation of the Rh crystallites [407].

This thermal behavior was exploited to independently control the particle size and distance of Rh clusters on $TiO_2(1\ 1\ 0)$ – (1×2) [409]. In a ‘seeding’ step, a small amount of Rh (0.001–0.050 ML) was deposited at room temperature and annealed at 1100 K. Further Rh deposition caused growth of the Rh nanoparticles and the formation of a narrow size distribution. The mechanism of this procedure is based on the large difference in the surface diffusion coefficient between Rh adatoms and Rh nanocrystallites larger than 1–2 nm. In the seeding step the average distance between the metal particles is controlled, the second step determines the particle size (2–50 nm). Growth at 1100 K resulted in crystallites with a well-defined shape, either hexagonal or elongated in the $[0\ 0\ 1]$ direction. When these large Rh crystallites (diameter of 10–15 nm) were annealed in H_2 at 750 K, dramatic morphological changes (corrosion or disruption) were observed to accompany the encapsulation process [407].

Highly dispersed rhodium clusters on $TiO_2(1\ 1\ 0)$ were grown with MOCVD [411,412]. A rhodium gem-dicarbonyl species, $Rh(CO)_2$, was prepared by the dissociative adsorption of $\{Rh(CO)_2Cl\}_2$. Desorption of CO at 500 K, or reaction with hydrogen at 300 K, results in the formation of a highly dispersed Rh_x^0 species from which the gem-dicarbonyl can be partially re-generated by exposure to CO. Heating the rhodium overlayer to higher temperatures leads to the nucleation of larger metallic particles from which the gem-dicarbonyl cannot be re-formed by exposure to CO.

$TiO_2(0\ 0\ 1)$. Growth of Rh on $TiO_2(0\ 0\ 1)$ at room temperature also showed 3D particles [413]. The particles showed a narrow size distribution, and coalesced upon annealing.

4.2.22. Iridium

The growth of Ir on $TiO_2(1\ 1\ 0)$ -(1×2) was studied by Berkó et al. [414,415]. At very low coverage Ir forms round nanoparticles which are mainly centered on the rows of the (1×2) terraces. Annealing of the iridium covered surface caused an perceivable increase of the particle size only above 700 K. The supported iridium nanoparticles of 1–3 nm exhibit a very high reactivity towards CO. As a result of the CO adsorption at 300 K, crystallites disrupt into smaller particles, and finally into atomically dispersed Ir. This feature was not observed for larger clusters of 8–10 nm size. Similar to the Rh/ $TiO_2(1\ 1\ 0)$ -(1×2) system, a method was developed to synthesize Ir nanoparticles in desired uniform sizes in the range 1.5–20.0 nm with constant interparticle distances [414]. The method consists of two steps: (i) vapor deposition of Ir metal in predetermined concentrations on titania at 300 K with a post-deposition annealing at 1200 K, and (ii) subsequent evaporation of Ir on this surface at 1200 K.

4.2.23. Nickel

$TiO_2(1\ 1\ 0)$. The growth of nickel on $TiO_2(1\ 1\ 0)$ was investigated with spectroscopic methods [416–421], and, more recently, with STM [422] and computational approaches [423].

Based on AES measurements, a S–K growth mode was postulated [417,419]. A first-principles study of the initial stages of Ni growth [423] indicated that Ni adsorbs preferentially on top of bridging oxygen atoms and that the bond strength between Ni adatoms and the substrate is much stronger than between Ni adatoms. EXAFS experiments on Ni/ $TiO_2(1\ 1\ 0)$ also indicated only two-dimensional (2D) growth of Ni [421]. A model was developed with Ni atoms forming chains in the channels determined by O atoms. However, more recent STM images clearly indicate a cluster growth at low coverages, in line with thermodynamic expectations [422]. At low coverages, the clusters appear round-shaped in STM, and substrate step edges act as nucleation sites at very low coverages. At higher coverages, the clusters expose well-defined facets.

Differing results on overlayer geometry are reported as well. XPD measurements indicated both, ($1\ 0\ 0$)- and ($1\ 1\ 1$)-oriented islands [417], and a LEED study was interpreted as hexagonal, ($1\ 1\ 1$) oriented islands, both parallel to $TiO_2(1\ 1\ 0)$ and tilted [418]. ‘Hut-clusters’ with the base consisting of ($1\ 1\ 0$)-oriented layers have been observed with STM and RHEED. The long and short sides of the ‘huts’ consist of $\{1\ 1\ 1\}$ - and $\{1\ 0\ 0\}$ -oriented facets [422].

Electron transfer from Ni to the substrate in the order of ca. $0.1e^-/Ni$ atom was estimated from spectroscopic measurements [416,417]. Electron donation of 0.37 and $0.27e^-/Ni$ atom to the bridging and in-plane oxygen atoms was calculated by Cao et al. [423]. At fractional monolayer coverages the charge transfer causes a decrease in work function, band bending, and a shift in XPS and AES levels.

A decrease in the XPS signal upon annealing was interpreted as diffusion of Ni into the substrate [416]. STM shows coalescence and coarsening of Ni clusters on $TiO_2(1\ 1\ 0)$ up to a temperature of 880 K, the morphology is stable above this temperature [422].

The adsorption of CO on Ni/ $TiO_2(1\ 1\ 0)$ films was studied by Onishi et al. [417] and in Møller and Wu [419]. CO adsorbs molecularly at all coverages. When a Ni film on $TiO_2(1\ 1\ 0)$ was exposed to air, it transformed into an epitaxial NiO overlayer. Reduction in UHV re-gained crystallographic spacings indicative of metallic Ni, but a NiO layer at the interface was postulated to account for the orientation of these clusters [422].

$TiO_2(1\ 0\ 0)$. Nickel deposition on $TiO_2(1\ 0\ 0)$ was studied by Bourgeois et al. [424–426]. The results were interpreted in terms of a S–K type growth mode with three nickel layers completed before clustering starts.

4.2.24. Palladium

$TiO_2(1\ 1\ 0)$. The growth of Pd/ $TiO_2(1\ 1\ 0)$ was investigated with STM [162,297,346,427–429] and spectroscopic techniques [10]. The growth mode is undoubtedly VW-like. When depositing at room temperature, the cluster size increases with coverage [162]. A marked tendency for nucleation of Pd clusters at step edges was observed, similar to the case of Ni growth. The nucleation and cluster site is influenced by the defect concentration, however, with more random distribution across the surface on a highly defective $TiO_2(1\ 1\ 0)$ surface [297]. From STM images at low coverages, nucleation at the fivefold coordinated Ti site was deduced [162]. A quantum-chemical DFT study modeled the Pd/ $TiO_2(1\ 1\ 0)$ system with Pd atoms and dimers adsorbed on TiO_2 clusters embedded in point charges [430]. In this theoretical study the preferred adsorption for Pd was on the bridging oxygen atoms for small coverages, and along the Ti rows for higher coverages. Pd forms a covalent bond, slightly polarized towards the surface, but without significant charge transfer. In the calculations, Pd dimers were not stable due to the strong bond with the substrate [430]. However, features in STM images were interpreted as dimers and trimers [162].

The geometry of thin films of Pd deposited on the $TiO_2(1\ 1\ 0)$ surface were investigated using coaxial impact-collision ion scattering spectroscopy (CAICISS) and RHEED [431]. Palladium islands in the range from 5 to 40 Å grew epitaxially on the TiO_2 surface with the orientation relationship of fcc $[1\ \bar{2}\ 1](1\ 1\ 1)||[0\ 0\ 1](1\ 1\ 0)TiO_2$. This orientation relationship was observed in the temperature range from room temperature to 1170 K. Clusters with predominantly $(1\ 1\ 1)$ orientation would be in agreement with the general trend for noble metal growth on $TiO_2(1\ 1\ 0)$, however, other orientations have been suggested for very small coverages (see below).

The thermal behavior of Pd was investigated by several groups. An STM study by Stone et al. [427] observed aggregation of the overlayer clusters, as well the formation of a (1×2) overlayer on the substrate after annealing to 773 K. This is supported by an STM study from Frenken and co-workers [429]. The decrease of the Pd intensity in AES was interpreted as due to sintering rather than encapsulation [427]. LEIS experiments in Persaud and Madey [10] showed encapsulation. A simultaneous appearance of a (2×1) superstructure and the encapsulation of the Pd islands was found after annealing at 1170 K in UHV by ion scattering techniques [431]. In the process of encapsulation, the crystal structure of the Pd islands remained unchanged. This suggests that the encapsulating material is transported by surface migration on the Pd particles. Heating in an O_2 atmosphere of 5×10^{-5} Torr did not remove the encapsulating material. Evidence for encapsulation upon annealing Pd/ $TiO_2(1\ 1\ 0)$ to 800 K in UHV was also found in an adsorption experiment [432]. Similarly conflicting results were found for Pt, where some research groups reported encapsulation upon UHV annealing, and others did not observe this effect. Possibly, these conflicting results could be resolved similarly as in the case of Pt (see below), and the reduction state of the sample could be a decisive factor on whether or not encapsulation occurs.

Heating as-deposited Pd clusters in oxygen has dramatic effects as observed in a high-temperature STM study by Bennett et al. [19,172]. The Pd nanoparticles on sub-stoichiometric $TiO_2(1\ 1\ 0)$ dissociatively adsorb O_2 at 673 K which “spills over” onto the support where further reaction takes place. The spillover oxygen re-oxidizes the surface by removing Ti^{n+} interstitial ions trapped in the

crystal lattice, preferentially re-growing TiO_2 around and over the particles. This process is similar to the surface restructuring in an oxygen atmosphere described in [Section 2.2.2.2](#), and was modeled in [\[433\]](#).

The adsorption of CO, and the corresponding bands in FT-RAIRS, was used to identify the orientation of the Pd cluster sides [\[434\]](#). STM work in Goodman and co-workers [\[162\]](#) confirmed that CO adsorption itself does not change the morphology of the clusters, although a CO background pressure during deposition did change the nucleation behavior. In the vibrational study of CO/Pd/ $\text{TiO}_2(1\ 1\ 0)$, at small coverages the Pd surfaces appeared to be constituted of mainly (1 0 0)- or (1 1 0)-type sites. When annealed to 500 K, the Pd clusters coalesce and CO adsorbs predominantly as a strongly bound linear species which was associated with edge sites on the Pd particles [\[434\]](#). At coverages above 10 ML, the palladium particles exhibit (1 1 1) facets parallel to the substrate and aligned with the $\text{TiO}_2(1\ 1\ 0)$ unit cell, as was also observed by other researchers. This ordering in the particles is enhanced by annealing. The sintering process of Pd clusters at high temperatures was also observed directly with STM [\[162,428\]](#). Theoretical results of CO/Pd₂/ TiO_2 (cluster) indicate that polarization effects cause the CO molecule to be less strongly bound as compared to a free Pd₂ dimer [\[430\]](#).

Adsorption of formic acid on Pd-promoted $\text{TiO}_2(1\ 1\ 0)$ was studied with HREELS [\[432\]](#). In general, group VIII metals dissociate formic acid, and observed bands of formate species were attributed to adsorption at the bare areas of the substrate (see [Section 5.2.1](#)). Additional C–O species correspond to CO bound to the Pd clusters, and to CO and HCO at the cluster perimeters.

$\text{TiO}_2(1\ 0\ 0)$. On the $\text{TiO}_2(1\ 0\ 0)$ -(1 × 3) surface, STM clearly revealed VW-like cluster growth [\[435\]](#). At a coverage of 0.01 ML-equivalent, 35 Å wide and 8 Å high clusters were observed. At higher coverage the clusters coalesce. They do not order within the troughs ([Fig. 23](#)) of the (1 × 3)-reconstructed surface.

4.2.25. Platinum

Platinum is one of the most studied metal overlayers on single-crystalline TiO_2 . The interest has been stimulated by the promotion effect of Pt in photocatalysis ([Section 5.3](#)), its use as an oxygen gas-sensor system, and by the fact that it is the classic SMSI system.

$\text{TiO}_2(1\ 1\ 0)$. As other late-transition metals, platinum does not cause an oxidation/reduction reaction at the interface, and the growth mode at room temperature is clearly VW-like on $\text{TiO}_2(1\ 1\ 0)$ and all the other faces studied [\[18\]](#). Nucleation on the fivefold coordinated Ti atoms was inferred from experimental and theoretical results [\[72,436\]](#). The growth and nucleation behavior on (1 × 1) and (cross-linked) (1 × 2) $\text{TiO}_2(1\ 1\ 0)$ surfaces was compared in a recent STM study [\[437\]](#). On the (1 × 1) surface, clusters nucleate randomly on terraces with no apparent preferred nucleation site. On the (1 × 2) surface, however, they grow preferentially on top of the bright rows in STM. These clusters are also thermally more stable than on the (1 × 1) surface. On vicinal surfaces with co-existent (1 × 2) and (1 × 1) termination, Pt clusters attach mostly to the end of the (1 × 2) rows [\[437\]](#). The interaction of Pt with the reduced Ti at the (1 × 2) surface (assumed was the added row structure in [Fig. 18c](#)) is thought to account for changes in the nucleation behavior [\[437\]](#).

The electronic structure of Pt-modified $\text{TiO}_2(1\ 1\ 0)$ -(1 × 1) surfaces was mapped out with photon energy-dependent and angular-resolved photoelectron spectroscopy [\[438\]](#). UPS measurements indicate no substantial hybridization between Pt and TiO_2 states, and very little charge transfer on stoichiometric surfaces [\[72\]](#). Electronic charge transfer was found between the Ti^{3+} ions of pre-reduced surfaces and

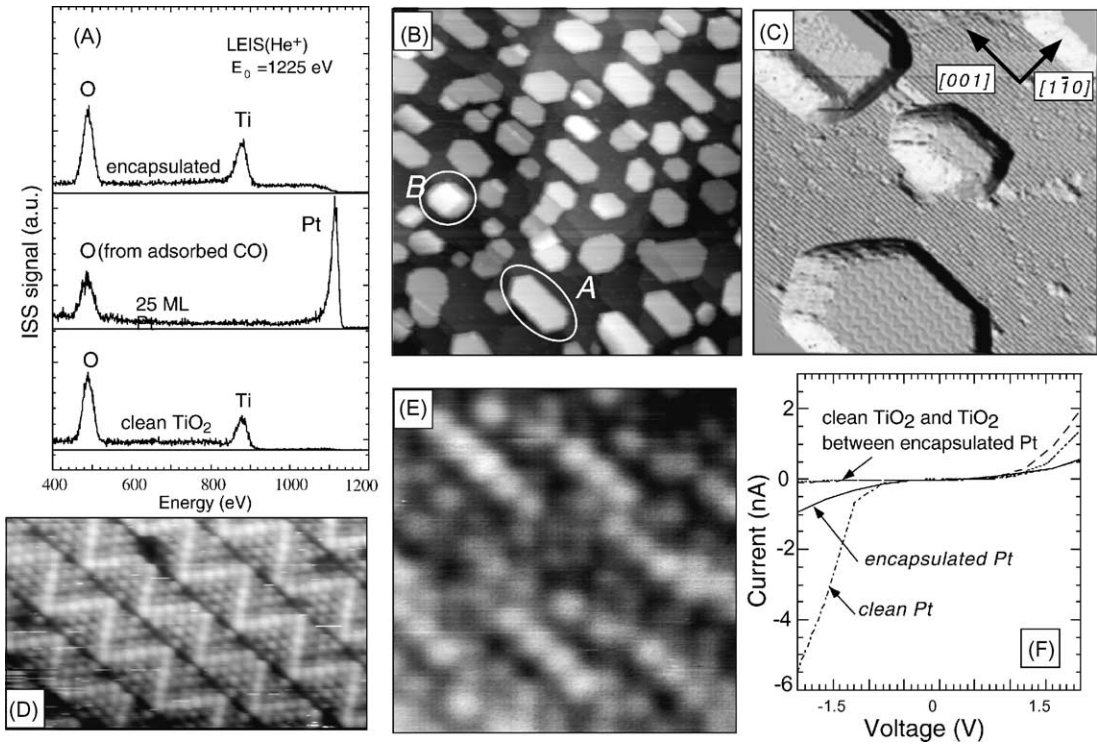


Fig. 47. Experimental results on an SMSI model system, Pt/TiO₂(1 1 0). (A) Low-energy He⁺ ion scattering (LEIS) spectra of (bottom) the clean TiO₂ (1 1 0) surface, (center) after evaporation of 25 ML Pt at room temperature, and (top) after high-temperature treatment caused encapsulation. (B)–(F) STM and STS results after the high-temperature treatment. (B) Overview (2000 Å × 2000 Å). Clusters are approximately 200 Å wide and 40 Å high. Most clusters show hexagonal shape elongated along the substrate [0 0 1] direction (type A). A few square clusters (type B) are seen. (C) Small-scale image (500 Å × 500 Å), filtered to show the structure of the encapsulation layer and the substrate. (D) Atomic-resolution image of an encapsulated hexagonal ‘type A’ cluster. (E) Atomic-resolution image of a square ‘type B’ cluster, showing an amorphous overlayer. (F) STS of the different surfaces. From Dulub et al. [20]. © 2000 The American Physical Society.

Pt [72]. The electrical properties of Pt/TiO₂(1 1 0) were also investigated [439], and the formation of a Schottky barrier was deduced from STS *I*–*V* curves.

Electron scattering techniques showed that the Pt clusters grow with their (1 1 1) face parallel to the substrate [18,440]. Mild annealing causes a sintering of the Pt particles. However, while STM images of annealed Pt clusters show that the majority of clusters are quasi-hexagonal (with an elongation along the [0 0 1] direction probably caused by diffusion effects), a minority of square clusters was also observed (Fig. 47). These probably have their (1 0 0) face parallel to the TiO₂(1 1 0) substrate.

Low-energy ion scattering experiments clearly show that UHV annealing at higher temperature causes encapsulation (Fig. 47A), and glancing-exit XPS identified the layer as highly reduced with (probably) Ti²⁺ species present [18]. No evidence for encapsulation was found in a study that employed very similar techniques [72]. In a convincing experiment by Chambers’ group it was shown that the reduction state of the substrate influences whether or not heat-treatment leads to an encapsulation of the Pt overlayer. On stoichiometric Nb-doped TiO₂(1 0 0) films, no encapsulation was observed. Platinum overlayers on conventionally reduced TiO₂ substrates did encapsulate at similar temperatures [190].

The overlayer in the SMSI state was imaged successfully with STM by Dulub et al. [20,71], see Fig. 47B–E. Most clusters (type A) have a hexagonal shape elongated along the substrate [0 0 1] direction and are, on average, 40 Å high and 200 Å wide. A few have a square shape (type B). Those are smaller. A simple calculation (taking into account the deposited amount of Pt (25 ML), the surface coverage after encapsulation ($\sim 40\%$), and the cluster height) shows that the clusters resemble ‘icebergs’ reaching several tens of Ångstroms deep into the substrate. The 500 Å \times 500 Å large image in Fig. 1c is filtered to visualize the 3D structure of the encapsulated clusters and the substrate. The tops of the clusters are smooth and flat, which is essential for atomically resolved STM measurements. (The Pt particles remind of the ‘pillbox’ shape observed in HREM images of a catalyst in the SMSI state [441].) On top of the type A clusters, striped ‘zigzags’ are visible. On different clusters the stripes are oriented either parallel to the substrate [0 0 1] direction or rotated by $\pm 60^\circ$. No clear preference for any rotational orientation was observed, nor a strict correlation between the directions of stripes and cluster elongations. Fig. 47D is an atomically resolved image of a type A cluster surface. The stripes are approximately 15 Å wide and consist of bright spots arranged in a hexagonal symmetry with a distance of 3 Å. The bright zigzag rows contain either 5 or 6 atoms along the close-packed directions and separate triangular areas consisting of 10 atoms. Surfaces of type B square clusters exhibit no apparent long-range order (Fig. 47E) with strings of 3–6 atoms oriented along the substrate [0 0 1] direction. The ‘type B’ clusters are probably crystallites with their (1 0 0) face parallel to the substrate. It is conceivable that such surfaces should be found at the sides of the hexagonal, (1 1 1)-oriented ‘type A’ clusters. STM current vs. voltage (I - V) curves have been taken from the clean sputter-annealed $\text{TiO}_2(1\ 1\ 0)$ surface, from $\text{TiO}_2(1\ 1\ 0)$ between encapsulated clusters, and from clusters of clean and encapsulated Pt (Fig. 47F). There is almost no difference in the I - V curves from clean TiO_2 and from TiO_2 between encapsulated clusters. The electronic structure of the substrate is not strongly affected by the encapsulated clusters. The electronic structure of the clusters changes from those typically observed for small metal clusters on TiO_2 [162] (“clean Pt”) to a more semiconductor-like behavior after encapsulation.

An atomic model of the zigzag structure in Fig. 47C was proposed in [20] and refined with DFT calculations in [302]. It consists of a TiO_x bilayer film on $\text{Pt}(1\ 1\ 1)$. The preferred interface with Pt has Ti with O as an overlayer that stays under considerable stress. It consists of a series of linear misfit dislocations at the relatively weak Ti/Pt interface that are 6/7 Ti/Pt rows wide. In addition, strong interactions at the O/Ti interface and O-layer strain also cause the Ti/Pt interface to abruptly change from hcp- to fcc-site Ti, producing linear dark stripes in Fig. 47C. Alternating hcp- and fcc-site triangles, each with 10 O-atoms, are separated by bridging O in an abrupt O/Ti misfit dislocation, thus producing a zigzag pattern. However, in the computations this structure is only stable if the corners of the zigzag consist of Ti atoms instead of O atoms. While filled-state STM images indicate the ends might be different than the line portions of the zigzag features, firm experimental evidence for such single Ti atoms is not yet available.

Adsorption of CO modified the growth of metallic Pt clusters, with more ‘wetting’ when evaporation was performed in a background of CO [442]. The substrate structure, i.e. (1 \times 1) vs. (1 \times 2) termination, was found to be influential for the surface chemistry of supported Pt clusters [437]. The adsorption of H_2O on model clusters was investigated using the Gaussian 90 (ab initio) program [443], and Pt was found to promote the H_2O adsorption process and hole trapping. However, experimentally an enhancement in the CO photo-oxidation reaction rate or yield is not observed in the presence of Pt metal clusters on the $\text{TiO}_2(1\ 1\ 0)$ surface [444] under UHV conditions.

TiO₂(1 0 0) and (0 0 1). The modification of TiO₂(1 0 0)-(1 × 3) surfaces was studied in a series of papers by Schierbaum et al. [445]. Photoemission spectroscopy of the as-evaporated film indicated the presence of small Pt clusters. The position and intensity of the Ti³⁺ feature of the (1 × 3) surface (see Section 2.3.2) was not altered significantly, and electronic charge transfer was virtually absent. Angle-resolved XPS measurements indicated a (1 1 1)-oriented overlayer. For (0 0 1)-oriented substrates the modulations in the XPD pattern were too weak for a reliable structural analysis.

Anatase (0 0 1)-(1 × 4). On the highly corrugated anatase (0 0 1)-(1 × 4) surface, Pt forms 3D clusters with a narrow size distribution on the terraces. Interestingly, Pt clusters migrated along the rows without coalescing to step edges via a cluster diffusion mechanism upon annealing in vacuum. Time-dependent autocorrelation analysis revealed that the diffusion occurred preferentially along the atomic rows [446].

4.2.26. Copper

The growth mode of Cu is clearly VW-like, as seen in LEIS measurements [447] and, more recently, STM [159,295]. 3D islands nucleate preferentially at step edges, with some nucleation occurring also at the terraces of the (1 × 1) surface [295], see Fig. 48. The islands have a narrow size distribution in the coverage regime displayed in Fig. 48, and the density rather than the island size increases with coverage. For higher coverages, the islands grow mainly in height. The apparent limitation on the island sizes for coverages below 0.5 ML is referred to as ‘self-limiting’ island growth by Chen et al. [295], and two possible explanations were proposed to account for this effect. In one case the rate at which

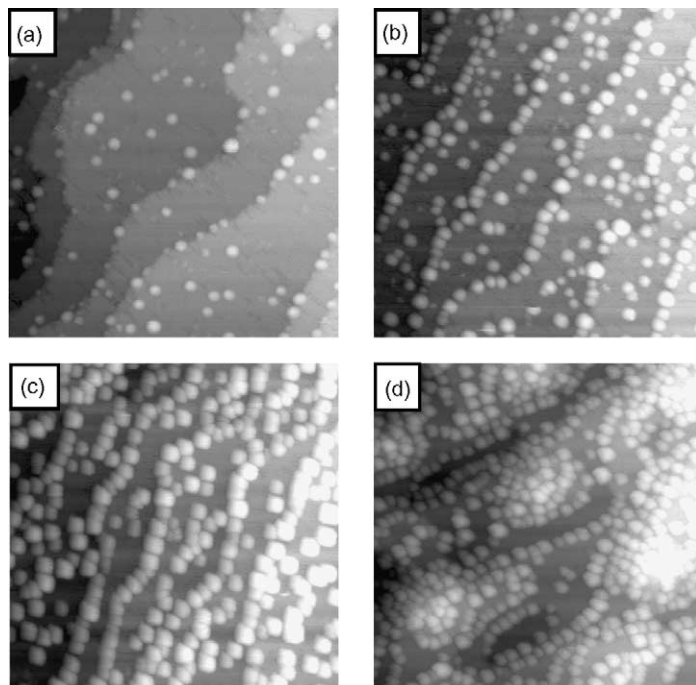


Fig. 48. STM images (1000 Å × 1000 Å) for various Cu coverages on TiO₂(1 1 0)-(1 × 1), dosed at room temperature: (a) 0.03 ML, (b) 0.13 ML, (c) 0.25 ML, and (d) 0.5 ML. The islands nucleate preferentially at step edges. From Chen et al. [295]. © 2000 Elsevier.

adatoms *attach* to existing islands drops rapidly as the island size increases. It was speculated that this could be due to strain fields that accommodate the lattice match between Cu and TiO₂(1 1 0). Adatoms rejected by the islands are then available for new islands. Alternatively, the rate at which adatoms reach existing islands drops rapidly as the Cu coverage increases; possibly due to continued nucleation of islands at defects at the TiO₂ surface.

Because of the high mobility of Cu on TiO₂, aggregation was even observed at low temperatures [447]. A lower bound for the diffusion constant of 4×10^{-20} cm²/s was estimated [295]. After evaporation on a hot surface, or after annealing of films deposited at room temperature, only 3D islands were observed with STM. These islands were much larger, were still mainly located at step edges, and exhibited a more regular, faceted shape. Again a self-limiting behavior was observed, but with the island size depending on temperature. The temperature-dependent growth morphology of Cu films on TiO₂(1 1 0) was also studied by Carroll et al. [448].

Thicker Cu films exhibit a (1 1 1) orientation on TiO₂(1 1 0) [447,449,450]. Detailed HREM images of the interface were given in [450]. Atomically sharp interfaces with no misfit dislocations were observed. The ⟨1 1 0⟩ direction of the Cu overlayer is aligned with the substrate's [0 0 1] direction. The overlayer is commensurate with [1 1 0] but incommensurate with [0 0 1]. Two equivalent domains, rotated by 180°, are possible and were observed experimentally [379,450]. They give rise to {1 1 1} stacking faults and microtwins which may occur as a result of coalescence of 3D islands with increasing film thickness. The structure of small Cu clusters was tested with FT-RAIRS with CO as a probe molecule. Two principal IR absorption bands at 2071 and 2094 cm⁻¹, corresponding to CO adsorption on Cu(1 1 1)-like and Cu(1 1 0)-like sites, were found [451].

The geometry of the interface was studied with SXRD [107]. Compared to an uncovered TiO₂(1 1 0) surface (Fig. 7, Table 3), the Ti atoms de-relax to their bulk-terminated positions. Large vertical and lateral displacements of oxygen atoms were observed, suggesting significant bonding between Cu and O.

Despite this interaction between O and Cu, no sign of an overlayer oxidation/substrate reduction was observed with photoemission and inverse photoelectron spectroscopy [396,447]. The height of Cu clusters in STM varied with the applied bias voltage [448]. This effect was used to quantify height variations in the Schottky barrier formed between Cu and TiO₂. A Cu overlayer surface state was found in angle-resolved photoemission spectroscopy for a 17 Å thick Cu film [452]. Compared to a Cu(1 1 1) surface this Shockley state was broadened and shifted and it exhibited a noncircular E vs. k_{\parallel} dispersion around Γ . The energy shift was interpreted as an effect of the surface step density while the k_{\parallel} asymmetry was attributed to the state to the nature of the overlayer growth which is only commensurate with the substrate along the GM Brillouin zone direction.

4.2.27. Silver

The growth of Ag clusters was unequivocally determined as 3D island growth on TiO₂(1 1 0)-(1 × 2) and (1 × 1) surfaces [308,453–456]. (Based on LEIS measurements, a 2D island growth was inferred for deposition of Ag at 125 K [457].) The islands nucleate along step edges on both surfaces rather than at flat terrace defect sites. For the same coverages, the silver clusters are bigger than Cu [456]. This is in agreement with the smaller affinity of Ag towards oxygen as compared to Cu (see Table 5) which implies a weaker interaction with the substrate. The cluster density is larger on the (1 × 2) surface and the cluster diameter and height is smaller than on the (1 × 1) surface. No chemical reaction was observed for neither a stoichiometric nor slightly sputtered surfaces, but XPS showed a strong peak

shift for very small clusters. According to the STM measurements of Chen et al. [456], Ag clusters deposited at room temperature are remarkably stable upon annealing to 900 K. When the Ag overlayer was deposited at 100 K, strong sintering effects occurred upon annealing to 300 K [453]. Ostwald ripening was also shown to occur upon exposure of 10 Torr O₂ at room temperature [308].

4.2.28. Gold

Supported Au catalysts can oxidize molecules such as CO at, or even below, room temperature. This is all the more surprising as neither flat Au nor TiO₂ by themselves are particularly active for CO or O₂ adsorption. On TiO₂(1 1 0) CO adsorbs on only weakly and oxygen molecules show a strong interaction only with defects (see Section 5.1). The seminal work by Haruta et al. [458,459] on Au-based catalysts for combustion of CO as well as a variety of other low-temperature oxidation and hydrogenation reactions, has stimulated quite some interest in this area. The reader is referred to two review articles, one on catalysis on gold by Bond and Thompson [460], and a second one on the growth, interactions, structure, and chemistry of gold deposited on TiO₂(1 1 0), recently published by Cosandey and Madey [294]. The in depth-description in these articles goes beyond the summary provided here.

It is now clear that for catalytic activity:

- (1) Au must be present in the form of small particles (generally with a diameter of <5 nm, with smaller clusters being more active, but there appears to be a minimum size for activity).
- (2) The Au clusters must be on the right kind of support (in the beginning it was thought that a reducible metal oxide such as TiO₂ or Fe₂O₃ is necessary, but in the meanwhile other supports such as SiO₂, MgO, or ZrO₂ have shown to be appropriate as well).
- (3) The preparation technique plays a big role, with ‘deposition–precipitation’ (a precursor to the Au is brought out of solution in the presence of a suspension of the support which acts as a nucleation agent) being primarily employed by the Haruta group and leading to a catalyst with small, active Au clusters.

The interrelated issues (1)–(3) raise a number of questions. For example, the fact that the clusters need to be small has several consequences. They certainly contain a number of Au atoms in undercoordinated sites, i.e., at edges and corners, and these special Au atoms might be relevant for activation of oxygen. (There seems to be an agreement that O₂ activation is the rate-limiting step for CO activation, with CO adsorbing/desorbing reversibly from both the Au cluster and the support.) A ‘quantum size effect’ might be important, i.e., the clusters are so small that do not exhibit metallic character which can influence the chemical reactivity [461]. The substrate does play a crucial role for activity, but it is unclear which one. It is surmised that the periphery between the Au cluster and the support is especially active, or that the substrate itself (e.g. defects on TiO₂) activate the O₂ that then migrates to the interface [462]. Also, the interaction with the substrate could change the lattice constant of Au, resulting in a strained lattice. In a related work on size-selected Au clusters on MgO [463], it has been pointed out that the Au clusters are slightly negatively charged and are most active when adsorbed on an F center.

Some of these questions are hoped to be addressed with the model system at hand, i.e., Au deposited on TiO₂(1 1 0) under UHV conditions. The growth of the metal overlayer is now well understood [464], and the (average) morphologies that evolve upon deposition at room temperature are schematically

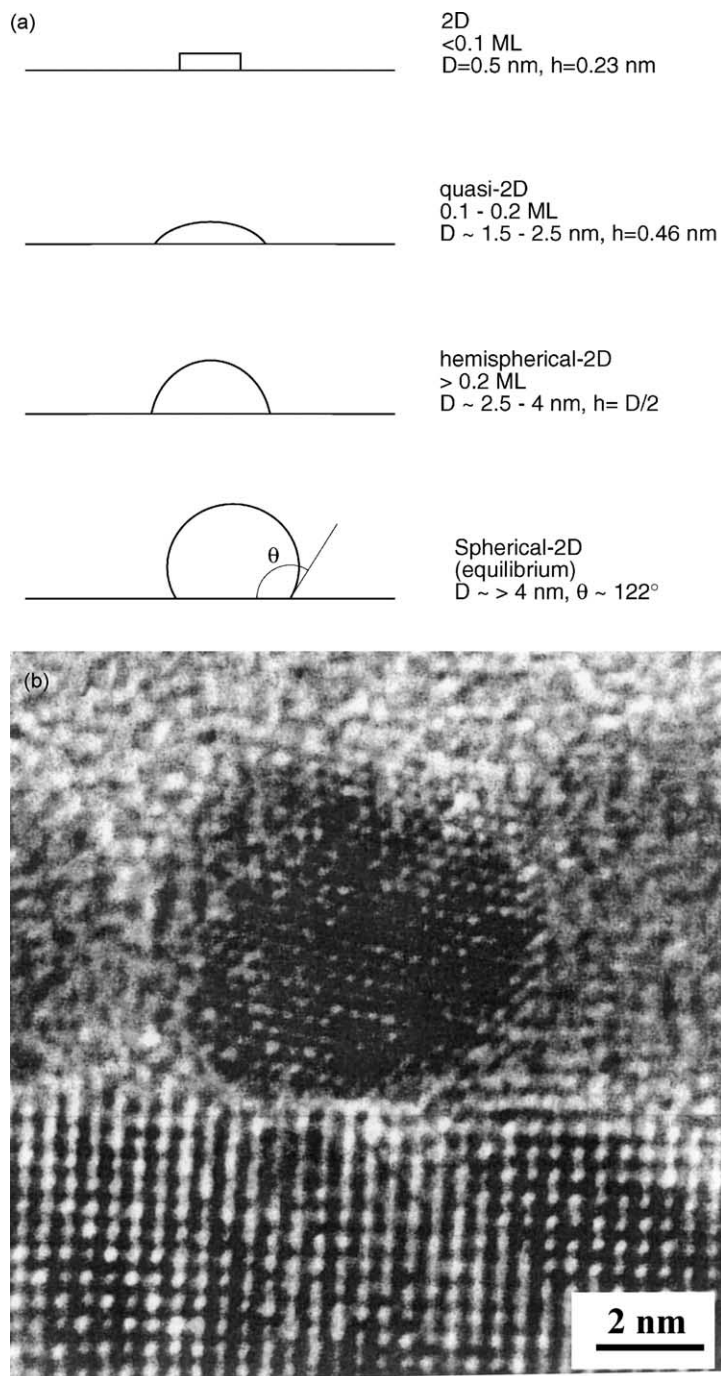


Fig. 49. (a) Schematic representation of the change in Au cluster morphology as a function of Au coverage on $\text{TiO}_2(1\ 1\ 0)$, from [464]. (b) HRTEM image of a Au cluster viewed in cross-section formed after UHV deposition of 1 nm Au on $\text{TiO}_2(1\ 1\ 0)$. The cluster has a truncated spherical shape with a small contact area and a large contact angle. The cluster size is ca. 5.8 nm. From Cosandey and Madey [294]. © 2001 World Scientific.

summarized in Fig. 49a. Very small coverages of Au show ‘true’ 2D growth, i.e., one-layer high, small islands, with nucleation at the Ti(5) sites and defects. The kinetic limitations during growth result in a ‘quasi-2D’ morphology, with two-layer high clusters. The critical coverage for this morphology, given in Fig. 49a, changes somewhat with temperature. These 2D clusters do not bind CO at room temperature, at least not much [464]. They are also not active for O₂ adsorption, but atomic oxygen is bound stronger [23] on 2D than on thicker clusters. Under these conditions, the oxidation of CO on this model system is very rapid at room temperature [23]. Such quasi-2D clusters are not yet metallic, as shown in an STS measurement by Goodman and co-workers [22]. In accompanying high-pressure studies this model system was active for CO oxidation, and the activity was related to the size of the band gap [22]. (These measurements, while suggestive to provide some of the answers to the above questions, should nevertheless be taken with some caution, as STS measurements of clusters on semiconductors are not easy to interpret.) XPS shifts of the 4f levels in the very initial stage (2D islands, <0.1 ML) are interpreted as final-state screening effects. As expected (Section 4.1.1), the shape of the substrate core levels is not changed, but some band bending (downward) during this initial stages of growth has been attributed to charge transfer from the cluster to the substrate [465]. It should also be pointed out that sometimes a shoulder that is present in XPS Au 4f levels of ‘real’ catalysts. However, the absence of this, possibly oxidized, Au in the model system might not be of too much relevant, since it is present in activated as well as deactivated catalysts, and since UHV-deposited Au/TiO₂(1 1 0) does show catalytic activity.

When more Au is deposited at room temperature, the Au clusters assume a hemispherical shape. Thicker layers show a worm-like percolation network. Upon annealing, clusters irreversibly change to an equilibrium shape which is quasi-spherical for smaller clusters (Fig. 49b) and faceted for thicker ones [24,294,306,465]. The cluster depicted in Fig. 49b might give an idea of the shape of an active particle. It is of about the right size range (a mean cluster diameter of 2–3 nm is quoted for optimum activity [460], but there is always a range in size distribution). The more hemispherical clusters in an annealed Au overlayer might be more relevant as model systems, as catalysts are typically calcinated (i.e. annealed) in air at elevated temperature after impregnation. Also, STM investigations at elevated pressures and temperature were performed recently by Kolmakov and Goodman [309,310], and change in cluster size was found for both, oxygen and CO background pressures, which also indicates that clusters will resemble more such an equilibrium shape rather than a (quasi)-2D island. However, there is an emphasis on ‘strong interfacial bonding’ between Au and the support that is necessary for a high activity. Just what this strong bonding might be, and how it would affect the particle shape, is unclear. Cosandey et al. [464] have analyzed HRTEM images of UHV-deposited Au clusters on TiO₂(1 1 0) and have found a (positive) interfacial energy that ranges around 900 mJ/m², depending on the size of the cluster and analysis technique used.

The epitaxial relationship between Au and rutile TiO₂(1 1 0) was mapped out by the same group [306,464]. Two kinds of orientation for (thicker) clusters have been found. In the first one the Au(1 1 1) layer is in direct contact with the TiO₂(1 1 0) substrate. The close-packed Au[$\bar{1}$ 1 0] direction is parallel to the substrate [0 0 1] direction, with a lattice mismatch of 2.6%. The perpendicular direction has a high lattice mismatch of 14.3%. This mismatch is reduced in the second configuration, where Au(1 1 2) is parallel to the TiO₂(1 1 0) substrate, again with [$\bar{1}$ 1 0]_{Au} parallel to [0 0 1]_{TiO₂}, but a better fit (mismatch of 8.4%) in the perpendicular direction. The epitaxial relationship between Au and anatase is described in [466]. Clearly, the Au particles are somewhat strained, but since this mismatch is expected to be different on different substrates, it might not be a major cause for the

change of Au from a noble metal in bulk form to a catalytically active material when present as a supported cluster.

As mentioned before, the metal/support interaction is subject to much speculation. On $\text{TiO}_2(1\ 1\ 0)$ there is some indication from STM studies that the clusters nucleate at defect sites [467]. These might anchor the clusters more firmly to the substrate, but could also provide some excess charge to render more anionic Au [468]. A recent photoemission study showed that $\text{TiO}_2(1\ 1\ 0)$ -supported Au clusters are active for SO_2 adsorption [469] and DFT calculations indicated that the Au could ‘attract’ the bulk defects in the reduced substrate towards the surface. This is an intriguing idea and it would be good if it were backed up with other experiments.

As pointed out in [294,460] a whole range of unanswered questions exists. For example, how does the cluster/substrate interface look like? What are the exact atomic positions? Can a system be prepared that mimics the active catalyst? What about anatase substrates? What is the role of bulk/surface defects for preparation of the catalyst and during the reaction? Are the clusters charged? Is their surface actually amorphous under reaction conditions [460]? What is the catalytically active state of oxygen? Some of these questions could possibly be addressed with a more in depth investigation of Au on single-crystalline TiO_2 surfaces, ideally hand-in-hand with high-pressure studies on model systems as well as real catalysts.

4.3. Conclusion

The number of papers published on metal overlayer growth on TiO_2 is truly impressive. Virtually all the 3d and 4d transition metals, all alkalis, and aluminum have been studied, and the most important materials of the 5d metals as well (Fig. 39, Table 6). (Interestingly, no studies of lanthanides or actinides on single-crystalline TiO_2 surfaces have been performed, at least not to this author’s knowledge.) It is intriguing that, with very few exceptions, all experimental investigations show a clear trend across the periodic table. Metals can be roughly classified in ‘non-reactive’ ones where no interfacial oxidation/reduction reaction happens, and reactive overlayers, where oxygen is extracted from the substrate and is incorporated into the films. The strength of this reaction scales with the heat of formation, and so does the tendency to wet the substrate. The nucleation behavior starts to be sufficiently well characterized. There is a clear trend for the epitaxial relationship of groups of overlayers with the substrate, and a predictive understanding of the thermal stability of the films has been obtained.

While the trends of metal/ TiO_2 growth are now rather well understood, comparably little effort has concentrated on the growth of metal *oxides* on TiO_2 , see the relative scarcity of such growth studies in Table 6. While reactive overlayers become oxidized on TiO_2 they do so on the cost of TiO_2 reduction. The interfacial reactions and the resulting overlayer properties might be quite different when an additional supply of oxygen is offered from the gas phase.

Although details are still missing for some elements, the rich body of experimental data on metals/ TiO_2 as a whole constitutes a systematic and conclusive data base. It should be a rewarding challenge for theorists to follow up with state-of-the-art calculations in order to provide insight that cannot be derived from experimental work alone. It is comforting to see that such works have started to appear. Adsorption on these rather well-characterized systems has also started to stimulate interest. Such studies should provide a next step in order to truly understand the promotional effects of supported metal catalysts. Finally, it will be interesting to see which of the concepts derived from the already rather complete work on metals on TiO_2 will be transferable to other oxide supports.

5. Surface chemistry of TiO₂

The adsorption of molecules and atoms, and their dissociation and/or reaction to other products, is certainly the most extensive area of study in the surface science of TiO₂. General considerations about different types of adsorption mechanisms at oxide surfaces are found in [1]. The discussion in this review is split (somewhat arbitrarily) into a section on inorganic and one on organic molecules. For convenience, information about the various molecules is briefly summarized in table format. It should be pointed out that recent structural investigations have rendered some surprises about the surface geometrical structure and morphology of TiO₂ surfaces (see Section 2) which might have affected results on molecular adsorption and surface chemistry. This is pointed out in cases where it is obvious that details of the surface structure of TiO₂, which were previously unknown, may have influenced the results. For the most part, however, the results have not been re-interpreted and the view of the surface structure was adopted that was given in the original articles.

5.1. Inorganic molecules

5.1.1. Hydrogen

The interaction of TiO₂ with hydrogen at higher pressures is interesting from a technological point of view. Pd-sensitized TiO₂ is used as a hydrogen sensor [470] and reducing oxide powders in a H₂ atmosphere is typically employed in catalysis [471]. UHV studies have consistently shown that TiO₂ surfaces do not interact strongly with molecular hydrogen [472]. High doses of H₂ (10⁵ L) at room temperature caused additional emission peaks in the valence band region in UPS [27]. In [131] it was argued that oxygen vacancies act as special adsorption sites for hydrogen. In contrast to molecular hydrogen, atomic H sticks to TiO₂(1 1 0) surfaces at room temperature [127]. Despite the weak interaction between molecular hydrogen and TiO₂, there are indications of a reduction when a TiO₂ surface is annealed in a H₂ atmosphere under high vacuum conditions [473,474].

It is possible that so-called ‘clean’ single-crystalline surfaces, obtained with the usual cleaning procedures, are to some extent covered by hydrogen (see also Section 2.2.1.4). The extent to which this occurs, as well as the form and the origin of the hydrogen, is still being debated. This adsorbed hydrogen could come from two sources. Firstly, it could come from the water in the residual gas pressure in the UHV chamber. The high sticking coefficient of H₂O together with the tendency to dissociate at vacancies (see Section 5.1.2) can quickly lead to a hydroxylation of all oxygen vacancies. Secondly, hydrogen from the bulk of TiO₂ crystals could end up at the surface. With RBS it was determined that a stoichiometric TiO₂ sample contains ca. 1 at.% hydrogen [475]. In a recent ion scattering/ion-induced recoil study, a TiO₂(1 1 0) was stepwise annealed to higher temperature. The O and H content was monitored during the heating excursion. The study comes to the surprising conclusion that all bridging oxygen atoms of a UHV-annealed surface are hydroxylated, even after annealing to 730 °C [476]. It needs to be pointed out, however, that this TiO₂ sample was not treated prior to the heating excursion. It is doubtful that such a high coverage with hydrogen is also found when a crystal is prepared by the usual sputter/annealing cycles in UHV (Table 7).

5.1.2. Water

For many reasons water is probably the most important adsorbate at TiO₂ surfaces. Many of the applications mentioned in Section 1.2, for example, almost all photocatalytic processes, are performed

Table 7
Survey of hydrogen adsorption on TiO₂ surfaces

Substrate	Techniques/adsorption/reaction	Reference
Rutile (1 0 0)-(1 × 3)	UPS, ELS, AES	[27]
Rutile (1 1 0), (1 0 0), (0 0 1)	UPS, TiO ₂ surfaces do not interact strongly with hydrogen	[759]
Rutile (1 1 0)	LEED, XPS, ELS, EPR, work function, surface conductivity	[511]
Rutile (1 1 0)	LEIS, molecular H ₂ does not adsorb at room temperature, atomic H sticks at room temperature	[127]
Rutile (1 1 0)	STM, O–H and Ti–H species on slightly defective TiO ₂ (1 1 0)	[133]
Rutile (1 1 0)	CAICISS, TOF-ERDA, 1 ML of H even after annealing to 730 °C	[476]

in an aqueous environment. Water vapor in the ambient interacts with TiO₂ surfaces, and surface hydroxyls can easily affect adsorption and reaction processes. Water is one of the main components in the residual gas in UHV chambers, hence it is an important adsorbate even in well-controlled experiments. The adsorption of water on TiO₂ has been of intense interest in recent years. It has been investigated with a variety of experimental and theoretical techniques, see Table 8. Recently, an excellent review article on water adsorption on solid surfaces was given by Henderson [477]. This work represents a substantial expansion from a previous review by Thiel and Madey [478] on the same subject. Because Henderson's article refers extensively to single-crystalline TiO₂ surfaces, the discussion on water TiO₂ is kept brief here. For an overview, most of the recent literature is summarized in Table 8, and a brief summary, especially on unclarified questions regarding adsorption on the TiO₂(1 1 0) surface, is given in the following. For many of the details, the interested reader is referred to Henderson's article [477].

Rutile (1 0 0). Experimental and theoretical studies for the most part agree that water can dissociate to some extent on perfect rutile (1 0 0) surfaces. Except for some early work [27], results from different spectroscopies generally indicate that water adsorbs both dissociatively and molecularly [174,479–484]. This is independent of steps, point defects [479–481], and the Ti³⁺ sites present at the (1 × 3)-reconstructed surface. The amount of dissociated water is slightly different at the (1 × 1) and (1 × 3)-reconstructed surface [197]. The sticking coefficient is unity at a sample temperature of 130 K [197]. Adsorption/desorption occurs reversibly, i.e., molecular water is the only desorption product, and the surface generally does not become oxidized. It has been reported that very high doses of water vapor or exposures to liquid water [484] causes oxidation of defects, but these results have not been reproduced in other studies [92,485]. Most theoretical results [214,241,486], but not all of them [105], agree with the notion of initial dissociative adsorption, followed by molecular adsorption at higher coverages.

Rutile (1 1 0). Despite the extensive work on water adsorption on rutile (1 1 0), see Table 8, there is a considerable disagreement on the initial adsorption behavior of water, especially between theoretical and experimental studies. While most of the experimental results agree that H₂O does not dissociate on TiO₂(1 1 0), except at defect sites, most theoretical studies predict dissociative adsorption.

Brinkley et al. [487] performed a molecular beam scattering study where they investigated the dynamical adsorption properties of water. A sticking probability of unity at all coverages and temperatures up to 600 K was found. The water molecule is trapped, with enough time to sample the potential energy surface of TiO₂(1 1 0) before desorption. It was also found that very few of the molecules dissociate, even in the limit of zero coverage. This is in agreement with TPD studies, most notably the ones published by Henderson [128,174] and Hugenschmidt et al. [175]. A high-temperature

Table 8

Survey of water adsorption on TiO₂ surfaces

Substrate	Techniques/adsorption/reaction	Reference
<i>Rutile (1 0 0), experiment</i>	Review of water adsorption on solid surfaces (includes extensive survey of water/TiO ₂)	[477]
Rutile (1 0 0)-(1 × 3), sputtered and with Ti overlayer	UPS, ELS, AES, TPD, water is adsorbed molecularly on TiO ₂ (1 0 0)-(1 × 3), but dissociates on Ti ³⁺ achieved through different surface pretreatments	[27]
Rutile (1 0 0)-(1 × 1), -(1 × 3); with point defects; vicinal surface	UPS, water adsorption independent of steps and O vacancies, adsorbs molecularly at 130 K and dissociates to form OH at 293 K	[479–481]
Rutile (1 0 0)-(1 × 1), -(1 × 3), sputtered	TPD, unity sticking probability at 130 K, dissociative and molecular states, desorbs exclusively as H ₂ O, water more weakly bound to the sputtered surface	[197]
Rutile (1 0 0)	TPD, isotopic labeling, dissociative desorption; recombinative desorption (see Fig. 51)	[174]
Rutile (1 0 0)	SIMS, traces of F enhance hydroxylation of the substrate	[482,483]
Rutile (1 0 0)	XPS, UPS, H ₂ O possibly heals vacancies created by e-beam and Ar bombardment	[484,760]
<i>Rutile (1 0 0), theory</i>		
Rutile (1 0 0)	Cluster calculations, dissociation of water	[486]
Rutile (1 0 0)	Hartree–Fock dissociative adsorption	[214]
Rutile (1 0 0)	Electronic structure calculations, dissociative adsorption is thermodynamically favored	[241]
Rutile (1 0 0)	SCF MO LCAO calculations, dissociative adsorption	[761]
Rutile (1 0 0)	Carr–Parinello MD simulation molecular adsorption on stoichiometric surface, spontaneous dissociation of water at an O vacancy	[105]
<i>Rutile (1 1 0), experiment</i>		
Rutile (1 1 0), Ar-bombarded	UPS, dissociative adsorption at low coverages	[762]
Rutile (1 1 0), Ar ⁺ and e-beam bombarded	UPS, HREELS, H ₂ O does not adsorb at stoichiometric surfaces at room temperature, dissociative adsorption at defects	[763]
Rutile (1 1 0) with vacancies	Photoemission, dissociative adsorption on vacancies and on regular lattice sites	[489]
Rutile (1 1 0)	LEIS, isotopic labeling, water adsorbs at vacancy sites	[127]
Rutile (1 1 0), defects	XPS, high exposures needed to heal electronic defect state	[764]
Rutile (1 1 0)	TPD, XPS, workfunction, first layer adsorbs at fivefold Ti ⁴⁺ sites; distinct second layer state at 180 K—‘bilayer’ structure with water molecules lying flat	[175]
Rutile (1 1 0)	HREELS, TPD, isotopic labeling, water adsorbs dissociatively for exposures up to 7×10^{13} mol/cm ² ; molecular for higher coverages; ideal surface not active for water dissociation (see Fig. 51), second water layer interacts mainly with bridging O sites	[128,174]
Rutile (1 1 0), (1 × 1), (1 × 2), and sputtered surface	Molecular beam scattering, TPD sticking coefficient of water = 1 up to 600 K; long residence time before desorption; only few of water molecules dissociate	[487]
Rutile (1 1 0)	TPD, dissociation of D ₂ O and production of D ₂ on defects created by thermal annealing, healing of vacancies	[490]
Rutile (1 1 0)	STM, terminal OH groups at Ti ⁴⁺ sites at step edges	[491]
Rutile (1 1 0)	STM, photoemission, water adsorbs molecularly at 150 K, dissociates at 290 K, strong lateral interaction leads to formation of water ‘chains’	[488]

Table 8 (Continued)

Substrate	Techniques/adsorption/reaction	Reference
Rutile (1 1 0)	STM, dissociation at point defects	[134]
Rutile (1 1 0)	MIES, UPS, dissociative adsorption at defects followed by multilayer adsorption; strong lateral interactions between adsorbed water molecules	[765]
<i>Rutile (1 1 0), theory</i>		
Rutile (1 1 0)	Cluster calculations, TiO ₂ (1 1 0) is catalytically active for water dissociation	[486]
Rutile (1 1 0)	Hartree–Fock dissociative adsorption	[214]
Rutile (1 1 0)	Self-consisted tight-binding embedded clusters, electronic structure of hydroxylated surface	[766,767]
Rutile (1 1 0)	DFT calculations, dissociative adsorption is most stable	[768]
Rutile (1 1 0)	Cluster calculation, dissociative adsorption is favored	[215]
Rutile (1 1 0)	SCF MO LCAO calculation, dissociative adsorption	[769]
Rutile (1 1 0)	DFT embedded cluster calculations	[242,518]
Rutile (1 1 0)	DFT calculations of dissociated H ₂ O in (1 × 2) geometry	[770]
Rutile (1 1 0)	DFT calculations, dissociative adsorption	[102]
Rutile (1 1 0)	First-principles MD calculations, dissociative adsorption	[492]
Rutile (1 1 0)	DFT and HF calculations, dissociative at low coverage, molecular and dissociative at higher coverages	[99]
Rutile (1 1 0)	DFT calculations, dissociative adsorption at lower coverage, molecular adsorption stabilized through intermolecular H bonding	[493]
Rutile (1 1 0)	SCF MO LCAO calculation, molecular adsorption stabilized by H bond formation	[761]
Rutile (1 1 0)	Electronic structure calculations dissociative adsorption is thermodynamically favored, potential barrier towards proton transfer	[241]
Rutile (1 1 0)	Embedded cluster calculations, molecular adsorption is energetically favored	[494]
Rutile (1 1 0)	Carr–Parinello MD simulation perfect TiO ₂ (1 1 0) surfaces adsorb undissociated water, no spontaneous dissociation at O vacancies	[105]
Rutile (1 1 0)	DFT calculations, on perfect surface: dissociation is endothermic at low coverages, weakly exothermic at high coverages; at defects: dissociation is exothermic	[134]
<i>Rutile (0 0 1), experiment</i>		
Rutile (0 0 1)	UPS, dissociative adsorption at 250 K, independent of Ti ³⁺ states; desorption as H ₂ O	[771,772]
Rutile (0 0 1)	UPS, AES, LEED, dissociative adsorption only	[773]
Rutile (0 0 1)	XPS, on stoichiometric and reduced surfaces	[473,774]
<i>Anatase</i>		
Anatase (1 0 1), (0 0 1)	DFT calculations, (1 0 1): molecular adsorption on Ti(5); hydrogen atoms of the water molecule align towards bridging oxygen atoms (0 0 1): dissociative adsorption up to 0.5 ML	[70]
Anatase (1 0 1)	First-principles MD calculations molecular adsorption	[553]
Anatase (1 0 1)	TPD and XPS, exclusively molecular adsorption	[495]
Anatase (0 0 1)	Hartree–Fock	[214]
Anatase (0 0 1)	Cluster calculations, dissociative adsorption is favored	[215]
Anatase (0 0 1)	Water co-adsorption with oxygen—see Table 9	[215]
Anatase (0 0 1)	Water co-adsorption with CO ₂ —see Table 10	[215]
Anatase (0 0 1)	Water co-adsorption with NH ₃ —see Table 12	[215]

Table 8 (Continued)

Substrate	Techniques/adsorption/reaction	Reference
<i>Liquid water/wettability</i>		
Rutile (1 1 0), (0 0 1), (1 0 0)	Contact angle measurements, XPS reversible wettability with UV-created defects (see Fig. 52)	[92,485]
Rutile (1 1 0)	SHG of H ₂ O/TiO ₂ (1 1 0) interface, UV-generated surface defects	[775]
Rutile (1 1 0)	X-ray standing waves, Rb and Sr ion distribution in electric double layer	[776]
Anatase (1 0 1), (0 0 1)	LEED, bulk-terminated surfaces, impedance spectroscopy measurements of flatband potential	[777]

tail in TPD spectra was attributed to recombinative desorption of water that has dissociated at defects, i.e., oxygen vacancies [128,174,175]. These authors conclude that the flat, unperturbed TiO₂(1 1 0) surface does not lead to dissociation of the water molecule, but that water dissociates at point defects. Most of the photoemission and other spectroscopic experiments listed in Table 8 are consistent with this idea, although there is some deviation in the details. For example, there is disagreement about the temperature at which water dissociates at point defects [128,488,489]. Also, while most authors report reversible adsorption, i.e., only H₂O leaves the surface upon heating, some studies [490] report the production of hydrogen molecules at point defects, combined with a healing of these defects [487]. It was pointed out [170,477] that the different preparation techniques of TiO₂ surfaces that can lead to drastically different surface morphologies and a range of undercoordinated sites (see Figs. 18 and 21) could possibly be a reason for the observed differences. Recent STM studies [134,488,491] support the earlier experimental results that dissociative adsorption occurs at defects, and that water molecules stay intact when adsorbed at flat terraces.

The difference between the adsorption behavior of water at the TiO₂(1 1 0) and (1 0 0) surfaces, exemplified in Fig. 50 is rationalized with the structural model proposed by Henderson (Fig. 51). Water

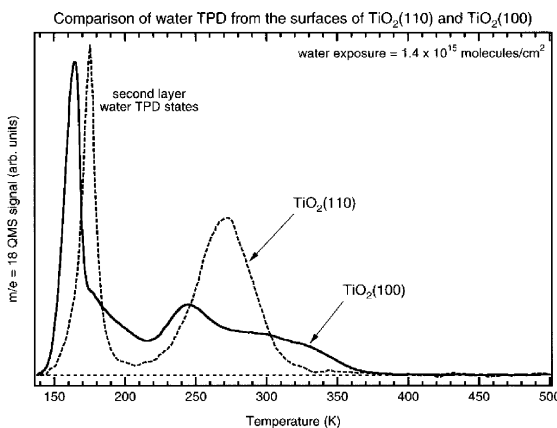


Fig. 50. Comparison of TPD spectra obtained from water adsorption on TiO₂(1 1 0) (dashed line) and TiO₂(1 0 0) (solid line). The water adsorption temperatures were 140 and 138 K, respectively. The traces exhibit significant differences in the number of monolayer desorption states and the relative amount of water desorbing above 300 K. Isotopic labeling studies indicate molecular adsorption on TiO₂(1 1 0), except for adsorption at defect sites which gives rise to a high-temperature peak (not shown in these traces). The TiO₂(1 0 0) surface dissociates water. From Henderson [174]. © 1996 The American Chemical Society.

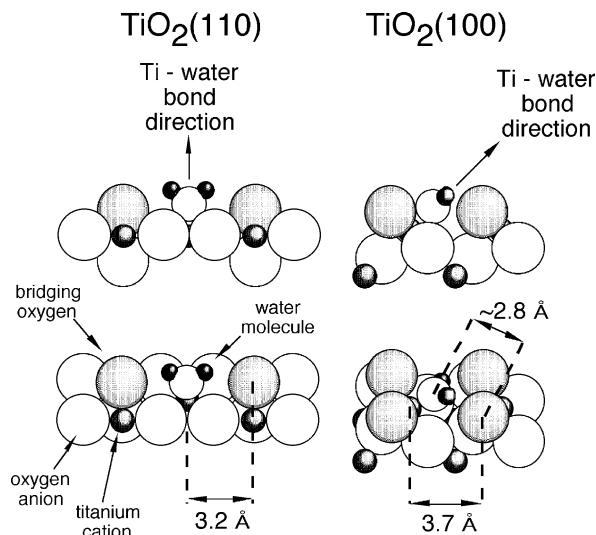


Fig. 51. Schematic model for the interaction of water with the (110) and (100) surfaces of TiO_2 in side and perspective view. Water binds at the acidic sites (the fivefold coordinated Ti^{4+} ions) on TiO_2 with the O-H bonds pointing away from the surface. On $\text{TiO}_2(110)$, the distance between the water molecule and the next bridging oxygen atoms is 3.2 \AA , precluding a hydrogen-bonding interaction between the adsorbed water molecule and the bridging oxygen atoms. On $\text{TiO}_2(100)$, the O-O distance between an adsorbed water molecule and a twofold coordinated O atoms is smaller, favoring hydrogen bonding and dissociation. From [174]. © 1996 The American Chemical Society.

is expected to adsorb at exposed fivefold coordinated Ti sites in each case with the hydrogen atoms pointing away from the surface. Since (multiple) hydrogen bonding interactions between the adsorbed species and the bridging oxygen atoms of the substrate are expected to facilitate proton transfer, the relative distance between the water molecule and the neighboring bridging oxygen atoms is of importance. On the $\text{TiO}_2(100)-(1 \times 1)$ surface, the molecule adsorbs in an inclined fashion, and the distance between the oxygen atom in the water molecule and the twofold coordinated substrate O^{2-} ions is small enough for a weak H-O interaction to occur. In contrast, the distance between an O atom adsorbed at a Ti atom and a neighboring bridging O^{2-} ion is more than 3 \AA on $\text{TiO}_2(110)$, precluding O-H interaction. This model would also explain why oxygen vacancies on $\text{TiO}_2(110)$ are particularly reactive towards H_2O dissociation. An H_2O molecule adsorbed in a vacancy would provide a geometrically particularly well-suited adsorption site for O-H interactions and dissociation.

Wang et al. [92,485] pointed out that water dissociation at these oxygen vacancies possibly has a *macroscopic* effect on the wetting ability of water, see Fig. 52. Generally, TiO_2 surfaces are oleophilic and hydrophobic, i.e., water does not wet the surface but oil does. However, after a TiO_2 sample was exposed to UV light, the contact angle of water droplets decreases to essentially zero degrees [92,485]. Storing such amphiphilic surfaces in the dark restores the hydrophobicity of the original surface. The surface stays oleophilic at all times, i.e., it exhibits ‘amphiphilicity’. Based on UHV studies, this is attributed to the creation of surface vacancies that dissociate water and form microscopic hydrophilic domains [92,485]. This effect is exploited in the production of antifogging and self-cleaning coatings on mirrors.

In stark contrast to the experimental results on $\text{H}_2\text{O}/\text{TiO}_2(110)$, most theoretical calculations indicate that dissociation of the water molecule is energetically favored on the perfect $\text{TiO}_2(110)$

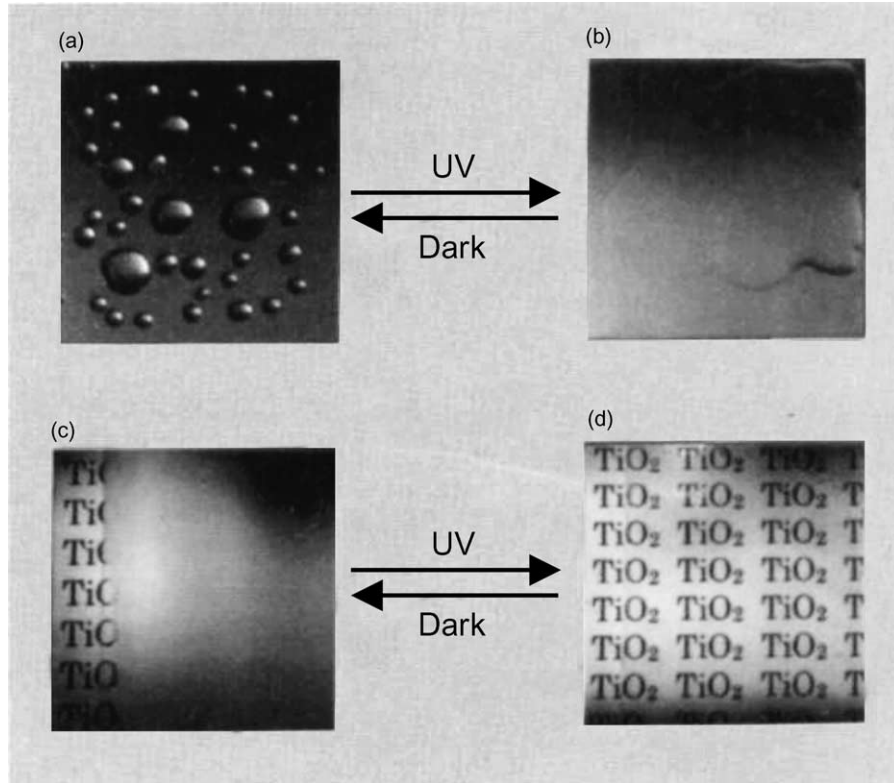


Fig. 52. Photographs from a $\text{TiO}_2(1\ 1\ 0)$ single crystal. (a) The surface is generally hydrophobic, and water droplets do not wet. (b) After ultraviolet irradiation, the surface becomes hydrophilic, presumably because of the formation of oxygen vacancies which facilitate the dissociation of water. (c) Exposure of a hydrophobic TiO_2 -coated glass to water vapor. The formation of fog (small water droplets) hinders the view of the text on the paper placed behind the glass. (d) Creation of an antifogging surface by ultraviolet irradiation. The high hydrophilicity prevents the formation of water droplets. The TiO_2 surface stays oleophilic, irrespective of the treatment. From Wang et al. [92]. © 1997 MacMillan Magazines Limited.

surface (see Table 8). Intermolecular H bonding was invoked to act as a stabilizing factor for a mixed dissociated/molecular state [99,492,493]. Other calculations point out that, while dissociative adsorption on rutile (110) is thermodynamically favored, it might be hindered by a potential barrier [241]. One cluster calculation showed molecular adsorption [494], while many others, using a similar approach, predict dissociative adsorption, see Table 8. A very recent DFT slab calculation by Norskov and co-workers [134] agrees with the experimental data (water dissociation is an endothermic and exothermic process on terraces and point defects, respectively), and it is argued that the configuration of the water molecules in test geometries plays an important role for the calculated energetics. A molecular dynamics simulation using the Carr–Parinello approach [105] found molecular adsorption on stoichiometric TiO_2 surfaces. However, these calculations do not reproduce other experimental results. Placing an H_2O molecule in a bridging oxygen vacancy did not lead to spontaneous dissociation on the $\text{TiO}_2(1\ 1\ 0)$ surface. Also, in [105] it was concluded that single OH groups are not stable on $\text{TiO}_2(1\ 1\ 0)$, in contradiction to recent STM data [134,488].

The adsorption behavior of thicker H₂O layers was investigated by several groups [128,174,175,197,477,487]. On TiO₂(1 1 0), a distinct second layer peak at 180 K is observed in TPD. This was interpreted as a ‘bilayer’ structure, where the second water layer lays flat [175] and, based on additional HREELS measurements, it was concluded that water in this second layer interacts only with the bridging oxygen atoms [128]. Water multilayers on TiO₂(1 0 0) (which partially dissociates water, see above), followed a zeroth-order desorption behavior. This is in contrast to multilayers on TiO₂(1 1 0), where deviations from this desorption behavior were found [128,174,197,477].

The adsorption of water on anatase surfaces has so far been mostly studied theoretically (see Table 8). On the basis of DFT and first-principles molecular dynamics calculations, Selloni and co-workers [70] concluded that water adsorbs molecularly on anatase (1 0 1). A TPD/XPS study by Herman et al. [495] confirms this prediction. Calculations of water adsorption on the anatase (0 0 1) surface [70,214] predict dissociative adsorption but have yet to be confirmed by measurements.

5.1.3. Oxygen

Because Ti is such a reactive element, oxygen-deficient surfaces are clearly expected to react with O₂. In many studies it has implicitly been assumed that oxygen exposure would just fill surface vacancies on TiO₂. It is only recently that the intricacies of the oxygen/defect interaction was investigated in more detail. (In this context, the reader is reminded that annealing reduced TiO₂(1 1 0) crystals in an oxygen background pressure causes a reoxidation of the crystal that leads to a restructuring of the whole surface. This phenomenon is discussed in Section 2.2.2.2.)

Photocatalytic studies [496–498] as well as co-adsorption studies of water and ammonia with oxygen-predosed surfaces [275,499,500] have revealed that the ‘filling’ of oxygen vacancies is not as simple as previously thought. Models for the adsorption of oxygen at low and somewhat higher temperatures were derived from these studies and are depicted in Fig. 53. Oxygen does not adsorb at 100 K to a stoichiometric TiO₂(1 1 0) surface. When a surface with 8% vacancies is exposed to O₂ at cryogenic temperatures, the saturation coverage is about three times the vacancy concentration [275]. This was rationalized with a model in which O₂[−] species are bound in the vicinity of a vacancy, see Fig. 53A. Most of these oxygen molecules desorb around 410 K; irradiation with 4.1 eV photons results in photodesorption [500]. Molecular oxygen, adsorbed at 105 K, was also found to be active for the photo-oxidation of CO [498]. From co-adsorption studies with water and ammonia it was concluded that O₂, when dosed at a temperature between 90 and 600 K, results in the filling of an oxygen vacancy and an oxygen adatom [499], see Fig. 53. These adatoms lead to additional dissociation of water. They disappear when the surface is heated to 600 K. The change in the SHG signal after O₂ adsorption at room temperature was attributed to the formation of a Ti⁴⁺:O^{2−} complex [501].

In this context, it should be noted that adsorption of oxygen (or another electronegative element) at fivefold coordinated Ti sites does not violate the rules for creating a stable surface (see Section 2.2.1.1). While a compensated surface under perfect vacuum conditions will have empty Ti sites, it has been shown for several oxides that the presence of a chemical environment can result in a surface that has a higher stability when covered with an adsorbate [502,503]. In particular, this is the case for RuO₂(1 1 0), which has the same rutile structure as TiO₂. Under the conditions of a high oxygen chemical potential the so-called ‘cus’-sites (5-fold coordinated Ru atoms) are preferably occupied with a singly coordinated O atom [504] (Table 9).

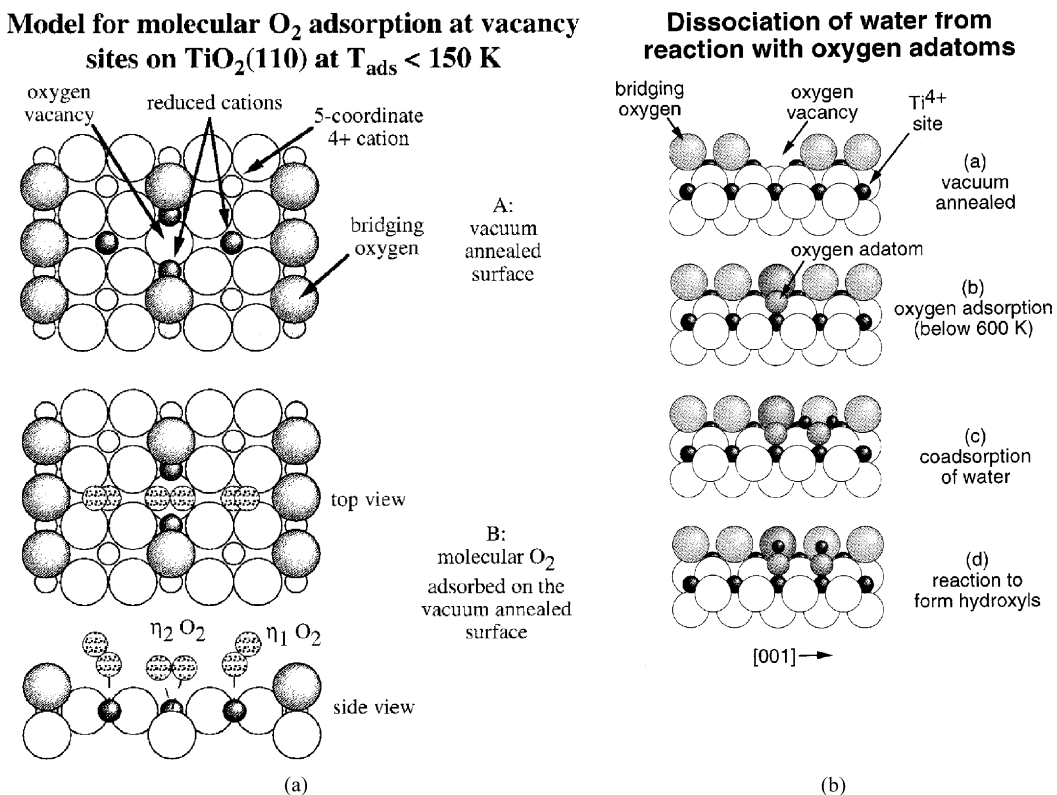


Fig. 53. (a) Schematic model for the bonding of O₂ to the vacuum-annealed TiO₂(110) surface at low temperatures. Model A shows the top view of the TiO₂(110) surface with an oxygen vacancy site. Model B shows top and side (along the [001] direction) views of O₂ molecules bonding at vacancy and non-vacancy sites. From Henderson et al. [275]. © 1999 The American Chemical Society. (b) Schematic model for the formation of oxygen adatoms from the interaction of O₂ with oxygen vacancies at higher temperatures, and for the role of these adatoms in dissociating coadsorbed water. From Epling et al. [499]. © 1998 Elsevier.

5.1.4. Carbon monoxide and carbon dioxide

5.1.4.1. CO. Adsorption of CO on metal-promoted TiO₂ surfaces was studied by several authors [23,395,415,430,434,505–509], and is partially discussed Section 4.2 (see also Table 6). Of particular interest in this context is the low-temperature oxidation of CO on nanosized, TiO₂-supported Au particles, discussed above (Section 4.2). In contrast to metal-promoted surfaces, the adsorption of CO on the clean TiO₂(110) surface is far less investigated experimentally [131,510–512], although this system was treated theoretically by a number of groups [242,513–520]. An early study by Göpel et al. [131,511] found oxygen vacancies to be special adsorption sites for H₂ and CO. de Segovia and co-workers [512] found only a small CO coverage after exposure of a sputtered surface to 10⁵ L. Nevertheless, this small amount of CO had a dramatic influence on the O⁺ ion yield in ESD.

Yates and co-workers [510] performed a TPD study of CO adsorption on stoichiometric and defective TiO₂(110) surfaces. CO was dosed at 105 K, and with increasing coverage, CO was found to desorb at ~170–135 K from the stoichiometric surface, see Fig. 54. From the TPD data, an initial activation

Table 9
Survey of oxygen adsorption on TiO_2 surfaces

	Substrate	Techniques/adsorption/reaction	Reference
O_2	Rutile (1 1 0)	Two adsorption states (α and β) with different photodesorption behavior and photocatalytic reactivity, see Section 5.3.3	[496–498]
	Rutile (1 1 0)	At 120 K three O_2 molecules adsorb in the vicinity of oxygen vacancies—see also co-adsorption with H_2O and NH_3	[275]
	Rutile (1 1 0)	At elevated temperatures—re-oxidation of the reduced bulk, ‘restructuring’, see Section 2.2.2.2	
$\text{O}_2 + \text{H}_2\text{O}$	Rutile (1 1 0)	SHG, XPS, O_2 ‘heals’ defects slowly, indication of a $\text{Ti}^{4+}:\text{O}^{2-}$ complex	[501]
	Rutile (1 1 0), with oxygen vacancies	Carr–Parinello MD simulation; O_2 dissociates in vacancy slowly	[105]
$\text{O}_2 + \text{H}_2\text{O}$	Rutile (1 1 0)	TPD, higher T : O_2 dissociates at vacancies and creates O adatoms, these facilitate dissociation; low T : molecular adsorption, O_2 coverage is three times that of O vacancies (see Fig. 53)	[275,499]
	Rutile (1 1 0)	TPD, SSIMS, EELS, UV-illumination of O_2 at vacancies leads to photodesorption; photolysis of an $\text{O}_2-\text{H}_2\text{O}$ adduct in thick water overlayer	[500]
$\text{O}_2 + \text{CO}$	Rutile (1 1 0)	see Table 10	

energy of 9.9 kcal/mol at zero coverage and a repulsive interaction of 2.2 kcal/mol was extracted. While this is lower than values reported in previous works [131,511,521], it is probably the study performed under the best-characterized conditions. On the ‘pre-annealed’ surface, containing O vacancies, CO remained on the surface up to 350 K (Fig. 54). Both surfaces, the stoichiometric and the

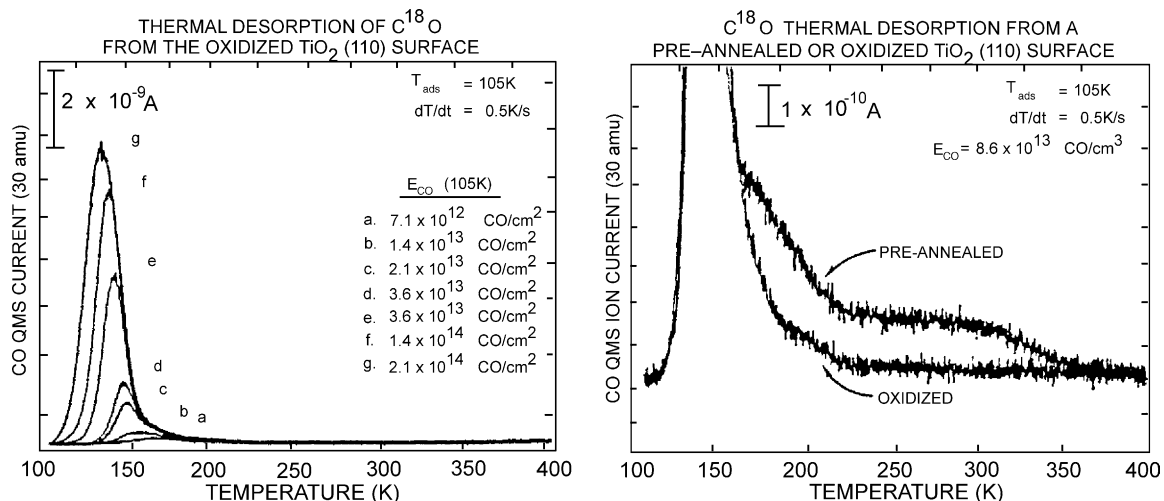


Fig. 54. (a) TPD spectra for ^{18}CO from the fully oxidized $\text{TiO}_2(1\ 1\ 0)$ surface. The ^{18}CO exposures displayed range from 7.1×10^{12} to 2.1×10^{14} molecules/ cm^2 . (b) Enlargement of the TPD spectra to show the high-temperature CO states from the oxidized and the annealed $\text{TiO}_2(1\ 1\ 0)$ surface. The CO exposure was 8.6×10^{13} $^{18}\text{CO}/\text{cm}^2$ for both surfaces. The high-temperature desorption features on the pre-annealed surface are attributed to CO interaction with point defects. From Linsebigler et al. [510]. © 1995 The American Chemical Society.

Table 10

Survey of the adsorption of C-containing inorganic molecules on TiO₂ surfaces

	Substrate	Techniques/adsorption/reaction	Reference
CO	Rutile (1 1 0)	XPS, AES, LEED, ELS	[131,511]
	Rutile (1 1 0)	ESD, AES, a high dosage of CO at sputtered surface produces only a small coverage	[512,549]
	Rutile (1 1 0)	TPD, CO adsorbs weakly on stoichiometric surface, desorbs at ~170 K (low coverage) to ~135 K (higher coverage); desorbs at higher temperatures on surface with O vacancies; see Fig. 54	[510]
CO + O ₂	Rutile (1 1 0)	TPD, photodesorption, O ₂ blocks active site for high-temperature CO desorption peak; O ₂ molecules at O vacancies photo-oxidize CO to CO ₂	[498,510,522]
CO	Rutile (1 1 0)	Theory: see Table 11	
CO ₂	Rutile (1 1 0)	LEED, XPS, ELS, surface conductivity, work function	[131]
CO ₂ + H ₂ O	Rutile (1 1 0)	TPD, SSIMS, HREELS, CO ₂ binds to vacancies slightly more strongly; linear bonding to regular Ti ⁴⁺ sites; CO ₂ is blocked/displaced by H ₂ O adsorption; formation of bi-carbonate when CO ₂ and H ₂ O are dosed simultaneously	[277]
CO ₂ + H ₂ O	Rutile (1 1 0), (1 0 0)	HREELS, photoreduction of CO ₂ in the presence of H ₂ O	[524]
CO ₂ + Na	Rutile (1 1 0)	Promotion with Na activates the TiO ₂ (1 1 0) surface for CO ₂ adsorption; formation of a CO ₃ complex (see Fig. 42)	[304,305,323, 325,326,328,342]

slightly defective one, show the same CO coverage at similar exposures. The saturation coverage was determined as $\sim 2.5 \times 10^{14}$ CO/cm², corresponding to about half the number of fivefold coordinated Ti ions. CO was the only desorbing product. No CO₂ production was observed. TPD measurements with isotopically labeled molecules showed no scrambling with substrate oxygen. When a surface with O vacancies was pre-dosed with O₂ at 105 K prior to CO adsorption, the high-temperature tail in the CO TPD spectrum was suppressed, indicating that the high-temperature features in Fig. 54 are due to adsorption at defect sites [510]. Pre-adsorbed O₂ molecules at the oxygen vacancies induce CO₂ photoproduction [498,522] (Table 10).

The adsorption of CO/TiO₂(1 1 0) was treated with different computational techniques, and a summary of the results is given in Table 11. Adsorption with the C-end down is consistently found to be energetically much more favorable than the alternative orientation, where the CO molecule would bind with the O-end down. Throughout these calculations the C–O bond distances are rather similar, but the adsorption energies vary considerably, with the experimental value from [510] being on the lower end of the given range. The decrease in binding energy with higher coverage, caused by the onset of repulsive interaction between CO molecules, is reproduced in slab calculations. Experimentally, the C–O stretching mode of the adsorbed CO molecule shows a red shift compared to a free molecule [523]. The calculated values of the red shifts of the C–O stretching mode vary considerably. A quantitative comparison with experiment is difficult because of lack of reliable vibrational spectroscopy results on well-characterized, single-crystalline rutile. However, the calculations seem to overestimate the amount of this shift [523] with one exception [516]. The CO/TiO₂(1 1 0) system is a good test case for a refinement of computational techniques. Several authors explored systematically how these theoretical results are influenced by the embedding method of the clusters, the basis set, and various corrections [242,513,516–520].

Table 11

Comparison of calculated equilibrium distances, CO vibrational shift $\Delta\nu$ with respect to the free CO frequency, and adsorption energies for CO molecule adsorbed on the TiO₂(1 1 0) surface at different coverages, θ^a

Reference	Model/orientation	θ	Ti–C or Ti–O (Å)	C–O (Å)	$\Delta\nu$ (cm ⁻¹)	E_{ads} (kcal/mol)
Kobayashi and Yamaguchi [514]	Cluster/-CO		2.500	1.150		17.00
Fahmi and Minot [515]	Slab/-CO	1	2.379	1.123	75	10.87
Fahmi and Minot [515]	Slab/-OC	1	2.340	1.132	139	6.73
Pacchioni et al. [517]	Slab-cluster/-CO		2.328–2.381	1.155–1.126	80–140	16.14–18.44
Pacchioni et al. [517]	Slab/-CO	1				11.5
Reinhard et al. [520]	Slab/-CO	0.5	2.34–2.73			5.4–17.5
Reinhard et al. [520]	Cluster/-CO		2.50 ± 0.20	1.110		6–12
Casarini et al. [242,518,519]	Cluster/-CO		2.344	1.126	56–72	6.7–26.5
Sorescu and Yates [513]	Slab/-CO	1	2.376	1.121	64	7.97
Sorescu and Yates [513]	Slab/-CO	0.5	2.320	1.119		11.10
Sorescu and Yates [513]	Slab/-OC	1	2.701	1.128	64	0.62
Sorescu and Yates [513]	Slab/-OC	0.5	2.666	1.129		2.71
Yang et al. [516]	Slab/-CO	1	2.37–2.54	1.129–1.126	28	18.21–5.76
Yang et al. [516]	Slab/-OC	1	2.45			6.68
Linsebigler et al. [510]	TPD	0				9.9
Linsebigler et al. [510]	TPD	0.68				7.7

^a Notations –OC and –CO pertain to the two possible orientations of the CO molecule on the rutile (1 1 0) surface, i.e., with C and O atoms towards the surface. Adapted from [513].

Based on their TPD measurements, Linsebigler et al [510] suggested that a CO moiety adsorbed close to an oxygen vacancy experiences an additional interaction with the vacancy that leads to a stronger bonding, Fig. 54. Only one calculation found an increase in binding energy of CO at defect sites [514], in agreement with experiment [510]. However, this calculation was performed with a rather small, unrelaxed cluster [514].

5.1.4.2. CO₂. Carbon dioxide interacts only weakly with the clean rutile (1 1 0) surface [131,277]. Promotion of a TiO₂(1 1 0) surface with half a monolayer Na surface leads to CO₂ adsorption at room temperature, this is discussed in the context of Fig. 42. On the clean surface, CO₂ was found to bind to oxygen vacancies slightly more strongly than to regular lattice sites, with desorption temperatures in TPD at ∼166 and ∼137 K, respectively [277]. The adsorption mechanism is precursor-mediated. From HREELS data it was concluded that the molecule is linearly bound. The co-adsorption of CO₂ with H₂O has been investigated by Henderson [277]. CO₂ adsorption is blocked by water. When H₂O is dosed on a CO₂-covered surface, the CO₂ is displaced. The two molecules only interact when dosed simultaneously, and possibly form a bi-carbonate species [277]. Irradiation of ultraviolet light causes the reduction of CO₂ when H₂O is present on TiO₂(1 0 0) and TiO₂(1 1 0) single crystal surfaces [524].

5.1.5. Nitrogen-containing molecules (N₂, NO, NO₂, N₂O, NH₃)

5.1.5.1. N₂ (Table 12). The adsorption of N₂ is important in the BET analysis of surface areas in powder materials. In addition, UV illumination of TiO₂ can be used for the photo-oxidative fixation of molecular nitrogen as an NO_x species [525].

Table 12

Survey of the adsorption of N-containing inorganic molecules on TiO₂ surfaces

	Substrate	Techniques/adsorption/reaction	Reference
N ₂	Rutile (1 1 0)	Cluster calculations, physisorption, end-on configuration exhibits attractive potential	[244]
	Rutile (1 1 0)	Monte Carlo simulation, at low pressures: adsorption on Ti in end-on orientation; at higher pressures: adsorption on bridging oxygens in side-on orientation	[526,527]
NO	Rutile (1 1 0)	TPD, NO reacts with O vacancies under formation of N ₂ O and oxidation of vacancy	[490]
	Rutile (1 1 0)	TPD, DFT slab calculations, physisorbed NO for low coverages, tilted molecule N-end down; lateral interaction for higher coverages; N ₂ O ₂ intermediate results in production of N ₂ O	[529]
	Rutile (1 1 0)	Cluster calculations, adsorption of NO on stoichiometric and O-deficient surface	[778]
	Rutile (1 1 0)	Photodesorption, rapid depletion of adsorbed NO, production of N ₂ O is dominant, production of NO after longer irradiation, see Fig. 55	[530]
NO + Na	Rutile (1 1 0)	XPS, UPS, EELS, LEED, Na-dosed surface is activated for NO adsorption	[305]
N ₂ O	Rutile (1 1 0)	SHG, XPS, UPS, N ₂ O heals defects, no N remains on the surface	[501,532]
NO ₂	Rutile (1 1 0)	SXPS, EXAFS, DFT calculations, NO ₂ adsorbs predominantly as NO ₃ through disproportionation on Ti sites, subsurface vacancies are important	[533]
NH ₃	Rutile (0 0 1)	UPS, TPD, adsorbs molecularly at room temperature, desorbs at 338 K, e-beam damage leads to NH ₂ and O _{lattice} H	[536]
	Rutile (1 1 0)	UPS, adsorbs mainly molecularly, desorption and dissociation at higher temperatures	[537]
	Rutile (1 1 0)	XPS, molecular adsorption, slightly lower coverage on surface with vacancies; ESD, mainly desorption on stoichiometric surface; mainly dissociation on reduced surface; NH ₃ overlayer suppresses O ⁺ desorption from substrate	[136,534]
	Rutile (1 1 0)	ESDIAD, upright molecule, H atoms rotate freely	[535]
NH ₃ + H ₂ O	Rutile (1 1 0)	Auger-photoelectron coincidence spectroscopy, molecular adsorption; vacancies are active sites for adsorption	[540]
	Rutile (1 1 0)	STM	[491]
	Rutile (1 1 0)	Molecular dynamics simulations, upright molecule, orientation depends on coverage	[539]
	Rutile (1 1 0)	Periodic Hartree–Fock calculations, NH ₃ adsorbs molecularly; co-adsorption with water leads to H bonds	[538]
NH ₃ + O ₂	Rutile (1 1 0)	TPD, O ₂ dissociation at point defects produces adatoms which presumably enhance dissociation of NH ₃	[499]

The physisorption of N₂ was treated theoretically [244,526,527]. According to cluster calculations the molecule physisorbs at TiO₂ surfaces in an end-on configuration [244]. The experimentally found high adsorption energy for zero coverages was reproduced in these calculations. An interaction potential was constructed for N₂/TiO₂ clusters of various stoichiometries [527], and was used in Monte-Carlo calculations of N₂ adsorption at 77 K [526]. For adsorption at low pressures (<1 Torr), every fivefold coordinated Ti site is occupied by one N₂ molecule; lateral repulsion between molecules causes an arrangement of N₂ in 1D zigzag chains. According to these calculations, the area covered by one N₂

molecule (19.2 and 9.6 Å² in the monolayer regime and multilayer regime, respectively) is quite different from the one usually used for determination of surface areas (16.2 Å²). Simulated adsorption isotherms also showed deviation from those expected from the BET model.

5.1.5.2. NO. Nitrogen oxides (NO_x) are major contributors to acid rain and ground-level ozone pollution and TiO₂ is used to photocatalytically oxidize NO_x [528]. In field studies it was found that TiO₂ under UV illumination converts nitric oxide (NO) to nitrogen dioxide (NO₂) and HNO₃. Molecular scale studies of NO adsorption on single-crystalline TiO₂ surfaces are useful for gaining an understanding of the underlying mechanisms [304,529,530].

For low coverage, weak molecular adsorption was observed [529,530]. Na deposition activates the TiO₂(1 1 0) surfaces for adsorption of NO and the formation of nitride [304]. Desorption of NO from the clean surface occurs around 127 K [529,530]. The temperature of this NO TPD peak is almost independent of coverage [529,530]. Lateral interactions of the adsorbed NO molecules lead to the formation of an N₂O reaction product. The production of this species is observed in TPD above certain critical coverages. N₂O molecules desorb at ~169 and ~250 K when the surface was exposed to dosages higher than 5.5 × 10¹⁴ and 2.2 × 10¹⁵ molecules/cm², respectively [529]. DFT slab calculations found as the favorable adsorption geometry a tilted NO molecule with the N end down [529]. The calculations showed formation of an N₂O₂ species for higher coverages which is bound much stronger than NO. In a previous TPD study [490], it was found that NO reacts reductively at the Ti³⁺ sites at oxygen vacancies to produce N₂O. The oxygen atoms in the adsorbate molecules are extracted by the TiO₂ surface and cause the oxidation of surface Ti³⁺ sites [490]. DFT calculations [529] showed that other molecules, such as N₂O or NO₂ bind weakly to the surface.

The effect of UV irradiation on NO adsorbed at single-crystalline TiO₂(1 1 0) was also investigated and the results were compared to experiments on compressed TiO₂ powders [530,531]. Fig. 55 shows representative traces of photodesorption followed with a mass spectrometer. NO is depleted by 3.6 eV photons with a quantum efficiency of unity, and the dominant process for this depletion is formation of N₂O. After the initial rapid depletion of NO, a slow NO production is observed in Fig. 55. It was conjectured that the NO production is related to the capture of photoproduced N₂O to the surface and its slow subsequent photodecomposition to NO(g). However, N₂O adsorption and photodesorption experiments on TiO₂ powder did not confirm this hypothesis [530]. Evidence for photodesorption at photon energies below the 3.2 eV band gap has also been observed [531], probably due to electronic excitations from defect-related filled electronic states in the band gap region.

5.1.5.3. N₂O. The efficiency to ‘heal’ oxygen vacancies with N₂O was studied with photoemission spectroscopy [532] and second harmonic generation [501,532]. It was found that N₂O fills oxygen vacancies at a similar rate as molecular oxygen. No nitrogen is deposited on the surface.

5.1.5.4. NO₂. The main product of the adsorption of NO₂ on TiO₂(1 1 0) surface is surface nitrate, NO₃, with a small amount of chemisorbed NO₂ [533]. Photoemission data and DFT calculations suggest that this surface nitrate forms through a disproportionation process



after adsorption at Ti sites. Exposure of defect-rich TiO₂ to NO₂ at 300 K healed both, surface and subsurface defects. Because NO₂ is a big molecule, this result implies that substrate O vacancies and

Photodesorption of NO/TiO₂(110)

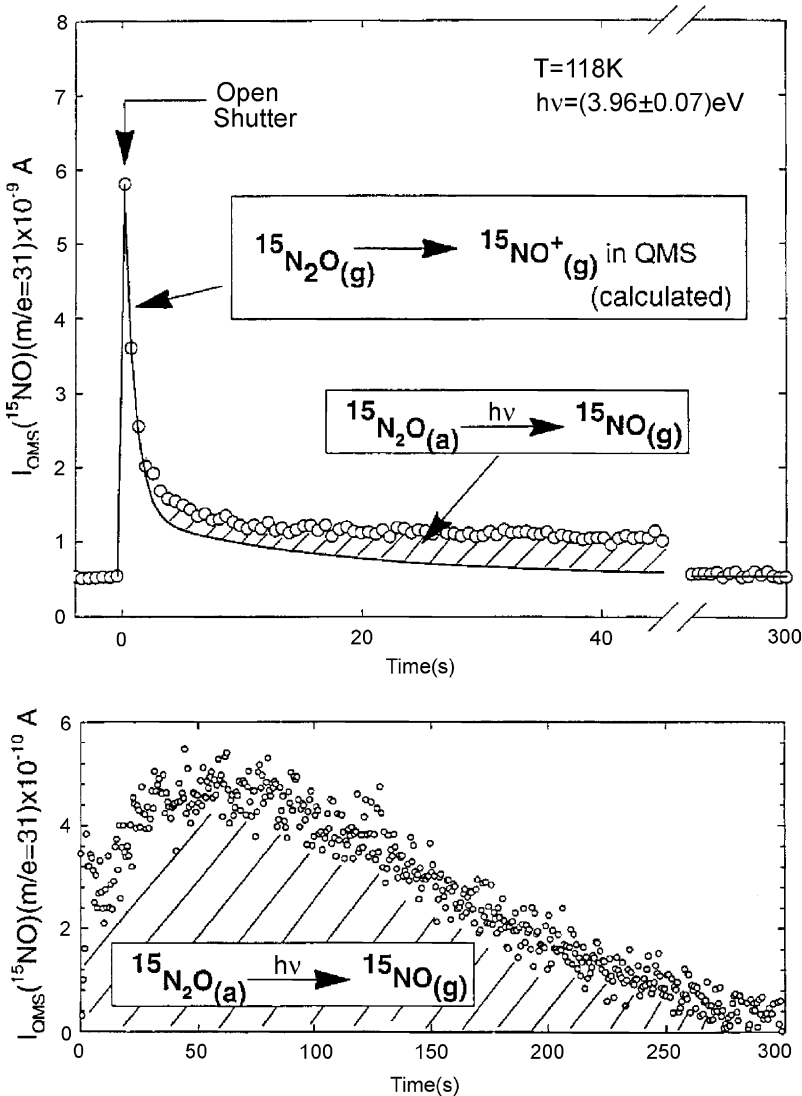


Fig. 55. ^{15}NO photodesorption from $\text{TiO}_2(1\ 10)$. In the upper panel is shown the decay rate of the ($m/e = 31$) signal with time. The majority of the signal originates from the $^{15}\text{NO}^+$ cracking product of an $^{15}\text{N}_2\text{O}$ photoproduct (represented by the continuous line in the upper panel). The cross-hatched region represents an additional photodesorption signal that originates as a result of the simultaneous production of NO which also yields an ($m/e = 31$) ion. From Rusu and Yates [531]. © 2000 The American Chemical Society.

related defects migrate towards the surface in the presence of NO_2 ; a thesis that is supported by DFT calculations [533]. This is yet another example for the importance of subsurface defects for the surface chemistry of TiO_2 . Such mechanisms are of potential importance when using an oxide for trapping or destroying NO_x species in the prevention of environmental pollution [533].

5.1.5.5. NH_3 . Ammonia adsorbs molecularly on $\text{TiO}_2(1\ 1\ 0)$ as well as $\text{TiO}_2(0\ 0\ 1)$ surfaces at room temperature. This was confirmed in several experiments [499,534–537] as well as theoretical calculations [538,539]. It binds with the N-end down to the fivefold coordinated Ti sites. ESDIAD measurements indicated that the H atoms are either randomly oriented or that the molecule is freely rotating around its C_{3v} axis [535]. These ESDIAD measurements were taken in a mass-resolved time-of-flight mode in order to suppress the O^+ signal from the $\text{TiO}_2(1\ 1\ 0)$ substrate that is emitted in normal direction [135]. The NH_3 overlayer efficiently neutralizes this O^+ signal [136]. On the stoichiometric substrate, electron bombardment results predominantly in desorption of the whole molecule and has a relatively small dissociation cross-section. On a sputter-reduced substrate, however, N–H bond scission dominates and e-beam bombardment can be used to form a Ti–O–N compound even at low temperatures [534,535]. Surprisingly, the NH_3 saturation coverage at room temperature is *smaller* on a UHV-annealed surface with point defects than on a stoichiometric surface. This can be explained if one assumes that NH_3 molecules bind more strongly to defect sites and effectively ‘block’ neighboring, regular Ti(5) adsorption sites [534,540]. When an oxygen deficient $\text{TiO}_2(1\ 1\ 0)$ surface is exposed NH_3 , the vacancies are filled up in a dissociative process. The resulting adatom leads to increased dissociation of the NH_3 molecule, similar to the case of $\text{O}_2/\text{H}_2\text{O}$ co-adsorption [499].

5.1.6. Sulfur-containing molecules (SO_2 , H_2S , S_n)

The removal of sulfur compounds from feedstocks is an important issue in the petrochemical industry. Sulfur poisoning of catalysts is a serious and costly problem in many refining processes. Reduction of sulfur content reduces corrosion, and environmental regulations limit the output of sulfur to the environment. Thus, fundamental insight into the interaction of S-containing molecules with model catalysts can possibly help to develop sulfur-resistant catalysts as well as catalysts for hydrodesulfurization. Technologically the Claus process



is used for hydrodesulfurization. It is mainly carried out on alumina catalysts, but titania is also used [11]. Adsorption and reaction of all molecules involved in the Claus process have been investigated on $\text{TiO}_2(1\ 1\ 0)$ surfaces (Table 13).

5.1.6.1. SO_2

5.1.6.1.1. $\text{TiO}_2(1\ 1\ 0)$. Several groups have studied the adsorption of SO_2 on $\text{TiO}_2(1\ 1\ 0)$, and somewhat conflicting reports were given on the surface chemistry of this system [541–545]. Smith et al. [543,544] detected no change in photoemission spectra from $\text{TiO}_2(1\ 1\ 0)$ for SO_2 exposures up to 10^6 L. It was concluded that SO_2 interacts only weakly with stoichiometric $\text{TiO}_2(1\ 1\ 0)$. However, a ‘violent’ interaction with sputtered surfaces was found, where SO_2 dissociates at defect sites. In fact, these authors reported that SO_2 exposure oxidizes sputter-reduced TiO_2 surfaces completely within the information depth of photoemission. SO_2 -induced oxidation was also found on single-crystalline Ti_2O_3 surfaces [543,544]. This implies that sub-surface defects migrate to the surface where they react, similar to the process that was invoked in a more recent study on NO_2 adsorption [533]. Smith and Henrich [544] found no indication for S–O bonds in XPS after exposure of SO_2 to a sputtered surface, and concluded that the S atom binds to Ti sites, forming TiS_2 -like structures.

Table 13

Survey of the adsorption of S-containing inorganic molecules on TiO₂ surfaces

	Substrate	Techniques/adsorption/reaction	Reference
SO ₂	Rutile (1 1 0)	UPS, XPS, weak interaction with stoichiometric surface, oxidizes sputtered TiO ₂ (1 1 0) completely at room temperature	[543,544]
	Rutile (1 1 0), (4 4 1)	XPS, UPS, LEED, SO ₃ ²⁻ on TiO ₂ (1 1 0) and stepped TiO ₂ (4 4 1), reacts with Ti ³⁺ to form S ²⁻	[545]
	Rutile (1 1 0)	NEXAFS	[541,542]
	Rutile (1 1 0)	ESD, ESDIAD	[546–549]
	Rutile (1 0 0), (1 × 1) and (1 × 3)	NEXAFS, chemisorbed SO ₂ (with molecular plane parallel to the surface) and SO ₄ ²⁻ ; SO ₂ reacts to SO ₄ ²⁻ at elevated temperature	[550,551]
H ₂ S	Rutile (1 1 0)	Photoemission on Ar ⁺ bombarded surface initial dissociation followed by molecular adsorption	[544,552]
	Rutile (1 1 0)	Cluster calculation, weak adsorption	[242,519]
S _n (<i>n</i> ≥ 2)	Anatase (1 0 1)	First-principles MD calculations, molecular adsorption	[553]
	Rutile (1 1 0)	STM, XPS, LEED, photoemission, adsorbs at Ti(5) and O vacancies at room temperature, replaces O at high temperature (Fig. 56); (3 × 1), (3 × 3), and (4 × 1) superstructures at 100–400 °C, depending on coverage; replacement of O atoms is mediated by bulk defects, see Fig. 58	[71,77,555,556,559]
	Rutile (1 1 0)	Photoemission, DFT calculations, adsorption at Ti sites, O vacancies, and SO _x at room temperature, S ₂ and S _n at low temperature; adsorption at high temperature involves <i>bulk</i> O vacancies	[557,558,779]

Onishi et al. [545] reported that SO₂ adsorbs on TiO₂ surfaces to form an SO₃²⁻-like complex. On a (stepped) TiO₂(1 1 0) surface, SO₃²⁻ was found as well as oxidation of Ti³⁺ sites, which was probably connected with the dissociation of the molecule [545]. NEXAFS measurements in Thornton and coworkers [541,542] point toward a chemisorbed SO₂ species at 100 K, which reacts to form SO₄²⁻ when the substrate is heated to temperatures ≥135 K. This surface sulfate species stays at the surface up to 450 K. A SO₃-like species was identified as the intermediate in this reaction. A model was suggested where the SO₂ molecule is incorporated into the bridging oxygen rows [541]. A small amount of S²⁻ species was also identified on the sample and attributed to dissociation at surface vacancies. Electron-stimulated desorption of SO₂ on TiO₂(1 1 0) was investigated by de Segovia and co-workers [546–549]. Adsorption of SO₂ as well as annealing an SO₂-covered surface changes the O⁺ ion yield and energy distribution. The ESDIAD pattern was not changed from the one of a clean surface, however.

5.1.6.1.2. TiO₂(1 0 0). Thornton's group also performed NEXAFS studies on SO₂ adsorbed on TiO₂(1 0 0) [550,551]. The surface chemistry on TiO₂(1 0 0) is also similar to the one on TiO₂(1 1 0), and the results from the TiO₂(1 0 0)-(1 × 1) resembled those from (1 × 3) reconstructed surfaces. SO₂ chemisorbs on TiO₂(1 0 0), and a ~0.5 ML coverage was achieved at 110 K. Polarization-dependent NEXAFS measurements were performed at substrate temperatures of 130, 200, and 500 K, in order to determine the geometry of SO₂, SO₃²⁻, and SO₄²⁻, respectively. Models were proposed where SO₂ adsorbs at exposed fivefold coordinated Ti sites, and both, SO₃²⁻ and SO₄²⁻, form through interaction with the bridging oxygen rows [550].

5.1.6.2. H_2S . The interaction of H_2S with TiO_2 surfaces was studied by Smith and Henrich [544,552] using photoemission techniques. The molecule interacts weakly with TiO_2 . UPS spectra were interpreted as dissociation of the molecule for small exposures, followed by molecular adsorption. A cluster calculation was performed with only one test geometry, i.e., with H_2S adsorbed with the S-end down and the hydrogens confined to the (0 0 1) plane [242,519]. A relatively large $Ti-S$ distance (3.1 Å) and a small interaction energy (7.0 kcal/mol) was found. As pointed out by the authors of this study [242,519], these values should be treated with caution because of the limited test geometries considered and the neglect of interadsorbate interactions. DFT-based slab calculations [553] on anatase (1 0 1) predict molecular adsorption with the plane of the molecule parallel, due to interaction between H and O atoms at the ridges of the anatase (1 0 1) surface (see Fig. 28). An adsorption energy of 0.49 eV (11.3 kcal/mol) was calculated.

5.1.6.3. Elemental sulfur (S_n , $n \geq 2$). The adsorption and reaction of elemental sulfur with TiO_2 was studied by this author's group as well as by Hrbek, Rodriguez, and co-workers, see Table 13. Sulfur was dosed from a UHV-compatible, electrochemical source as described by Bechtold and co-workers [554]. Such a source typically delivers elemental sulfur in the form of S_n ($n \geq 2$). The adsorption behavior, mechanism, and the resulting surface structures on $TiO_2(1\bar{1}0)$ depend drastically on the sample temperature, see Fig. 56.

When sulfur is dosed at room temperature, it dissociates and adsorbs at the fivefold coordinated Ti atoms, probably in an on-top configuration [77,555,556]. This can clearly be seen in Fig. 56A where S atoms are visible as large, white spots situated along the bright rows of the empty-states STM image. The S atoms are quite mobile in STM and no ordered superstructure appears at higher coverages. Sulfur also adsorbs readily on oxygen vacancies as evidenced by the disappearance of the defect-related band gap state in valence band photoemission spectra [556]. High-resolution core-level spectra were fitted with three peaks that were attributed to SO_x groups as well as sulfur bonded to Ti rows and O vacancies [557]. In addition, S_2 and S_n species were detected on the surface after sulfur was dosed at low temperature.

When S is dosed at elevated temperature (≥ 120 °C), or when a surface is first exposed to S at room temperature and then heated up, S switches adsorption sites from the position of the Ti rows to the position of the bridging oxygen rows (Fig. 56B). The S2p core level binding energy in XPS shifts to lower binding energy, contrary to what is expected for SO_x formation. Also, the Ti2p core levels show a

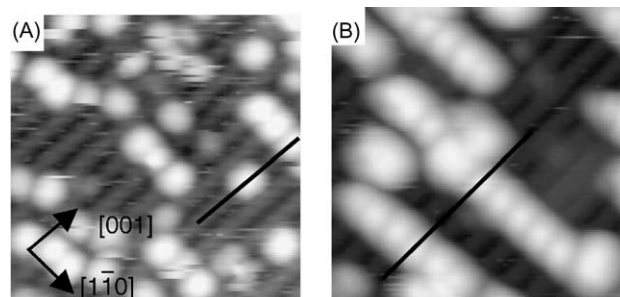


Fig. 56. Empty-states STM images of sulfur adsorbed on $TiO_2(1\bar{1}0)$. (A) At room temperature, bright S atoms are located at the bright rows (at the fivefold coordinated Ti atoms). (B) Sulfur dosed at 300 °C. Sulfur is located at the dark substrate rows (at the position of the bridging oxygen rows).

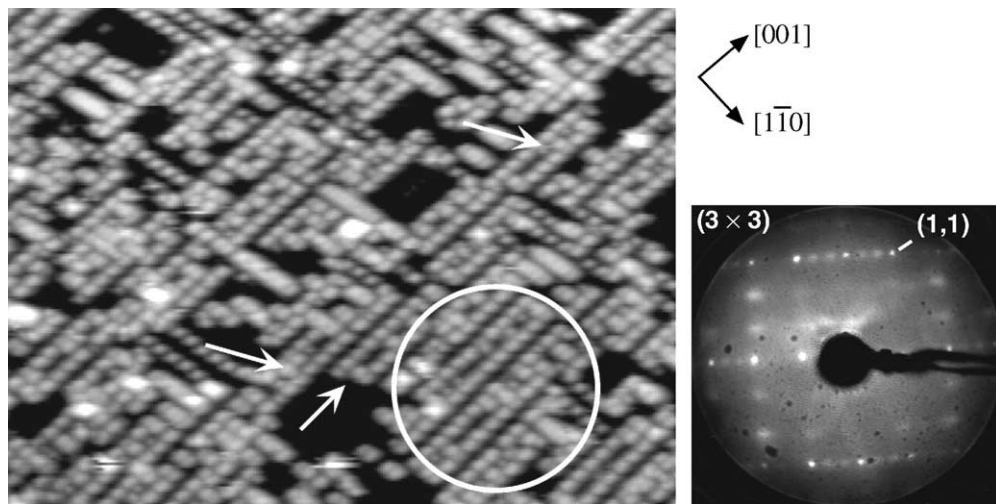


Fig. 57. STM and LEED of 0.55 ML sulfur adsorbed at 400 °C, forming a (3 × 3)-S superstructure. In the STM image ($300\text{ \AA} \times 220\text{ \AA}$, +1.4 V, 0.5 nA) bright double rows run along the [0 0 1] direction. Occasionally, additional S atoms adsorb within these rows, some of which are marked by arrows. A model was suggested where these rows represent sulfur atoms that have replaced in-plane oxygen atoms. From Hebenstreit et al. [555]. © 2001 Elsevier.

distinct shoulder [77,220,557], and a Ti3d-derived state appears in the band gap [556]. This points towards a *replacement* of bridging oxygen atoms, rather than an adsorption on them. Depending on the sample temperature and S coverage, different superstructures evolve at the $\text{TiO}_2(1\ 1\ 0)$ surface [77,555]. A (3 × 1)-S, (3 × 3)-S, and (4 × 1)-S structure was observed with LEED and STM. An example for a S-induced superstructure is shown in Fig. 57. The preparation parameters, structural units, and adsorption models of these structures are discussed in [77,555]. They consist of S atoms replacing surface oxygen atoms, both the in-plane and bridging oxygens. The electronic structure of these high-temperature adsorption states was mapped out with resonant photoemission [556].

Hrbek et al. [558] observed that virtually all surface oxygen can be replaced by S within the information depth of XPS. The replacement of oxygen by S is thermodynamically ‘uphill’, i.e., the heat of formation of Ti–S bonds is lower than that of Ti–O bonds. Also, the reaction takes place at rather low temperature ($\geq 120\text{ }^\circ\text{C}$), where desorption of O atoms is unlikely. There is experimental and theoretical evidence [71,557–560] that bulk defects are involved in the surface sulfidation process. For example, it was observed that S, adsorbed at room temperature, does not react with the surface but only desorbs on a light, slightly reduced sample. However, when the experiment was repeated with a darker, more bulk-reduced sample, some of the S stayed at the surface up to fairly high coverages, and this S switched the adsorption site. Fig. 58 shows another example of the influence of bulk defects on S adsorption [559]. A pristine, stoichiometric sample was cleaned and then exposed to S at 300 °C; at this temperature, S replaces oxygen. The S coverage was measured with XPS. The sample was then cleaned and heated for several hours in UHV to a temperature of 700 °C. This caused an increase in the level of bulk reduction, and a darkening of the sample color. The adsorption experiment was then repeated with the same S flux and exposure time. The amount of adsorbed S increased with the level of bulk reduction. The following model was suggested to account for the observed behavior: at elevated temperatures, bulk defects (O vacancies and Ti interstitials) become mobile and can migrate to the surface. Sulfur adsorbs at the

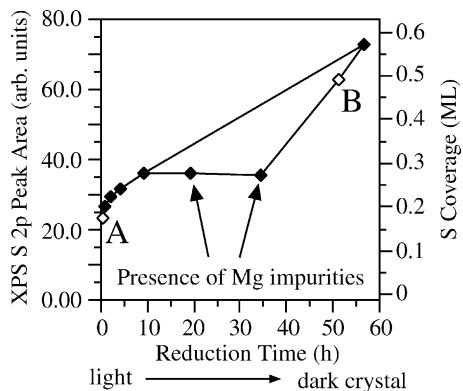


Fig. 58. Sulfur coverage of S/TiO₂(1 1 0) after adsorption at 300 °C. Each data point represents a separate adsorption experiment with similar S flux and exposure time. The cleaned sample was reduced between the experiments by heating at 700 °C in UHV. The more reduced the bulk of the sample becomes the more S adsorbs at the surface. The second increase of the lower curve is caused by the depletion of Mg-segregated impurities due to cleaning cycles (sputtering and annealing). From Hebenstreit et al. [559]. © 2001 Elsevier.

fivefold coordinated Ti atoms on the TiO₂(1 1 0) surface. It is weakly bound, rather mobile, diffuses along the Ti rows, and desorbs after a while. If the S atom encounters an oxygen vacancy (or a Ti interstitial), it reacts, binds more strongly, and becomes trapped. The probability of the latter process increases with the concentration of bulk defects, and the flux of defects to the surface.

It was pointed out that such a bulk-defect dependent adsorption process might be important in the behavior of titania as desulfurization catalyst and in the design of more S-resistant catalytic materials.

5.1.7. Halogen-containing molecules (Cl₂, CrO₂Cl₂, HI)

5.1.7.1. Cl₂. The adsorption of Cl at TiO₂(1 1 0) was studied experimentally [106,109,561] as well as theoretically [106,562]. The chlorine was dosed from an electrochemical source [554] in the form of Cl₂. It dissociates at room temperature and adsorbs at the fivefold coordinated Ti atoms in an on-top configuration [106,562]. Oxygen vacancies, if present, are filled preferentially [106,561], Table 14.

Table 14
Survey of the adsorption of halogen-containing inorganic molecules on TiO₂ surfaces

	Substrate	Techniques/adsorption/reaction	Reference
Cl ₂	Rutile (1 1 0)	STM, dissociates, high transient mobility ('cannon-ball' adsorption) at low coverages, see Figs. 59 and 60	[109]
	Rutile (1 1 0)	DFT calculations, STM, photoemission, precursor adsorbs at Ti ⁴⁺ ions, adsorption in oxygen vacancies is favored	[106]
	Rutile (1 1 0)	DFT calculations	[562]
	Rutile (1 1 0)	STM, XPS, photoemission, adsorbs at Ti(5) at room temperature, replaces O at elevated temperatures	[561]
CrO ₂ Cl ₂	Rutile (1 1 0)	TPD, AES, workfunction, SSIMS, XPS	[570]
HI	Anatase (1 0 1)	First-principles MD calculations, dissociative adsorption	[553]

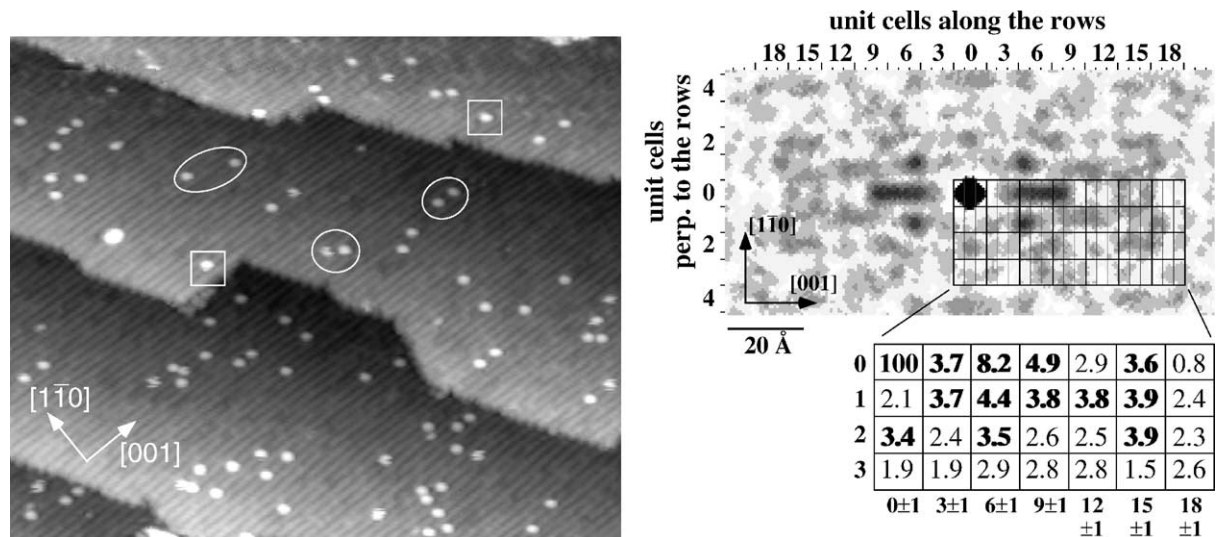


Fig. 59. Left: STM image of a $\text{TiO}_2(1\bar{1}0)$ surface exposed to 0.07 Cl_2 at room temperature ($400\text{\AA} \times 380\text{\AA}$, $V_s = +1.6\text{ V}$, $I_t = 1.6\text{ nA}$). Adsorbed chlorine atoms appear as bright round spots on the bright rows parallel to the $[001]$ direction (on fivefold coordinated Ti atoms). Most Cl atoms are paired. Some of the Cl–Cl pairs and single chlorine adatoms are marked with circles and squares, respectively. Right: autocorrelation of Cl–Cl distances in STM images with the same Cl coverage as shown on the left side. Probabilities are given for areas of three unit cells to smooth the statistical scatter and to account for the limited accuracy of position determination along $[001]$. Probabilities that are significantly higher than the average value of 2% are printed in bold. From [109].

The adsorption mechanism of Cl is quite interesting, as it represents an experimental verification of ‘hot’ surface atoms (atoms with high kinetic energy that result from a dissociative adsorption process) which is a matter of some debate in the literature [563–567]. At low coverages, deposited at room temperature, clearly correlated Cl–Cl pairs are observed [109], see Fig. 59. This was explained with the

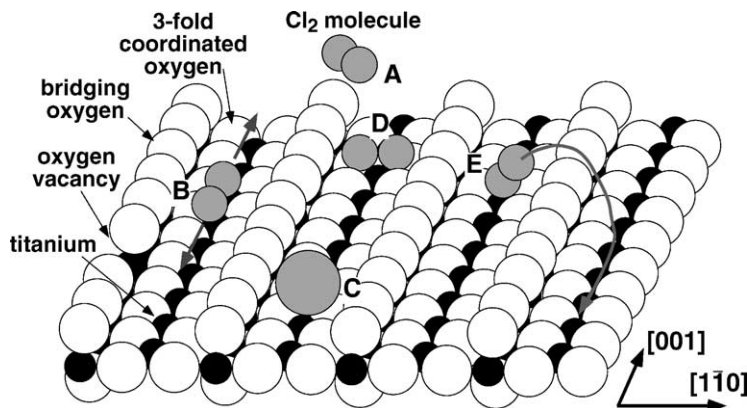


Fig. 60. Model for the high transient mobility of chlorine atoms that gives rise to the widely separated Cl–Cl pairs in Fig. 59. Labels (A)–(E) are explained in the text. From [109].

model in Fig. 60. The Cl_2 molecule approaches the surface (A). Cl_2 dissociation on Ti atoms is an exothermic process, and part of this excess energy can be transferred into kinetic energy. If a Cl_2 molecule dissociates in a trough (B) the Cl atoms stay confined to the Ti rows and can possibly move a long distance before their energy is accommodated (B). The distribution of Cl pairs in Fig. 59 points towards a correlation across bridging oxygen rows as well, however. Such widely spaced Cl–Cl pairs could be explained by a ‘cannon-ball’ mechanism where the Cl_2 molecule adsorbs in an approximately upright position (E). One Cl atom ‘shoots’ out into the vacuum, similar to an abstractive adsorption process observed for halogens on Si [568,569]. Because of the high electronegativity of chlorine, this atom will likely be negatively charged, and attracted by its own image charge. It was suggested [109] that, depending on the orientation of this nanoscopic ‘cannon’, this Cl atom may land in the neighboring trough or even further away from the original adsorption point. (The configurations labeled D and C in Fig. 60 describe the (unlikely) scenario that Cl_2 dissociates in a precursor that is oriented perpendicular to the Ti rows (D) and the van-der Waals radius of an Cl^- ion, respectively.) When the ‘cannon’ is oriented perpendicular to the surface, the Cl is emitted into the vacuum. The presence and number of ‘single’ Cl atoms in Fig. 59 was taken as an indicator for this ‘cannonball’ process.

The described mechanism was based on STM images alone. More recent photoemission results have shown that Cl adsorbs also in O vacancies, as the defect-related gap state in photoemission spectra is quenched rapidly when Cl is dosed to a slightly defective surface at room temperature. FLAPW calculations indicate that Cl atoms that are adsorbed in oxygen vacancies will not be observed with STM, as they are expected to have an image contrast similar to bridging oxygen atoms [106]. This implicates that the ‘single’ Cl atoms in Fig. 59 could be the ‘leftover’ partner from a dissociated Cl_2 pair where the other Cl atom fills a vacancy in the bridging oxygen rows. As pointed out in [561] these recent insights would then lead to a slight modification of the originally proposed model. The Cl molecule could also ‘explode’ above the surface. This explosion would be initiated by capture of an electron from the surface which would result in an unstable Cl_2^- moiety. The resultant Cl^- ions could possibly cover large distances above the surface before they land in a trough.

The FLAPW calculations mentioned above also predicted that adsorption of a Cl atom in an O vacancy is an energetically much more stable situation as compared to Cl adsorption at the sites of the fivefold coordinated Ti atoms [106]. STM measurements of chlorine adsorption [561], performed at elevated temperature, confirm this prediction. When Cl is dosed above a temperature of ~ 150 °C, the Cl replaces bridging oxygen atoms. Other features, possibly some sort of Ti–O–Cl complex, are also formed. The high-temperature adsorption process is mediated by bulk defects, similar to the process discussed in the context of S adsorption (Fig. 58). The calculations also investigated the STM image contrast of adsorbed Cl [106]. As pointed out several times, the STM image contrast on TiO_2 is largely electronic. Hence it is somewhat surprising that a negatively charged atom with hardly any empty DOS should be imaged bright in empty-states STM images. Analysis of calculated charge-density contours shows that the unfilled Ti states underneath the adsorbed Cl atom are considerably changed which leads to the observed bright spots in STM.

5.1.7.2. Other halogen-containing molecules. Hazardous hexavalent Cr(VI) is often present in waste water streams, and TiO_2 can be useful for the photoreduction of Cr(VI) to the more benign trivalent Cr(III). With this application in mind, the adsorption of chromyl chloride on $\text{TiO}_2(1\ 1\ 0)$ was studied with surface science techniques by Alam et al. [570]. It was suggested that the reduction and potential

Table 15

Survey of the adsorption of rare gas atoms on TiO₂ surfaces

	Substrate	Techniques/adsorption/reaction	Reference
Ar + H ₂ O	Rutile (1 0 0), (1 1 0)	Computer simulation of adsorption isotherms	[572]
Xe	Rutile (1 1 0)	Monte Carlo simulation	[573]
	Rutile (1 1 0)	Simulations, Xe behaves fluid-like in 1D troughs along [0 0 1]	[574]

immobilization of Cr(VI) species on TiO₂ materials may occur thermally if the appropriate surface defect sites are present. The adsorption and photo-oxidation/desorption of methyl halides is treated in [Section 5.3.1](#). The adsorption of hydrogen iodide on anatase (1 0 1) was treated with first-principles molecular dynamics simulations by Selloni et al. [\[553\]](#). The molecule dissociates and binds with an adsorption energy of 0.67 eV (15.45 kcal/mol).

5.1.8. Rare gases (Ar, Xe)

This author is not aware of any experimental studies of rare gas adsorption on single-crystalline TiO₂ surfaces. One exception is a study of Pt growth on TiO₂, where photoemission of adsorbed Xe (PAX) was used as a spectroscopic technique to measure changes in the local work function [\[571\]](#). The adsorption of Ar [\[572\]](#) and Xe [\[573,574\]](#) has been simulated with Monte-Carlo methods, however.

It should be mentioned here that substantial amounts of Ar can be found in AES and XPS measurements of previously sputtered samples, even if their surfaces have been fully annealed. Ar atoms that are trapped sub-surface have an influence on surface chemistry on metals [\[575,576\]](#), but it has not been investigated if a similar effect exists on TiO₂ ([Table 15](#)).

5.2. Adsorption and reaction of organic molecules

This part is divided into subsections where organic adsorbates are loosely grouped by their functional groups. The main results of adsorption and reaction studies on these adsorbates are summarized in table format. Formic acid and other carboxylic acids have become the most investigated organic molecules on single-crystalline TiO₂ surfaces ([Table 16\(a\)](#)). Because many of the higher carboxylic acids follow the behavior of formic acid, the adsorption and reaction of HCOOH is discussed in some detail in the first part of [Section 5.2.1](#).

A large number of reactions of higher organic molecules was studied in Barteau's group. Differently prepared TiO₂(0 0 1) surfaces were used, in particular two differently reconstructed surfaces, which are commonly referred to as '{1 1 4}'- and '{0 1 1}-faceted' surfaces,³ see [Section 2.4](#). The UHV studies were often compared to results from powder materials. A particularly intriguing reaction is the isomerization of alkynes ([Section 5.2.4](#)). This reaction is very sensitive to the reduction state of the sample. Some of the results are summarized in the following, but the reader is also referred to a series of excellent review articles by Barteau et al. [\[6,551,577–580\]](#) on the adsorption and reaction of higher organic molecules.

³ According to recent STM results, the assignment of these reconstructions as faceted surfaces is questionable, see [Section 2.4](#) and [Fig. 25](#). An atomic model is still lacking at this point, thus these surfaces are still quoted as '{1 1 4}-faceted' and '{0 1 1}-faceted'.

Table 16

Survey of the adsorption and reaction of organic molecules on TiO₂ surfaces

Molecule	Substrate	Adsorption/reaction	Reference
(a) Survey of the adsorption and reaction of carboxylic acids on TiO ₂ surfaces			
Formic acid, HCOOH	All rutile surfaces	Dissociative adsorption as formate plus hydroxyl; molecular at low temperatures and higher coverages	Reviews, see [551]
	Rutile (1 1 0)	Orders as p(2 × 1) structure with 0.5 ML coverage above 250 K; STM shows c(4 × 2) overlayer at 22% of the saturation coverage	[581,599]
	Rutile (1 1 0)	Adsorption geometry from photoelectron diffraction, see Fig. 61	[585,586]
	Rutile (1 1 0)	Adsorption geometry from NEXAFS	[589]
	Rutile (1 1 0)	Vibrational spectra, detection of minority species (Fig. 61) from IRAS	[588]
	Rutile (1 1 0)	Vibrational spectra from HREELS	[582,585]
	Rutile (1 1 0)	Non-contact AFM of single formate ions	[594,595,600]
	Rutile (1 1 0)	STM of single formates	[108]
	Rutile (1 1 0)	STM: diffusion mainly along [0 0 1] direction, see Fig. 62	[596,598]
	Rutile (1 1 0)	Theory: diffusion influenced by neighboring H atoms	[591]
	Rutile (1 1 0)	Theory: (CRYSTAL program) acidic cleavage; leads to bi-dentate formate	[592]
	Rutile (1 1 0)	Theory: DFT and pseudo-plane wave, dissociative adsorption	[102]
	Rutile (1 1 0)	switchover from dehydration (DCOOD → CO ₂ + H ₂ O) to dehydrogenation (DCOOD → CO and H ₂) around 500 K	[581,606]
	Rutile (1 1 0)	CO main decomposition product, small amounts of H ₂ CO, desorption of H ₂ O before onset of decomposition; scrambling with ¹⁸ O from ¹⁸ O-enriched surface	[582]
	Rutile (1 1 0)- (1 × 2) (added 'Ti ₂ O ₃ ' row)	STM: no adsorption at (1 × 2) rows	[122]
Highly reduced rutile (1 1 0), cross-linked (1 × 2)		STM: adsorption at cross-links, high-temperature reaction, produces (1 × 1) islands (Fig. 63)	[584]
Rutile (1 1 0), Ar-bombarded		Dehydration and dehydrogenation independent of annealing history of ion-bombarded sample	[780]
Defective rutile (1 1 0) (defects by sputtering, e-beam)		Coverage scales with reduced Ti sites	[593]
Thin TiO ₂ film		Adsorption as bi-dentate on (1 1 0)-terminated surface, as monodentate at c(2 × 6) surface	[432]
Rutile (4 4 1)		Adsorption at step edges in possibly tilted configuration	[545]
Rutile (1 0 0)-(1 × 3)		Scrambling with ¹⁸ O from ¹⁸ O-enriched surface, decomposition at 550 K to CO, H ₂ CO; trace of HC=CH; H ₂ O desorbs before HCOOH decomposition	[196]

Table 16 (Continued)

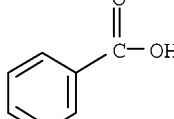
Molecule	Substrate	Adsorption/reaction	Reference
	Rutile (1 0 0)-(1 × 1)	Main decomposition product CO, no HC≡CH or H ₂ CO; H ₂ O desorbs before decomposition	[196]
	Rutile (0 0 1)-‘{1 1 0} faceted’	Unimolecular HCOOH decomposition above 550 K to CO and CO ₂	[603]
	Rutile (0 0 1)-‘{1 1 4}-faceted’	Formation of H ₂ CO in addition to CO and CO ₂	[603]
	Rutile (0 0 1)	On reduced surface: H ₂ CO via unimolecular decomposition, oxidizes surface; on oxidized surface: H ₂ CO via bimolecular coupling of two HCOO ⁻ molecules	[583]
	Anatase (1 0 1)	Theory: DFT slab calculations, HCOOH adsorbs molecularly as monodentate, desorption promoted by co-adsorbed water, NaCOOH adsorbs dissociatively as bi-dentate	[605]
Acetic acid, CH ₃ COOH	All rutile surfaces	Dissociative adsorption to acetate and hydroxyl	[551]
	Rutile (1 1 0)	STM, ESDIAD, LEED: (2 × 1) overlayer, molecule stands upright	[608,614, 781,782]
	Rutile (1 1 0)	NEXAFS: molecule stands upright	[589]
	Rutile (1 1 0)	Non-contact AFM measurements	[600,610,611]
	Rutile (1 1 0)- (1 × 2) (added Ti ₂ O ₃ row)	STM at 580 K shows decrease of acetate coverage, possibly via decomposition into ketene	[609]
	Rutile (0 0 1) sputtered; ‘{0 1 1}-faceted’; ‘{1 1 4}-faceted’	No ordered overlayer in LEED, saturation acetate coverage at room temperature ca. half of that on the TiO ₂ (1 1 0)	[608,781]
	Rutile (1 1 0)	Adsorbs both molecularly and dissociatively at 200 K, only dissociatively at 300 K; decomposition products depend on surface pretreatment, see Fig. 66	[604]
Propanoic acid, C ₂ H ₅ COOH	Rutile (1 1 0)	NEXAFS: p(2 × 1) overlayer at 300 K, acetate in a bi-dentate coordination and upright position	[551,589]
	Rutile (0 0 1) sputtered; ‘{0 1 1}-faceted’; ‘{1 1 4}-faceted’	TPD; dominant reaction products: CO, CO ₂ , C4 products (butene, butadiene), acrolein; divinyl ketone (only on ‘{1 1 4}-faceted’ surface)	[604]
Acrylic acid, CH ₂ =CHCOOH	Rutile (0 0 1) sputtered	TPD, XPS, scanning kinetic spectroscopy; reaction products contain ethene, ethyne, butene, butadiene, divinyl ketone (only on ‘{1 1 4}-faceted’ surface)	[612]
Benzoic acid, C ₆ H ₅ COOH 	Rutile (0 0 1) sputtered; ‘{0 1 1}-faceted’; ‘{1 1 4}-faceted’	Adsorbs both molecularly and dissociatively at 200 K, only dissociatively at 300 K; decomposition products depend on surface pretreatment	[604]
	Rutile (1 1 0)	ESDIAD and LEED: p(2 × 1) overlayer at 300 K, benzoate with upright aromatic ring; dimerization in STM	[551,613]

Table 16 (Continued)

Molecule	Substrate	Adsorption/reaction	Reference
Bi-isonicotinic acid 	Rutile (1 1 0)	NEXAFS, XPS, Hartree–Fock calculations; see Fig. 67 for adsorption geometry; molecular at multilayers	[615,783]
Oxalic acid, HOOC–COOH	Rutile and anatase 'polymers'	Dissociative adsorption as oxalate ($\text{C}_2\text{O}_4^{2-}$) ions, more strongly on 'anatase' than 'rutile' models	[617]
Glycine 	Rutile (1 1 0)	UPS, SXPS: adsorbs as zwitterionic ion; high cross-section for photon damage	[618]
Maleic anhydride 	Rutile (1 1 0)-(1 × 2)	UPS, SXPS	[619]
	Rutile (0 0 1), sputtered	TPD, semi-empirical calculations show dissociation of one COC bond upon adsorption; decomposition into CO, CO_2 , acetylene ($\text{HC}\equiv\text{CH}$), ketene ($\text{H}_2\text{C}=\text{C}=\text{O}$), vinylacetylene ($\text{HC}\equiv\text{CCH}=\text{CH}_2$), butene, traces of butadiene ($\text{H}_2\text{C}=\text{CHCH}=\text{CH}_2$), and benzene (C_6H_6)	[620]

(b) Survey of the adsorption and reaction of alcohols on TiO_2 surfaces

Methanol, CH_3OH	Various TiO_2 surfaces	For a review, see Ref. [551, Chapter 10]	
	Rutile (1 1 0)	XPS, UPS, LEED, TPD: molecular adsorption at 289 K, no ordered overlayer observed	[545]
	Rutile (1 1 0)	TPD, HREELS, SSIMS: majority of adlayer is molecular, some dissociative adsorption, see Fig. 68, recombines upon annealing; CH_3OH the only desorption product; co-adsorbed water has little or no influence on surface chemistry; co-adsorption of O_2 : O adatoms, produced by adsorption at vacancies at 300 K lead to increased dissociation; molecularly adsorbed O_2 at 150 K oxidizes CH_3OH to H_2CO	[621]
	Rutile (1 1 0)	Theory: dissociation and molecular adsorption have equivalent energy in high-coverage limit, dissociation preferred at low coverage	[102,623]
	Rutile (1 1 0)	Electron-bombardment of methanol adsorbed at 135 K	[151]
	Rutile (1 1 0)	Theory: electronic structure calculations, molecular adsorption is thermodynamically favored, but energetic barrier for proton transfer	[241]
	Rutile (1 0 0)	Theory: electronic structure calculations, molecular adsorption is thermodynamically favored	[241]
	Rutile (4 4 1)	Molecular adsorption	[545]
	Rutile (0 0 1) Ar^+ bombarded, '{0 1 1}-faceted', '{1 4 4}-faceted'	Molecularly adsorbed methanol desorbs below 300 K; 50% dissociated molecules recombine at 365 K, remaining methoxides decompose to CH_4 , dimethyl ether ($\text{CH}_3\text{O–CH}_3$), formaldehyde (CH_2O) and CO; selectivity of reaction products depends on surface	[627]

Table 16 (Continued)

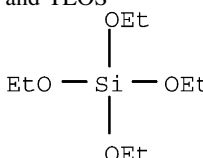
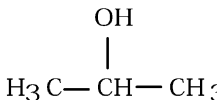
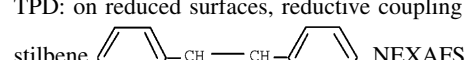
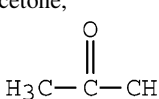
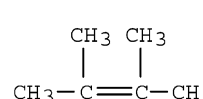
Molecule	Substrate	Adsorption/reaction	Reference
Ethanol, C ₂ H ₅ OH	Rutile (0 0 1) with point defects	UPS, TPD: dissociative adsorption at 300 K, coverage-dependent dissociation energy, main thermal desorption products H ₂ , CO, and CH ₃ OH; minor quantities of CH ₄ , CH ₂ O, and H ₂ O	[628]
D-Ethanol (EtOD) and TEOS	Rutile (0 0 1), '{0 1 1}-faceted'	TPD: both molecularly and dissociatively adsorbed at 200 K, only dissociatively at 300 K. Desorption products are ethylene (C ₂ H ₄) and acetaldehyde (CH ₃ CHO)	[629]
	Rutile (1 1 0)	TPD: formation of surface ethoxy groups by dissociative adsorption of deuterated ethanol or TEOS, co-adsorbed with water and hydroxyls; two ethoxy species: one that is bound to a Ti(5) atom, desorbs as ethanol at ~250–400 K; second ethoxy species adsorbs at oxygen vacancies and decomposes into ethylene and ethanol at 650 K	[630]
<i>n</i> -Propanol (CH ₃ –CH ₂ –CH ₂ –OH), 2-propanol	Rutile (0 0 1), '{0 1 1}-faceted'	TPD: dissociative adsorption; predominantly recombinative desorption; <i>n</i> -propanol decomposition into C ₃ H ₆ and C ₂ H ₅ CO; 2-propanol decomposition into C ₃ H ₅	[629]
			
2-Propanol	Rutile (1 1 0), (1 0 0)	Rutile (1 1 0): photocatalytic reaction to acetone and water in the presence of O ₂ ; rutile (1 0 0): thermally activated dissociation	[666–668]
(c) Survey of the adsorption and reaction of aldehydes on TiO ₂ surfaces			
Formaldehyde, H ₂ CO	Rutile (1 1 0)	TPD: deoxygenation at surface Ti ³⁺ sites when point defects are present	[490]
	Rutile (0 0 1)	TPD: oxidized surface: formation of methanol via the Cannizzaro reaction; on reduced surface formation of methanol, CO and CO ₂ , probably through complete decomposition into C _{ads} , H _{ads} , and O _{lattice}	[632]
Acetaldehyde, H ₃ C–C=O	Rutile (0 0 1)	TPD: aldol condensation to form crotonaldehyde, CH ₃ CH=CHCHO, and crotyl alcohol (CH ₃ CH=CHCH ₂ OH) on stoichiometric surfaces; butene, H ₃ C–CH ₂ –CH ₂ –CH ₃ on reduced surfaces	[633,634]
Benzaldehyde	Rutile (0 0 1)	TPD: on reduced surfaces, reductive coupling to stilbene  , NEXAFS investigations of reaction intermediates	[635,636]
Acetone, 	Rutile (0 0 1)	TPD: on reduced surfaces major pathway the reductive coupling to symmetric olefins with twice the carbon number of the reactant 2 acetone → 2,3-dimethyl-2-butene 	[638]

Table 16 (Continued)

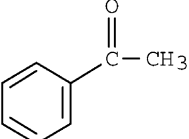
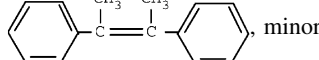
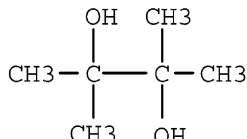
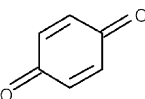
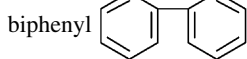
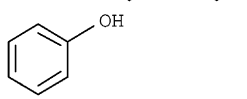
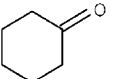
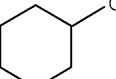
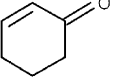
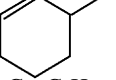
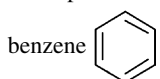
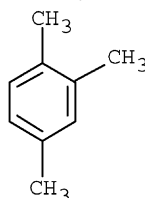
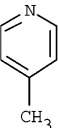
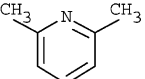
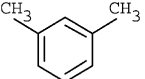
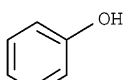
Molecule	Substrate	Adsorption/reaction	Reference
 Acetophenone	Rutile (0 0 1)	TPD: on reduced surfaces major pathway the reductive coupling to symmetric olefins with twice the carbon number of the reactant $2 \text{ acetophenone} \rightarrow 2,3\text{-diphenyl-2-butene}$  reaction path to pinacol 	[638]
 <i>p</i> -Benzoquinone	Rutile (0 0 1)	TPD: reduction and coupling reactions to benzene, biphenyl  terphenyl, and phenol 	[639,640]
 Cyclohexanone	Rutile (0 0 1)	TPD: on sputter-reduced surface reduction to cyclohexanol  and reductive coupling to $\text{H}_{10}\text{C}_6=\text{C}_6\text{H}_{10}$	[640]
 Cyclohexenone	Rutile (0 0 1)	TPD: on sputter-reduced surface reduction to cyclohexenol  and reductive coupling to $\text{H}_8\text{C}_6=\text{C}_6\text{H}_8$	[640]
(d) Survey of adsorption and reactions related to the trimerization of alkynes on TiO ₂ surfaces			
Acetylene, HC≡CH	Reduced rutile (0 0 1)	TPD: predominantly cyclomerization to	[641]
		 benzene	
Methylacetylene (butyne), $\text{CH}_3\text{C}\equiv\text{CH}$	Reduced rutile (0 0 1)	TPD: cyclotrimerization to trimethylbenzene	[641,642]
			

Table 16 (Continued)

Molecule	Substrate	Adsorption/reaction	Reference
2-Butyne (di-methylacetylene) $\text{CH}_3-\text{C}\equiv\text{C}-\text{CH}_3$	Reduced rutile (0 0 1)	TPD: predominantly cyclomerization to hexamethylbenzene 	[641]
<i>tert</i> -Butylacetylene 	Reduced rutile (0 0 1)	TPD: cyclization to the C ₁₈ -cyclotrimer 	[643]
Trimethylsilyl-acetylene, $(\text{CH}_3)_3\text{Si}-\text{C}\equiv\text{CH}$	Reduced rutile (0 0 1)	TPD: cyclotrimerization to tri-trimethylsilylbenzene 	[644]
Allene, $\text{H}_2\text{C}=\text{C}=\text{CH}_2$	Rutile (0 0 1)	TPD: reduced surfaces: principal reaction hydrogenation to propylene, $\text{H}_3\text{C}-\text{CH}=\text{CH}_2$; minor channels: dimerization to dimethylene, cyclobutane , benzene, and an open-chain C_6H_{10} dimer; dimerization is suppressed on oxidized surfaces	[645]
Cyclooctatetraene 	Rutile (0 0 1)	TPD: converts to benzene and cyclooctatriene on reduced TiO_2 , not a major intermediate of alkyne cyclooligomerization; NEXAFS of adsorption geometry	[646,647]
(e) Survey of adsorption and reactions of pyridine, its derivates, and other aromatic molecules on TiO_2 surfaces			
Pyridine 	Rutile (1 1 0)	TPD, XPS, STM, MD calculations: pyridine is weakly physisorbed, not bound to specific sites at $\text{TiO}_2(1\ 1\ 0)$ terraces; TPD: two peaks at 220 and 270 K, multilayers at 160 K; XPS: no peak shift of N1s, STM: high mobility	[650]

Table 16 (Continued)

Molecule	Substrate	Adsorption/reaction	Reference
4-Methylpyridine 	Rutile (1 1 0)	STM: diffuses at room temperature, strongly adsorbed at fourfold coordinated Ti atoms at step sites, activity of Ti step atoms depends on step orientation, exchange between pyridine adsorbed at step sites and terrace sites	[124]
	Rutile (1 1 0)	STM at elevated temperature and pyridine background pressure: condensation at partially hydrogenated pyridines	[652]
	Rutile (1 1 0)	Theory: DFT calculations of binding site	[653]
	Rutile (1 1 0)	STM: three adsorption geometries identified	[654]
2,6-Methylpyridine 	Rutile (1 1 0)	TPD similar to pyridine; STM: molecules are somewhat less mobile than pyridine	[650]
<i>m</i> -Xylene 	Rutile (1 1 0)	TPD similar to pyridine	[650]
Benzene 	Rutile (1 1 0) Rutile (1 0 0)- (1 × 1) and (1 × 3)	TPD: two peaks at 200 and 260 K, no multilayers AES, UPS, XPS: adsorbs tilted on (1 × 3), flat on (1 × 1) at submonolayers; electron-stimulated processes: X-ray or electron irradiation induces polymerization	[650] [651]
Phenol 	Rutile (1 1 0)	STM in air	[648,649]

(f) Survey of adsorption and reactions of silanes on TiO₂ surfaces

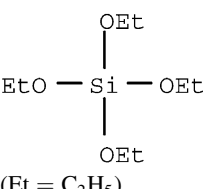
Tetraethoxysilane (TEOS)	Rutile (1 1 0)	TPD, LEED, XPS: dissociates between 200 and 350 K to form adsorbed Si(OEt) ₂ and EtO; EtO decomposes at 650 K to ethylene (CH ₂ =CH ₂) and H which react with EtO to form EtOH (ethanol); SiO ₂ remains on the surface; pre-dosed water: increases dissociation probability, reacts with adsorbed EtO form EtOH; Si(OEt) ₂ not affected by water	[656,630]
 (Et = C ₂ H ₅)			

Table 16 (Continued)

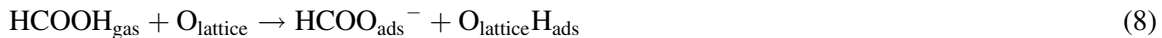
Molecule	Substrate	Adsorption/reaction	Reference
Vinyl-triethoxysilane (VTES)	Rutile (1 1 0)	XPS, TPD: dissociates and produces adsorbed Si(OEt)–(CH=CH ₂), and OEt _{ads}	[655]
Diethyl-diethoxy-silane (DEDS)	Rutile (1 1 0)	XPS, TPD: dissociates and produces adsorbed EtO; SiEt ₂ ; and EtOSiEt ₂ which are bound via Si–O–Ti bonds	[655]
Aminopropyl-triethoxysilane (APS)	Rutile (1 1 0)	XPS, TPD: does not dissociate on TiO ₂ (1 1 0)	[655]
(3,3,3-Trifluoro-propyl) trimethoxysilane (FPTS)	Rutile (1 1 0)	TPD, XPS, SSIMS: adsorbs dissociatively, forms CF ₃ CH ₂ CH ₂ SiOCH ₃ (bound via two Si–O _{lattice} bonds), and –OCH ₃ groups bound to Ti ⁴⁺ sites; 620 K: CF ₃ CH ₂ CH ₂ – ligand decomposes through elimination of β-H (forms CF ₃ CH=CH ₂ gas) or CF ₃ group (forms CH ₂ =CH ₂ gas); –OCH ₃ decomposes at 550–600 K to methane (CH ₄), formaldehyde (HCHO), and methanol (CH ₃ OH); co-adsorbed water: –OCH ₃ desorbs as methanol at ~300 K	[657]
(g) Survey of adsorption and photo-reactions of methyl halides on TiO ₂ surfaces			
CH ₃ Cl	Rutile (1 1 0)	Photo-oxidation with UV light: co-adsorbed molecular oxygen and surface defects essential for photo-oxidation; products H ₂ CO, CO, H ₂ O, HCl; no oxidation with hydroxyls without co-adsorbed oxygen	[664,665]
	Rutile (1 1 0)	Not active for photodesorption when adsorbed by itself, photodesorbs when co-adsorbed with CH ₃ I	[676]
CH ₃ Br	Rutile (1 1 0)	Single-photon desorption process for low fluences, substrate-mediated; laser-induced thermal desorption dominant for fluences $\geq 7 \text{ mJ/cm}^2$	[676]
CD ₃ I	Rutile (1 1 0)	TPD, XPS, irradiation with 254 and 334 nm photons	[671]
	Rutile (1 1 0)	Photodesorption at variable wavelength, REMPI: production of CD ₃ radicals; direct excitation of adsorbate of the primary mechanism	[672,673]

Table 16 (Continued)

Molecule	Substrate	Adsorption/reaction	Reference
CH_3I	Rutile (1 1 0)	TOF-REMPI: in multilayer film C–I bonds are aligned close to the surface normal in anti-parallel arrangement; at fractional monolayer coverage predominantly in a parallel orientation with the iodine close to the surface and the Me group pointing away from the surface	[670]
	Rutile (1 1 0)	Photodesorption with 257 nm of films adsorbed at 90 K; photofragments: CH_4 , C_2H_6 , I_2 , C_2H_2 , $\text{C}_2\text{H}_5\text{I}_2$, $\text{C}_2\text{H}_5\text{I}$	[674]
	Rutile (1 1 0)	Single-photon desorption process for low fluences, substrate-mediated; laser-induced thermal desorption dominant for fluences $\geq 7 \text{ mJ/cm}^2$	[676]
	Rutile (1 1 0)	Post-irradiation TPD of photofragments	[675]
	Rutile (1 1 0)	Photodesorption (257 and 320 nm) in dependence of thickness: Antoniewicz-type mechanism up to 1 ML; suppressed photodesorption yield between 1 and 5 ML; solvation of excited substrate electron into overlayer for coverages $> 5 \text{ ML}$ and subsequent desorption from the surface	[677]
	Rutile (1 1 0)	TPD and photodesorption; films grow stochastically at 90 K, change of film morphology with annealing	[678]

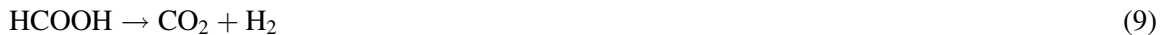
5.2.1. Carboxylic acids (formic acid, acetic acid, propanoic acid, acrylic acid, benzoic acid, bi-isonicotinic acid, oxalic acid, glycine, maleic anhydride)

5.2.1.1. *Formic acid (HCOOH)*. Two recent reviews (Chapters 6 and 10 in [551]) give excellent summaries of the adsorption geometry and chemistry of formic acid on TiO_2 , respectively. Generally, formic acid dissociates at rutile TiO_2 surfaces to give formate



Here the H atom forms a hydroxyl with a surface atom $\text{O}_{\text{lattice}}$. Quantitative information about the adsorption sites, geometry, and lateral interaction between formates and hydroxyls were obtained, see the next section.

Usually, two principal overall decomposition reactions are considered to occur at elevated temperatures. Either dehydrogenation, which produces carbon dioxide and hydrogen from the original formic acid molecule



or dehydration



which renders carbon monoxide and water. The intricacies of these reaction processes at the atomic level were investigated by several groups [196,581–584], and are discussed below.

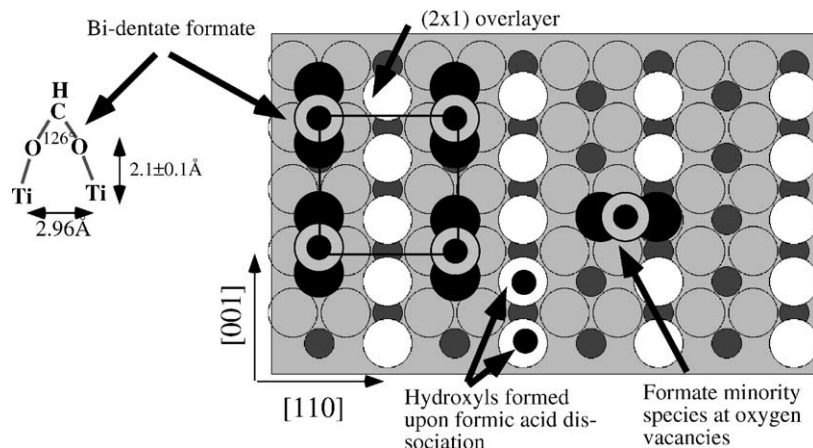


Fig. 61. Model for formic acid adsorbed on $\text{TiO}_2(1\ 1\ 0)$. Formic acid dissociates at the surface. The resulting formate ion binds to two fivefold coordinated Ti atoms in a bi-dentate fashion. The adsorption geometry was mapped out with XPD and NEXAFS [586,589]. A minority species adsorbed at the positions of missing bridging oxygen atoms was postulated by Hayden et al. [588].

5.2.1.2. Formate: adsorption geometry and structure

5.2.1.2.1. $\text{TiO}_2(1\ 1\ 0)$ - (1×1) . Adsorption at cryogenic temperature renders both, formate and (at higher coverages) molecular formic acid. The molecularly adsorbed multilayers desorb at 164 K [582]. Below 350 K, a saturation coverage of formate ions (0.5 ML, with 1 ML defined as one molecule per surface unit cell/per exposed fivefold coordinated Ti atom) form a regular $p(2 \times 1)$ structure, see Fig. 61. The adsorption geometry was mapped out in detail by combining several photoelectron diffraction approaches [585–587]. The majority of the HCOO^- molecules are adsorbed in a bi-dentate fashion, with the oxygen atoms bridge-bonded between two fivefold coordinated Ti atoms (see Fig. 61) and the molecular plane oriented in $(0\ 0\ 1)$ direction. A RAIRS study [588] has concluded that there is a minority species present, with the molecular plane oriented parallel to the $[1\bar{1}\ 0]$ direction. This species is probably adsorbed at the vacancies in the bridging oxygen rows. When these minority species are included in the analysis, the results from the photoelectron diffraction measurements [585–587] are consistent with recent NEXAFS measurements [589]. The vertical Ti–O distance was determined as 2.1 Å and the O–C–O bond angle was estimated as $126 \pm 4^\circ$. This agrees well with theoretical calculations [102,590–593].

Single formate ions can be observed with STM and non-contact AFM techniques [108,594–600]. The images are consistent with the adsorption site at the Ti atoms displayed in Fig. 61. Correlation analysis of STM images of formate ions at small coverages indicate a tendency for a $c(4 \times 2)$ configuration in addition to a $p(2 \times 1)$ structure [599]. This maximizes the distance between CHOO^- ions and minimizes their mutual repulsive interaction. The $p(2 \times 1)$ structure is possibly stabilized by co-adsorbed H through reaction (8) [590,591]. Isolated formate ions are quite immobile when imaged at room temperature [108,594–600]. In an instructive STM experiment performed by Onishi and Iwasawa [598], small areas of a $p(2 \times 1)$ -formate surface were ‘cleared off’ (probably by field desorption) by scanning with a higher bias voltage. This area filled up by diffusion mainly along the fivefold coordinated Ti rows, see Fig. 62. Interestingly, the boundaries moved quite uniformly, and single

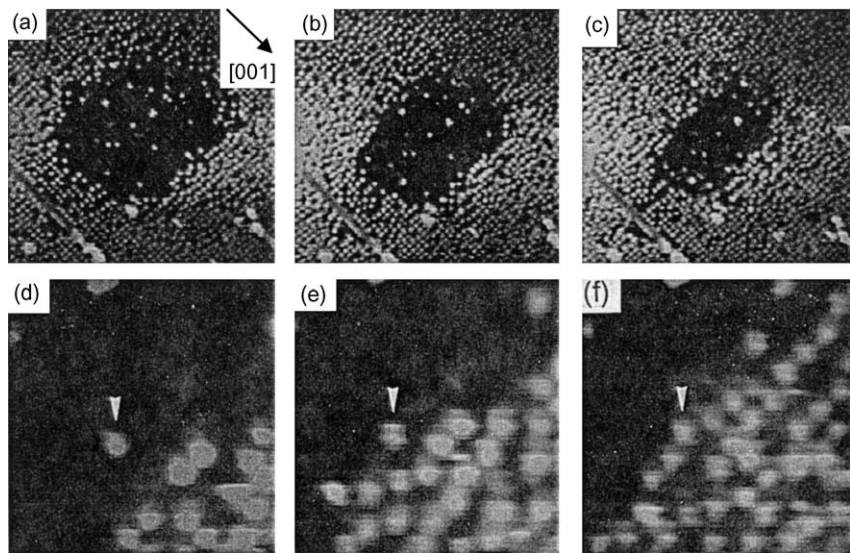


Fig. 62. Serial STM images from a (2×1) -formate layer on $\text{TiO}_2(1\ 1\ 0)$. Before these images were taken, a square region was rastered with a high sample bias voltage, and scans (a)–(c) were recorded 15, 26, and 35 min after the rastering. In the small area scans an isolated formate ion merged into the migrating monolayer (d)–(f). From Onishi and Iwasawa [598]. © 1996 Elsevier.

formate molecules in the cleared area only became mobile when hit by the moving front of formate ions. A concerted diffusion of the H atoms adsorbed at the bridging oxygen atoms in conjunction with the formates was inferred from first-principles calculations [591].

5.2.1.2.2. $\text{TiO}_2(1\ 1\ 0)$ - (1×2) . As discussed in Section 2.2.2, two configurations seem to co-exist for the (2×1) reconstruction of $\text{TiO}_2(1\ 1\ 0)$. When 3 L formic acid were dosed on a surface with several bright strands, the (1×1) terminated substrate areas were almost completely covered by a (2×1) -formate overlayer, but no formate ions were observed at the bright strands [122]. This gives credibility to the ‘added Ti_2O_3 ’ row model that was originally proposed in the same paper. In this model no Ti^{4+} species are exposed (Fig. 18b) that would provide adsorption sites for formate.

However, when formic acid was dosed on a cross-linked (1×2) surface on a heavily reduced surface (which is thought to consist of added $\text{TiO}_2(1\ 1\ 0)$ rows interconnected by ‘rosette-like’ structures), formate was observed to stick predominantly to the cross-links [584]. When a (1×2) -formate covered surface was ramped to higher temperature, desorption was observed as well as the formation of (1×1) -terminated islands, see Fig. 63. It was proposed that oxygen atoms that are formed during the decomposition of formic acid are inserted into the lattice via reaction with interstitial Ti^{3+} ions. The other fragments (such as CO) would desorb. In a similar high-temperature STM experiment in Iwasawa et al. [126], bright spots located on the bridging oxygen rows have been tentatively assigned as carboxylate (CO_3^{2-}) reaction intermediates.

5.2.1.2.3. Modified $\text{TiO}_2(1\ 1\ 0)$ surfaces. In one of the early adsorption studies, a stepped $\text{TiO}_2(4\ 4\ 1)$ surface was used for adsorption of several molecules. The results were compared with a flat $\text{TiO}_2(1\ 1\ 0)$

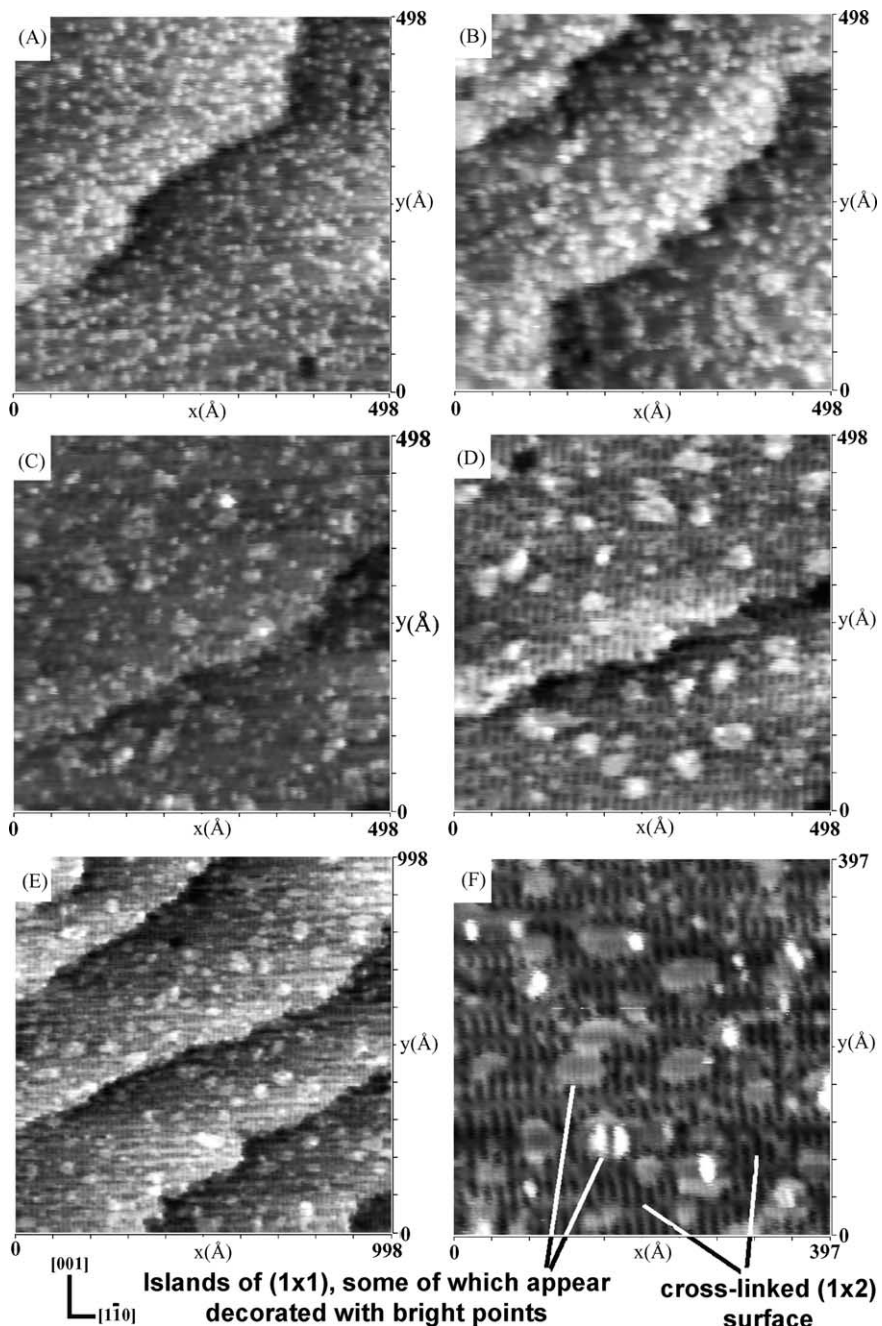


Fig. 63. STM images of a highly bulk reduced $\text{TiO}_2(1\ 1\ 0)$ sample covered with formic acid at room temperature during a temperature ramp of 2 K/min. The images were recorded at (A) ~ 390 K, 52 min; (B) ~ 420 K, 66 min; (C) 460 K, 82 min; (D) 470 K, 90 min; (E) 480 K, 97 min and finally after stabilizing the temperature at (F) 570 K, 180 min. The crystal exhibits a cross-linked (1×2) reconstruction. With increasing time and temperature the number of individual bright formate features declines while small islands form within the (1×2)-reconstructed terraces. The islands show a (1×1) termination at 570 K. All images were taken at 0.1 nA, 1 V. From Bennett et al. [584]. © 2000 Elsevier.

crystal [545]. The (4 4 1) surface has a regular step structure which is indexed as $[3(1\ 1\ 0) \times (1\ 1\ 1)]$ [545]. It contains a substantial fraction of Ti^{3+} ions. The differences in work function between the stepped and the flat surfaces was attributed to inclined species at the step edges.

Reducing $\text{TiO}_2(1\ 1\ 0)$ surfaces by sputtering or electron bombardment creates more adsorption sites for formate [593]. The formate coverage scales with the reduction state of the surface, and little or no ‘healing’ of Ti^{3+} sites is observed upon formic acid exposure at room temperature.

Thin films of TiO_2 were synthesized by depositing Ti on a Ni surface and oxidizing the metal overlayer [601]. It had been shown previously [602] that an oxidized $\text{Ni}_{94}\text{Ti}_6$ alloy gives two different surfaces depending on the preparation conditions. These exhibit either a $\text{TiO}_2(1\ 1\ 0)$ termination or a quasi-hexagonal $c(2 \times 6)$ overlayer. HREELS from formic acid adsorbed on a four-layer $\text{TiO}_2(1\ 1\ 0)$ film indicated a bi-dentate adsorption geometry (Fig. 61). In contrast, a three-layer film with a quasi-hexagonal surface gives a separation between the symmetric and asymmetric OCO stretching frequencies that is closer to the one expected for monodentate bonding [601].

5.2.1.2.4. Other TiO_2 surfaces. The adsorption and decomposition of formic acid on the (1×3) -reconstructed surface of $\text{TiO}_2(1\ 0\ 0)$ was described by Henderson [196] and is discussed in more detail below. Formic acid dissociates as in reaction (8). No ordered LEED pattern was observed, and no details of the adsorption geometry were given in this study.

Formic acid adsorption and reaction on rutile $(0\ 0\ 1)$ was investigated by Barteau and co-workers [583,603,604]. Again, adsorption occurs via reaction (8), with no further details on the adsorption geometry given.

5.2.1.2.5. Anatase. As mentioned above, studies of single-crystalline anatase surfaces are just starting to appear. The adsorption of formic acid and HCOONa was studied with DFT calculations in a slab geometry by Vittadini et al. [605]. In contrast to $\text{TiO}_2(1\ 1\ 0)$, the most stable adsorption geometry of formate is predicted to be a molecular monodentate configuration, hydrogen-bonded to the bridging oxygen atoms. When co-adsorbed with water, it stays in the monodentate coordination, but dissociates through interaction with nearby water molecules. Sodium formate, HCOONa , is predicted to dissociate on the dry and the water-covered surface, and to adsorb in a bridging bi-dentate geometry.

5.2.1.3. Reaction of formic acid. As described in reactions (Eqs. (9) and (10)) above, dehydration (products $\text{H}_2 + \text{CO}_2$) and/or dehydrogenation (products $\text{H}_2\text{O} + \text{CO}$) are the two main reaction mechanisms of HCOOH on TiO_2 surfaces. On the $\text{TiO}_2(1\ 1\ 0)$ surface, both reactions were observed [581,606] upon DCOOD exposure on $\text{TiO}_2(1\ 1\ 0)$ surfaces. Representative TPD results are displayed in Fig. 64. The desorbing D_2 molecules at 400 K were attributed to a recombination of hydroxyls



Moreover, a mixture of CO , CO_2 , D_2 , D_2O , and DCOOD was released around 570 K. Thus both, an overall dehydration as well as a dehydrogenation reaction, would take place at this temperature. The reaction products were also measured under ‘catalytic conditions’, i.e., at the hot surface and under formic acid pressures of 10^{-5} to 10^{-3} Pa (10^{-10} to 10^{-6} Torr). The dehydrogenation reaction (9) (resulting in $\text{D}_2 + \text{CO}_2$) is dominant below 500 K. Its rate is nearly independent of formic acid pressure, but increases with surface temperature. The unimolecular decomposition of formate was

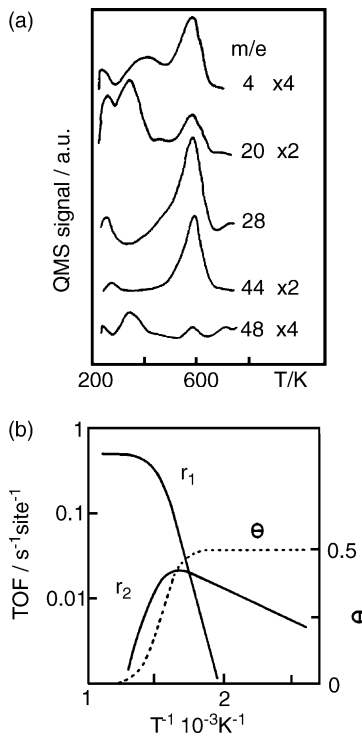


Fig. 64. (a) TPD spectra following 3L DCOOD exposure on $\text{TiO}_2(1\ 1\ 0)$ at 230 K. Note the release of D_2 , D_2O , CO , and CO_2 around 570 K. (b) Reaction rates of formic acid on $\text{TiO}_2(1\ 1\ 0)$ simulated as a function of reaction temperature. r_1 : dehydration, r_2 : dehydrogenation; θ : coverage of formates. From Onishi et al. [581]. © 1994 Academic Press.

proposed as the rate-controlling step with an activation barrier of $120 \pm 10 \text{ kJ/mol}$. It proceeds in the following fashion



where O_{form} represents an oxygen atom of formate origin. Reaction between the surface hydroxyl and a formic acid molecule from the gas phase would form D_2O



closing the catalytic cycle. Above 500 K, dehydration occurs more rapidly than dehydrogenation. This reaction depends on the pressure, and a bimolecular reaction between an adsorbed formate and a gaseous formic acid molecule, as in



was suggested as an alternative path after decomposition of the adsorbed formate molecule. The kinetic parameters derived from these experiments were used for modeling the kinetics of the reactions, see Fig. 64b.

While these results and the proposed reactions could be obtained by re-arranging the parent molecule, recent TPD studies point out that the reactions might be more intricate, and the substrate

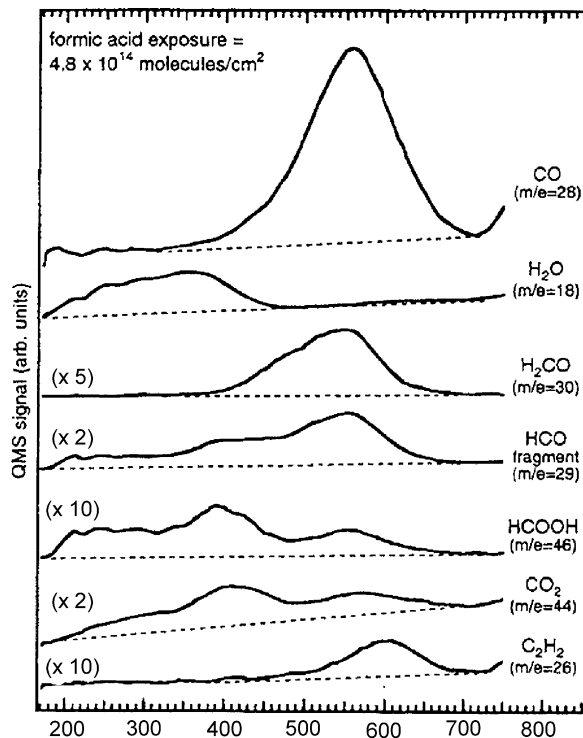


Fig. 65. TPD spectra from a formic acid exposure of 4.8×10^{14} molecules/cm² (monolayer saturation) to the TiO₂(1 0 0)-(1 × 3) surface at 170 K. Note that most of the H₂O desorption is completed before the onset of CO desorption. From Henderson [196]. © 1995 The American Chemical Society.

itself might play a major role in the decomposition of formate. A TPD/SSIMS study [196,582], combined with ¹⁸O labeling of either the surface (by replacing most of the surface ¹⁶O atoms by ¹⁸O), or the adsorbate (using ¹⁸O-containing reactants), is quite instructive in this respect.

The results on the microfaceted TiO₂(1 0 0)-(1 × 3)⁴ surface are considered first [196]. They show the same general trend as similar experiments on the (1 1 0) surface [582]. Results from TPD desorption products after exposure of a monolayer of formic acid on TiO₂ at 170 K are displayed in Fig. 65. The major reaction product is CO, which desorbs around 550 K in a near-first-order process. While this points towards a dehydration reaction, it is puzzling that desorption of water is nearly completed *before* CO or other reaction products leave the surface. It should be pointed out that adsorbed CO is not stable on TiO₂ at these high temperatures (see Section 5.1.4), i.e., the amount of desorbing CO is reaction-limited. This means that the majority of the desorbing water is formed in a process that is *independent from the decomposition of the formate ions*. Very similar results (i.e., CO

⁴ The {1 1 0}-faceted model for the TiO₂(1 0 0)-(1 × 3) surface was adopted in [196], see Fig. 23b. As discussed above, recent measurements seem to indicate that this simple model might not be valid. However, this does not affect the considerations about formic acid decomposition in a major way. It is sufficient to assume—and well supported by experimental evidence—that this surface contains reduced Ti³⁺ ions and that twofold coordinated, bridging oxygen atoms are present as well.

desorption as the major reaction product at 550 K, where most of the H₂O has already left the surface) was observed on a TiO₂(1 1 0) surface [582]. One possibility is that water is formed when two of the surface hydroxyls that have formed during the dissociative adsorption of formic acid (Eq. (8)) combine as

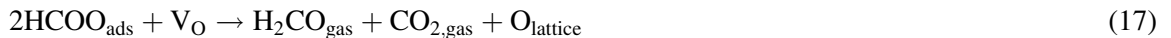


For example, the two OH groups that are sketched in Fig. 61 on a rutile (1 1 0) surface could recombine and leave the surface as water. This would cause the creation of a vacancy V_O, i.e., a (temporary) reduction of the surface. HREELS measurements on TiO₂(1 1 0) point in this direction [582]. As expected from this scenario, a substantial fraction of water desorbs as H₂¹⁸O desorbing from an ¹⁸O-enriched surfaces.

As seen from Fig. 65, formaldehyde, H₂CO, is also a major desorbing species from TiO₂(1 0 0)-(1 × 3). Barteau and co-workers [583,603] pointed out that reduced Ti species are capable of promoting the formation of formaldehyde from formic acid. It can be produced either in an unimolecular reaction



or in a bimolecular reaction



The reaction in Eq. (17) is the dominant decomposition channel on the ‘{1 1 4}-faceted’ TiO₂(0 0 1) surface which contains substantial amounts of fourfold coordinated Ti ions [603]. Because of the presence of undercoordinated Ti³⁺ ions on TiO₂(0 0 1)-(1 × 3), it is not too surprising that H₂CO is a major product of formate decomposition at this surface as well. However, it was found by Henderson [582] that a small amount of formaldehyde was also produced on a TiO₂(1 1 0) surface, in contrast to the results by Onishi et al. displayed in Fig. 64. Possibly, the temporary oxygen vacancies, created by reaction (15) play a role in this process.

One oxygen atom results from either reaction (16) or (17). It could be incorporated into the lattice at vacancy sites produced by water desorption (Eq. (15)). An alternative scenario is suggested by the STM images in Fig. 63. The images show the substantial oxidation capacity of formic acid at elevated temperatures. This means that the resultant O atom could also react with Ti interstitials from the reduced bulk.

The next product displayed in the TPD spectra in Fig. 65 is formic acid. (The HCO fragment in Fig. 65 is a cracking product of H₂CO and HCOOH in the mass spectrometer.) Multilayers evolve when higher formic acid dosages are used. The trace in Fig. 65 shows two features, and the one at higher temperatures coincides with the release of CO from the surface. Possibly, decomposition of formate results in the release of protons that can lead to a recombination with adsorbed formate



The reactions described in Eqs. (15)–(19) leave open an interesting question, however. When decomposition of formate results mainly in evolution of CO and is decoupled from the formation of water, what happens with the hydrogen? Especially on the TiO₂(1 1 0) surface, the relatively small

amounts of hydrogen-containing species (HCOOH , H_2O , H_2CO , and C_2H_2) do not balance the amount of CO produced [582]. It was speculated that the excess H diffuses into the bulk [196]. Such a process was observed on $\text{ZnO}(0\ 0\ 0\bar{1})$ [607], but this possibility has not yet been explored for TiO_2 .

Little or no CO_2 production was observed in the TPD spectra in Fig. 65, again in contrast to Onishi's results. (The trace in Fig. 65 comprises also the mass spectrometer cracking fragments from desorbing formic acid and other molecules.) In addition, no H_2 evolution was observed on either the $\text{TiO}_2(1\ 0\ 0)$ - (1×3) , the $\text{TiO}_2(1\ 0\ 0)$ - (1×1) , or the $\text{TiO}_2(1\ 1\ 0)$ - (1×1) surface. Thus the overall dehydrogenation reaction (Eq. (9)) was not observed in Henderson's experiments [196,582].

5.2.1.4. Formic acid—conclusion. The adsorption of formic acid is one of the best-investigated organic systems at this point. The adsorption geometry of the formate molecule on $\text{TiO}_2(1\ 1\ 0)$ is sufficiently well known for more intricate studies, such as trying to understand the complexities of the diffusion process [590,591]. The fact that it can be observed directly with scanning probe techniques has also contributed to the understanding of this adsorption reaction. However, it is unclear at this point what causes the different results for formic acid decomposition/reaction that were obtained by different groups using virtually the same systems and techniques. It is now clear that the substrate plays a very active role in the decomposition and reaction processes; surface atoms are incorporated in the reaction products, and the substrate itself is re-oxidized upon formate decomposition. It would be well worth an investigation what high-temperature processes occur under which conditions, and in how far the reduction state of the TiO_2 sample itself plays a role.

5.2.1.5. Acetic acid (CH_3COOH). The adsorption of acetic acid generally follows the same trends found for formic acid. Far fewer investigations were performed on this molecule, however.

At room temperature on $\text{TiO}_2(1\ 1\ 0)$, acetic acid adsorbs as acetate H_3CCOO^- in a (2×1) structure, with the two O molecules bonded in a bridging (bi-dentate) configuration across two fivefold coordinated Ti atoms with the C–C bond perpendicular to the surface. This puts the H atoms in the methyl group parallel to the surface plane. ESDIAD measurements show two contributions in the H^+ emission. A lobe peaked at normal emission is surrounded by a ring. The H^+ ions in the normal emission are attributed to surface hydroxyls that are formed during the dissociative adsorption, similar to reaction (8) for formic acid. The H^+ ions in the ring most likely stem from the $-\text{CH}_3$ moiety of the acetate molecule that freely rotates around the molecular axis. NEXAFS experiments also indicate that the molecule stands upright, with an overall twist angle of the molecular plane of $26 \pm 5^\circ$ from the $[0\ 0\ 1]$ direction [589]. Adsorption of acetic acid on the (1×2) surface does not modify the LEED pattern, but ESDIAD reveals H^+ desorption with a weaker off-normal contribution consistent with the Ti_2O_3 model of the reconstruction. The overall coverage on a (1×2) -reconstructed surface is also smaller [608].

The decomposition of acetic acid was directly observed with STM by Onishi et al. [609]. STM images after a temperature jump to 580 K were analyzed. The number of bright spots on the surface decreased exponentially with time. This was assigned as a unimolecular decomposition of acetate to release ketene



Plotting of the number of the bright spots in consecutive STM images against time on a semi-log scale results in a rate constant of $(4 \pm 1) \times 10^{-3} \text{ s}^{-1}$. This agrees well with a rate law deduced from a thermal desorption study [604]. In addition to the acetate molecules, a few immobile, bigger species

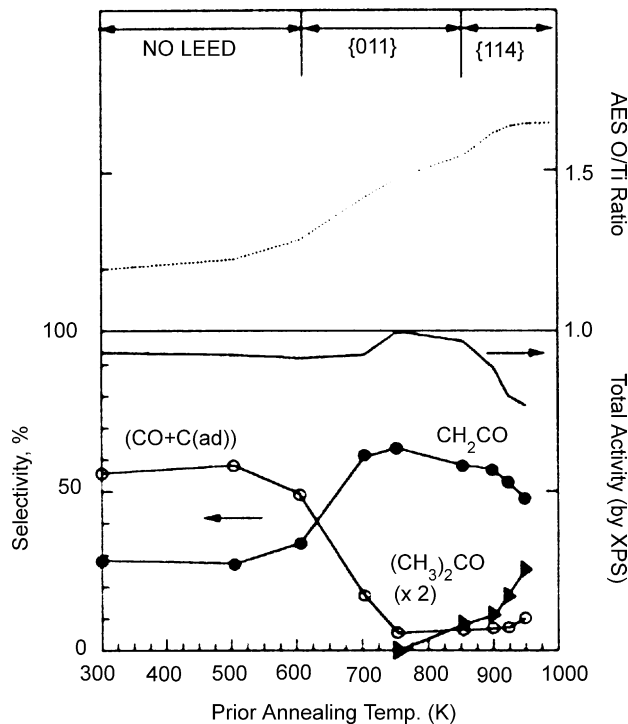


Fig. 66. Selectivity of CH_3COOH decomposition on differently pretreated $\text{TiO}_2(0\ 0\ 1)$ surfaces. The selectivity is defined as the fraction of total carbon appearing in each product. From Kim and Barteau [604]. © 1990 Academic Press.

were observed and assigned as carbonaceous residues formed in a side reaction. These disappeared at higher temperatures.

It is possible to distinguish between co-adsorbed formate and acetate molecules with non-contact AFM. The latter appear higher in the images [600,610]. Acetate molecules at the boundary between different (2×1) domains were observed to be mobile during scanning with the AFM tip [611]. The fluctuations were explained invoking interactions between hydroxyl H atoms and acetate.

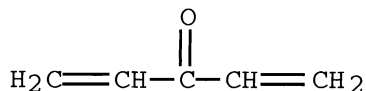
A comprehensive TPD/XPS study on differently treated $\text{TiO}_2(0\ 0\ 1)$ surfaces was performed by Kim and Barteau [604]. The surface structure and the degree of reduction after different pretreatments is depicted in Fig. 66. At 390 K, approximately 15% of acetates desorb via recombinative adsorption as acetic acid, together with some water. Decomposition occurred at higher temperatures via three different pathways as summarized in Fig. 66. On the sputtered, oxygen deficient surface ("no LEED" in Fig. 66), the main decomposition product is atomic C that is then burned off as CO via reaction with surface oxygen. On a more oxidized surface, ketene (CH_2CO) is produced via a net dehydration reaction



that peaks in selectivity at the ' $\{0\ 1\ 1\}$ -faceted' surface. On the ' $\{1\ 1\ 4\}$ -faceted' surface, production of another decomposition product, acetone (CH_3COCH_3) was observed. This surface might contain Ti cations in several undercoordinated sites and production of acetone may take place through a bimolecular reaction where two acetate molecules are coordinated to a common Ti^{4+} surface cation.

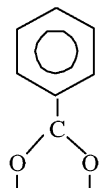
5.2.1.6. Propanoic acid (C_2H_5COOH). Both the adsorption on rutile (1 1 0) and the reaction on rutile (0 0 1) surfaces occur analogous to other acetic acid reactions. Adsorption of propanoic acid probably forms propanoates which order in a (2 × 1) overlayer. The bond geometry in NEXAFS experiments indicate an upright molecule [589]. Two main decomposition products are formed at elevated temperatures. Methyl ketene ($CH_3HC=CO$) forms through unimolecular dehydration on ‘{0 1 1}-faceted’ $TiO_2(0\ 0\ 1)$ surfaces. TPD data on the ‘{1 1 4}-faceted’ surface were consistent with formation of 3-pentanone (di-ethyl ketone, $CH_3CH_2COCH_2CH_3$) [604].

5.2.1.7. Acrylic acid ($CH_2=CHCOOH$). TPD, XPS, and scanning kinetic spectroscopy were employed to study the kinetics of acrylic acid decomposition on $TiO_2(0\ 0\ 1)$ [612]. In the latter technique, the crystal is pre-dosed as in a regular TPD measurement, but a flux of molecules (provided by a background pressure of the order of 5×10^{-9} Torr in the reported experiment) is kept above the sample surface. This allows the observation of high-temperature reaction paths that are often not accessible in a regular TPD experiment. Most likely, adsorption occurs dissociatively as acrylate ($CH_2=CHCOO^-$) and is little affected by the $CH_2=CH-$ (olefin) side chain. A range of reaction products due to the olefin fragment can be seen that are absent in the case of propanoic acid decomposition [604]. These include C4 products (butene and butadiene) and benzene. The formation of di-vinyl ketone



is only seen on the ‘{1 1 4}-faceted’ surface [604].

5.2.1.8. Benzoic acid (C_6H_5COOH). An ESDIAD/LEED study of benzoic acid adsorption at room temperature indicates that it adsorbs dissociatively with the two oxygen atoms bridge-bonded to fivefold coordinated Ti atoms [613]. The ESDIAD H^+ pattern was interpreted as an upright benzoate molecule with an upright phenyl ring such as in



STM images showed a dimerization of the benzoate rings along the $[1\bar{1}0]$ direction [614].

5.2.1.9. Bi-isonicotinic acid. The adsorption of more complex acids was extended to bi-isonicotinic acid (2,2'-bipyridine-4,4'-dicarboxylic acid) in an XPS/NEXAFS study, combined with quantum chemical (INDO) calculations [615]. This molecule is the ligand that anchors organometallic dyes to TiO_2 nanoparticles in electrochemical applications such as in the ‘Grätzel cell’ [29], see Section 5.3.2. The proposed adsorption geometry, derived from the calculations and consistent with the experimental data, is shown in Fig. 67. The bonding follows in principle the trend expected from formate and benzoate adsorption. The molecule binds to two neighboring Ti rows in a bi-dentate fashion through the dehydroxylated O atoms, and is connected via the rings along the $[\bar{1}\ 1\ 0]$ direction. N1s NEXAFS spectra were modeled successfully using this adsorption geometry in a cluster model [616].

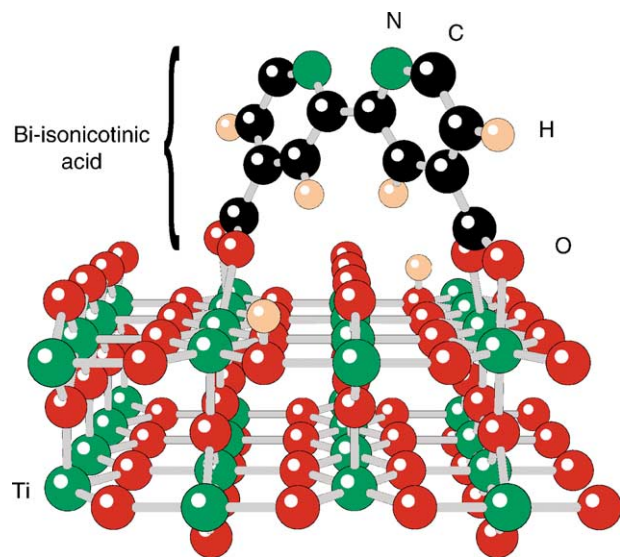
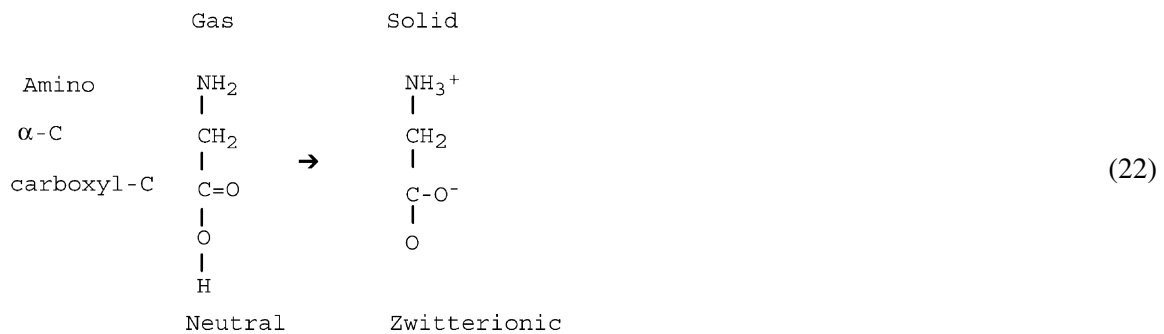


Fig. 67. Calculated structure of bi-isonicotinic acid adsorbed on $\text{TiO}_2(110)$. From Persson et al. [616]. © 2000 The American Chemical Society.

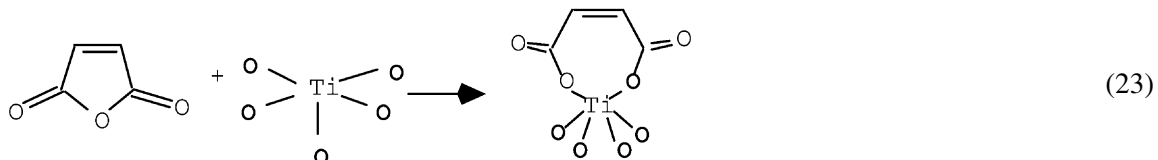
5.2.1.10. Oxalic acid (HOOC-COOH). Fahmi et al. [617] performed theoretical investigation of oxalic acid (a planar molecule with the two formate groups linked together in two possible configurations). The study was motivated by the observation that crystal growth of the two polymorphs of titanium dioxide, rutile and anatase, are strongly affected by the presence of oxalic acid. The growth of rutile is enhanced, suggesting that it binds to anatase more strongly. The surfaces were modeled with ‘polymers’ (essentially Ti atoms surrounded by a square of oxygen atoms, and arranged either in a linear ‘rutile’ or a square ‘anatase’) fashion. The calculations suggest that oxalic acid undergoes dissociation, i.e., a splitting of both H atoms. The resulting oxalate ion, $\text{C}_2\text{O}_4^{2-}$, is bonded through the oxygen atom to neighboring Ti atoms.

5.2.1.11. Glycine ($\text{NH}_2\text{CH}_2\text{COOH}$). Multilayers of glycine, adsorbed on $\text{TiO}_2(110)$, were studied with synchrotron radiation-based UV light [618,619]. This linear molecule consists of three groups and two configurations are possible, as in

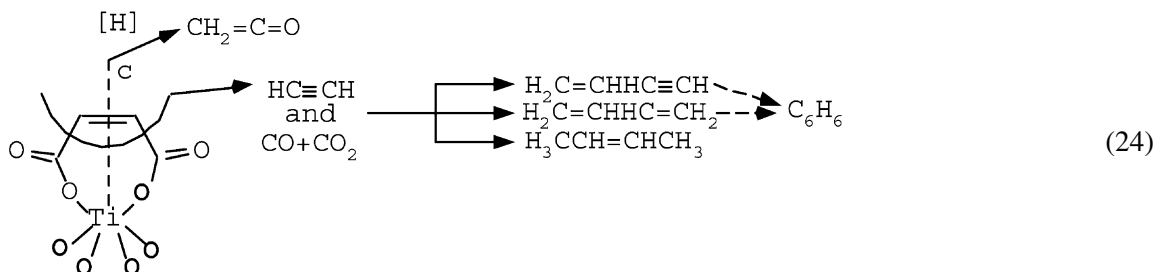


UPS spectra of shallow core and valence levels indicate that it adsorbs in multilayers of the zwitterionic ion where the H atom from the carboxyl group transfers to the amino group to form an NH_3^+ radical. The resulting molecule is bi-polar. Photon damage of the glycine layers occurs fast (cross-section of $5.4 \times 10^{-16} \text{ cm}^2$, comparable with electron excitation in the gas phase). Small coverages on the $\text{TiO}_2(1\ 1\ 0)-(1\times 2)$ surface indicate dissociative adsorption where most of the amino group is released into the gas phase.

5.2.1.12. Maleic anhydride. Maleic anhydride is not a carboxylic acid; but it is still listed here as it exhibits some similarities in its adsorption and reaction pathways at the $\text{TiO}_2(0\ 0\ 1)$ surface [620]. Adsorption at a $\text{TiO}_2(0\ 0\ 1)$ surface was modeled with semi-empirical calculations of a relaxed $\text{Ti}_{13}\text{O}_{45}\text{H}_{38}$ cluster. Of the considered adsorption geometries, the most stable configuration was dissociative adsorption. A model was suggested where one C–O–C bond was broken and bonded to one Ti and a neighboring oxygen atom in the following fashion



The observed reaction products (see Table 16) were rationalized with the following scheme:



Here the adsorbed molecule may dissociate via two pathways, either parallel or perpendicular to the molecular *c*-axis. The TPD data suggest breaking of the C=C bond and formation of ketene with a hydrogen atom that could either come from more complete dissociation of maleic anhydride or as an impurity from the bulk. A cut of the molecule in perpendicular direction would result in the formation of acetylene as well as CO and CO_2 . Formation of C4 and C6 products could evolve from coupling of acetylene adsorbed on surface defects.

5.2.2. Alcohols (methanol, higher alcohols)

5.2.2.1. Methanol. The adsorption of methanol was studied on various TiO_2 (rutile) surfaces (Table 16(b)). Experiments and theory agree that both, molecular and dissociative adsorption take place. Dissociation happens via breaking of the O–H bond of CH_3OH , leading to an adsorbed methoxy species and, probably, a hydroxylated bridging oxygen atom. Several adsorption configurations are separated by a very small or maybe even negligible barrier at room temperature. Interestingly, only

molecular desorption was observed on $\text{TiO}_2(1\ 1\ 0)$, even when point defects are present. In contrast, a variety of reaction products form on $\text{TiO}_2(1\ 0\ 0)$.

5.2.2.1.1. Methanol on $\text{TiO}_2(1\ 1\ 0)$. The most extensive and recent adsorption study of methanol on the rutile ($1\ 1\ 0$) surface was performed by Henderson et al. [151,621]. An earlier study by Onishi et al. [545] reported molecular adsorption at room temperature; an ordered overlayer was not observed. Henderson's results also showed that the majority of molecules adsorbs intact, and leaves the surface around 295 K. Methanol is the only carbon-containing species in TPD spectra, and no evidence for residual decomposition products was observed in repeated TPD experiments. The $\text{TiO}_2(1\ 1\ 0)$ surface in this experiment contained about 8% vacancies [621], and a TPD peak at 480 K was attributed to recombinative adsorption of dissociated products at vacancy sites. Isotopic scrambling TPD and SSIMS experiments showed that methanol desorbing at 350 K is possibly formed via recombinative desorption from dissociated methoxy species at non-vacancy sites. Monolayer coverage is reached around 3.4×10^{14} molecules/cm². This is consistent with XPS results after room-temperature adsorption [622]. A weak, streaky LEED pattern (Fig. 68) is consistent with a coverage of 2/3 ML, and the model displayed in Fig. 68 can rationalize the observed results for monolayer coverages [621]. Higher exposures lead to CH_3OH molecules hydrogen-bonded to the bridging oxygen atoms and multilayers.

First-principles calculations were performed using density functional theory and pseudopotentials [623]. The rather powerful VASP code [624–626] was applied in both the static and dynamic mode. Three adsorbed species were considered at different coverages and configurations; molecularly adsorbed CH_3OH , surface methoxy (formed by O–H bond scission), and species formed via C–O bond scission, i.e., a CH_3^+ ion and an OH^- group. (In the gas phase it is far easier to break the latter bond, however, the calculations show that this process appears to be activated at the $\text{TiO}_2(1\ 1\ 0)$ surface.) The adsorption energy of molecular CH_3OH and the different dissociative species is similar. Repulsive and attractive intermolecular interactions play a major role, which leads to a coverage dependence for the stable configuration. Spontaneous O–H bond breaking was observed in molecular dynamics calculations of adsorbed CH_3OH . In this sense, the model in Fig. 68 must be regarded as one of several possibilities. The tendency for molecular vs. dissociative adsorption, and the role of H-bonding, was compared to other R–OH molecules in [102].

Co-adsorbed water showed weak to no changes in the surface chemistry of methanol [621]. Co-adsorbed oxygen opens up new decomposition channels. Oxygen exposure to a slightly defective $\text{TiO}_2(1\ 1\ 0)$ surfaces leads to dissociation of the O_2 molecules which results in O adatoms. This leads to additional O–H bond cleavage, and the formation of H_2CO above 600 K. When O_2 molecules were adsorbed at 150 K, an additional low-temperature desorption peak of H_2CO was observed, possibly formed via an abstraction of an H atom from an adsorbed methoxy species.

A high cross-section for electron-stimulated desorption/decomposition was reported [151]. This is probably the reason why the LEED pattern in Fig. 68 was very “fragile” and faded after a few seconds [621], and why no LEED pattern was observed in other studies. In ESD experiments [151], surfaces were prepared to contain the saturated monolayer, methoxy species only, and methoxy species adsorbed at vacancies only. Electron bombardment of these different systems consistently showed high cross-sections for decomposition, and a variety of products, depending on coverage, adsorption state, and adsorption site.

5.2.2.1.2. Methanol on $\text{TiO}_2(0\ 0\ 1)$ and $\text{TiO}_2(1\ 0\ 0)$. The adsorption and thermal desorption of methanol on differently pretreated $\text{TiO}_2(0\ 0\ 1)$ surfaces was studied by Kim and Barteau [627]. At 200 K, methanol

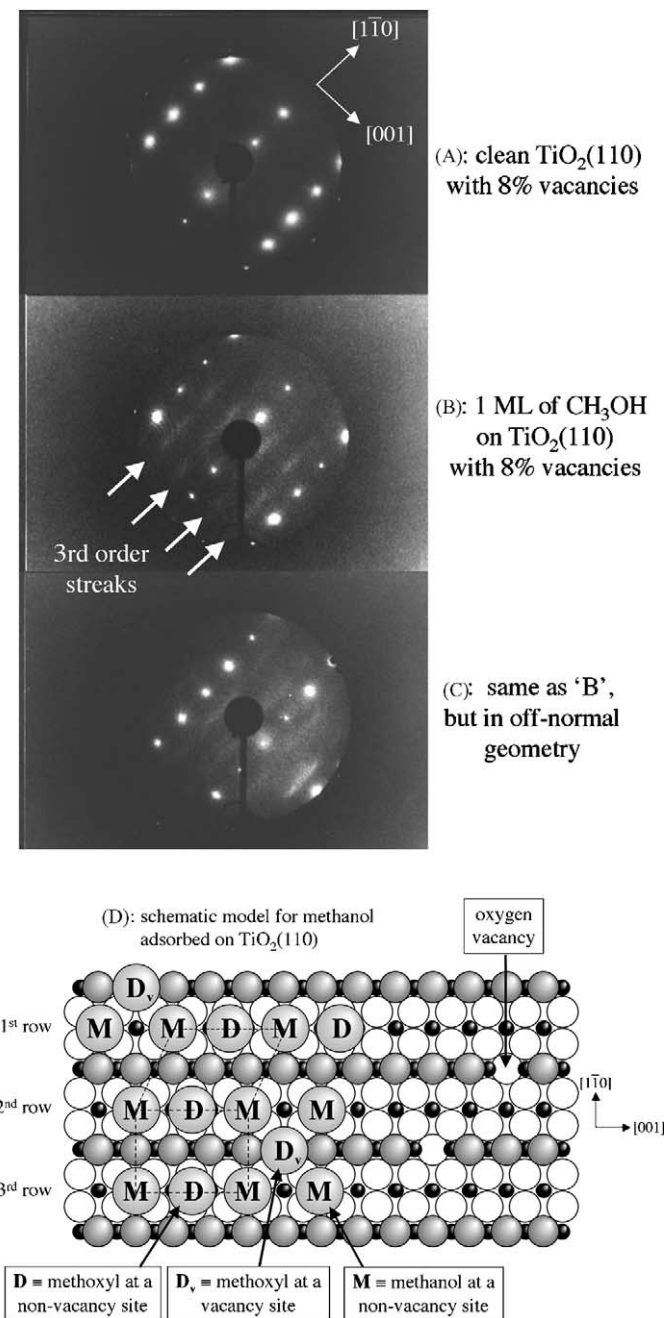


Fig. 68. LEED patterns and proposed overlayer structure of methanol adsorbed on $\text{TiO}_2(110)$. (A) Clean $\text{TiO}_2(110)$ surface with 8% vacancies in the bridging oxygen rows, (B) LEED patterns of a monolayer of CH_3OH , (C) same but in off-normal geometry. (D) Model of CH_3OH adsorption based on LEED, TPD, and SSIMS results. Dissociative adsorption at oxygen vacancies as surface methoxies (D_v) blocks nearby adsorption sites. A poorly ordered, mixed layer of 1/3 dissociated methoxy species (D), bridge-bonded to two fivefold coordinated Ti atoms, and 2/3 molecular methanol (M), in on-top geometry, could account for the $(3 \times n)$ LEED pattern in B and C. From Henderson et al. [621]. © 1999 Royal Society of Chemistry.

adsorbs both dissociatively and molecularly, with molecular CH₃OH desorbing below room temperature. This is consistent with UPS results [628]. Half of the dissociated methoxy species were removed via recombinative desorption as methanol. The other half left the surface in a variety of reaction products (see Table 16(b)) at higher temperatures. The selectivity for the product formation depends on the degree of undersaturation of the substrate surface atoms. Methane is thought to be produced by deoxygenation of the adsorbed methoxy group on oxygen vacancies and was found to occur with the highest selectivity at the ‘{0 1 1}-faceted’ surface. Dimethyl ether (CH₃—O—CH₃) was observed only at the ‘{1 1 4}-faceted’ surface, and probably forms via disproportionation of pairs of methoxides coordinated to fourfold coordinated Ti cations. On the sputtered surface, methoxides adsorbed at 300 K decompose into CO. The influence of point defects on methanol adsorption was investigated by Román et al. [628]. On both, the TiO₂(1 1 0) and the TiO₂(1 0 0) surface, the methanol coverage increased with the number of defects created by electron or Ar⁺ bombardment [628].

5.2.2.2. Higher alcohols. The adsorption and photo-reaction of 2-propanol on TiO₂(1 1 0) and TiO₂(1 0 0) was studied by Engel and co-workers and is discussed in Section 5.3.3. The adsorption and reaction of ethanol as well as higher aliphatic alcohols (*n*-propanol, *iso*-propanol) on TiO₂(0 0 1) was studied by Kim and Barteau [629]. Ethanol adsorbs at 200 K in a mixed layer as molecular C₂H₅OH and dissociated ethoxy species C₂H₅O. The molecular ethanol desorbs below 300 K, and adsorption at room temperature leads to an ethoxylated surface. About half of the ethoxy species recombine with a proton



and desorb as ethanol. The other half decomposes to produce either acetaldehyde



or ethylene



The adsorption of the two isomers of propanol on the same surface is qualitatively similar to the one observed for ethanol [629]. Co-adsorbed hydroxyls are obviously important for the recombination reaction (Eq. (25)). Water adsorption on a TiO₂(1 1 0) surface covered with ethoxy species was investigated by Gamble et al. [630]. The surface ethoxys were prepared by dissociative adsorption of either deuterated ethanol or tetraethoxysilane (TEOS). Two different species were identified. One that recombined with surface hydroxyls in the temperature range 250–400 K, and desorbed as ethanol gas (Eq. (25)). This species were attributed to an ethoxy group adsorbed on a fivefold coordinated Ti atom. The second species was attributed to bind to oxygen vacancies, similar to the methoxy species in Fig. 68. This one binds to two undersaturated Ti atoms and decomposes at 650 K, giving ethylene (Eq. (27)) and ethanol. These results are in good agreement with studies of hydroxylated rutile powder materials [631].

5.2.3. Aldehydes (RCHO) and ketones (RCOCH₃) (formaldehyde, acetaldehyde, benzaldehyde, acetone, acetophenone, *p*-benzoquinone, cyclohexanone, cyclohexenone)

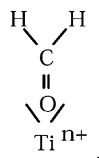
Three different aldehydes with increasing complexity were investigated by Barteau and co-workers [632–636] (Table 16(c)). All the experiments were performed on TiO₂(0 0 1) single crystals, either right

after sputtering (“reduced surfaces”) or after annealing (oxidized surfaces). Reductive coupling to dimers of the parent molecule was observed on reduced surfaces for the higher aldehydes.

5.2.3.1. Formaldehyde. Adsorption of formaldehyde, HCHO, was studied in [490,632]. Upon reaction on stoichiometric TiO₂(0 0 1) surfaces, formation of methanol is observed which leaves the surface together with formaldehyde. It is thought that the formation of methanol occurs in a Cannizzaro-type [637] reaction. In this reaction, aldehydes disproportionate when treated with concentrated NaOH or other strong bases. One molecule of aldehyde oxidizes another one to the acid and is itself reduced to the primary alcohol,



In the case of TiO₂, it was suggested that the formaldehyde adsorbs on a cation through σ lone pair donation from the oxygen of the carbonyl



in agreement with the observations in [490]. Under incorporation of an oxygen atom from the TiO₂ substrate it would then form a dioxymethylene species. Hydride transfer from one dioxymethylene to a neighboring one would give one methoxide, which later desorbs as a methanol, and a formate ion.

On reduced TiO₂ surfaces, additional desorption of methanol and formaldehyde was observed around 550 K. The formaldehyde probably decomposes completely to adsorbed carbon, hydrogen, and oxygen



which is incorporated into the lattice and partially oxidizes the surface. The H is consumed by reduction of another formaldehyde molecule to a methoxide species



which then desorbs as methanol. The adsorbed carbon, C_{ads}, that is formed through reaction (29) is oxidized to CO and CO₂. Thus, the formation of methanol on the reduced surface does not involve formation of formate as in the Cannizzaro reaction.

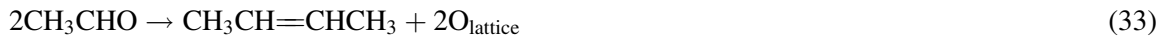
5.2.3.2. Acetaldehyde. In contrast to formaldehyde, acetaldehyde, H₃CCHO was found to couple to C4 products on TiO₂(0 0 1) [633,634]. The C–C bond formation is relatively structure insensitive, as it occurs on ‘{1 1 4}’- and ‘{0 1 1}-faceted’ surfaces. Primary products are either crotonaldehyde



or crotyl alcohol



Cannizzaro disproportionation into acetate plus ethoxides is a minor reaction channel. On sputter-reduced surfaces, reductive coupling to form butene



was the dominant reaction pathway.

Thermally created point defects on $\text{TiO}_2(1\ 1\ 0)$ cause an extraction of the O atom from the adsorbed formaldehyde molecule to yield C_2H_4 [490]. No deoxygenation reaction was observed on stoichiometric surfaces.

5.2.3.3. Benzaldehyde. The adsorption and thermal reaction of benzaldehyde  on Ar^+ -sputtered, reduced $\text{TiO}_2(0\ 0\ 1)$ surfaces produces stilbene, two phenol rings coupled via a C=C double bond [635]. This reductive coupling occurs only in the presence of undercoordinated Ti atoms. The stilbene yield decreased by an order of magnitude when the $\text{TiO}_2(0\ 0\ 1)$ surface was oxidized by annealing to 850 K prior to benzaldehyde adsorption. NEXAFS measurements were performed to determine the reaction intermediates [636]. A benzaldehyde-covered surface was progressively heated to higher temperatures, and Ti L-edge, as well as O and C K-edge spectra were taken. It was concluded that all of the oxygen originally contained in the carbonyl groups is donated to the surface by 300 K, and that the phenyl rings are oriented 54° with respect to the surface. These rings become more parallel as stilbene is produced.

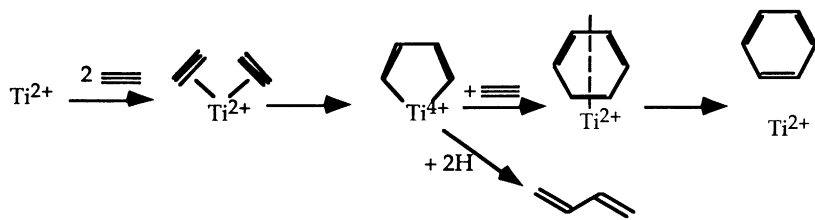
5.2.3.4. Acetone and acetophenone. Several ketones (RCOCH_3) were investigated by Pierce and Barteau [638] on $\text{TiO}_2(0\ 0\ 1)$ surfaces. Acetone (where $\text{R} = \text{H}_3$) and acetophenone (where $\text{R} = \text{phenyl ring}$) molecules were adsorbed either directly after sputtering, or after annealing of the sputter-reduced substrate. On the reduced surface, the primary reaction is the dimerization to a symmetric olefin with twice the carbon number of the reactant, see Table 16(c). For acetone, the main product is 2,3-dimethyl-2-butene, for acetophenone 2,3-diphenyl-2-butene. Very high conversion (up to 90% for acetophenone) and selectivity was found for carbonyl coupling. This reaction and the rate of activity and selectivity is comparable to the formation of stilbene from benzaldehyde mentioned above. In all cases, the yield for C–C coupling was greatly reduced on more stoichiometric surfaces.

5.2.3.5. Cyclic ketones. In addition to acetophenone, several other cyclic ketones were investigated by Idriss and Barteau [639,640] on reduced $\text{TiO}_2(0\ 0\ 1)$ surfaces, see Table 16(c). For *p*-benzoquinone  coupling reactions were observed to bi- and terphenyl. XPS measurements indicated that even higher oligomers are formed. These are non-volatile and remain on the surface at elevated temperatures. Like the monofunctional alkynes and ketones, reductive coupling of *p*-benzoquinone requires Ti cations in oxidation states lower than +4. Other reaction products include unimolecular reduction to benzene and phenol.

Cyclohexanone  and cyclohexenone  also couple reductively to $\text{C}_6\text{H}_{10}=\text{C}_6\text{H}_{10}$ and $\text{C}_6\text{H}_8=\text{C}_6\text{H}_8$ compounds, respectively. In each case, the reduced surface becomes oxidized by incorporation of the resulting O atoms into the lattice.

5.2.4. Cyclo-trimerization of alkynes ($\text{RC}\equiv\text{CH}$) on reduced TiO_2 surfaces and related reactions

A very interesting class of reactions are the trimerization of alkynes on reduced TiO_2 surfaces to form aromatic compounds (Table 16(d)). This process was investigated thoroughly by Barteau and



Scheme 1.

co-workers [641–647] and was found for a number of alkynes. In all cases, this reaction occurred only on reduced surfaces (produced by sputtering) that contained substantial amounts of Ti^{2+} . The reaction scheme for the most simple molecule, acetylene, $\text{HC}\equiv\text{CH}$, is thought to occur as in Scheme 1.

In Scheme 1, two acetylene molecules would bind to such an undercoordinated Ti^{2+} site and form a five-membered ring (a metallocyclopentadiene) consisting of C_4H_4 and the lattice Ti^{2+} ion, which becomes oxidized in the cyclization process. A third acetylene molecule is incorporated into the ring, forming benzene, which desorbs at around 400 K [641]. During benzene formation, the substrate atom is reduced to Ti^{2+} , and the catalytic cycle is closed. Other reactions include dimerization to dienes (e.g. propene, $\text{H}_2\text{C}=\text{CH}-\text{CH}=\text{CH}_2$, in the case of acetylene in Scheme 1), and unimolecular hydrogenation to olefins (e.g. acetylene to ethene, $\text{CH}_2=\text{CH}_2$).

Fig. 69 shows the influence of the reduction state of the substrate on the activity of the TiO_2 sample, in this case for methylacetylene, $\text{CH}_3\text{C}\equiv\text{CH}$. After sputtering, the yield for trimerization to trimethyl benzene (an aromatic ring with three methyl groups, see Table 16(d)), dimerization, and hydrogenation of the parent molecule is highest. XPS showed that annealing above 600 K oxidizes the TiO_2 surface; and that the yields for all reaction products decrease dramatically when the surface becomes oxidized [641].

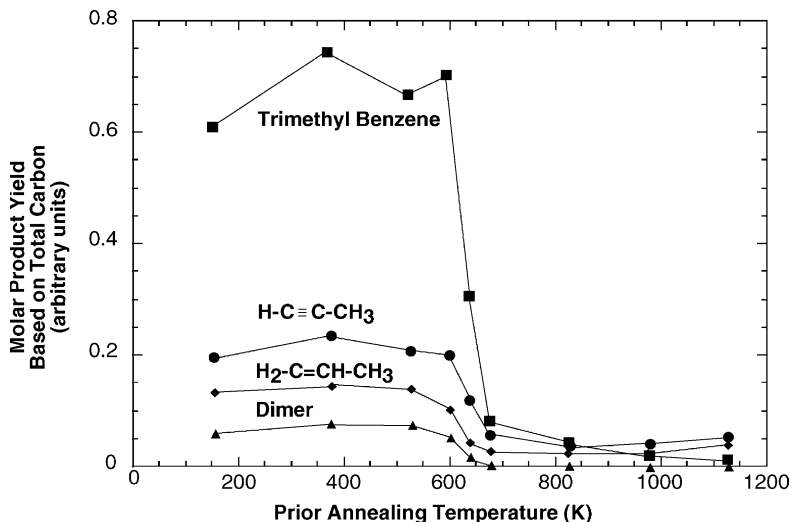


Fig. 69. Molar yield of products from TPD of methylacetylene, $\text{CH}_3\text{C}\equiv\text{CH}$, as a function of annealing temperature after Ar^+ ion bombardment of a $\text{TiO}_2(0\ 0\ 1)$ surface. The yields were scaled so that the total yield of a carbon-containing species from the Ar^+ -bombarded surface (300 K) sums to unity. For annealing temperatures above 600 K, the substrate re-oxidizes, and the activity for cyclotrimerization decreases. From Pierce and Barteau [641]. © 1994 The American Chemical Society.

An analysis of cracking patterns of different trimethyl benzenes in the quadrupole mass spectrometer indicated that the 1,2,4 isomer is the most abundant species (see Table 16(d)). This implies a random insertion of acetylenic units (\equiv) into the aromatic ring.

Similar reactions were found for higher alkynes, basically acetylene molecules functionalized with groups with increasing complexity (see Table 16(d) for the reactants and cyclic products). It even occurs for a hetero-atom containing alkyne, trimethylsilylacetylene, albeit not with a very high selectivity [644].

The validity of reaction in Scheme 1 was tested by adsorption/thermal desorption of two molecules, allene, and cyclooctatetraene. Thermal desorption of allene ($\text{CH}_2=\text{C}=\text{CH}_2$), an isomer to methylacetylene, $\text{CH}_3\text{C}\equiv\text{CH}$, [645] showed as the principal product propylene, $\text{CH}_3\text{CH}=\text{CH}_2$, through hydrogenation. For sputtered TiO_2 surfaces three dimeric products were observed (dimethylene cyclobutane, benzene, and an open-chain C_6H_{10} dimer, see Table 16(d)). No formation of trimethylbenzene, or any other trimer product was observed, indicating that an unsaturated triple bond is necessary for the trimerization reaction.

An alternative intermediate to the metallocyclopentadiene (Scheme 1) has been tested in [647]. It is conceivable that a pair of C4 ligands combine to form a C8 ligand, cyclooctatetraene ($\text{COT} \text{---} \text{C}_8$) which would then decompose to benzene and a C2 fragment. When COT was adsorbed on a reduced TiO_2 surface, it did indeed produce benzene, albeit at a higher temperature than the one where formation of aromatic rings by trimerization of acetylene is observed. In addition, the formation of cyclooctatriene C_8 was observed to occur at the same temperature as benzene formation, pointing to the same metallacycle reaction intermediate. This makes COT an unlikely intermediate for the alkyne trimerization. Recent NEXAFS measurements analyzed the probable adsorption geometry of COT on the sputter-reduced surface [646].

5.2.5. STM of pyridine, its derivates, and other aromatic molecules (pyridine, 4-methylpyridine, benzene, *m*-xylene, phenol)

As pointed out several times throughout this review, STM is uniquely suited to directly monitor and visualize surface adsorption reactions. In addition to the studies on formate and higher organic acids, mentioned above, adsorption of pyridine and its derivates were studied with STM (Table 16(e)). Iwasawa's group is the foremost leader in this respect, and most of the examples reviewed here are drawn from this group. It should also be mentioned that one of the first STM images of an aromatic molecule was obtained by imaging phenol on a rutile (1 1 0) surface in air [648,649].

Pyridine is a Lewis base (the N atom in the aromatic ring acts as an electron donor), and is typically used for titration of acidic sites in catalysts. The molecule is thought to adsorb on electron acceptors, i.e., the exposed cations on metal oxides. Hence, the molecule is expected to bind with the N-end down to the Ti atoms on the TiO_2 surface. However, a combined XPS/TPD/STM study showed that pyridine is generally only physisorbed on $\text{TiO}_2(1\ 1\ 0)$ [650]. In this study it was found that the N1s line of pyridine does not show a chemical shift in XPS. In addition, the TPD spectra of pyridine and benzene (the aromatic ring without the N atom) are rather similar, indicating the absence of a N-Ti bond. In order to test this, TPD was performed on adsorbed 2,6-dimethylpyridine (2,6-DMP, with two CH_3 groups attached to the C atoms next to the N, see Table 16(e)) and *m*-xylene (the same configuration, but with the absence of the N in the ring). The rather similar TPD results for all these molecules indicate that electrostatic van-der Waals interactions play a major role in the adsorption of all

molecules. Molecular dynamics simulations support this view, and indicate that a flat adsorption geometry for both, pyridine and benzene adsorption. This is in agreement with an electron spectroscopy study of benzene on TiO₂(1 0 0)-(1 × 1) [651].

In agreement with the weak bonding of pyridine, atomically resolved STM images from a TiO₂(1 1 0) surface show that the molecule is rather mobile [124,650]. However, pyridine binds more strongly to steps with certain orientations. An analysis of step directions shows that only steps where fourfold coordinated Ti atoms reside are active for strong pyridine adsorption at room temperature [124]. Even there, an exchange between pyridine molecules adsorbed on terraces and at step edges is frequently observed. The 2,6-DMP was somewhat less mobile in STM [650]. Pyridine also seemed to desorb during scanning at room temperature [650]. A thermally activated adsorption of a minority species was observed in STM measurements under a pyridine background pressure of 1×10^{-6} Pa (1×10^{-8} mbar) and a sample temperature of 350 K [652]. Under these conditions, particles were observed to form and grow at the surface. It was proposed that stable species are formed, possibly via dehydrogenation, which then would act as nucleation sites for the growth of larger pyridine condensates.

DFT of pyridine on TiO₂(1 1 0) [653] showed that the most stable adsorption state is the upright configuration with the 2,6-hydrogen atoms interacting with bridging oxygen atoms via a hydrogen-bond-like interaction. A flat-lying pyridine was found with a low surface diffusion barrier along the [0 0 1] direction. Conceivably, these correspond to movable species observed by STM. In agreement with STM results [124,650], fourfold coordinated Ti atoms obtained by removal of two adjacent bridging oxygen atoms were found to be stronger Lewis acid sites than fivefold coordinated Ti atoms.

STM experiments with 4-methylpyridine (4-MP, with a CH₃ group attached opposite to the N-end of the aromatic ring, see Table 16(e)) seem to confirm the idea of a mobile, flat lying, and less mobile, upright species [654]. When this molecule adsorbs in an upright position, it should stick out from the surface much higher than a flat-lying species, giving rise to a higher topographic contrast than pyridine. Indeed, three species were identified in STM, and were assigned as upright, flat immobile, and flat mobile 4-MP molecules. The flat, mobile species was the majority species. Both, the upright and the flat immobile 4-MP's were attributed to being adsorbed at sites next to a bridging oxygen vacancy.

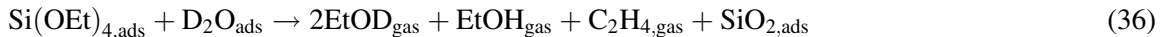
5.2.6. Adsorption and reaction of silanes (RSiX₃) (TEOS, diethyldiethoxysilane, vinyltriethoxysilane, aminopropyltriethoxysilane, (3,3,3-trifluoropropyl)-trimethoxysilane)

Silanes in the form of RSiX₃ (where X represents a halide, alkoxide, or alkyl group; and R an organofunctionality) are often referred to as ‘coupling agents’ because they can act as a bridge between organic and inorganic layers. X is a hydrolyzable, leaving group that attaches the Si to the surface, and the functional groups R are chosen to form protective layers, chemically modify electrodes, or immobilize large functional groups such as biomolecules on surface [655]. A series of silanes on clean and water-predosed TiO₂(1 1 0) surfaces were investigated by Campbell and co-workers [630,655–657], see Table 16(f).

The simplest molecule, TEOS, consists of a central Si atom bound to four ethoxy groups (EtO, where Et equals C₂H₅). At low coverages it readily dissociates, splitting off one or several EtO groups. Multilayers form at high dosages at low temperatures. Heating of a TEOS monolayer releases ethanol and ethylene in a 1:1 ratio around 650 K, suggesting a transfer of hydrogen between ethoxy species as in



This reaction leaves a lattice oxygen at the surface, similar to the reaction of ethoxys on $\text{TiO}_2(0\ 0\ 1)$ [629]. The presence of pre-dosed water facilitates the dissociation of the TEOS molecule, probably via elimination of the EtO groups via reaction with water. It also leads to a low-temperature (350 K) desorption peak of EtOH. Annealing adsorbed TEOS to 750 K (with or without co-adsorbed D_2O), produces a disordered SiO_2 layer in the net reaction



Vinyltriethoxysilane (VTES, where one of the Et groups in TEOS is substituted by a $-\text{CH}=\text{CH}_2$ group, see Table 16(f)) and diethyldiethoxysilane (DEOS, basically a TEOS molecule but with two EtO groups substituted by Et) also dissociate on the clean $\text{TiO}_2(1\ 1\ 0)$ surface in the absence of water by splitting off two EtO groups [655]. High-temperature reaction again produces a SiO_2 surface layer with ethanol, ethylene, and (in the case of VTES) $\text{CH}\equiv\text{CH}$ as reaction products. Aminopropyltriethoxysilane (APS, with a $(\text{CH}_2)_3-\text{NH}_2$ group substituting one EtO in TEOS) does not dissociate on $\text{TiO}_2(1\ 1\ 0)$ in any measurable quantity [655].

The fourth silane investigated by Campbell and co-workers [657], (3,3,3-trifluoropropyl)trimethyloxysilane (FPTS, where Si is coordinated to three $-\text{OCH}_3$ groups and a $-\text{CH}_2-\text{CH}_2-\text{CF}_3$ group) turned out to be more reactive than the ethoxysilanes considered. This molecule also adsorbs dissociatively by splitting off $-\text{OCH}_3$ groups. SSIMS showed that these bind to exposed Ti sites, and that the Si in the remaining $(\text{CF}_3\text{CH}_2\text{CH}_2)\text{Si}(\text{OCH}_3)$ complex binds to two lattice oxygens (two bridging oxygen atoms in the proposed model [657]). The $-\text{OCH}_3$ groups decompose at 550–650 K to form methane, formaldehyde, and methanol gases. The $\text{CF}_3\text{CH}_2\text{CH}_2$ ligand also decomposes around 620 K. Water facilitates the formation of methanol which desorbs at considerably lower temperatures (~ 300 K).

5.3. Photocatalysis on TiO_2

The photoactivity of TiO_2 is one of its technologically most attractive properties. The creation of electron–hole pairs through irradiation of light, either in TiO_2 itself, or in adsorbed molecules, and the following chemical or electron transfer reactions are at the heart of TiO_2 -based photodevices applied in a range of areas. Intense research was initiated by Fujishima and Honda's [25] discovery that water can be photocatalytically split into hydrogen and oxygen. As this discovery was made at the height of the oil price hikes in the seventies, it was immediately embraced as an inexpensive and safe way to produce energy. However, the use of TiO_2 for hydrogen production never reached commercialization, although there is a recent interest in reviving this issue. Many other useful reactions can be induced over irradiated TiO_2 , and a very brief review is given in the next section. The band gap of TiO_2 is relatively wide and its absorption properties are not well matched to the frequency spectrum of natural sun light. The functionalization of the TiO_2 surface with dye molecules has made TiO_2 -based solar cells much more efficient for the conversion of solar energy into electric energy (Section 5.3.2). Many fundamental questions on understanding and improving the photocatalytic activity of TiO_2 are open at this point, and may be addressed by studying photocatalytic reactions on single-crystalline surfaces under UHV conditions. The current literature on such studies is summarized in Section 5.3.3.

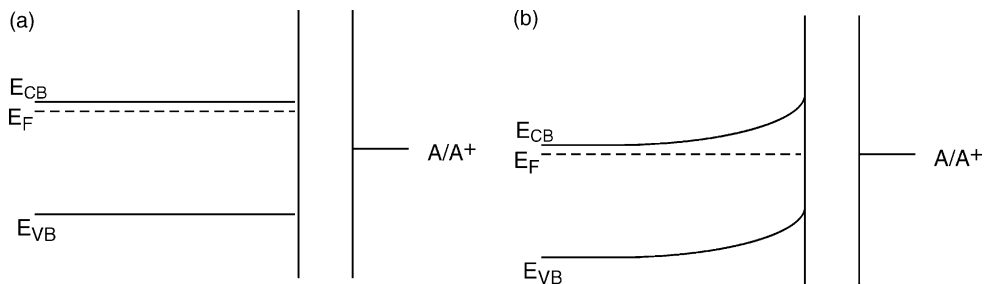


Fig. 70. Band structure in an n-type semiconductor (a) before contact with an electrolyte (flat band situation) and (b) in contact with an electrolyte.

5.3.1. Heterogeneous photocatalysis

Various aspects of the photocatalytic activity of TiO_2 are reviewed in [30,38,41,43,658]. The reactions accomplished through photocatalysis can involve oxidations and oxidative cleavages, reductions, geometric and valence isomerizations, substitutions, condensations, and polymerizations [658]. Of special interest is the employment of TiO_2 -based photocatalysts in remediation processes. Here complete mineralization is desired, i.e., the conversion of organic compounds to CO_2 , H_2O , NO_3^- , or other simple basic products.

The primary excitation process results in an electron in the conduction band and a hole in the valence band (Fig. 70a, Eq. (37)). When TiO_2 is in contact with an electrolyte, the Fermi level equilibrates with the redox potential of the redox couple. The resulting Schottky barrier (Fig. 70b) drives the electron and the hole in different directions. (It has been pointed out that the picture of a Schottky barrier formation is no longer valid when size of the photocatalytic TiO_2 particles approach nanoscopic dimensions [659].) The components of the electron–hole pair, when transferred across the interface, are capable of reducing and oxidizing an adsorbate, forming a singly oxidized electron donor and a singly reduced electron acceptor, Eqs. (37)–(42).



These processes result in anion or cation radicals which can undergo further reactions. Hydroxyl radicals are generally considered the most important species in the photocatalytic degradation of organics, although not in UHV-based studies (see Section 5.3.3). It is generally held that hole capture is directly through OH and not via water first, i.e., through Eq. (40) rather than Eq. (39). The $1b_1$ orbital of water lies above the 1π level of OH [477], so one might expect water to be better at ‘capturing’ a hole than OH, but the radical-cation of water may be neutralized before decomposing into an OH radical.

Also, it is mostly assumed that the surface is OH covered and therefore the hole is directly transferred to OH. UHV studies would be needed to correct or reinforce this assumption.

It has been observed that the photocatalytic activity of TiO₂ is completely suppressed in the absence of an electron scavenger such as molecular oxygen. Because the conduction band of TiO₂ is almost completely isoenergetic with the reduction potential of oxygen in inert solvents, adsorbed oxygen serves as an efficient trap for photogenerated electrons. The resulting species, superoxide, O₂^{•-}, is highly active and can attack other adsorbed molecules. Several other oxidation processes, in addition to reactions (Eqs. (38)–(42)) can occur as well [38,41,500]. Often, loading of TiO₂ with Pt and addition of H₂O₂ (Eq. (42)) enhance the overall efficiency of the photocatalytic degradation processes.

In order for photocatalysis to be efficient, electron–hole pair recombination must be suppressed before the trapping reactions occur at the interface. The recombination reaction occurs very fast, and the resulting low quantum efficiency is one of the main impediments for the use of TiO₂. While degradation of airborne pollutants has lead to an explosion of TiO₂-permeated paints and papers to clean up everything from cigarette smoke to acetaldehyde, TiO₂-based systems to treat contaminated water are severely suffering from the low yield, and their economic feasibility was questioned [660].

5.3.2. Photovoltaic cells

The use of TiO₂-based systems for the conversion of sunlight into electric energy involves a range of interesting fundamental questions. The most successful device is the so-called ‘Grätzel cell’. Fig. 71a shows the functioning principle of this dye-sensitized photovoltaic cell, which was originally proposed in [29]. The fundamental and technical aspects of this cell are reviewed in [659,661]. It consists of an electrode covered with colloidal, nanostructured TiO₂, which has been sintered together to form a percolating network. The mesoporous structure of the film exhibits a porosity of up to 50% and provides a very high surface area. The pores between the particles are interconnected. The colloidal TiO₂ film is supported on glass that is covered with a transparent conducting oxide (TCO) layer. The surface of the colloidal TiO₂ film is covered with a monolayer of dye. Photon excitation of the dye (S) results in an electron in an excited state (S^{*}). This electron is injected very rapidly (within a few picoseconds) into the conduction band of TiO₂. The backward reaction, i.e., charge recombination, occurs at a much slower rate (within a millisecond time frame). The electron injected in the TiO₂ conduction band then travels through the colloidal film to the back electrode. Interestingly, the as-prepared nanostructured TiO₂ film has a very high electrical resistivity but conducts electricity quite well when illuminated [659,661]. The transport through the mesoporous film is not well understood, possibly trap states within the particles or on their surfaces, as well as screening of the electron by the electrolyte, are major factors. The electrode with the TiO₂ film is connected to a counterelectrode (a piece of glass, covered with a TCO layer). The gap between the electrodes is typically filled with a molten salt containing a redox mediator (A/A⁻). The iodide-triiodide redox couple (I⁻/I₃⁻) works best, and the redox reaction is catalyzed by a small amount of Pt on the surface of the counterelectrode. The electric circuit is closed when the photo-oxidized dye molecules are reduced by electron transfer from the electrolyte. The operating voltage of the cell is given by the potential difference between the conduction band of the colloidal TiO₂ and the redox potential (relative to an SCE electrode) of the I⁻/I₃⁻ redox couple. In the case of the Grätzel cell, the voltage is in the order of 0.4 V, and currents between 16 and 20 mA/cm² can be achieved under standard operating conditions. Currently the overall efficiency of the photovoltaic cell is in the order of 10%.

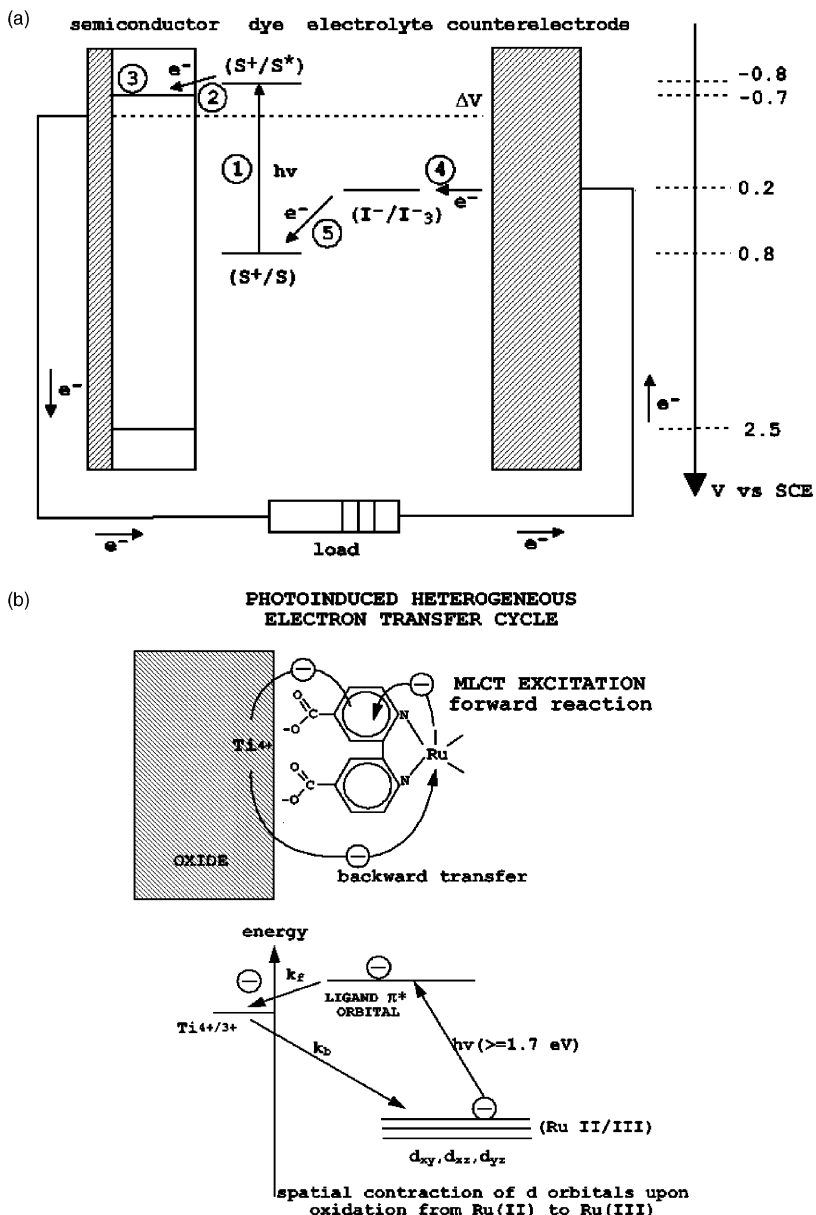


Fig. 71. (a) Schematic representation of the principle of the dye-sensitized photovoltaic cell [29]. Indicated are the electron energy levels in the three different phases important for the functioning of the cell. The system consists of a RuL₂(SCN)₂ dye adsorbed on a colloidal TiO₂ layer and the I⁻/I₃⁻ redox couple in the electrolyte. The cell voltage under illumination corresponds to the potential difference, ΔV , between the quasi-Fermi level of TiO₂ and the electrochemical potential of the electrolyte. S stands for sensitizer (the dye); S*, electronically excited sensitizer, S⁺, oxidized sensitizer. (b) Molecular orbital diagram for ruthenium complexes anchored to the TiO₂ surface by a carboxylated bipyridyl ligand. The visible light absorption of these types of complexes is the so-called metal-to-ligand charge transfer (MLCT) transition. The carboxylate groups are directly coordinated to the surface titanium ions producing intimate electronic contact between the sensitizer and the semiconductor. From Hagfeldt and Grätzel [659]. © 1995 The American Chemical Society.

The interface between the sensitizer and the TiO_2 surface is critical for the functioning of the cell and is of fundamental interest for surface investigations [615,662,663]. Several sensitizers were tried, and the most promising ones have the general structure $\text{ML}_2(\text{X})_2$, where L stands for 2,2'-bipyridyl-4,4'-dicarboxylic acid, M for Ru or Os, and X for halides, thiocyanate, or water. The structure of the most often used dye, the ruthenium complex *cis*-RuL₂-(NCS)₂, is sketched in Fig. 71b. This dye, often called ‘N₃’, is very stable and accomplishes a close to quantitative photon to electron conversion in the spectrum of visible light. (Recently, a black dye was found that shows a better light absorption behavior in the infrared region [661].) The photoexcitation process occurs between a ground state electron on the Ru center to a ligand orbital (metal to ligand charge transfer, MLCT, see Fig. 71b). The dye is anchored with two carboxylate groups to the TiO_2 surface, possibly in a fashion discussed in Section 5.2.1.9 and Fig. 67. The fast electron injection, which is essential for the functioning of the cell, is attributed to the hybridization between the π^* orbital of the carboxylate with the 3d electrons of the exposed fivefold coordinated Ti ions [663]. The backward reaction is slow because it involves electron transfer from TiO_2 to the oxidized ruthenium metal whose electronic overlap with the Ti wave functions is small, see Fig. 71b. As a model system, the adsorption of bi-isonicotinic acid on rutile (1 1 0) was studied with XPS and NEXAFS [615], see Section 5.2.1 and Fig. 67. The colloidal TiO_2 film has the anatase structure, however, and mostly (1 0 1), (1 0 0), and (0 0 1) faces are exposed. The adsorption of formic acid on anatase (1 0 1) was modeled with first-principles calculations [605]. Electrochemical measurements on anatase (1 0 1) single crystals show a much smaller efficiency for electron injection from the dye to the substrate as compared to nanophase films (with mostly the (1 0 1) face exposed) [209]. Perhaps this is a sign for the importance of surface defects in the injection process.

5.3.3. Photocatalysis on single-crystalline TiO_2

5.3.3.1. Oxygen, water, CO, and CO_2 . In UHV-based photocatalytic studies, vacancies in the bridging oxygen rows of $\text{TiO}_2(1\ 1\ 0)$ play a major role [43,444,496–498,500,522,531,664–668]. As discussed above (Section 5.1.3), these vacancies serve as adsorption site for O_2 molecules. Two species, originally termed ‘α’ and ‘β’ state by Yates and co-workers [496,497,522], were observed to chemisorb at vacancies. The α species, produced by adsorption at 105 K, can be activated to oxidize CO [496,497,522]. Lattice oxygen is not chemically involved in the CO_2 production [522], and, interestingly, the reaction is not enhanced by the presence of Pt [444]. Depending on surface preparation, two different defect states, termed ‘ α_1 ’ and ‘ α_2 ’ state, can be created on the $\text{TiO}_2(1\ 1\ 0)$ surface [498], which are both active for CO_2 production. Dosing oxygen at elevated temperatures, or annealing a sample with oxygen in the ‘α’ state, produces the ‘β’ state which photodesorbs and does not catalyze the CO oxidation reaction. Oxygen vacancies and molecular oxygen adsorbed at these defect sites also proved important in the photo-oxidation of $\text{CH}_3\text{Cl}/\text{TiO}_2(1\ 1\ 0)$ [664,665]. The threshold for photoexcitation is 3.1 eV, indicating that excitations within the TiO_2 substrate are important. Interestingly, surface hydroxyl groups do not oxidize methylchloride in the absence of adsorbed oxygen, which points out that Eq. (41) is more important than reactions (39) and (40), at least under UHV conditions.

The ternary system consisting of molecular oxygen, water, and rutile (1 1 0) has been investigated with TPD and spectroscopic techniques [500]. Molecular oxygen was dosed on a $\text{TiO}_2(1\ 1\ 0)$ surface with oxygen vacancies at 115 K. Irradiation with 4.1 eV photons lead to the photodesorption of the O_2 molecules adsorbed at the oxygen vacancies. However, the adsorbed oxygen is not removed completely and a photocatalytically active intermediate is formed in reaction with water. This intermediate was

tentatively assigned as hydrogen peroxy species. When the oxygen-precovered surface was covered with thick ice layers and irradiated with photons, a very sharp O₂ peak was observed in TPD spectra. This was interpreted as a trapping of the O₂ molecules in the ice layers.

5.3.3.2. Alcohols. Brinkley and Engel [666–668] studied the photocatalytic reaction of 2-propanol to acetone and water on TiO₂(1 1 0) and TiO₂(1 0 0). Only the most tightly bound propanol molecules were reactive for the photocatalytic dehydrogenation reaction, and no reaction was found in the absence of co-adsorbed O₂. Electron trapping at the adsorbed O₂ molecule (Eq. (41)) was invoked. From a combination of TPD and molecular beam experiments, it was found that about 0.08% of surface sites are active. The presence of oxygen vacancies increases the number to 0.15. It was suggested that steps, kinks, oxygen vacancies, and other sites that can adsorb O₂ strongly are active sites for the photocatalytic reaction. An intrinsic ‘heterogeneity’ of the ‘fully oxidized’ surface was concluded from these studies. This observation is in line with the quite complex nature of oxidized TiO₂(1 1 0) surface revealed in more recent STM studies of oxidized surfaces (see Section 2.2.2). Interestingly, the oxidation of 2-propanol is dominated by a thermal reaction channel on the TiO₂(1 0 0) surface. The thermally activated reaction on this surface is attributed to the proximity of bridging oxygen atoms to the propanol adsorption sites (the exposed Ti(5) atoms), which leads to a thermally activated dissociation. Henderson [174] suggested a similar mechanism to account for the difference in the water dissociation reaction on these two surfaces, see Section 5.1.2.

Recently, embedded cluster calculations of an adsorbed water molecule on a small rutile (1 1 0) cluster were performed [669]. It was found that the excited electron is located in the subsurface region, and that the hole is localized at the surface oxygen atoms and enhances the radical character of the hydroxyl group, in agreement with the notion that the OH radical is the active species for TiO₂ photocatalysis (Eq. (40)).

5.3.3.3. CHX₃ (X = Cl, Br, I). A series of adsorption and photodesorption studies was performed by Stair, Weitz, and co-workers [670–678], see Table 16(g) Methyl iodide (CH₃I) weakly physisorbs at TiO₂(1 1 0) and the monolayer desorbs around ~170 K [674]. The morphology of CH₃I films was deduced from TPD and UV-light desorption measurements [678]. At 90 K, films grow stochastically. Depending on the annealing temperature, either a Stranski–Krastanov type morphology (2D film with 3D clusters after annealing to 120 K) or a 2D film can be created. From TOF-REMPI measurements it was concluded that CD₃I molecules arrange themselves in a flat orientation in the monolayer regime [677]. The C–I bond lies roughly parallel to the surface normal, and the molecules are in an antiparallel configuration in the multilayer regime.

Laser irradiation in the UV regime produces CH₄, C₂H₆, I₂, C₂H₂, C₂H₅I₂, C₂H₅I [674,675]. The laser-induced desorption of CH₃I films was studied in dependence of the surface coverage. The initial excitation involves moving an electron from the TiO₂ substrate into a vertical affinity level [671,676,677]. Presumably, CH₃I molecules in the monolayer regime desorb in an Antoniewicz-type process (where the initial excitation of the adsorbed molecule results in an ion which moves towards the surface and is expelled into the vacuum when it is neutralized [679]). When the coverage is increased, the signal of desorbing CH₃I molecules is weakened due to collisional interactions within the film. For thicker films (>5 ML), the photodesorption signal increases again. It was proposed that photoexcited electrons solvate in the overlayer, which then induces desorption from the CH₃I film’s surface. The photodesorption of CH₃Br behaves similarly to CH₃I. In contrast, CH₃Cl was not found to photodesorb, when adsorbed by itself. Photodesorption was observed when it was co-adsorbed with CH₃I.

6. Summary and outlook

Titanium dioxide is a fascinating material from a surface science point of view. So much is known now about its surface geometric and electronic structure, and about fundamental steps in surface reactions, yet, so much is still to be learned. The main lessons that can be drawn from the previous chapters are summarized in the following paragraphs. In addition to gaining an ever better understanding of surface structure, geometry, and reactivity of TiO_2 itself, two issues will be important in future research. The first is, how can the lessons learned from TiO_2 be applied to other metal oxide systems? The surface science of metal oxides is a still growing field, and it will be interesting to see the applicability and limits of using TiO_2 as a prototype for other metal oxides. The second issue is probably even more important, how can the fundamental knowledge at the molecular scale, obtained in surface studies, be put to direct use for the many applications where TiO_2 surfaces play a role? As outlined in [Section 1.2](#) of this paper, TiO_2 is a technologically very important material, and the insights from surface-science studies could possibly help in a wide range of technical areas useful to society. A few thoughts related to these emerging topics are given in the following.

6.1. What has been learned and what is missing?

$\text{TiO}_2(1\ 1\ 0)$ is now well accepted as the quintessential bulk model oxide and this surface is being used routinely as a starting point for exploring new phenomena on oxides. Yet, the system is complex enough that it might still deliver some surprises. The combination of spectroscopic, diffraction, and imaging techniques, applied by many different groups world-wide over the course of many years, has delivered a very complete picture of the rutile $(1\ 1\ 0)$ surface. The stoichiometric surface and many of the different configurations of defects are now well characterized. Simple schemes, such as the concept of autocompensation (see [Section 2.2.1.1](#)), are a very useful first approach to interpret experimental results. Yet, one has to be careful; too simplistic approaches (e.g. explanations for reconstructions that involve an ordered array of oxygen vacancies or microfacets) have proven wrong upon closer inspection. TiO_2 has also become a model system for theorists to test, sharpen, and refine first-principles calculations of complex materials. The combined effort of experiment and theory has lead to a level of knowledge that is certainly unsurpassed for any metal oxide. Still, it is somewhat exasperating that important discrepancies between theory and experiment are still unresolved, such as the relaxation of the bridging oxygens ([Section 2.2.1.2](#)), the position of the defect state in the band gap on reduced surfaces ([Section 3.2.1](#)), and the adsorption state of water on rutile $(1\ 1\ 0)$ ([Section 5.1.2](#)).

From an experimental point of view, $\text{TiO}_2(1\ 1\ 0)$ is a wonderful sample to work with, but the exact preparation conditions are very important for the surface geometric and defect structure ([Section 2.2.3](#))—which can be curse and opportunity at the same time. Other orientations of rutile TiO_2 are still less well understood; most notably the $\text{TiO}_2(0\ 0\ 1)$ surface, where a confirmed atomic model of common reconstructions is still lacking. This is particularly unfortunate, as it has been the substrate of choice for many reactions of more complex organic molecules, see [Section 5.2](#), and of many (photo)electrochemical studies on single-crystalline TiO_2 [471,680–695]. Surface chemistry studies of organics are particularly important as they provide a link between fundamental research and applications in heterogeneous catalysis. It would be useful if relatively complex reactions were performed on the much better characterized $\text{TiO}_2(1\ 1\ 0)$ surface, and if the atomic-scale mechanisms were re-inspected, once a more accurate picture of the atomic geometry has been worked out.

The ‘other’ TiO_2 structure, anatase, which is technologically quite relevant, is now being investigated ([Section 2.6](#)). One will have to find out if the use of thin film and mineral samples is practical, but the first results on this material, and the progress that is being made, is quite promising.

The growth of metal overlayers, clusters and ultrathin films on TiO_2 has yielded a very complete picture. Any researcher interested in metal/oxide systems can learn much from the material summarized in [Section 4](#). It is beautiful to see how the main traits of metal overlayers follow general trends across the whole periodic table, and how this ties in with the rich details available for almost any metallic adsorbate on TiO_2 . The wealth of results on metals/ TiO_2 should give scientists, especially theorists, a good playing field for pushing our understanding of the technologically so important metal/metal oxide interface.

The next step in the attempt to provide more insight into heterogeneous catalysis should certainly involve chemistry on these metal/oxide systems. Will the metal/ $\text{TiO}_2(1\ 1\ 0)$ system be a useful model in this respect? The characterization of encapsulated Pt and Pd clusters in the SMSI state (see [Sections 4.2.24](#) and [4.2.25](#) on the growth of Pd and Pt) seems to have happened after the surge of interest in these systems is over, but the issue of gold-related catalysis is currently quite ‘hot’ and the surface science of TiO_2 , especially in relation to defect structures, might help to come up with good answers to many of the open questions ([Section 4.2.28](#)).

Perhaps one of the main lessons from recent research is the close relationship between bulk and surface properties in TiO_2 . It has been known for a long time that surface defects are important on metal oxides, but now it is clear that *bulk* defects have to be considered as well. The equilibration between bulk and surface defects that takes place at somewhat elevated temperatures has serious consequences for the surface morphology and structure ([Section 2.2.2](#)) as well as surface chemistry ([Section 5.1](#)). An adsorbate is affected by bulk defects provided it: (1) interacts stronger with surface defects than with the perfect surface (which, in essence, means almost *any* molecule or atom), and (2) the interaction with the surface takes place under conditions where the rate of diffusion of subsurface defects to the surface is comparable to the adsorption rate (i.e., at only slightly elevated temperatures or pressures). In this sense, the bulk defect concentration is quite an important property. It has become a common practice among researchers to quote the crystal color (see [Fig. 5](#)) as a qualitative measure for the defect concentration, but this is certainly an area where more quantitative studies about the different kind of defects, their depth distribution and diffusion properties towards and across the surface are needed.

6.2. TiO_2 in relation to other transition metal oxides

Considering at the mere number of publications ([Fig. 1](#)), TiO_2 is *the* model transition metal oxide. Yet, how much of the results and concepts surveyed in the proceeding chapters can be and will be applied to the surface science of other metal oxides?

One point that cannot be emphasized strongly enough is to ‘look before you do’—*first* perform a thorough characterization of the surface structure and morphology *before* performing other experiments. After all, much of the results discussed in [Section 2](#) have only been found recently. Who would have anticipated that the prevalence of ‘ (1×2) -type rows, even when LEED shows a (1×1) surface, the ‘rosette’ structure, or the influence of the bulk state on the surface morphology [[156](#)]? For historic reasons, much of TiO_2 -based research was performed before STM and AFM with (near) atomic resolution was applied. What is now known about the local surface structure puts in question parts of this results; something that can and needs to be avoided with other oxide system. As

Henrich and Cox [1] have pointed out in their 1993 monograph, surface preparation of metal oxides is a research project in itself—the experience with TiO_2 certainly proves this statement.

Other oxides with rutile structure. For the class of metal oxides with the rutile structure— SnO_2 , RuO_2 , CrO_2 , MnO_2 , VO_2 —exploring the similarities and also differences to rutile TiO_2 should be valuable in two respects. First, progress on these other oxides will proceed much more rapidly, without many of the detours taken in TiO_2 . Second, it will be interesting to see how many of the structural and chemical properties are specific to the rutile structure and what should be attributed to the Ti cation.

For example, the second-most studied oxide surface with rutile structure, SnO_2 , is still relatively unexplored. Upon annealing a $\text{SnO}_2(1\ 1\ 0)$ surface, a series of reconstructions evolve that have been characterized with LEED [696]. More recently, some of these reconstructions have been observed with STM [697–699] (as pointed out, a necessary first step to *really* understand this surface). For these structures, ordered arrays of oxygen vacancies have been suggested [696,700,701]; an approach that has fabulously failed for TiO_2 ([Section 2.2.2](#)). Of course one should not jump to conclusions too quickly and rule out that ordered O vacancies indeed do form on SnO_2 —it could well be possible that the fact that Sn is most stable in oxidation states 4+ and 2+ stabilizes these structures, much in contrast to Ti, which has a rich phase diagram with many stable phases ([Fig. 4](#)). Still, a look at TiO_2 suggests to test other possibilities, for example, structures involving interstitial Sn atoms.

Metallic ruthenium and its interaction with oxygen has long been investigated for its use as a possible catalyst for CO oxidation [702]. Perhaps not unsurprisingly, ruthenium is oxidized under reaction conditions, and the resulting $\text{RuO}_2(1\ 1\ 0)$ film is the catalytically active phase [703]. This observation has stimulated a flurry of activity and has caused RuO_2 to become a runner-up (with SnO_2) to be the second-most investigated oxide with rutile structure. Vacancies in the rows of bridging oxygens are an issue here as well. However, quite central for the activity of $\text{RuO}_2(1\ 1\ 0)$ are oxygen atoms adsorbed at ‘cus’ sites plays, i.e., in on-top sites at fivefold coordinated Ru atoms [504,704]. Even under UHV conditions such sites are occupied at slightly elevated pressures. No indication for these oxygens at $\text{TiO}_2(1\ 1\ 0)$ so far; could such sites become important when one goes to high even higher pressures? Because RuO_2 is a metallic material, imaging with STM is possible over a much wider range of bias voltages. Bright protrusions in STM images are attributed to O atoms [705], in contrast to STM on $\text{TiO}_2(1\ 1\ 0)$ ([Section 2.2.1.3](#))—maybe a warning sign that ‘imaging the surface cation’ is not automatically a given in atomically resolved STM of metal oxides. So far almost all experiments have been performed on the thin film that forms on Ru upon oxidation. RuO_2 single crystals of sufficient size can be grown [706], but have not yet been widely employed in surface studies. As pointed out above, the interaction with the bulk is important for the surface chemistry of TiO_2 —perhaps this is something to consider also in the case of RuO_2 .

For the other isostructural oxides, MnO_2 , VO_2 , and CrO_2 , large single crystals are not available, but rutile $\text{TiO}_2(1\ 1\ 0)$ acts an important substrate in growth experiments, see [Section 4.2](#) and [Table 6](#). These oxides exhibit quite interesting bulk and/or surface properties, e.g. the half-magnetic ferromagnetic nature of CrO_2 or the catalytic activity of TiO_2 -supported VO_2 . As has been mentioned above, the growth of metal oxide on TiO_2 is a somewhat neglected field, at least compared to the growth of metal overlayers on this substrate. The possibility of a controlled and tailored growth of these interesting oxides on $\text{TiO}_2(1\ 1\ 0)$ should provide impetus to look more closely into interface issues of oxide/oxide systems.

Other titanates. Certainly TiO_2 is of importance for other titanates—the (0 0 1) surface of perovskite titanates such as SrTiO_3 or BaTiO_3 can be terminated with a surface layer of either TiO_2 or MO (M = Sr, B, Ca, etc.) stoichiometry. Because perovskite oxides are widely used as substrates for

epitaxial growth of superconductors and dielectric materials, there is some interest in exploring the best recipes for surface preparation of SrTiO_3 [67,707]. For example, it is well-known that an etching procedure produces an exclusively TiO_2 -terminated surface [707]. Interestingly, the reconstructions that occur upon high-temperature annealing of SrTiO_3 are not yet completely understood. Again, in the light of TiO_2 -based research, it is questionable if ordered oxygen vacancies (which seem to come to mind immediately) are a good model, and recent studies indicate that this indeed not the case [708,709]. On the other hand, point defects, a significant issue in TiO_2 surface chemistry, might be both similar and different because of the presence of another cation.

Other oxides. Only a few semiconducting oxides can be investigated in bulk form with surface science techniques. Often the alternative approach is taken, i.e., growing a crystalline ultrathin film on a metallic substrate [3,287,710]. It is often a matter of necessity to use these systems, especially when oxides are too insulating as bulk single crystals. Again, one important lesson from TiO_2 is that the bulk *does* matter—for the formation of surface defects, during surface preparation, for adsorption processes, in reactivity or encapsulation experiments. Maybe this is not so important in the case of non-reducible oxides such as MgO or Al_2O_3 , but for reducible *transition* metals oxides that exhibit several phases, it is likely that similar processes happen at relatively low temperatures. In this respect, it might be interesting to compare the reactivity of ultrathin oxide films (maybe even an ultrathin TiO_2 film) one-to-one with studies on bulk-crystals in order to find out just what the applicability and limitation of film model systems are.

6.3. TiO_2 —mixed and doped

Most metal oxides, when used in the technical applications are ‘functionalized’ through doping, or are used in combination with other oxides, and so is TiO_2 . For example, doping with traces of early transition metals and/or lanthanides increases the quantum yield in photocatalytic degradation processes, and TiO_2 in gas sensors is usually doped with noble metals. Indeed, most of the other industrial applications cited in Section 1.2 employ doped TiO_2 instead of the pure material. Doping can have a variety of consequences as it may alter the structure, electronic properties, or thermal stability of this material. From a surface science perspective, an unraveling of all these factors is an almost completely unexplored (though possibly highly rewarding) territory. There is now sufficient information on pure TiO_2 that one can confidently go one step further and introduce—in a well-controlled way—impurities and dopants. This brings surface studies not only one step closer to complex reality, the few examples of surface investigations on doped TiO_2 [153,374,376,711,712] show that the local variations of electronic structure are also quite interesting from a fundamental point of view. The most striking example is the influence of Co doping on the magnetic properties of TiO_2 anatase [55,56]. This novel dilute ferromagnetic semiconductor was found in a combinatorial study by Matsumoto et al. [55]. While doping has long been used to improve the performance of TiO_2 -based devices, rationally tailoring the surface properties of this material with atomic-sized control should provide opportunity to create specific surface structures, control defects and their diffusivity, and tailor electronic properties.

6.4. Nanostructured TiO_2

The current international trend (or, more accurately, ‘hype’) to synthesize, characterize, and investigate ‘nano’ materials has also embraced TiO_2 . This material lends itself quite well to building

tiny structures in all sorts of sizes and shapes. Such nano-TiO₂ is typically produced in a sol–gel process, where a titanium alkoxide or halide (TiCl₄, TiF₄) is hydrolyzed, often in the presence of a template such as nano-spheres, nano-rods or anodic porous alumina [713,714,715], but other techniques have been used as well [716–719].

The structures that have been made—nano-rods, whiskers, wires, spheres, ordered holes—are simply fascinating. For example perfectly ordered TiO₂ ‘nano-whiskers’, i.e., flat anatase platelets a few nanometer wide and several tens of nanometer long, were produced by Zhu and Ding [720]. In this case, the selective coordination of acetate groups on specific lattice planes was invoked to account for the oriented growth. (Incidentally, the speculation about the anchoring of this group to the different surfaces in [720] could certainly be answered by surface scientists, considering how much is now known about acetates on rutile, Section 5.2.1. Just one example how interrelated ‘nano’ and surface research are.) Another beautiful construction are hollow TiO₂ ‘microspheres’, ca. 20 μm in diameter with a wall only a few tens of nanometer thick, synthesized by Iida et al. [721]. Yin et al. [722] have succeeded in ‘functionalizing’ such hollow spheres by packing small Ag particles onto the interior surface of the inside void. It was suggested that these nanoparticles could then be etched out, leaving behind nanoholes in microspheres. It was speculated that these structures could be used as extremely tiny containers for encapsulation in the delivery of drugs or the protection of biologically active agents [722]. Or one could dream as these spheres becoming the tiniest ‘microreactors’ for catalytic reactions. More mundane applications would be as a low-density filler materials.

The formation of periodic arrangements of nanostructured TiO₂ can also be achieved. For example, the formation of a zeolite-like mesoporous materials has been accomplished for TiO₂ and other metal oxides [719,723]. Such high-surface area materials could be interesting for catalytic applications or in photonics. The formation of films with a self-organized nanostructure is explored for improving devices based on photo-active TiO₂ (Section 5.3.2). A hexagonal arrangement of anatase nanocrystals was achieved [724] and rod-like single-crystalline anatase particles could be brought into a regular cubic array [715]. These periodic arrangements are achieved through a balance of electrostatic forces in the solution. They exhibit an extremely regular pore size and a high surface area. The smallest nano-rods in [715] have predominantly (1 0 0)-oriented surfaces (a surface that has just recently been characterized with surface science techniques [231]). Such a structure would allow to investigate the influence of surface orientation on the performance of dye-sensitized solar cells (Section 5.3.2) or electrochromic devices.

Interestingly, TiO₂ nanostructures are almost invariably either amorphous or of anatase form—another good motivation for surface scientists to find out more about the surfaces of this TiO₂ polymorph. There is a clear connection between the surface properties, the rational development of improved synthesis routes, and the possible usefulness in applications of nanomaterials. Hence the lessons, learned from atomic-scale investigations such as the ones reviewed in this paper, could be quite valuable for synthesis-oriented researchers. Conversely, using well-characterized nanostructures instead of single crystals in surface chemistry experiments might be a promising and exciting new approach. Research ‘in the nanoworld’ provides almost unlimited nourishment for imagination on how these tiny structures could be used—and often a glaring gap to real technical developments. In the case of TiO₂, however, the proven performance improvement of nano-scaled structures in photo-active devices shows that a cross-fertilization between surface studies and synthesis of nano-TiO₂ could be valuable well beyond the realm of fundamental research.

6.5. Going beyond single crystal and UHV studies

If research on oxides is viewed as an important attempt to bridging the (in)famous materials gap, then research on ‘dirty’ oxides (in the sense described above, i.e., mixed, doped, nano-sized, polycrystalline, etc.) will certainly constitute the next logical step. Of course the key factor is doing so without sacrificing the degree of control that is provided by UHV studies and single crystals. In this sense, newly emerging techniques are particularly important, such as the SEM/STM that has been applied by Asari and Souda [725] to image selected corns of polycrystalline Degussa P25 powder. More of such studies are needed, especially in combination with the tailored nanostructures mentioned in [Section 6.4](#).

If one wants to link surface-science studies closer to applications, it is also vital to bring surface science out of UHV (‘bridging the pressure gap’ as it is often termed [726]). This would further test the relevance of the acquired knowledge for technical applications. Many specific questions are awaiting an answer, for example, How stable are the various defects under high-pressure environments? Are point defects as important for adsorption and reactions as UHV-based adsorption experiments suggest? Do step edges (which do not seem to be too critical under UHV conditions) play a more important role in a high-pressure environment? Can one link surface reactivity and local coordination, i.e., by purposely creating arrays of undersaturated atoms (e.g. in a rosette network)? Is the interaction with the bulk already a significant factor at room temperature if one goes to high enough pressures? Scanning probe, spectroscopic and optical techniques, compatible with high pressures, are currently being developed [726–730]. TiO₂ could be a wonderful test system for these newly emerging techniques if one considers its often defect-driven surface chemistry (and, otherwise, relative inertness) combined with clear spectroscopic evidence for defect structures.

As pointed out several times throughout this review, the photoactivity of TiO₂ is one of its most interesting and attractive property. Studies of photoactivity can conveniently be combined with UHV techniques, as shown in an impressive way by Yates and co-workers. A clear outcome of these studies (see [Section 5.3.3](#)) is the dominating role of defects. Probing into the effect of the local environment on photoactivity, e.g. with low-*T* STM, is an experiment that just waits to be taken up by someone. UHV-based photocatalytic studies have shown some important differences to chemistry in a wet environment, e.g. the (relative) unimportance of hydroxyl groups [664] or the absence of the enhancing effect of Pt for CO oxidation [444]. The combination of (photo-) electrochemical measurements with surface analytical techniques, e.g. in reaction cells attached to UHV chambers, quite successful for metal surfaces, has hardly been explored for TiO₂. There are ample examples of photoelectrochemical measurements on TiO₂ single crystals [28,209,227,471,680–695,731]. Unfortunately (from a surface science perspective), most of these studies have been performed on the rutile (0 0 1) surface, which is an inherently unstable surface with an atomic-scale structure that is not yet resolved ([Section 2.4](#)). Also, from today’s point of view, most of these surfaces were poorly characterized; the usually applied preparation techniques of reduction in an H₂ atmosphere and polishing and etching can lead to segregation of impurities and will introduce many surface defects [695,732]. Still, there are many indications that surface defects play a big role in the photochemical activity [209,680,731]—it is just not known which ones and how. With the background of atomic-scale investigations of surface defects ([Section 2.2.1.4](#)), it would be well-worth an effort to find out how different surface terminations, orientations, and structures influence photo-reactivity.

6.6. Concluding remarks

As is often the case when reviewing the current literature on a subject, glaring gaps and omissions become clear. While much work has been done, and much has been achieved, the surface(s) of TiO₂ are far from being completely resolved, as was pointed out throughout this review. Some of the more important open questions are re-emphasized in the last few sections. There is ample need for addressing important, fundamental problems, as well as much excitement for significant contributions that help to resolve these. Because TiO₂ is used in so many different fields it would be very unfortunate if the rich and detailed knowledge that has been accumulated in recent years would go unnoticed by researchers in more applied areas. While some of these results reviewed here might turn out to be of mere fundamental interest and irrelevant for the particular environment, application or problem, some might help when trying to understand the behavior of this material. TiO₂ will be important for years to come, and it is hoped that this review will help to link the more fundamental and more applied lines of research on this great material.

Acknowledgements

Foremost, I would like to thank Prof. Theodore E. Madey for stimulating my initial interest in TiO₂, for his continued support throughout the years, and for his encouragement to write this review. I owe warm thanks to Dr. Michael A. Henderson for many insightful discussions and suggestions, and for giving me access to his comprehensive data base on TiO₂ surfaces; to Dr. Matthias Batzill for critically reading this manuscript; to many colleagues for providing me with unpublished results as well as reprints, preprints, and electronic versions of their figures; and to my students and post-docs for downloading and copying numerous articles and for help with figures and tables. The National Science Foundation, the Department of Energy, NASA, and the Louisiana Board of Regents are acknowledged for their continuing support of our work on TiO₂ surfaces. I want to thank the Alexander von Humboldt—Foundation for financial support and Prof. H.J. Freund from the Fritz-Haber Institute, Germany, for his kind hospitality during the final stages of writing this manuscript.

References

- [1] V.E. Henrich, P.A. Cox, *The Surface Science of Metal Oxides*, Cambridge University Press, Cambridge, 1994.
- [2] C. Noguera, *Physics and Chemistry of Oxide Surfaces*, Cambridge University Press, Cambridge, 1996.
- [3] H.-J. Freund, *Angew. Chem. Int. Ed. Engl.* 36 (1997) 452.
- [4] C.T. Campbell, *Surf. Sci. Rep.* 27 (1997) 1.
- [5] J.P. LaFemina, *Crit. Rev. Surf. Chem.* 3 (1994) 297.
- [6] M.A. Barreau, *J. Vac. Sci. Technol. A* 11 (1993) 2162.
- [7] D.A. Bonnell, *Prog. Surf. Sci.* 57 (1998) 187.
- [8] R.J. Lad, *Surf. Rev. Lett.* 2 (1995) 109.
- [9] R.J. Lad (Ed.), *Surface Structure of Crystalline Ceramics*, vol. 1, Elsevier, Amsterdam, 1996.
- [10] R. Persaud, T.E. Madey, Growth, structure and reactivity of ultrathin metal films on TiO₂ surfaces, in: D.A. King, D.P. Woodruff (Eds.), *The Chemical Physics of Solid Surfaces*, vol. 8, Elsevier, Amsterdam, 1997.
- [11] C.N. Satterfield, *Heterogeneous Catalysis in Industrial Practice*, 2nd ed., McGraw-Hill, New York, 1991.
- [12] J. Biener, J. Wang, R.J. Madix, *Surf. Sci.* 442 (1999) 47.

- [13] Q. Guo, S. Lee, D.W. Goodman, *Surf. Sci.* 437 (1999) 38.
- [14] M. Sambi, G. Sangiovanni, G. Granozzi, F. Parmigiani, *Phys. Rev. B* 54 (1996) 13464.
- [15] Z. Zhang, V.E. Henrich, *Surf. Sci.* 277 (1992) 263.
- [16] G.L. Haller, D.E. Resasco, *Adv. Catal.* 36 (1989) 173.
- [17] J.M. Pan, T.E. Madey, *Catal. Lett.* 20 (1993) 269.
- [18] F. Pesty, H.P. Steinrück, T.E. Madey, *Surf. Sci.* 339 (1995) 83.
- [19] R.A. Bennett, P. Stone, M. Bowker, *Catal. Lett.* 59 (1999) 99.
- [20] O. Dulub, W. Hebenstreit, U. Diebold, *Phys. Rev. Lett.* 84 (2000) 3646.
- [21] M. Ando, T. Kobayashi, M. Haruta, *Catal. Today* 36 (1997) 135.
- [22] M. Valden, X. Lai, D.W. Goodman, *Science* 281 (1998) 1647.
- [23] V.A. Bondzie, S.C. Parker, C.T. Campbell, *Catal. Lett.* 63 (1999) 143.
- [24] L. Zhang, F. Cosandey, R. Persaud, T.E. Madey, *Surf. Sci.* 439 (1999) 73.
- [25] A. Fujishima, K. Honda, *Nature* 238 (1972) 37.
- [26] V.E. Henrich, G. Dresselhaus, H.J. Zeiger, *Phys. Rev. Lett.* 36 (1976) 1335.
- [27] W.J. Lo, Y.W. Chung, G.A. Somorjai, *Surf. Sci.* 71 (1978) 199.
- [28] H.O. Finklea, *Semiconductor Electrodes*, Elsevier, Amsterdam, 1988.
- [29] B. O'Regan, M. Grätzel, *Nature* 353 (1991) 737.
- [30] K. Rajeswar, *J. Appl. Electrochem.* 15 (1985) 1.
- [31] A. Mills, H.R. Davies, D. Worsley, *Chem. Soc. Rev.* 22 (1993) 417.
- [32] P.-C. Maness, S. Smolinski, W.A. Jacoby, *Appl. Environ. Microbiol.* 65 (1999) 4094.
- [33] Y. Paz, Z. Luo, L. Rabenberg, A. Heller, *J. Mater. Res.* 10 (1995) 2842.
- [34] I. Poulios, P. Spathis, P. Tsoumparis, *J. Environ. Sci. Health* 34 (1999) 1455.
- [35] R. Cai, K. Hashimoto, K. Itoh, Y. Kubota, A. Fujishima, *Bull. Chem. Soc. Jpn.* 64 (1991) 1268.
- [36] A. Fujishima, R. Cai, K. Hashimoto, H. Sakai, Y. Kubota, *Trace Met. Environ.* 3 (1993) 193.
- [37] H. Sakai, R. Baba, K. Hashimoto, Y. Kubota, A. Fujishima, *Chem. Lett.* (1995) 185.
- [38] O. Legrini, E. Oliveros, A.M. Braun, *Chem. Rev.* 93 (1993) 671.
- [39] D. Bahnemann, J. Cunningham, M.A. Fox, E. Pelizzetti, P. Pichat, N. Serpone, *Photocatalytic treatment of waters*, in: G. Helz, R. Zepp, D. Crosby (Eds.), *Aquatic and Surface Photochemistry*, CRC Press, 1994, 261 pp.
- [40] D.Y. Goswami, *Engineering of the solar photocatalytic detoxification and disinfection processes*, in: K.W. Boer (Ed.), *Advances in Solar Energy*, vol. 10, American Solar Energy Society, Boulder, CO, 1995, 165 pp.
- [41] A. Heller, *Acc. Chem. Res.* 28 (1995) 503.
- [42] M. Hoffman, S. Martin, W. Choi, D. Bahnemann, *Chem. Rev.* 95 (1995) 69.
- [43] A.L. Linsebigler, G. Lu, J.T. Yates Jr., *Chem. Rev.* 95 (1995) 735.
- [44] G. Sheveglieri (Ed.), *Gas Sensors*, Kluwer Academic Publishers, Dordrecht, 1992.
- [45] P.K. Dutta, A. Ginwalla, B. Hogg, B.R. Patton, B. Chwieroth, Z. Liang, P. Gouma, M. Mills, S. Akbar, *J. Phys. Chem.* 103 (1999) 4412.
- [46] Y. Xu, K. Yao, X. Zhou, Q. Cao, *Sens. Actuators B* 13–14 (1993) 492.
- [47] U. Kirner, K.D. Schierbaum, W. Göpel, B. Leibold, N. Nicoloso, W. Weppner, D. Fischer, W.F. Chu, *Sens. Actuators B* 1 (1990) 103.
- [48] Kronos International, 1996.
- [49] F.A. Grant, *Rev. Mod. Phys.* 31 (1959) 646.
- [50] L.G. Phillips, D.M. Barbano, *J. Dairy Sci.* 80 (1997) 2726.
- [51] J. Hewitt, *Cosmet. Toiletries* 114 (1999) 59.
- [52] H. Selhofer, *Vacuum Thin Film* (August 1999) 15.
- [53] E. Garfunkel, E. Gusev, A. Vul (Eds.), *Fundamental Aspects of Ultrathin Dielectrics on Si-based Devices*, NATO Science Series, Kluwer Academic Publishers, Dordrecht, 1998.
- [54] S.A. Campbell, H.-S. Kim, D.C. Gilmer, B. He, T. Ma, W.L. Gladfelter, *IBM J. Res. Develop.* 43 (1999) 383.
- [55] Y. Matsumoto, T. Shono, T. Hasegawa, T. Fukumura, M. Kawasaki, P. Ahmet, T. Chikyow, S. Koshihara, H. Koinuma, *Science* 291 (2001) 854.
- [56] S.A. Chambers, S. Thevuthasan, R.F.C. Farrow, R.F. Marks, J.U. Thiele, L. Folks, M.G. Samant, A.J. Kellock, N. Ruzycki, D.L. Ederer, U. Diebold, *Appl. Phys. Lett.* 79 (2001) 3467.
- [57] P. Bonhote, E. Gogniat, M. Grätzel, P.V. Ashrit, *Thin Solid Films* 350 (1999) 269.

- [58] J.R. Sambrano, J. Andres, A. Beltran, F.R. Sensato, E.R. Leite, F.M.L.G. Stamato, E. Longo, Int. J. Quantum Chem. 65 (1997) 625.
- [59] B.D. Ratner, A.S. Hoffman, F.J. Schoen, J.E. Lemons (Eds.), Biomaterials Science—An Introduction to Materials in Medicine, Academic Press, San Diego, 1996.
- [60] C. Sittig, M. Textor, N.D. Spencer, M. Wieland, P.H. Vallotton, J. Mater. Sci. 10 (1999) 35.
- [61] J. Lausmaa, M. Ask, U. Rolander, B. Kasemo, Mater. Res. Soc. Symp. Proc. 110 (1988) 647.
- [62] P.W. Tasker, J. Phys. C 12 (1979) 4977.
- [63] U. Diebold, J.M. Pan, T.E. Madey, Surf. Sci. 333 (1995) 845.
- [64] N.M. Harrison, X.G. Wang, J. Muscat, M. Scheffler, Faraday Discuss., Chem. Soc. 114 (1999) 305.
- [65] G.V. Samsonov, The Oxide Handbook, IFI/Plenum Press, New York, 1982.
- [66] L.S. Dubrovinsky, N.A. Dubrovinskaya, V. Swamy, J. Muscat, N.M. Harrison, R. Ahuja, B. Holm, B. Johansson, Nature 410 (2001) 653.
- [67] U. Diebold, Specimen treatment: preparation of metal compound materials (mainly oxides), in: C.A. Czanderna, C.J. Powell, T.E. Madey (Eds.), Specimen Handling, Treatments, Beam Effects and Depth Profiling, vol. 4, 1999.
- [68] M. Ramamoorthy, D. Vanderbilt, Phys. Rev. B 49 (1994) 16721.
- [69] A. Zangwill, Physics at Surfaces, Cambridge, 1988.
- [70] A. Vittadini, A. Selloni, F.P. Rotzinger, M. Grätzel, Phys. Rev. Lett. 81 (1998) 2954.
- [71] U. Diebold, M. Li, O. Dulub, E.L.D. Hebenstreit, W. Hebenstreit, Surf. Rev. Lett. 5–6 (2000) 613.
- [72] K.D. Schierbaum, S. Fischer, M.C. Torquemada, J.L. de Segovia, E. Román, J.A. Martín-Gato, Surf. Sci. 345 (1996) 261.
- [73] M.A. Henderson, Surf. Sci. 343 (1995) L1156.
- [74] M.A. Henderson, Surf. Sci. 419 (1999) 174.
- [75] M. Li, W. Hebenstreit, L. Gross, U. Diebold, M.A. Henderson, D.R. Jennison, P.A. Schultz, M.P. Sears, Surf. Sci. 437 (1999) 173.
- [76] R.A. Bennett, P. Stone, N.J. Price, M. Bowker, Phys. Rev. Lett. 82 (1999) 3831.
- [77] E.L.D. Hebenstreit, W. Hebenstreit, U. Diebold, Surf. Sci. 461 (2000) 87.
- [78] E. Yagi, R. Hasiguti, M. Aono, Phys. Rev. B 54 (1996) 7945.
- [79] R.R. Hasiguti, E. Yagi (1994).
- [80] P. Kofstad, J. Less-Common Met. 13 (1967) 635.
- [81] D.J. Smith, L.A. Bursill, M.G. Blanchin, Philosophical Mag. A 50 (1984) 473.
- [82] L.A. Bursill, D.J. Smith, Nature 309 (1984) 319.
- [83] L.A. Bursill, M.G. Blanchin, D.J. Smith, Proc. Roy. Soc. London Ser. A 391 (1984) 351.
- [84] G.S. Rohrer, V.E. Henrich, D.A. Bonnell, Science 250 (1990) 1239.
- [85] H. Nörenberg, R.E. Tanner, K.D. Schierbaum, S. Fischer, G.A.D. Briggs, Surf. Sci. 396 (1998) 52.
- [86] H. Nörenberg, G.A.D. Briggs, Surf. Sci. 404 (1998) 738.
- [87] R.A. Bennett, S. Pouston, P. Stone, M. Bowker, Phys. Rev. B 59 (1999) 10341.
- [88] P.W. Murray, N.G. Condon, G. Thornton, Phys. Rev. B 51 (1995) 10989.
- [89] J. Sasaki, N.L. Peterson, K. Hoshino, J. Phys. Chem. Solids 46 (1985) 1267.
- [90] H.B. Huntington, G.A. Sullivan, Phys. Rev. Lett. 14 (1965) 177.
- [91] S.D. Elliott, S.P. Bates, Phys. Chem. Chem. Phys. 3 (2001) 1954.
- [92] R. Wang, K. Hashimoto, A. Fujishima, M. Chikuni, E. Kojima, A. Kitamura, M. Shimohigoshi, T. Watanabe, Nature 388 (1997) 431.
- [93] Y. Gao, S.A. Chambers, Mater. Res. Soc. Symp. Proc. 401 (1996) 85.
- [94] G. Charlton, P.B. Hoowes, C.L. Nicklin, P. Steadman, J.S.G. Taylor, C.A. Muryn, S.P. Harte, J. Mercer, R. McGrath, D. Norman, T.S. Turner, G. Thornton, Phys. Rev. Lett. 78 (1997) 495.
- [95] B. Hird, R.A. Armstrong, Surf. Sci. 420 (1999) L131.
- [96] B. Hird, R.A. Armstrong, Surf. Sci. 385 (1997) L1023.
- [97] E. Asari, T. Suzuki, R. Souda, Phys. Rev. B 61 (2000) 5679.
- [98] A. Verdini, M. Sambi, F. Bruno, D. Cvetko, M.D. Negra, R. Gotter, L. Floreano, A. Morgante, G.A. Rizzi, G. Granozzi, Surf. Rev. Lett. 6 (1999) 2101.
- [99] P.J.D. Lindan, J. Muscat, S. Bates, N.M. Harrison, M. Gillan, Faraday Discuss., Chem. Soc. 106 (1997) 135.
- [100] D. Vogtenhuber, R. Podloucky, A. Neckel, S.G. Steinemann, A.J. Freeman, Phys. Rev. B 49 (1994) 2099.

- [101] P. Reinhardt, B.A. Heß, Phys. Rev. B 50 (1994) 12015.
- [102] S.P. Bates, G. Kresse, M.J. Gillan, Surf. Sci. 409 (1998) 336.
- [103] D.R. Hamann, Phys. Rev. B 56 (1997) 14979.
- [104] K.M. Glassford, J.R. Chelikowsky, Phys. Rev. B 46 (1992) 1284.
- [105] W. Langel, Surf. Sci. 496 (2002) 141.
- [106] D. Vogtenhuber, R. Poducky, J. Redinger, E.L.D. Hebenstreit, W. Hebenstreit, U. Diebold, Phys. Rev. B 65 (2002) 125411/1.
- [107] G. Charlton, P.B. Howes, C.A. Muryn, H. Raza, N. Jones, J.S.G. Taylor, C. Norris, R. McGrath, D. Norman, T.S. Turner, G. Thornton, Phys. Rev. B 61 (2000) 16117.
- [108] H. Onishi, Y. Iwasawa, Chem. Phys. Lett. 226 (1994) 111.
- [109] U. Diebold, W. Hebenstreit, G. Leonardelli, M. Schmid, P. Varga, Phys. Rev. Lett. 81 (1998) 405.
- [110] U. Diebold, J.F. Anderson, K.O. Ng, D. Vanderbilt, Phys. Rev. Lett. 77 (1996) 1322.
- [111] P.J. Møller, M.-C. Wu, Surf. Sci. 224 (1989) 265.
- [112] O. Gölseren, R. James, D.W. Bullett, Surf. Sci. 377–379 (1997) 150.
- [113] R.E. Tanner, M.R. Castell, G.A.D. Briggs, Surf. Sci. 412 (1998) 672.
- [114] A. Szabo, T. Engel, Surf. Sci. 329 (1995) 241.
- [115] Q. Guo, I. Cocks, E.M. Williams, J. Phys. D 31 (1998) 2231.
- [116] U. Diebold, J. Lehman, T. Mahmoud, M. Kuhn, G. Leonardelli, W. Hebenstreit, M. Schmid, P. Varga, Surf. Sci. 411 (1998) 137.
- [117] S. Fischer, A.W. Munz, K.D. Schierbaum, W. Göpel, Surf. Sci. 337 (1995) 17.
- [118] K.-i. Fukui, H. Onishi, Y. Iwasawa, Phys. Rev. Lett. 79 (1997) 4202.
- [119] T.R. Albrecht, P. Grütter, D. Horne, D. Rugar, J. Appl. Phys. 69 (1991) 668.
- [120] M. Reichling, C. Barth, Phys. Rev. Lett. 83 (1999) 768.
- [121] B. Grossmann, P. Piercy, Phys. Rev. Lett. 74 (1995) 4487.
- [122] H. Onishi, K.-i. Fukui, Y. Iwasawa, Bull. Chem. Soc. Jpn. 68 (1995) 2447.
- [123] H. Onishi, Y. Iwasawa, Surf. Sci. 313 (1994) L783.
- [124] S. Suzuki, Y. Yamaguchi, H. Onishi, K.-i. Fukui, T. Sasaki, Y. Iwasawa, Catal. Lett. 50 (1998) 117.
- [125] S. Gan, Y. Liang, D.R. Baer, Phys. Rev. B 63 (2001) 121401/1.
- [126] Y. Iwasawa, H. Onishi, K.-i. Fukui, S. Suzuki, T. Sasaki, Faraday Discuss., Chem. Soc. 114 (1999) 259.
- [127] J.M. Pan, B.L. Maschhoff, U. Diebold, T.E. Madey, J. Vac. Sci. Technol. A 10 (1992) 2470.
- [128] M.A. Henderson, Surf. Sci. 355 (1996) 151.
- [129] C.A. Jenkins, D.M. Murphy, J. Phys. Chem. B 103 (1999) 1019.
- [130] L.Q. Wang, D.R. Baer, M.H. Engelhard, Surf. Sci. 320 (1994) 295.
- [131] W. Göpel, G. Rocker, R. Feierabend, Phys. Rev. B 28 (1983) 3427.
- [132] D. Vogtenhuber, Private communication.
- [133] S. Suzuki, K.-i. Fukui, H. Onishi, Y. Iwasawa, Phys. Rev. Lett. 84 (2000) 2156.
- [134] R. Schaub, P. Thostrup, N. Lopez, E. Lægsgaard, I. Stensgaard, J.K. Nørskov, F. Besenbacher, Phys. Rev. Lett. 87 (2001) 266104/1.
- [135] M.L. Knotek, P.J. Feibelman, Surf. Sci. 90 (1979) 78.
- [136] U. Diebold, T.E. Madey, Phys. Rev. Lett. 72 (1994) 1116.
- [137] E. Bertel, R. Stockbauer, T.E. Madey, Surf. Sci. 141 (1984) 355.
- [138] L.Q. Wang, D.R. Baer, M.H. Engelhard, A.N. Shultz, Surf. Sci. 344 (1995) 237.
- [139] S.A. Joyce, Private communication.
- [140] A. Berkó, E. Krivan, J. Vac. Sci. Technol. B 15 (1997) 25.
- [141] M.R. McCartney, D.J. Smith, Surf. Sci. 250 (1991) 169.
- [142] A.N. Shultz, W. Jang, W.M.I. Hetherington, D.R. Baer, L.Q. Wang, M.H. Engelhard, Surf. Sci. 339 (1995) 114.
- [143] T.E. Madey, B.L. Maschhoff, Unpublished results.
- [144] M. Li, W. Hebenstreit, U. Diebold, Phys. Rev. B 61 (2000) 4926.
- [145] L.P. Zhang, M. Li, U. Diebold, Surf. Sci. 412 (1998) 242.
- [146] H. Nörenberg, J.H. Harding, Appl. Surf. Sci. 142 (1999) 174.
- [147] H. Nörenberg, J.H. Harding, Phys. Rev. B 59 (1999) 9842.
- [148] H. Nörenberg, J.H. Harding, Surf. Sci. 473 (2001) 151.

- [149] J.F. Anderson, M. Kuhn, U. Diebold, K. Shaw, P. Stoyanov, D. Lind, Phys. Rev. B 56 (1997) 9902.
- [150] S. Gan, Y. Liang, D.R. Baer, Surf. Sci. 459 (2000) L498.
- [151] M.A. Henderson, S. Otero-Tapia, M.E. Castro, Surf. Sci. 412 (1998) 252.
- [152] M.A. Henderson, Private communication.
- [153] M. Batzill, B. Katsiev, D.J. Gaspar, U. Diebold, Phys. Rev. B 66 (2002).
- [154] G.S. Rohrer, V.E. Henrich, D.A. Bonnell, Surf. Sci. 278 (1992) 146.
- [155] H. Nörenberg, G.A.D. Briggs, Surf. Sci. 404 (1998) 738.
- [156] M. Li, W. Hebenstreit, U. Diebold, A.M. Tyryshkin, M.K. Bowman, G.G. Dunham, M.A. Henderson, J. Phys. Chem. B 104 (2000) 4944.
- [157] R.A. Bennett, Phys. Chem. Commun. 3 (2000) (web-based journal).
- [158] M. Sander, T. Engel, Surf. Sci. 302 (1994) L263.
- [159] M. Wagner, O. Kienzle, D.A. Bonnell, M. Rühle, J. Vac. Sci. Technol. A 16 (1998) 1078.
- [160] P.W. Murray, N.G. Condon, G. Thornton, Surf. Sci. 323 (1995) L281.
- [161] A. Berkó, F. Solymosi, Langmuir 12 (1996) 1257.
- [162] C. Xu, X. Lai, G.W. Zajac, D.W. Goodman, Phys. Rev. B 56 (1997) 13464.
- [163] C.L. Pang, S.A. Haycock, H. Raza, P.W. Murray, G. Thornton, O. Gürseren, R. James, D.W. Bullett, Phys. Rev. B 58 (1998) 1586.
- [164] E. Asari, R. Souda, Phys. Rev. B 60 (1999) 10719.
- [165] K.O. Ng, D. Vanderbilt, Phys. Rev. B 56 (1997) 10544.
- [166] Q. Guo, I. Cocks, E.M. Williams, Phys. Rev. Lett. 77 (1996) 3851.
- [167] R.E. Tanner, M.R. Castell, G.A.D. Briggs, Surf. Sci. 437 (1999) 263.
- [168] C.L. Pang, S.A. Haycock, H. Raza, G. Thornton, O. Gürseren, R. James, D.W. Bullett, Surf. Sci. 437 (1999) 261.
- [169] H. Onishi, Y. Iwasawa, Phys. Rev. Lett. 76 (1996) 791.
- [170] M. Li, W. Hebenstreit, U. Diebold, Surf. Sci. 414 (1998) L951.
- [171] M. Li, W. Hebenstreit, U. Diebold, M.A. Henderson, D.R. Jennison, Faraday Discuss., Chem. Soc. 114 (1999) 245.
- [172] R.A. Bennett, P. Stone, M. Bowker, Faraday Discuss., Chem. Soc. 114 (1999) 267.
- [173] P. Stone, R.A. Bennett, M. Bowker, New J. Phys. 1 (1999) 8.
- [174] M.A. Henderson, Langmuir 12 (1996) 5093.
- [175] M.B. Hugenschmidt, L. Gamble, C.T. Campbell, Surf. Sci. 302 (1994) 329.
- [176] H. Raza, C.L. Pang, S.A. Haycock, G. Thornton, Phys. Rev. Lett. 82 (1999) 5265.
- [177] H. Raza, C.L. Pang, S.A. Haycock, G. Thornton, Appl. Surf. Sci. 140 (1999) 271.
- [178] J. Muscat, N.M. Harrison, G. Thornton, Phys. Rev. B 59 (1999) 2320.
- [179] P.J.D. Lindan, N.M. Harrison, J.M. Holender, M.J. Gillan, M.C. Payne, Surf. Sci. 364 (1996) 431.
- [180] P.J. Hardman, P.L. Wincott, Phys. Rev. B 60 (1999) 11700.
- [181] Y.W. Chung, W.J. Lo, G.A. Somorjai, Surf. Sci. 64 (1977) 588.
- [182] P.J. Hardman, N.S. Prakash, C.A. Muryn, G.N. Raikar, A.G. Thomas, R.J. Blake, Phys. Rev. B 47 (1993) 16056.
- [183] C.A. Muryn, G. Tirvengadum, J.J. Crouch, D.R. Warburton, G.N. Raikar, G. Thornton, D.S.-L. Law, J. Phys. C. 1 suppl. B (1991) 265.
- [184] M.C. Wu, P.J. Møller, Surf. Sci. 224 (1989) 250.
- [185] G.W. Clark, L.L. Kesmodel, Ultramicroscopy 41 (1992) 77.
- [186] P. Zschack, J.B. Cohen, Y.W. Chung, Surf. Sci. 262 (1992) 395.
- [187] P.W. Murray, F.M. Leibsle, H.J. Fisher, C.F.J. Flipse, C.A. Muryn, G. Thornton, Phys. Rev. Lett. 46 (1992) 12877.
- [188] P.W. Murray, F.M. Leibsle, C.A. Muryn, H.J. Fisher, C.F.J. Flipse, G. Thornton, Phys. Rev. Lett. 72 (1994) 689.
- [189] P.W. Murray, F.M. Leibsle, C.A. Muryn, C.F.J. Flipse, G. Thornton, Surf. Sci. 321 (1994) 217.
- [190] Y. Gao, Y. Liang, S.A. Chambers, Surf. Sci. 365 (1996) 638.
- [191] P.M. Oliver, S.C. Parker, J. Purton, D.W. Bullett, Surf. Sci., Part B 307–309 (1994) 1200.
- [192] H. Zajonz, H.L. Meyerheim, T. Gloege, W. Moritz, D. Wolf, Surf. Sci. 398 (1998) 369.
- [193] E. Landree, L.D. Marks, P. Zschack, C.J. Gilmore, Surf. Sci. 408 (1998) 300.
- [194] L.D. Marks, R. Plass, D.L. Dorset, Surf. Rev. Lett. 4 (1997) 1.
- [195] Q. Guo, I. Cocks, E.M. Williams, Surf. Sci. 366 (1996) 99.
- [196] M.A. Henderson, J. Phys. Chem. 99 (1995) 15253.
- [197] M.A. Henderson, Surf. Sci. 319 (1994) 315.

- [198] R.H. Tait, R.V. Kasowski, Phys. Rev. B 20 (1979) 5178.
- [199] L.E. Firment, Surf. Sci. 116 (1982) 205.
- [200] G.E. Poirier, B.K. Hance, M. White, J. Vac. Sci. Technol. B 10 (1992) 6.
- [201] B.A. Watson, M.A. Barteau, Chem. Mater. 6 (1994) 771.
- [202] K.-i. Fukui, R. Tero, Y. Iwasawa, Jpn. J. Appl. Phys., Part 1 40 (2001) 4331.
- [203] H. Nörenberg, F. Dinelli, G.A.D. Briggs, Surf. Sci. 446 (2000) L83.
- [204] H. Nörenberg, F. Dinelli, G.A.D. Briggs, Surf. Sci. 436 (1999) L635.
- [205] H. Onishi, T. Aruga, C. Egawa, Y. Iwasawa, Surf. Sci. 199 (1988) 54.
- [206] A. Howard, C.E.J. Mitchell, D. Morris, R.G. Egdell, S.C. Parker, Surf. Sci. 448 (2000) 131.
- [207] H. Uetsuka, A. Sasahara, H. Onishi, Jpn. J. Appl. Phys., Part 1 39 (2000) 3769.
- [208] T. Ohno, K. Sarukawa, M. Matsumura, J. Phys. Chem. B 105 (2001) 2417.
- [209] L. Kavan, M. Grätzel, S.E. Gilbert, C. Klemenz, H.J. Scheel, J. Am. Chem. Soc. 118 (1996) 6716.
- [210] J.M.G. Amores, V.S. Escrivano, G. Busca, J. Mater. Chem. 5 (1995) 1245.
- [211] C. Byun, J.W. Jang, I.T. Kim, K.S. Hong, B.-W. Lee, Mater. Res. Bull. 32 (1997) 431.
- [212] P. Arnal, R.J.P. Corriu, D. Leclercq, P.H. Mutin, A. Vioux, J. Mater. Chem. 6 (1996) 1925.
- [213] T. Oyama, Y. Iimura, K. Takeuchi, T. Ishii, J. Mater. Sci. Lett. 15 (1996) 594.
- [214] A. Fahmi, C. Minot, Surf. Sci. 304 (1994) 343.
- [215] T. Bredow, K. Jug, Surf. Sci. 327 (1995) 398.
- [216] M. Lazzeri, A. Vittadini, A. Selloni, Phys. Rev. B 63 (2001) 155409/1.
- [217] M. Lazzeri, A. Vittadini, A. Selloni, Phys. Rev. B 65 (2002) 119901/1.
- [218] G.S. Herman, Y. Gao, T.T. Tran, J. Osterwalder, Surf. Sci. 447 (1999) 201.
- [219] G.S. Herman, M.R. Sievers, Y. Gao, Phys. Rev. Lett. 84 (2000) 3354.
- [220] W. Hebenstreit, N. Ruzycki, G.S. Herman, Y. Gao, U. Diebold, Phys. Rev. B 64 (2000) R16344.
- [221] G.S. Herman, Y. Gao, Thin Solid Films 397 (2001) 157.
- [222] R. Hengerer, B. Bolliger, M. Erbudak, M. Grätzel, Surf. Sci. 460 (2000) 162.
- [223] J. Woning, R.A. van Santen, Chem. Phys. Lett. 101 (1983) 541.
- [224] S. Chen, M.G. Mason, H.J. Gysling, G.R. Paz-Pajult, T.N. Blanton, K.M. Chen, C.P. Fictorie, W.L. Gladfelter, A. Franciosi, P.I. Cohen, J.F. Evans, J. Vac. Sci. Technol. A 11 (1993) 2419.
- [225] D.S. Lind, S.D. Berry, G. Chern, H. Mathias, L.R. Testardi, Phys. Rev. B 45 (1992) 1838.
- [226] W. Sugimura, A. Yamazaki, H. Shigetani, J. Tanaka, T. Mitsuhashi, Jpn. J. Appl. Phys. 36 (1997) 7358.
- [227] R. Hengerer, L. Kavan, M. Grätzel, J. Electrochem. Soc. 147 (2000) 1467.
- [228] Y. Liang, S. Gan, S.A. Chambers, E.I. Altman, Phys. Rev. B 63 (2001) 235402/1.
- [229] R.E. Tanner, A. Sasahara, Y. Liang, E.I. Altman, H. Onishi, J. Phys. Chem. B 106 (2002) 8211.
- [230] M. Lazzeri, A. Selloni, Phys. Rev. Lett. 87 (2001) 266105/1.
- [231] N. Ruzycki, G. Herman, L.A. Boatner, U. Diebold, Surf. Sci., submitted.
- [232] P.A. Cox, Transition Metal Oxides—An Introduction to Their Electronic Structure, Properties, Clarendon Press, Oxford, 1992.
- [233] P.J.D. Lindan, N.M. Harrison, M.J. Gillan, J.A. White, Phys. Rev. B 55 (1997) 15919.
- [234] D. Vogtenhuber, R. Podloucky, J. Redinger, E.L. Bullock, L. Patthey, S.G. Steinemann, Proc. Electrochem. Soc. 15 (1994) 96.
- [235] J. Goniakowski, C. Noguera, Surf. Sci. 319 (1994) 68.
- [236] J. Purton, D.W. Bullett, P.M. Oliver, S.C. Parker, Surf. Sci. 336 (1995) 166.
- [237] N. Yu, J.W. Halley, Phys. Rev. B 51 (1995) 4768.
- [238] J. Goniakowski, C. Noguera, Surf. Sci. 323 (1995) 129.
- [239] K.D. Schierbaum, W.X. Xu, Int. J. Quantum Chem. 57 (1996) 1121.
- [240] S. Kimura, M. Tsukada, Appl. Surf. Sci. 132 (1998) 587.
- [241] K.F. Ferris, L.Q. Wang, J. Vac. Sci. Technol. A 16 (1998) 956.
- [242] M. Casarin, C. Maccato, A. Vittadini, J. Phys. Chem. B 102 (1998) 10745.
- [243] P.K. Schelling, N. Yu, J.W. Halley, Phys. Rev. B 58 (1998) 1279.
- [244] F. Rittner, R. Fink, B. Boddenberg, V. Staemmler, Phys. Rev. B 57 (1998) 4160.
- [245] A.T. Paxton, L. Thiên-Nga, Phys. Rev. B 57 (1998) 1579.
- [246] S. Matsushima, K. Kobayashi, M. Kohyama, Kitakyushu Kogyo Koto Senmon Gakko Kenkyu Hokoku 32 (1999) 155.

- [247] T. Albaret, F. Finocchi, C. Noguera, Faraday Discuss., Chem. Soc. 114 (1999) 285.
- [248] M. Ramamoorthy, R.D. King-Smith, D. Vanderbilt, Phys. Rev. B 49 (1994) 7709.
- [249] S.P. Bates, G. Kresse, M.J. Gillan, Surf. Sci. 385 (1997) 386.
- [250] P.J.D. Lindan, N.M. Harrison, Surf. Sci. 479 (2001) L375.
- [251] M. Tsukada, C. Satoko, H. Adachi, J. Phys. Soc. Jpn. 44 (1978) 1043.
- [252] R.V. Kasowski, R.H. Tait, Phys. Rev. B 20 (1979) 5168.
- [253] M. Tsukada, C. Satoko, H. Adachi, J. Phys. Soc. Jpn. 47 (1979) 1610.
- [254] S. Munnix, M. Schmeits, Surf. Sci. 126 (1983) 20.
- [255] S. Munnix, M. Schmeits, Phys. Rev. B 28 (1983) 7342.
- [256] S. Munnix, M. Schmeits, Phys. Rev. B 30 (1984) 2202.
- [257] S. Munnix, M. Schmeits, Phys. Rev. B 31 (1985) 3369.
- [258] K.M. Glassford, N. Troullier, J.L. Martins, J.R. Chelikowsky, Sol. State Commun. 76 (1990) 635.
- [259] R. Heise, R. Courths, S. Witzel, Solid State Commun. 84 (1992) 599.
- [260] R. Heise, R. Courths, Springer Ser. Surf. Sci. 33 (1993) 91.
- [261] Z. Zhang, S.P. Jeng, V.E. Henrich, Phys. Rev. B 43 (1991) 12004.
- [262] U. Diebold, H.S. Tao, N.D. Shinn, T.E. Madey, Phys. Rev. B 50 (1994) 14474.
- [263] R. Heise, R. Courths, Surf. Sci. 288 (1993) 658.
- [264] A.E. Taverner, P.C. Hollamby, P.S. Aldridge, R.G. Egdell, W.C. Mackrodt, Surf. Sci. 288 (1993) 653.
- [265] A.K. See, R.A. Bartynski, J. Vac. Sci. Technol. A 10 (1992) 2591.
- [266] A.K. See, M. Thayer, R.A. Bartynski, Phys. Rev. B 47 (1993) 13722.
- [267] L. Soriano, M. Abbate, J. Vogel, J.C. Fuggle, A. Fernandez, A.R. Gonzalez-Elipe, M. Sacchi, J.M. Sanz, Surf. Sci. 290 (1993) 427.
- [268] R. Brydson, B.G. Williams, W. Engel, H. Sauer, E. Zeitler, J.M. Thomas, Solid State Commun. 64 (1987) 609.
- [269] F.M.F. de Groot, J. Electr. Spectrosc. Rel. Phen. 67 (1993) 529.
- [270] F.M.F. de Groot, J. Electr. Spectrosc. Rel. Phen. 62 (1993) 111.
- [271] U. Diebold, N.D. Shinn, Surf. Sci. 343 (1995) 53.
- [272] J. Biener, M. Bäumer, R.J. Madix, Surf. Sci. 432 (1999) 178.
- [273] P.J. Hardman, G.N. Raikar, C.A. Muryn, G. van der Laan, P.L. Wincott, G. Thornton, D.W. Bullett, P.A.D.M.A. Dale, Phys. Rev. B 49 (1994) 7170.
- [274] Y. Aiura, Y. Nishihara, Y. Haruyama, T. Komeda, S. Kodaira, Y. Sakisaka, T. Maruyama, H. Kato, Physica B 196 (1994) 1215.
- [275] M.A. Henderson, W.S. Epling, C.L. Perkins, C.H.F. Peden, U. Diebold, J. Phys. Chem. B 103 (1999) 5328.
- [276] W. Göpel, J.A. Anderson, D. Frankel, M. Jaehnig, K. Phillips, J.A. Schäfer, G. Rocker, Surf. Sci. 139 (1984) 333.
- [277] M.A. Henderson, Surf. Sci. 400 (1998) 203.
- [278] J. Muscat, N.M. Harrison, G. Thornton, Phys. Rev. B 59 (1999) 15457.
- [279] U. Diebold, T.E. Madey, Surf. Sci. Spectra 4 (1998) 227.
- [280] J.T. Mayer, U. Diebold, T.E. Madey, E. Garfunkel, J. Electr. Spectrosc. Rel. Phen. 73 (1995) 1.
- [281] L.S. Dake, R.J. Lad, Surf. Sci. Spectra 4 (1998) 232.
- [282] A.E. Bocquet, T. Mizokawa, K. Morikawa, A. Fujimori, S.R. Barman, K. Maiti, D.D. Sarma, Y. Tokura, M. Onoda, Phys. Rev. B 53 (1996) 1161.
- [283] G. Rocker, J.A. Schäfer, W. Göpel, Phys. Rev. B 30 (1984) 3704.
- [284] L.L. Kesmodel, J.A. Gates, Y.W. Chung, Phys. Rev. B 23 (1981) 489.
- [285] P.A. Cox, R.G. Egdell, S. Eriksen, W.R. Flavell, J. Electr. Spectrosc. Rel. Phen. 39 (1986) 117.
- [286] S. Eriksen, R.G. Egdell, Surf. Sci. 180 (1987) 263.
- [287] M.-C. Wu, C.A. Estrada, D.W. Goodman, Phys. Rev. Lett. 67 (1991) 2910.
- [288] P.A. Cox, A.A. Williams, Surf. Sci. 152–153 (1985) 791.
- [289] S.A. Chambers, Surf. Sci. Rep. 39 (2000) 105.
- [290] L. Thiêñ-Nga, A.T. Paxton, Phys. Rev. B 58 (1998) 13233.
- [291] S.H. Overbury, P.A. Bertrand, G.A. Somorjai, Chem. Rev. 75 (1975) 547.
- [292] J.M. Pan, T.E. Madey, J. Vac. Sci. Technol. A 11 (1993) 1667.
- [293] C.R. Henry, Surf. Sci. Rep. 31 (1998) 231.
- [294] F. Cosandey, T.E. Madey, Surf. Rev. Lett. 8 (2001) 73.
- [295] D.A. Chen, M.C. Bartelt, K.F. McCarty, Surf. Sci. 450 (2000) 78.

- [296] O. Dulub, L.A. Boatner, U. Diebold, *Surf. Sci.* 504 (2002) 271.
- [297] M.J.J. Jak, C. Konstapel, A. van Kreuningen, J. Chrost, J. Verhoeven, J.W.M. Frenken, *Surf. Sci.* 474 (2001) 28.
- [298] S.J. Tauster, Strong-metal support interactions. Facts and uncertainties, in: Proceedings of the Strong Metal-Support Interactions, Symposium at the 189th Meeting of the American Chemical Society, Miami Beach, FL, 1986.
- [299] A.K. Datye, D.S. Kalakkad, M.H. Yao, *J. Catal.* 155 (1995) 148.
- [300] M.-H. Yao, HREM study of strong metal–support interaction in Pt/TiO₂, in: Proceedings of the 51st Annual Meeting of the Microscopy Society of America, 1993, San Francisco.
- [301] P.L.J. Gunter, J.W. Niemandsverdriet, G.A. Somorjai, *Catal. Rev., Sci. Eng.* 39 (1997) 77.
- [302] D.R. Jennison, O. Dulub, W. Hebenstreit, U. Diebold, *Surf. Sci.* 492 (2001) L677.
- [303] M. Bowker, *J. Phys. Chem.* 106 (2002) 4688.
- [304] H. Onishi, T. Aruga, C. Egawa, Y. Iwasawa, *Shokubai* 29 (1987) 518.
- [305] H. Onishi, T. Aruga, C. Egawa, Y. Iwasawa, *J. Chem. Soc., Faraday Trans.* 85 (1989) 2597.
- [306] F. Cosandey, R. Persaud, L. Zhang, T.E. Madey, *Mater. Res. Soc. Symp. Proc.* 440 (1997) 383.
- [307] A. Kolmakov, D.W. Goodman, *Catal. Lett.* 70 (2000) 93.
- [308] X. Lai, T.P.S. Clair, D.W. Goodman, *Faraday Discuss.*, *Chem. Soc.* 114 (1999) 279.
- [309] A. Kolmakov, D.W. Goodman, *Surf. Sci.* 490 (2001) L597.
- [310] A. Kolmakov, D.W. Goodman, *Catal. Lett.* 70 (2000) 93.
- [311] M. Grätzel, *MRS Bull.* (October 1993) 61.
- [312] M.K. Jain, M.C. Bhatnagar, G.L. Sharma, *Sens. Actuators* 55 (1999) 180.
- [313] A.M. Efstathiou, D. Boudovas, N. Vamvouka, X.E. Verykios, *J. Catal.* 140 (1993) 1.
- [314] V.N. Ageev, S.M. Solov'ev, *Phys. Solid State* 42 (2000) 2159.
- [315] V.N. Ageev, S.M. Solov'ev, *Surf. Sci.* 480 (2001) 1.
- [316] A. Stashans, S. Lunell, R. Bergstroem, A. Hagfeldt, S.E. Lindquist, *Phys. Rev. B* 53 (1996) 159.
- [317] R. van de Krol, A. Goossens, E.A. Meulenkamp, *J. Electrochem. Soc.* 146 (1999) 3150.
- [318] R. van de Krol, A. Goossens, J. Schoonman, *J. Phys. Chem.* 103 (1999) 7151.
- [319] M.A. San Miguel, C.J. Calzado, J.F. Sanz, *J. Phys. Chem. B* 105 (2001) 1794.
- [320] Y. Iwasawa, *Acid Base Catal.*, *Proc. Int. Symp.* (1989) 267.
- [321] R. Souda, W. Hayami, T. Aizawa, Y. Ishizawa, *Phys. Rev. B* 48 (1993) 17255.
- [322] R. Souda, W. Hayami, T. Aizawa, Y. Ishizawa, *Surf. Sci.* 285 (1993) 265.
- [323] H. Onishi, Y. Iwasawa, *Catal. Lett.* 38 (1996) 89.
- [324] J. Nerlov, Q. Ge, P.J. Møller, *Surf. Sci.* 348 (1996) 28.
- [325] P.J. Møller, *NATO ASI Ser., Ser. E* 331 (1997) 267.
- [326] J. Nerlov, S.V. Christensen, S. Weichel, E.H. Pedersen, P.J. Møller, *Surf. Sci.* 371 (1997) 321.
- [327] B. Hird, R.A. Armstrong, *Surf. Sci.* 431 (1999) L570.
- [328] A. Gutierrez-Sosa, J.F. Walsh, R. Lindsay, P.L. Wincott, G. Thornton, *Surf. Sci.* 435 (1999) 538.
- [329] M.A. San Miguel, C.J. Calzado, J.F. Sanz, *Surf. Sci.* 409 (1998) 92.
- [330] M.A. San Miguel, C.J. Calzado, J.F. Sanz, *Int. J. Quantum Chem.* 70 (1998) 351.
- [331] J.F. Sanz, C.M. Zicovich-Wilson, *Chem. Phys. Lett.* 303 (1999) 111.
- [332] T. Albaret, F. Finocchi, C. Noguera, A. De Vita, *Phys. Rev. B* 65 (2002) 035402/1.
- [333] R. Heise, R. Courths, *Surf. Rev. Lett.* 2 (1995) 147.
- [334] R. Heise, R. Courths, *Surf. Sci.* 333 (1995) 1460.
- [335] R.J. Lad, L.S. Dake, *Mater. Res. Soc. Symp. Proc.* 238 (1992) 823.
- [336] T. Bredow, *Int. J. Quantum Chem.* 75 (1999) 127.
- [337] D. Purdie, B. Reihl, G. Thornton, *J. de phys. IV* 4 (1994) 163.
- [338] G. Thornton, *Vacuum* 43 (1992) 1133.
- [339] K. Prabhakaran, D. Purdie, R. Casanova, C.A. Muryn, P.J. Hardman, P.L. Wincott, G. Thornton, *Phys. Rev. B* 45 (1992) 6969.
- [340] B.E. Hayden, G.P. Nicholson, *Surf. Sci.* 274 (1992) 277.
- [341] A.G. Thomas, P.J. Hardman, C.A. Muryn, H.S. Dhariwal, A.F. Prim, G. Thornton, E. Román, J. de Segovia, *J. Chem. Soc., Faraday Trans.* 91 (1995) 3569.
- [342] M. Brause, V. Kempfer, *Surf. Sci.* 476 (2001) 78.
- [343] A.W. Grant, C.T. Campbell, *Phys. Rev. B* 55 (1997) 1844.

- [344] M. Brause, S. Skordas, V. Kempfer, *Surf. Sci.* 445 (2000) 224.
- [345] L.S. Dake, R.J. Lad, *Surf. Sci.* 289 (1993) 297.
- [346] X. Lai, T.P.S. Clair, M. Valden, D.W. Goodman, *Prog. Surf. Sci.* 59 (1998) 25.
- [347] X. Lai, C. Xu, D.W. Goodman, *J. Vac. Sci. Technol. A* 16 (1998) 2562.
- [348] D.L. Carroll, Y. Liang, D.A. Bonnell, *J. Vac. Sci. Technol. A* 12 (1994) 2298.
- [349] L.S. Dake, R.J. Lad, *J. Vac. Sci. Technol. A* 13 (1995) 122.
- [350] G. Rocker, W. Göpel, *Surf. Sci.* 181 (1987) 530.
- [351] U. Diebold, T.E. Madey, Unpublished results.
- [352] N.J. Price, J.B. Reitz, R.J. Madix, E.I. Solomon, *J. Electr. Spectrosc. Rel. Phen.* 99 (1999) 257.
- [353] M. Sambi, E. Pin, G. Saniovanni, L. Zaratin, G. Granozzi, F. Parmigiani, *Surf. Sci.* 349 (1996) L169.
- [354] J. Biener, M. Bäumer, R. Madix, *Surf. Sci.* 450 (2000) 12.
- [355] J.M. Pan, B.L. Maschhoff, U. Diebold, T.E. Madey, in: *Proceedings of the Fourth International Conference on Struct. Surf. IV*, 1994, p. 613.
- [356] R.J. Madix, J. Biener, M. Bäumer, A. Dinger, *Faraday Discuss.*, *Chem. Soc.* 114 (1999) 67.
- [357] J. Wang, J. Biener, R.J. Madix, *J. Phys. Chem.* 104 (2000) 3286.
- [358] M. Sambi, M.D. Negra, G. Granozzi, Z.S. Li, J.H. Jorgensen, P.J. Møller, *Appl. Surf. Sci.* 142 (1999) 146.
- [359] M.D. Negra, M. Sambi, G. Granozzi, *Surf. Sci.* 436 (1999) 227.
- [360] M.D. Negra, M. Sambi, G. Granozzi, *Surf. Sci.* 461 (2000) 118.
- [361] G.S. Wong, D.D. Kragten, J.M. Vohs, *Surf. Sci.* 452 (2000) L293.
- [362] G.S. Wong, D.D. Kragten, J.M. Vohs, *J. Phys. Chem. B* 105 (2001) 1366.
- [363] J. Marien, T. Wagner, M. Rühle, *Mater. Res. Soc. Symp. Proc.* 441 (1997) 27.
- [364] J. Marien, T. Wagner, M. Rühle, *Materialwiss. Grundlagen Symp.* 7 (1997) 859.
- [365] J. Marien, T. Wagner, C. Duscher, A. Koch, M. Rühle, *Surf. Sci.* 446 (2000).
- [366] Y. Gao, S.A. Chambers, *J. Mater. Res.* 11 (1996) 1025.
- [367] Y. Gao, S.A. Chambers, *Mater. Lett.* 26 (1996) 217.
- [368] Y. Gao, Y. Liang, S.A. Chambers, *Surf. Sci.* 348 (1996) 17.
- [369] S.A. Chambers, Y. Gao, Y.J. Kim, M.A. Henderson, S. Thevuthasan, S. Wen, K.L. Merkle, *Surf. Sci.* 365 (1996) 625.
- [370] S.A. Chambers, Y. Gao, R.J. Smith, *J. Vac. Sci. Technol. A* 14 (1996).
- [371] Y. Gao, Y. Liang, S.A. Chambers, *Surf. Sci.* 365 (1996) 638.
- [372] S. Thevuthasan, N.R. Shivaparan, S.A. Chambers, *Appl. Surf. Sci.* 115 (1997) 381.
- [373] S.A. Chambers, Y. Gao, S. Thevuthasan, S. Wen, K.L. Merkle, N. Shivaparan, R.J. Smith, *Mater. Res. Soc. Symp. Proc.* 436 (1997) 475.
- [374] S.A. Chambers, Y. Gao, Y.J. Kim, *Surf. Sci. Spectra* 5 (1998) 211.
- [375] M. Casarin, C. Maccato, A. Vittadini, *Phys. Chem. Chem. Phys.* 1 (1999) 3793.
- [376] D. Morris, Y. Dou, J. Rebane, C.E.J. Mitchell, R.G. Egdell, D.S.L. Law, A. Vittadini, M. Casarin, *Phys. Rev. B* 61 (2000) 13445.
- [377] U. Diebold, J.M. Pan, T.E. Madey, *Surf. Sci.* 288 (1993) 896.
- [378] J.M. Pan, U. Diebold, L. Zhang, T.E. Madey, *Surf. Sci.* 295 (1993) 411.
- [379] J.M. Pan, B.L. Maschhoff, U. Diebold, T.E. Madey, *Surf. Sci.* 291 (1993) 381.
- [380] T.E. Madey, U. Diebold, J.M. Pan, *Springer Ser. Surf. Sci.* 33 (1993) 147.
- [381] H.A. Bullen, S.J. Garrett, *Chem. Mater.* 14 (2002) 243.
- [382] S. Petigny, B. Domenichini, H. Mostefa-Sba, E. Lesniewska, A. Steinbrunn, S. Bourgeois, *Appl. Surf. Sci.* 142 (1999) 114.
- [383] K. Asakura, W.J. Chun, Y. Iwasawa, *Jpn. J. Appl. Phys.* 1 (1999) 40.
- [384] K. Asakura, W.J. Chun, Y. Iwasawa, *Shinku* 42 (1999) 450.
- [385] W.J. Chun, K. Asakura, Y. Iwasawa, *Appl. Surf. Sci.* 100 (1996) 143.
- [386] W.J. Chun, K. Asakura, Y. Iwasawa, *J. Phys. IV* 2 (1997) 921.
- [387] W.J. Chun, K. Asakura, Y. Iwasawa, *Chem. Phys. Lett.* 288 (1998) 868.
- [388] W.J. Chun, K. Asakura, Y. Iwasawa, *J. Phys. Chem. B* 102 (1998) 9006.
- [389] W.J. Chun, K. Asakura, Y. Iwasawa, *Catal. Today* 44 (1998) 309.
- [390] Y. Yamaguchi, W.J. Chun, S. Suzuki, H. Onishi, K. Asakura, Y. Iwasawa, *Res. Chem. Intermed.* 24 (1998) 151.
- [391] J. Haber, P. Nowak, J. Stoch, *Bull. Pol. Acad. Sci., Chem.* 45 (1997) 139.
- [392] V. Blondeau-Patissier, B. Domenichini, A. Steinbrunn, S. Bourgeois, *Appl. Surf. Sci.* 175–176 (2001) 674.

- [393] S.A. Chambers, Y. Liang, *Surf. Sci.* 420 (1999) 123.
- [394] D. Brugniau, S.D. Parker, G.E. Rhead, *Thin Solid Films* 121 (1984) 247.
- [395] J. Deng, D. Wang, X. Wei, R. Zhai, H. Wang, *Surf. Sci.* 249 (1991) 213.
- [396] A.K. See, R.A. Bartynski, *Phys. Rev. B* 50 (1994) 12064.
- [397] H. Mostefa-Sba, B. Domenichini, S. Bourgeois, *Surf. Sci.* 437 (1999) 107.
- [398] R.J. Lad, V.E. Henrich, *J. Vac. Sci. Technol. A* 7 (1989) 1893.
- [399] R.J. Lad, V.E. Henrich, *Phys. Rev. B* 39 (1989) 13478.
- [400] G.A. Rizzi, A. Magrin, G. Granozzi, *Surf. Sci.* 443 (1999) 277.
- [401] G.A. Rizzi, A. Magrin, G. Granozzi, *Phys. Chem. Chem. Phys.* 1 (1999) 709.
- [402] G.A. Rizzi, M. Sambi, A. Magrin, G. Granozzi, *Surf. Sci.* 454–456 (2000) 30.
- [403] L. Atanasoska, R.T. Antanasoski, F.H. Pollak, W.E. O’Grady, *Surf. Sci.* 230 (1990) 95.
- [404] K. RavindranathanThampi, L. Lucarelli, J. Kiwi, *Langmuir* 7 (1991).
- [405] Y. Shao, W. Chen, E. Wold, J. Paul, *Langmuir* 10 (1994) 178.
- [406] S.N. Towle, G.E. Brown Jr., G.A. Parks, *J. Colloid Interf. Sci.* 217 (1999) 299.
- [407] A. Berkó, G. Menesi, F. Solymosi, *Surf. Sci.* 372 (1997) 202.
- [408] A. Berkó, I. Ulrych, K.C. Prince, *J. Phys. Chem. B* 102 (1998) 3379.
- [409] A. Berkó, F. Solymosi, *Surf. Sci.* 400 (1998) 281.
- [410] C. Linsmeier, Surface-analytical Investigations of Supported Rhodium Model Catalysts, Ludwig-Maximilians Universität, 1994.
- [411] J. Evans, B.E. Hayden, J.F.W. Mosselmans, A.J. Murray, *NATO ASI Ser., Ser. C* 398 (1993) 179.
- [412] B.E. Hayden, A. King, M.A. Newton, *Surf. Sci.* 397 (1998) 306.
- [413] G.E. Poirier, B.K. Hance, J.M. White, *J. Phys. Chem.* 97 (1993) 5965.
- [414] A. Berkó, G. Klivenyi, F. Solymosi, *J. Catal.* 182 (1999) 511.
- [415] A. Berkó, F. Solymosi, *Surf. Sci.* 411 (1998) L900.
- [416] C.C. Kao, S.C. Tsai, M.K. Bahl, Y.W. Chung, W.J. Lo, *Surf. Sci.* 95 (1980) 1.
- [417] H. Onishi, T. Aruga, C. Egawa, Y. Iwasawa, *Surf. Sci.* 233 (1990) 261.
- [418] M.C. Wu, P.J. Møller, *Springer Ser. Surf. Sci.* 24 (1991) 652.
- [419] M.C. Wu, P.J. Møller, *Surf. Sci.* 250 (1991) 179.
- [420] M.C. Wu, P.J. Møller, *Surf. Sci.* 279 (1992) 23.
- [421] S. Bourgeois, P.L. Seigneur, M. Perdereau, D. Chandesris, P.L. Fevre, H. Magnan, *Thin Solid Films* 304 (1997) 267.
- [422] R.E. Tanner, I. Goldfarb, M.R. Castell, G.A.D. Briggs, *Surf. Sci.* 486 (2001) 167.
- [423] P.L. Cao, D.E. Ellis, V.P. Dravid, *J. Mater. Res.* 14 (1999) 3684.
- [424] S. Bourgeois, D. Diakite, F. Jomard, *Surf. Sci.* 217 (1989) 78.
- [425] S. Bourgeois, F. Jomard, M. Perdereau, *Surf. Sci.* 249 (1991) 194.
- [426] S. Bourgeois, D. Diakité, F. Jomard, M. Perdereau, R. Poirault, *Surf. Sci.* 217 (1989) 78.
- [427] P. Stone, R.A. Bennett, S. Poulston, M. Bowker, *Surf. Sci.* 435 (1999) 501.
- [428] P. Stone, *Chem. Commun.* 13 (1998) 1369.
- [429] M.J.J. Jak, C. Konstapel, A. van Kreuning, J. Verhoeven, J.W.M. Frenken, *Surf. Sci.* 457 (2000) 295.
- [430] T. Bredow, G. Pacchioni, *Surf. Sci.* 426 (1999) 106.
- [431] T. Suzuki, R. Souda, *Surf. Sci.* 448 (2000) 33.
- [432] Z. Chang, G. Thornton, *Surf. Sci.* 459 (2000) 303.
- [433] A.J. Ramirez-Cuesta, R.A. Bennett, P. Stone, P.C.H. Mitchell, M. Bowker, *J. Mol. Catal. A* 167 (2001) 171.
- [434] J. Evans, B.E. Hayden, G. Lu, *Surf. Sci.* 360 (1996) 61.
- [435] P.W. Murray, J. Shen, G. Thornton, *Surf. Sci.* 380 (1997).
- [436] S. Fischer, K.D. Schierbaum, W. Göpel, *Vacuum* 48 (1997) 601.
- [437] S. Gan, Y. Liang, D.R. Baer, M.R. Sievers, G.S. Herman, C.H.F. Peden, *J. Phys. Chem. B* 105 (2001) 2412.
- [438] S. Fischer, J.A. Martin-Gago, E. Román, K.D. Schierbaum, J.L. de Segovia, *J. Electr. Spectrosc. Rel. Phen.* 83 (1997) 217.
- [439] K.D. Schierbaum, X. Wei-Xing, S. Fischer, W. Göpel, *Springer Ser. Surf. Sci.* 33 (1993) 268.
- [440] K. Tamura, M. Kudo, M. Owari, Y. Nihei, *Chem. Lett.* 11 (1986) 1921.
- [441] R.T. Baker, E.B. Prestidge, R.L. Garten, *J. Catal.* 56 (1979) 390.
- [442] H.P. Steinrück, F. Pesty, L. Zhang, T.E. Madey, *Phys. Rev. B* 51 (1995) 2427.

- [443] W.-x. Xu, K.D. Schierbaum, W. Göpel, Chem. Res. Chin. Univ. 11 (1995) 219.
- [444] A. Linsebigler, C. Rusu, J.T. Yates Jr., J. Am. Chem. Soc. 118 (1996) 5284.
- [445] K.D. Schierbaum, S. Fischer, G. Thornton, Surf. Sci. 391 (1997) 196.
- [446] S. Gan, A. El-azab, Y. Liang, Surf. Sci. 479 (2001) L369.
- [447] U. Diebold, J.M. Pan, T.E. Madey, Phys. Rev. B 47 (1993) 3868.
- [448] D.L. Carroll, M. Wagner, M. Rühle, D.A. Bonnell, J. Mater. Res. 12 (1997) 975.
- [449] P.J. Møller, M.C. Wu, Surf. Sci. 224 (1989) 265.
- [450] P. Lu, F. Cosandey, Interf. Sci. 2 (1994) 169.
- [451] Z. Chang, S. Haq, G. Thornton, Surf. Sci. 467 (2000) L841.
- [452] P.L. Wincott, J.S.G. Irwin, G. Jones, P.J. Hardman, G. Thornton, S. Weichel, P.J. Møller, V.R. Dhanak, Surf. Sci. 379 (1997) 242.
- [453] K. Luo, T.P. St. Clair, X. Lai, D.W. Goodman, J. Phys. Chem. 104 (2000) 3050.
- [454] D. Martin, J. Jupille, Y. Borensztein, Surf. Sci. 404 (1998) 433.
- [455] D. Martin, F. Creuzet, J. Jupille, Y. Borensztein, P. Gadenne, Surf. Sci. 379 (1997) 958.
- [456] D.A. Chen, M.C. Bartelt, K.F. McCarty, Surf. Sci. 464 (2000) L708.
- [457] C. Su, J.C. Yeh, J.L. Lin, J.C. Lin, Appl. Surf. Sci. 169–170 (2001) 366.
- [458] M. Haruta, Catal. Today 36 (1997) 153.
- [459] M. Haruta, S. Tsubota, T. Kobayashi, H. Kageyama, M.J. Genet, B. Delmont, J. Catal. 144 (1993) 175.
- [460] G.C. Bond, D.T. Thompson, Catal. Rev.-Sci. Eng. 418 (1999) 319.
- [461] M. Valden, S. Pak, X. Lai, D.W. Goodman, Catal. Lett. 56 (1998) 7.
- [462] J.-D. Grunwaldt, A. Baiker, J. Phys. Chem. B 103 (1999) 1002.
- [463] A. Sanchez, S. Abbet, U. Heiz, W.-D. Schneider, H. Häkkinen, R. N. Barnett, U. Landmann, J. Phys. Chem. A 103 (1999).
- [464] F. Cosandey, L. Zhang, T.E. Madey, Surf. Sci. 474 (2001) 1.
- [465] L. Zhang, R. Persaud, T.E. Madey, Phys. Rev. B 56 (1997) 10549.
- [466] T. Akita, K. Tanaka, S. Tsubota, M. Haruta, J. Electr. Microsc. 49 (2000) 657.
- [467] X. Lai, T.P. St. Clair, D.W. Goodman, Prog. Surf. Sci. 59 (1998) 25.
- [468] M. Okumura, Y. Kitagawa, M. Haruta, K. Yamaguchi, Chem. Phys. Lett. 346 (2001) 163.
- [469] J.A. Rodriguez, G. Liu, T. Jirsak, J. Hrbek, Z. Chang, J. Dvorak, A. Maiti, J. Am. Chem. Soc. 124 (2002) 5242.
- [470] H. Kobayashi, K. Kishimoto, Y. Nakato, H. Tsubomura, Sens. Actuators B 13 (1993) 125.
- [471] P. Salvador, M.L. Garcia Gonzalez, F. Munoz, J. Phys. Chem. 96 (1992) 10349.
- [472] V.E. Henrich, R.L. Kurtz, Phys. Rev. B 23 (1981) 6280.
- [473] M.S. Lazarus, T.K. Sham, Chem. Phys. Lett. 92 (1982) 670.
- [474] Q. Zhong, J.M. Vohs, D.A. Bonnell, J. Am. Ceram. Soc. 76 (1993) 1137.
- [475] W.E. Wallace, Q. Zhong, J. Genzer, R.J. Composto, D.A. Bonnell, J. Mater. Res. 8 (1993) 1629.
- [476] T. Fujino, M. Katayama, K. Inudzuka, T. Okuno, K. Oura, T. Hirao, Appl. Phys. Lett. 79 (2001) 2716.
- [477] M.A. Henderson, Surf. Sci. Rep. 46 (2002) 1.
- [478] P.A. Thiel, T.E. Madey, Surf. Sci. Rep. 7 (1987) 211.
- [479] C.A. Muryn, G. Tirvengadum, J.J. Crouch, D.R. Warburton, G.N. Raiker, G. Thornton, D.S.L. Law, Phys. Rev. B 1 (1989) SB127.
- [480] G. Thornton, Springer Ser. Surf. Sci. 33 (1993) 115.
- [481] C.A. Muryn, P.J. Hardman, J.J. Crouch, G.N. Raiker, G. Thornton, D.S.L. Law, Surf. Sci. 251–252 (1991) 747.
- [482] S. Bourgeois, F. Jomard, M. Perdereau, Surf. Sci. 279 (1992) 349.
- [483] S. Bourgeois, L. Gitton, M. Perdereau, J. Chim. Phys. Phys.-Chim. Biol. 85 (1988) 413.
- [484] L.Q. Wang, P.X. Skiba, A.N. Shultz, D.R. Baer, M.H. Engelhard, Mater. Res. Soc. Symp. Proc. 432 (1997) 45.
- [485] R. Wang, N. Sakai, A. Fujishima, T. Watanabe, K. Hashimoto, J. Phys. Chem. B 103 (1999) 2188.
- [486] R.F. Nalewajski, A.M. Koester, T. Bredow, K. Jug, J. Mol. Catal. 82 (1993) 407.
- [487] D. Brinkley, M. Dietrich, T. Engel, P. Farrall, G. Gantner, A. Schafer, A. Szuchmacher, Surf. Sci. 395 (1998) 292.
- [488] I.M. Brookes, C.A. Muryn, G. Thornton, Phys. Rev. Lett. 87 (2001) 266103/1.
- [489] R.L. Kurtz, R. Stockbauer, T.E. Madey, E. Román, J.L. de Segovia, Surf. Sci. 218 (1989) 178.
- [490] G. Lu, A. Linsebigler, J.T. Yates Jr., J. Phys. Chem. 98 (1994) 11733.
- [491] S. Suzuki, K.-i. Fukui, H. Onishi, T. Sasaki, Y. Iwasawa, Stud. Surf. Sci. Catal. 132 (2001) 753.
- [492] P.J.D. Lindan, N.M. Harrison, J.M. Holender, M.J. Gillan, Chem. Phys. Lett. 261 (1996) 246.

- [493] P.J.D. Lindan, N.M. Harrison, M.J. Gillan, Phys. Rev. Lett. 80 (1998) 762.
- [494] E.V. Stefanovich, T.N. Truong, Chem. Phys. Lett. 299 (1999) 623.
- [495] G.S. Herman, Z. Dohnalek, N. Ruzycki, U. Diebold, J. Phys. Chem. B, submitted.
- [496] G. Lu, A. Linsebigler, J.T. Yates Jr., J. Chem. Phys. 102 (1995) 4657.
- [497] G. Lu, A. Linsebigler, J.T. Yates Jr., J. Chem. Phys. 102 (1995) 3005.
- [498] C.N. Rusu, J.T. Yates Jr., Langmuir 13 (1997) 4311.
- [499] W.S. Epling, C.H.F. Peden, M.A. Henderson, U. Diebold, Surf. Sci. 412 (1998) 333.
- [500] C.L. Perkins, M.A. Henderson, J. Phys. Chem. B 105 (2001) 3856.
- [501] A.N. Shultz, W.M. Hetherington, Iii, D.R. Baer, L.Q. Wang, M.H. Engelhard, Surf. Sci. 392 (1997) 1.
- [502] X.-G. Wang, W. Weiss, S. Shaikhutdinov, M. Ritter, M. Petersen, F. Wagner, R. Schlögl, M. Scheffler, Phys. Rev. Lett. 81 (1998) 1038.
- [503] X.-G. Wang, A.M. Chaka, M. Scheffler, Phys. Rev. Lett. 84 (2000) 3659.
- [504] K. Reuter, M. Scheffler, Phys. Rev. B 65 (2001) 035406.
- [505] A. Boffa, C. Lin, A.T. Bell, G.A. Somorjai, J. Catal. 149 (1994) 149.
- [506] M.C. Torquemada, J.L. de Segovia, Surf. Sci. 331–333 (1995) 219.
- [507] M.-C. Wu, P.J. Møller, Surf. Sci. 250 (1991) 179.
- [508] A. Berkó, G. Menesi, F. Solymosi, J. Phys. Chem. 100 (1996) 17732.
- [509] D.W. Goodman, T.P.S. Clair, X. Lai, M. Valden, Morphology and electronic structure of metal clusters supported on TiO₂(1 1 0), in: Book of Abstracts, Proceedings of the 217th ACS National Meeting, Anaheim, CA, March 1999.
- [510] A. Linsebigler, G. Lu, J.T. Yates Jr., J. Chem. Phys. 103 (1995) 9438.
- [511] G. Rocker, W. Göpel, Surf. Sci. 175 (1986) L675.
- [512] M.C. Torquemada, J.L. de Segovia, E. Román, Surf. Sci. 337 (1995) 31.
- [513] D.C. Sorescu, J.T. Yates Jr., J. Phys. Chem. B 102 (1998) 4556.
- [514] H. Kobayashi, M. Yamaguchi, Surf. Sci. 214 (1989) 466.
- [515] A. Fahmi, C. Minot, Organometall. Chem. 478 (1994) 67.
- [516] Z. Yang, R. Wu, Q. Zhang, D.W. Goodman, Phys. Rev. B 63 (2001) 045419/1.
- [517] G. Pacchioni, A.M. Ferrari, P.S. Bagus, Surf. Sci. 350 (1996) 159.
- [518] M. Casarin, C. Maccato, A. Vittadini, Appl. Surf. Sci. 142 (1999) 196.
- [519] M. Casarin, C. Maccato, A. Vittadini, J. Phys. Chem. B 103 (1999) 3510.
- [520] P. Reinhardt, M. Causa, C.M. Marian, B.A. Heß, Phys. Rev. B 54 (1996) 14812.
- [521] G.B. Raupp, J.A. Dumesic, J. Phys. Chem. 89 (1985) 5240.
- [522] A. Linsebigler, G. Lu, J.T. Yates Jr., J. Phys. Chem. 100 (1996) 6631.
- [523] K. Tanaka, J.M. White, J. Catal. 79 (1983) 81.
- [524] H. Yamashita, N. Kamada, H. He, K. Tanaka, S. Ehara, M. Anpo, Chem. Lett. 5 (1994) 855.
- [525] R.I. Bickley, R.K.M. Jayanty, J.A. Navio, C. Real, M. Macias, Surf. Sci. 251–252 (1991) 1052.
- [526] F. Rittner, B. Boddenberg, M.J. Bojan, W.A. Steele, Langmuir 15 (1999) 1456.
- [527] F. Rittner, B. Boddenberg, R.F. Fink, V. Staemmler, Langmuir 15 (1999) 1449.
- [528] S. Wang, B. Raman, D.H. Chen, K.Y. Li, J.A. Colapret, Chem. Oxid. 5 (1997) 289.
- [529] D.C. Sorescu, C.N. Rusu, J.T. Yates Jr., J. Phys. Chem. B 104 (2000) 4408.
- [530] C.N. Rusu, J.T. Yates Jr., J. Phys. Chem. B 105 (2001) 2596.
- [531] C.N. Rusu, J.T. Yates Jr., J. Phys. Chem. 104 (2000) 1729.
- [532] L.Q. Wang, A.N. Shultz, D.R. Baer, M.H. Engelhard, J. Vac. Sci. Technol. A 14 (1996) 1532.
- [533] J.A. Rodriguez, T. Jirsak, G. Liu, J. Hrbek, J. Dvorak, A. Maiti, J. Am. Chem. Soc. 123 (2001) 9597.
- [534] U. Diebold, T.E. Madey, J. Vac. Sci. Technol. A 10 (1992) 2327.
- [535] U. Diebold, T.E. Madey, Springer Ser. Surf. Sci. 31 (1993) 284.
- [536] E. Román, J.L. de Segovia, Surf. Sci. 251/252 (1991) 742.
- [537] E.L. Román, J.L. de Segovia, R.L. Kurtz, T.E. Madey, Surf. Sci. 273 (1992) 40.
- [538] A. Markovits, J. Ahdjoudj, C. Minot, Surf. Sci. 365 (1996) 649.
- [539] D. Paschek, A. Geiger, AIP Conf. Proc. 330 (1995) 349.
- [540] W.K. Siu, R.A. Bartynski, S.L. Hulbert, J. Chem. Phys. 113 (2000) 10697.
- [541] D.R. Warburton, D. Purdie, C.A. Muryn, K. Prabhakaran, P.L. Wincott, G. Thornton, Surf. Sci. 269/270 (1992) 305.

- [542] C.A. Muryn, D. Purdie, P. Hardman, A.L. Johnson, N.S. Prakash, G.N. Raiker, G. Thornton, D.S.L. Law, Faraday Discuss., Chem. Soc. 89 (1990) 77.
- [543] K.E. Smith, J.L. Mackay, V.E. Henrich, Phys. Rev. B 35 (1987) 5822.
- [544] K.E. Smith, V.E. Henrich, J. Vac. Sci. Technol. A 7 (1989) 1967.
- [545] H. Onishi, T. Aruga, C. Egawa, Y. Iwasawa, Surf. Sci. 193 (1988) 33.
- [546] C.L. Greenwood, E.M. Williams, G. Thornton, S.L. Bennett, E. Román, J.L. de Segovia, M.C. Torquemada, Surf. Sci. 288 (1993) 386.
- [547] M.C. Torquemada, J.L. de Segovia, E. Román, G. Thornton, E.M. Williams, S.L. Bennett, Springer Ser. Surf. Sci. 31 (1993) 289.
- [548] M.C. Torquemada, J.L. de Segovia, J. Vac. Sci. Technol. A 12 (1994) 2318.
- [549] J.L. de Segovia, M.C. Torquemada, E. Román, J. Phys.: Cond. Matt. 5 (1993) A 139.
- [550] H. Raza, S.P. Harte, A. Rodriguez, Surf. Sci. 366 (1996) 519.
- [551] M.A. Barteau, in: D.P. Woodruff (Ed.), *The Chemical Physics of Solid Surfaces*, vol. 9, Oxide Surfaces, Elsevier, Amsterdam, 2001.
- [552] K.E. Smith, V.E. Henrich, Surf. Sci. 217 (1989) 445.
- [553] A. Selloni, A. Vittadini, M. Grätzel, Surf. Sci. 402–404 (1998) 219.
- [554] W. Heegemann, K.H. Meister, E. Bechtold, K. Hayek, Surf. Sci. 49 (1975) 161.
- [555] E.L.D. Hebenstreit, W. Hebenstreit, U. Diebold, Surf. Sci. 470 (2001) 347.
- [556] E.L.D. Hebenstreit, W. Hebenstreit, H. Geisler, S.N. Thornburg, C.A. Ventrice Jr., D.A. Hite, P.T. Sprunger, U. Diebold, Phys. Rev. B 64 (2001) 115418/1.
- [557] J. Hrbek, J.A. Rodriguez, T. Jirsak, J. Dvorak, J. Electr. Spectrosc. Rel. Phen. 119 (2001) 201.
- [558] J. Hrbek, J.A. Rodriguez, J. Dvorak, T. Jirsak, Collect. Czech. Chem. Commun. 66 (2001) 1149.
- [559] E.L.D. Hebenstreit, W. Hebenstreit, H. Geisler, C.A. Ventrice Jr., P.T. Sprunger, U. Diebold, Surf. Sci. 486 (2001) L467.
- [560] U. Diebold. Understanding metal oxide surfaces at the atomic scale: STM investigations of bulk-defect dependent surface processes, in: X.P.C.B. Carter, K. Sickafus, H.L. Tuller, T. Wood (Eds.), *Material Research Society Symposium Proceedings*, vol. 654, Materials Research Society, 2001.
- [561] E.L.D. Hebenstreit, W. Hebenstreit, C.A. Ventrice Jr., H. Geisler, D.A. Hite, P.T. Sprunger, U. Diebold, Surf. Sci. 505 (2002) 336.
- [562] D. Vogtenhuber, R. Podloucky, J. Redinger, Surf. Sci. 454–456 (2000) 369.
- [563] H. Brune, J. Wintterlin, R.J. Behm, G. Ertl, Phys. Rev. Lett. 68 (1992) 624.
- [564] C. Engdahl, G. Wahnström, Surf. Sci. 312 (1994) 429.
- [565] B. Kasemo, E. Törnqvist, J.K. Nørskov, B.I. Lundqvist, Surf. Sci. 89 (1979) 554.
- [566] G. Wahnström, A.B. Lee, J. Strömquist, J. Chem. Phys. 105 (1996) 326.
- [567] J. Wintterlin, R. Schuster, G. Ertl, Phys. Rev. Lett. 77 (1996) 123.
- [568] J.A. Jensen, C. Yan, A.C. Kummel, Phys. Rev. Lett. 76 (1996) 1388.
- [569] Y.L. Li, D.P. Pullman, J.J. Yang, A.A. Tsekouras, D.B. Gosalvez, K.B. Laughlin, Z. Zhang, M.T. Schulberg, D.J. Gladstone, M. McGonigal, S.T. Ceyer, Phys. Rev. Lett. 74 (1995) 2603.
- [570] M. Alam, M.A. Henderson, P.D. Kaviratna, G.S. Herman, C.H.F. Peden, J. Phys. Chem. B 102 (1998) 111.
- [571] P. Dolle, K. Markert, W. Heichler, N.R. Armstrong, K. Wandelt, K.S. Kim, R.A. Fiato, J. Vac. Sci. Technol. A 4 (1986) 1465.
- [572] V.A. Bakaev, W.A. Steele, Langmuir 8 (1992) 1372.
- [573] F. Rittner, D. Paschek, B. Boddenberg, Langmuir 11 (1995) 3097.
- [574] W.A. Steele, Fortschr.Ber. VDI, Reihe 555 (1998) 47.
- [575] P. Jakob, M. Gsell, D. Menzel, J. Chem. Phys. 114 (2001) 10075.
- [576] M. Gsell, P. Jakob, D. Menzel, Science 280 (1998) 717.
- [577] H. Idriss, M.A. Barteau, Adv. Catal. 45 (2000) 261.
- [578] H. Idriss, M. Libby, M.A. Barteau, Catal. Lett. 15 (1992) 13.
- [579] M.A. Barteau, Stud. Surf. Sci., Catalysis A 130 (2000) 105.
- [580] M.A. Barteau, Chem. Rev. 96 (1996) 1413.
- [581] H. Onishi, T. Aruga, Y. Iwasawa, J. Catal. 146 (1994) 557.
- [582] M.A. Henderson, J. Phys. Chem. B 101 (1997) 221.
- [583] H. Idriss, V.S. Lusvardi, M.A. Barteau, Surf. Sci. 348 (1996) 39.

- [584] R.A. Bennett, P. Stone, R. Smith, M. Bowker, *Surf. Sci.* 454–456 (2000) 390.
- [585] S.A. Chambers, M.A. Henderson, Y.J. Kim, S. Thevuthasan, *Surf. Rev. Lett.* 5 (1998) 381.
- [586] S.A. Chambers, S. Thevuthasan, Y.J. Kim, G.S. Herman, Z. Wang, E. Tober, R. Ynzunza, J. Morais, C.H.F. Peden, K. Ferris, C.S. Fadley, *Chem. Phys. Lett.* 267 (1997) 51.
- [587] S. Thevuthasan, G.S. Herman, Y.J. Kim, S.A. Chambers, C.H.F. Peden, Z. Wang, R.X. Ynzunza, E.D. Tober, J. Morais, C.S. Fadley, *Surf. Sci.* 401 (1998) 261.
- [588] B.E. Hayden, A. King, M.A. Newton, *J. Phys. Chem. B* 103 (1999) 203.
- [589] A. Gutierrez-Sosa, P. Martinez-Escalano, H. Raza, R. Lindsay, P.L. Wincott, G. Thornton, *Surf. Sci.* 471 (2001) 163.
- [590] P. Käckell, K. Terakura, *Appl. Surf. Sci.* 166 (2000) 370.
- [591] P. Käckell, K. Terakura, *Surf. Sci.* 461 (2000) 191.
- [592] J. Ahdjoudj, C. Minot, *Catal. Lett.* 46 (1997) 83.
- [593] L.Q. Wang, K.F. Ferris, A.N. Schultz, D.R. Baer, M.H. Engelhard, *Surf. Sci.* 380 (1997) 352.
- [594] K.-i. Fukui, H. Onishi, Y. Iwasawa, *Chem. Phys. Lett.* 280 (1997) 296.
- [595] K.-i. Fukui, H. Onishi, Y. Iwasawa, *Appl. Surf. Sci.* 140 (1999) 259.
- [596] H. Onishi, Y. Iwasawa, *Jpn. J. Appl. Phys.* 33 (1994) L1338.
- [597] H. Onishi, K.-i. Fukui, Y. Iwasawa, *Colloids Surf. A* 109 (1996) 335.
- [598] H. Onishi, Y. Iwasawa, *Surf. Sci.* 358 (1996) 773.
- [599] H. Onishi, K.-i. Fukui, Y. Iwasawa, *Jpn. J. Appl. Phys.* 38 (1999) 3830.
- [600] A. Sasahara, H. Uetsuka, H. Onishi, *J. Phys. Chem. B* 105 (2001) 1.
- [601] Z. Chang, G. Thornton, *Surf. Sci.* 462 (2000) 68.
- [602] A. Atrei, U. Bardi, G. Rovida, *Surf. Sci.* 391 (1997) 216.
- [603] K.S. Kim, M.A. Barteau, *Langmuir* 6 (1990) 1485.
- [604] K.S. Kim, M.A. Barteau, *J. Catal.* 125 (1990) 353.
- [605] A. Vittadini, A. Selloni, M. Grätzel, *J. Phys. Chem.* 104 (2000) 1300.
- [606] H. Onishi, T. Aruga, Y. Iwasawa, *J. Am. Chem. Soc.* 115 (1993) 10460.
- [607] A. Ludviksson, R. Zhang, C.T. Campbell, K. Griffiths, *Surf. Sci.* 313 (1994) 64.
- [608] I.D. Cocks, Q. Guo, R. Patel, E.M. Williams, E. Román, J.L. de Segovia, *Surf. Sci.* 379 (1997) 135.
- [609] H. Onishi, Y. Yamaguchi, K.-i. Fukui, Y. Iwasawa, *J. Phys. Chem.* 100 (1996) 9582.
- [610] A. Sasahara, H. Uetsuka, H. Onishi, *Surf. Sci.* 481 (2001) L437.
- [611] K.-i. Fukui, Y. Iwasawa, *Surf. Sci.* 464 (2000) L719.
- [612] D.J. Titheridge, M.A. Barteau, H. Idriss, *Langmuir* 17 (2001) 2120.
- [613] Q. Guo, I. Cocks, E.M. Williams, *Surf. Sci.* 393 (1997) 1.
- [614] Q. Guo, E.M. Williams, *Surf. Sci.* 435 (1999) 322.
- [615] L. Patthey, H. Rensmo, P. Persson, K. Westermark, L. Vayssieres, A. Stashans, A. Petersson, P.A. Brühwiler, H. Siegbahn, S. Lunell, N. Mårtensson, *J. Chem. Phys.* 110 (1999) 5913.
- [616] P. Persson, S. Lunell, P.A. Bruhwiler, J. Schnadt, S. Sodergren, J.N. O'Shea, O. Karis, H. Siegbahn, N. Mårtensson, M. Bassler, L. Patthey, *J. Chem. Phys.* 112 (2000) 3945.
- [617] A. Fahmi, C. Minot, P. Fourre, P. Nortier, *Surf. Sci.* 343 (1995) 261.
- [618] E. Soria, E. Román, E.M. Williams, J.L. de Segovia, *Surf. Sci.* 435 (1999) 543.
- [619] E. Soria, I. Colera, J.L. de Segovia, *Surf. Sci.* 451 (2000) 188.
- [620] J.N. Wilson, D.J. Titheridge, L. Kieu, H. Idriss, *J. Vac. Sci. Technol. A* 18 (2000) 1887.
- [621] M.A. Henderson, S. Otero-Tapia, M.E. Castro, *Faraday Discuss.*, *Chem. Soc.* 114 (1999) 313.
- [622] L.Q. Wang, K.F. Ferris, J.P. Winokur, A.N. Shultz, D.R. Baer, M.H. Engelhard, *J. Vac. Sci. Technol. A* 16 (1998) 3034.
- [623] S.P. Bates, M.J. Gillan, G. Kresse, *J. Phys. Chem. B* 102 (1998) 2017.
- [624] G. Kresse, J. Furthmüller, *Phys. Rev. B* 54 (1996) 11169.
- [625] G. Kresse, J. Furthmüller, *Comput. Mater. Sci.* 6 (1996) 15.
- [626] G. Kresse, J. Hafner, *Phys. Rev. B* 47 (1993) 558.
- [627] K.S. Kim, M.A. Barteau, *Surf. Sci.* 223 (1989) 13.
- [628] E. Román, F.J. Bustillo, J.L. de Segovia, *Vacuum* 41 (1990) 40.
- [629] K.S. Kim, M.A. Barteau, *J. Mol. Catal.* 63 (1990) 103.
- [630] L. Gamble, L.S. Jung, C.T. Campbell, *Surf. Sci.* 348 (1996) 1.
- [631] V.S. Lusvardi, M.A. Barteau, W.R. Dolinger, W.E. Farneth, *J. Phys. Chem.* 100 (1996) 18183.

- [632] H. Idriss, K.S. Kim, M.A. Barteau, *Surf. Sci.* 262 (1992) 113.
- [633] H. Idriss, K.S. Kim, M.A. Barteau, *J. Catal.* 139 (1993) 119.
- [634] H. Idriss, M.A. Barteau, *Catal. Lett.* 40 (1996) 147.
- [635] H. Idriss, K.G. Pierce, M.A. Barteau, *J. Am. Chem. Soc.* 116 (1994) 3063.
- [636] A.B. Sherrill, V.S. Lusvardi, J. Eng., J.G. Chen, M.A. Barteau, *Catal. Today* 63 (2000) 43.
- [637] S. Cannizzaro, *Ann. Chemie Pharmac.* 88 (1853) 129.
- [638] K.G. Pierce, M.A. Barteau, *J. Org. Chem.* 60 (1995) 2405.
- [639] H. Idriss, M.A. Barteau, *Langmuir* 10 (1994) 3693.
- [640] H. Idriss, M.A. Barteau, Reductive coupling of cyclic ketones on reduced titania (0 0 1) single crystal surfaces, in: M. Guisnet (Ed.), *Heterogeneous Catalysis and Fine Chemicals III*, vol. 78, Elsevier, Amsterdam, 1993, 463 pp.
- [641] K.G. Pierce, M.A. Barteau, *J. Phys. Chem.* 98 (1994) 3882.
- [642] K.G. Pierce, V.S. Lusvardi, M.A. Barteau, Catalytic formation of carbon–carbon bonds in ultrahigh vacuum: cyclotrimerization of alkynes on reduced TiO₂ surfaces, in: J.W. Hightower, W.N. Delgass, E. Iglesia, A.T. Bell (Eds.), *Proceedings of the 11th International Congress on Catalysis—40th Anniversary, Studies in Surface Science and Catalysis*, vol. 101, Elsevier, Amsterdam, 1996.
- [643] K.G. Pierce, M.A. Barteau, *Surf. Sci.* 326 (1995) L473.
- [644] A.B. Sherrill, M.A. Barteau, *J. Mol. Catal. A* 184 (2002) 301.
- [645] K.G. Pierce, M.A. Barteau, *J. Mol. Catal.* 94 (1994) 389.
- [646] A.B. Sherrill, J.W. Medlin, J.G. Shen, M.A. Barteau, *Surf. Sci.* (2001).
- [647] A.B. Sherrill, V.S. Lusvardi, M.A. Barteau, *Langmuir* 15 (1999) 7615.
- [648] K. Sakamaki, K. Itoh, A. Fujishima, Y. Gohshi, *J. Vac. Sci. Technol. A* 8 (1990) 614.
- [649] K. Sakamaki, S. Matsunaga, K. Itoh, A. Fujishima, Y. Gohshi, *Surf. Sci.* 219 (1989) L531.
- [650] S. Suzuki, Y. Yamaguchi, H. Onishi, T. Sasaki, K.-i. Fukui, Y. Iwasawa, *J. Chem. Soc., Faraday Trans. 94* (1998) 161.
- [651] H. Raza, P.L. Wincott, G. Thornton, R. Casanova, A. Rodriguez, *Surf. Sci.* 402–404 (1998) 710.
- [652] S. Suzuki, H. Onishi, K.-i. Fukui, Y. Iwasawa, *Chem. Phys. Lett.* 304 (1999) 225.
- [653] T. Sasaki, K.-i. Fukui, Y. Iwasawa, *Stud. Surf. Sci. Catal.* 132 (2001) 749.
- [654] S. Suzuki, H. Onishi, T. Sasaki, K.-i. Fukui, Y. Iwasawa, *Catal. Lett.* 54 (1998) 177.
- [655] L. Gamble, L.S. Jung, C.T. Campbell, *Langmuir* 11 (1995) 4505.
- [656] L. Gamble, M.B. Hugenschmidt, C.T. Campbell, T.A. Jurgens, J.W. Rogers Jr., *J. Am. Chem. Soc.* 115 (1993) 12096.
- [657] L. Gamble, M.A. Henderson, C.T. Campbell, *J. Phys. Chem. B* 102 (1998) 4536.
- [658] M.A. Fox, M.T. Dulay, *Chem. Rev.* 93 (1993) 341.
- [659] A. Hagfeldt, M. Grätzel, *Chem. Rev. (Washington, DC)* 95 (1995) 49.
- [660] E. Wilson, *C&EN* 1 (1996) 29.
- [661] A. Hagfeldt, M. Grätzel, *Acc. Chem. Res.* 33 (2000) 269.
- [662] V. Shklover, M. Grätzel, *Proc. SPIE-Int. Soc. Opt. Eng.* 3469 (1998) 134.
- [663] K.S. Finnie, J.R. Bartlett, J.L. Woolfrey, *Langmuir* 14 (1998) 2744.
- [664] G. Lu, A. Linsebigler, J.T. Yates Jr., *J. Phys. Chem.* 99 (1995) 7626.
- [665] J.C.S. Wong, A. Linsebigler, G. Lu, J. Fan, J.T. Yates Jr., *J. Phys. Chem.* 99 (1995) 335.
- [666] D. Brinkley, T. Engel, *Surf. Sci.* 415 (1998) L1001.
- [667] D. Brinkley, T. Engel, *J. Phys. Chem. B* 102 (1998) 7596.
- [668] D. Brinkley, T. Engel, *J. Phys. Chem. B* 104 (2000) 9836.
- [669] V. Shapovalov, E.V. Stefanovich, T.N. Truong, *Surf. Sci.* 498 (2002) L103.
- [670] D.H. Fairbrother, V.P. Holbert, K.A. Briggman, P.C. Stair, E. Weitz, *Proc. SPIE Int. Soc. Opt. Eng.* 2547 (1995) 248.
- [671] S.J. Garrett, V.P. Holbert, P.C. Stair, E. Weitz, *J. Chem. Phys.* 100 (1994) 4615.
- [672] S.J. Garrett, V.P. Holbert, P.C. Stair, E. Weitz, *J. Chem. Phys.* 100 (1994) 4626.
- [673] V.P. Holbert, S.J. Garrett, P.C. Stair, E. Weitz, *Surf. Sci.* 346 (1996) 189.
- [674] S.H. Kim, K.A. Briggman, P.C. Stair, E. Weitz, *J. Vac. Sci. Technol. A* 14 (1996).
- [675] S.H. Kim, P.C. Stair, E. Weitz, *Langmuir* 14 (1998) 4156.
- [676] S.H. Kim, P.C. Stair, E. Weitz, *J. Chem. Phys.* 108 (1998) 5080.
- [677] S.H. Kim, P.C. Stair, E. Weitz, *Chem. Phys. Lett.* 302 (1999) 511.
- [678] S.H. Kim, P.C. Stair, E. Weitz, *Surf. Sci.* 445 (2000) 177.

- [679] P. Antoniewicz, Phys. Rev. B 21 (1980) 3811.
- [680] M.L. Garcia Gonzalez, P. Salvador, J. Electroanal. Chem. 325 (1992) 369.
- [681] M.L. Garcia Gonzalez, P. Salvador, J. Electroanal. Chem. 326 (1992) 323.
- [682] M.L. Garcia Gonzalez, A. Martinez Chaparro, P. Salvador, J. Photochem. Photobiol. A 73 (1993) 221.
- [683] D. Tafalla, M. Pujadas, P. Salvador, Surf. Sci. 215 (1989) 190.
- [684] P. Salvador, Surf. Sci. 192 (1987) 36.
- [685] D. Tafalla, P. Salvador, Ber. Bunsenges. Phys. Chem. 91 (1987) 475.
- [686] M.T. Spitler, M. Calvin, J. Chem. Phys. 66 (1977) 4294.
- [687] J.M. Lantz, R. Baba, R.M. Corn, J. Phys. Chem. 97 (1993) 7392.
- [688] J.M. Lantz, R.M. Corn, J. Phys. Chem. 98 (1994) 9387.
- [689] P.R. Unwin, A.J. Bard, J. Phys. Chem. 96 (1992) 5035.
- [690] C.M. Wang, T.E. Mallouk, J. Phys. Chem. 94 (1990) 4276.
- [691] K. Shaw, P. Christensen, A. Hamnett, Electrochim. Acta 41 (1996) 719.
- [692] H. Yanagi, S. Chen, P.A. Lee, K.W. Nebesny, N.R. Armstrong, A. Fujishima, J. Phys. Chem. 100 (1996) 5447.
- [693] S.E. Gilbert, J.H. Kennedy, Surf. Sci. 225 (1990) L1.
- [694] S.E. Gilbert, J.H. Kennedy, J. Electrochem. Soc. 135 (1988) 2385.
- [695] F.R.F. Fan, A.J. Bard, J. Phys. Chem. 94 (1990) 3761.
- [696] D.F. Cox, T.B. Fryberger, S. Semancik, Surf. Sci. 224 (1989) 121.
- [697] F.H. Jones, R. Dixon, J.S. Foord, R.G. Egdell, J.B. Pethica, Surf. Sci. 367 (1997) 376.
- [698] C.L. Pang, S.A. Haycock, H. Raza, P.J. Møller, G. Thornton, Phys. Rev. B 62 (2000) R7778.
- [699] M. Sinner-Hettenbach, M. Göthelid, J. Weissenrieder, H. von Schenck, T. Weiβ, N. Barsan, U. Weimar, Surf. Sci. 477 (2001) 2001.
- [700] I. Manassidis, J. Goniakowski, L.N. Kantorovich, M.J. Gillan, Surf. Sci. 339 (1995) 258.
- [701] A. Atrei, E. Zanazzi, U. Bardi, G. Rovida, Surf. Sci. 475 (2001) L223.
- [702] H. Over, Prog. Surf. Sci. 58 (1998) 249.
- [703] H. Over, Y.D. Kim, A.P. Seitsonen, S. Wendt, E. Lundgren, M. Schmid, P. Varga, A. Morgante, G. Ertl, Science 287 (2000).
- [704] Y.D. Kim, A.P. Seitsonen, S. Wendt, J. Wang, C. Fan, K. Jacobi, H. Over, G. Ertl, J. Phys. Chem. B 105 (2001) 3752.
- [705] H. Over, A.P. Seitsonen, E. Lundgren, M. Schmid, P. Varga, Surf. Sci. 515 (2002) 143.
- [706] S.B. Basame, D. Habel-Rodriguez, D.J. Keller, Appl. Surf. Sci. 183 (2001) 62.
- [707] M. Kawasaki, K. Takahashi, T. Maeda, R. Tsuchiya, M. Shinohara, O. Ishiyama, T. Yonezawa, M. Yoshimoto, H. Koinuma, Science 266 (1994) 1540.
- [708] M.R. Castell, Surf. Sci. 516 (2002) 33.
- [709] N. Erdman, K.R. Poepelmeier, M. Asta, O. Warschkow, D.E. Ellis, L.D. Marks, Nature 419 (2002) 55.
- [710] W. Weiss, W. Ranke, Prog. Surf. Sci. 70 (2002) 1.
- [711] A.E. Taverner, A. Gulino, R.G. Egdell, T.J. Tate, Appl. Surf. Sci. 90 (1995) 383.
- [712] M. Batzill, E.L.D. Hebenstreit, W. Hebenstreit, U. Diebold, Chem. Phys. Lett., in press.
- [713] P. Hoyer, Langmuir 12 (1996) 1411.
- [714] S.M. Liu, L.M. Gan, L.H. Liu, W.D. Zhang, H.C. Zheng, Chem. Mater. 14 (2002) 1391.
- [715] S.D. Burnside, V. Shklover, C. Barbe, P. Comte, F. Arendse, K. Brookes, M. Grätzel, Chem. Mater. 10 (1998) 2419.
- [716] J.E. Sunstrom IV, W.R. Moser, B. Marhik-Guerts, Chem. Mater. 8 (1996).
- [717] H.A. Bullen, S.J. Garrett, Nano Lett. 2 (2002) 739.
- [718] K. Subramanya Mayya, D.I. Gittins, F. Caruso, Chem. Mater. 13 (2001) 3833.
- [719] F. Schüth, Chem. Mater. 13 (2001) 3184.
- [720] Y.C. Zhu, C.X. Ding, Nanostruct. Mater. 11 (1999) 427.
- [721] M. Iida, T. Sasaki, M. Watanabe, Chem. Mater. 10 (1998) 3780.
- [722] Y. Yin, Y. Lu, B. Gates, Y. Xia, Chem. Mater. 13 (2001) 1146.
- [723] P. Yang, D. Zhao, D.I. Margolese, B.F. Chmelka, G.D. Stucky, Nature 396 (1998) 152.
- [724] T. Moritz, J. Reiss, K. Diesner, D. Su, A. Chemseddine, J. Phys. Chem. B 101 (1997) 8052.
- [725] E. Asari, R. Souda, Surf. Sci. 486 (2001) 203.

- [726] H.-J. Freund, H. Kuhlenbeck, J. Libuda, G. Rupprechter, M. Bäumer, H. Hamann, *Top. Catal.* 15 (2001) 201.
- [727] D.F. Ogletree, H. Bluhm, G. Lebedev, C.S. Fadley, Z. Hussain, M. Salmeron, *Rev. Sci. Instrum.* 73 (2002) 3872.
- [728] P.B. Rasmussen, B.L.M. Hendriksen, H. Zeijlemaker, H.G. Ficke, J.W.M. Frenken, *Rev. Sci. Instrum.* 69 (1988) 3879.
- [729] B.L.M. Hendriksen, J.W.M. Frenken, *Phys. Rev. Lett.* 89 (2002) 046101.
- [730] K.Y. Kung, P. Chen, F. Wei, G. Rupprechter, Y.R. Shen, G.A. Somorjai, *Rev. Sci. Instrum.* 72 (2001) 1806.
- [731] P.A.M. Hotsenpiller, J.D. Bolt, W.E. Farneth, J.B. Lowekamp, G.S. Rohrer, *J. Phys. Chem. B* 102 (1998) 3216.
- [732] T. Miki, H. Yanagi, *Langmuir* 14 (1998) 3405.
- [733] M. Svetina, L. Colombi Ciacchi, O. Sbaizero, S. Meriani, A. De Vita, *Acta Mater.* 49 (2001) 2169.
- [734] G. Chiarello, R. Barberi, E. Colavita, *Appl. Surf. Sci.* 99 (1996) 15.
- [735] Z. Chang, S. Piligkos, P.J. Møller, *Phys. Rev. B* 64 (2001) 165410/1.
- [736] J. Evans, B.E. Hayden, G. Lu, *J. Chem. Soc., Faraday Trans.* 92 (1996) 4733.
- [737] H.R. Sadeghi, V.E. Henrich, *Appl. Surf. Sci.* 19 (1984) 330.
- [738] B.E. Hayden, A. King, M.A. Newton, *Chem. Phys. Lett.* 269 (1997) 485.
- [739] F. Cosandey, P. Lu, *Structure and Properties of Interfaces in Ceramics Symposium, Mater. Res. Soc.* 1995, pp. 301–306.
- [740] M. Bowker, P. Stone, R. Bennett, N. Perkins, *Surf. Sci.* 497 (2002) 155.
- [741] S. Fischer, K.D. Schierbaum, W. Göpel, *Sens. Actuators B* 31 (1996) 13.
- [742] S. Fischer, F. Schneider, K.K. Schierbaum, *Vacuum* 47 (1996) 1149.
- [743] W.-x. Xu, K.D. Schierbaum, W. Göpel, *J. Solid State Chem.* 119 (1995) 237.
- [744] K. Tamura, U. Bardi, Y. Nihei, *Surf. Sci.* 216 (1989) 209.
- [745] K. Tamura, M. Owari, Y. Nihei, *Bull. Chem. Soc. Jpn.* 61 (1988) 1539.
- [746] K. Tamura, M. Kudo, M. Owari, Y. Nihei, *Chem. Lett.* (1986) 1921.
- [747] M. Marien, T. Wagner, D.L. Carroll, J. Marien, D.A. Bonnell, M. Rühle, *MRS Bull.* XXII (1997) 42.
- [748] P.J. Møller, S.A. Komolov, E.F. Lazneva, *Springer Ser. Surf. Sci.* 33 (1993) 156.
- [749] M.C. Wu, P.J. Møller, *Chem. Phys. Lett.* 171 (1990) 136.
- [750] M.C. Wu, P.J. Møller, *Surf. Sci.* 235 (1990) 228.
- [751] D. Abriou, D. Gagnot, J. Jupille, F. Creuzet, *Surf. Rev. Lett.* 5 (1998) 387.
- [752] X. Lai, D.W. Goodman, *J. Molec. Catal.* 162 (2000) 33.
- [753] C.C. Chusuei, X. Lai, K.A. Davis, E.K. Bowers, J.P. Fackler, D.W. Goodman, *Langmuir* 17 (2001) 4113.
- [754] C. Xu, D.W. Goodman, *Chem. Phys. Lett.* 263 (1996) 13.
- [755] Z. Yang, R. Wu, D.W. Goodman, *Phys. Rev. B* 61 (2000) 14066.
- [756] S.C. Parker, A.W. Grant, V.A. Bondzie, C.T. Campbell, *Surf. Sci.* 441 (1999) 10.
- [757] V.A. Bondzie, S.C. Parker, C.T. Campbell, *J. Vac. Sci. Technol. A* 17 (1999) 1717.
- [758] N. Nilius, N. Ernst, H.J. Freund, *Surf. Sci.* 478 (2001) L327.
- [759] V.E. Henrich, R.L. Kurtz, *Phys. Rev. B* 23 (1981) 6280.
- [760] L.Q. Wang, K.F. Ferris, M.H. Engelhard, *Surf. Sci.* 440 (1999) 60.
- [761] V.V. Lobanov, *Zh. Fiz. Khim.* 70 (1996) 1440.
- [762] V.E. Henrich, G. Dresselhaus, H.J. Zeiger, *Solid State Commun.* 24 (1977) 623.
- [763] S. Eriksen, P.D. Naylor, R.G. Egddell, *Spectrochim. Acta, Part 43A* 12 (1987) 1535.
- [764] D.R. Baer, L.Q. Wang, A.N. Shultz, J.L. Daschbach, W.M. Hetherington III, M.H. Engelhard, in: *Proceedings of the New Tech. Charact. Corros. Stress Corros.*, 1996, p. 73.
- [765] S. Krischok, O. Hofft, J. Gunster, J. Stultz, D.W. Goodman, V. Kempter, *Surf. Sci.* 495 (2001) 8.
- [766] J. Goniakowski, S. Bouette-Russo, C. Noguera, *Surf. Sci.* 284 (1993) 315.
- [767] J. Goniakowski, C. Noguera, *Surf. Sci.* 330 (1995) 337.
- [768] J. Goniakowski, M.J. Gillan, *Surf. Sci.* 350 (1996) 145.
- [769] V.V. Lobanov, *Zh. Fiz. Khim.* 70 (1996) 2267.
- [770] D. Vogtenhuber, R. Podloucky, J. Redinger, *Surf. Sci.* 404 (1998) 798.
- [771] F.J. Bustillo, E. Román, J.L. de Segovia, *Vacuum* 39 (1989) 659.
- [772] F.J. Bustillo, E. Román, J.L. de Segovia, *Vacuum* 41 (1990) 19.
- [773] P.B. Smith, S.L. Bernasek, *Surf. Sci.* 188 (1987) 241.
- [774] T.K. Sham, M.S. Lazarus, *Chem. Phys. Lett.* 68 (1979) 426.

- [775] E. Kobayashi, K. Matsuda, G. Mizutani, S. Ushioda, *Surf. Sci.* 428 (1999) 294.
- [776] P. Fenter, L. Cheng, S. Rihs, M. Machesky, M.J. Bedzyk, N.C. Sturchio, *J. Colloid Interf. Sci.* 225 (2000) 154.
- [777] R. Hengerer, L. Kavan, B. Bolliger, M. Erbudak, M. Grätzel, *Mater. Res. Soc. Symp. Proc.* 623 (2000) 43.
- [778] L.M. Wu, Y.F. Zhang, Y. Li, J.Q. Li, L.X. Zhou, *Jiegou Huaxue* 18 (1999) 304.
- [779] J.A. Rodriguez, J. Hrbek, J. Dvorak, T. Jirsak, A. Maiti, *Chem. Phys. Lett.* 336 (2001) 377.
- [780] Y. Yamaguchi, H. Onishi, Y. Iwasawa, *J. Chem. Soc., Faraday Trans.* 91 (1995).
- [781] I.D. Cocks, Q. Guo, E.M. Williams, *Surf. Sci.* 390 (1997) 119.
- [782] Q. Guo, I. Cocks, E.M. Williams, *J. Chem. Phys.* 106 (1997) 2924.
- [783] P. Persson, A. Stashans, R. Bergstrom, S. Lunell, *Int. J. Quantum Chem.* 70 (1998) 1055.